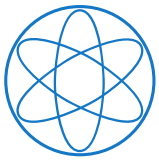


FAKULTÄT FÜR PHYSIK
TECHNISCHE UNIVERSITÄT MÜNCHEN

Active Line Ratio Spectroscopy on Thermal Helium at ASDEX Upgrade

Michael Thomas Griener

Vollständiger Abdruck der von der Fakultät für Physik der Technischen Universität München zur Erlangung des akademischen Grades eines Doktors der Naturwissenschaften genehmigten Dissertation.

Vorsitzende(r):	Prof. Dr. Björn Garbrecht
Prüfer(in) der Dissertation:	1. Prof. Dr. Ulrich Stroth
	2. Priv.-Doz. Dr. habil. Frank Eisenhauer

Die Dissertation wurde am 30. Mai 2018 bei der Technischen Universität München eingereicht und durch die Fakultät für Physik am 12. Juli 2018 angenommen.

FAKULTÄT FÜR PHYSIK
TECHNISCHE UNIVERSITÄT MÜNCHEN

Active Line Ratio Spectroscopy on Thermal Helium at ASDEX Upgrade

Author: Michael Thomas Griener
Supervisor: Prof. Dr. Ulrich Stroth
Advisor: Univ.-Doz. Dr. Elisabeth Wolfrum

Submission Date: May 30^{th}, 2018

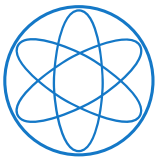

HELMHOLTZ
RESEARCH FOR GRAND CHALLENGES

EUROfusion

Abstract

Nuclear fusion is foreseen as one of the sustainable concepts for future electricity power production. The most advanced approach toward a fusion power plant is the magnetic confinement of high temperature plasmas in tokamaks and stellarators. In these devices, the plasma column outside the last closed magnetic flux surface features a rapid decay. In this region of open field lines, called scrape-off layer (SOL), heat and power are transported to the divertor via transport parallel to the magnetic field. The local power deposited directly on the first wall depends strongly on the transport perpendicular to the magnetic field driven by filamentary turbulence. These mechanisms can seriously damage the first wall materials of the devices. With the goal of gaining a better understanding of steady-state as well as fast transport processes, this thesis describes the design and implementation of a thermal helium beam as plasma edge diagnostic for the ASDEX Upgrade (AUG) tokamak. This diagnostic provides simultaneous measurements of the electron density n_e and electron temperature T_e with high spatiotemporal resolution.
For thermal helium beam emission line ratio spectroscopy, neutral helium is locally injected into the plasma. Measured line ratios can be used together with a collisional radiative model (CRM) to reconstruct the underlying electron temperature and density. Ratios from the same spin species are used for electron density reconstruction, whereas spin-mixed ratios are sensitive to electron temperature changes.

The suitability of specific line ratios for diagnostic purposes depends on the investigated n_e and T_e range. To test which line ratio combinations are best suitable in the plasma edge region of AUG, the line resolved emission intensities of seven He I lines were measured for different plasma scenarios. The resulting n_e and T_e profiles were compared to other available diagnostics at AUG, which also enabled the validation of different CRMs.
The information gained from this study facilitates the development and bench-marking of a dedicated set of hardware components for the fast thermal helium beam diagnostic. A special piezoelectric valve is placed inside the vacuum chamber close to the plasma periphery. It enables the local injection and fast chopping of thermal gas beams. The valve can be used for variable applications due to its outstanding performance regarding switching times and the flexibility in the utilized gas species and flux between 10^{18}–10^{21} particles per second.
The achieved spatial resolution of helium beam spectroscopy of up to 3 mm relies on the localized helium injection combined with a newly designed optical head. It is equipped with 53 lines of sight which are aligned parallel to the magnetic field lines in the observation region. The optics cover a radial as well as poloidal distance of 8 cm of the plasma edge region.

The line emission of four He I lines are measured with a newly developed 32 channel polychromator system. It is based on dichroic mirrors to separate the wavelengths, small band interference filters and linear array photomultiplier tubes. The achieved high signal level allows a data acquisition rate of 900 kHz.

Within this thesis, active line ratio spectroscopy on helium was performed at ASDEX Upgrade for the first time, enabled by the newly developed hardware system. The thermal helium beam diagnostic supplements the AUG edge diagnostics, offering fast and spatially highly resolved electron temperature and density measurements which cover the plasma edge and SOL region. The high spatiotemporal resolution allows the measurement of perturbations of electron temperature and density in microsecond times scales. Edge localized modes (ELMs), filaments and other turbulent structures are resolved, allowing the simultaneous determination of n_e and T_e of single structures for the first time. The diagnostic capabilities are demonstrated with selected measurements during regime transitions from L-mode over I-phase to H-mode as well as from I-mode to H-mode. This showed, e.g. the flattening of plasma profiles during I-phase bursts. Furthermore, the radial localization of fast oscillating modes and the estimation of their impact on n_e and T_e is possible, as demonstrated with the weakly coherent mode during I-mode. In addition it is demonstrated that the thermal helium beam diagnostic can be used to measure propagation velocities of intermittent events. In agreement with literature, the distribution of radial velocities of inter-ELM filaments peaks at 340 m/s, whereas filaments during ELMs are much faster with 1.4 km/s.

Zusammenfassung

Kernfusion könnte in der Zukunft einen Beitrag zur nachhaltigen Erzeugung elektrischer Energie leisten. Die vielversprechendsten Konzepte zur Entwicklung eines Kraftwerks sind Tokamaks und Stellaratoren, in denen thermische Fusionsplasmen magnetisch eingeschlossen werden. Besonders bedeutend ist hierbei die Plasmarandregion, in welcher das Plasma außerhalb der letzten geschlossenen magnetischen Flussfläche rasch zerfällt. Diese Region offener Feldlinien nennt man Abschälschicht. Hier werden Teilchen und Energie zum Divertor und zur Gefäßwand transportiert. Die Leistungsabfuhr wird durch den Transport parallel zu den Feldlinien dominiert, welche in der nahen Abschälschicht zum Divertor führen. Durch orthogonal zu den magnetischen Flussflächen verlaufenden, turbulenzgetriebenen Transport können Filamente aber auch direkt die Gefäßwand erreichen. Aufgrund der enormen Belastung, der die Gefäßwand und der Divertor durch den Leistungseintrag ausgesetzt sind, muss das Verständnis der Transportprozesse verbessert werden. Hierfür wurde im Rahmen dieser Arbeit eine thermische Heliumstrahldiagnostik für den Plasmarand von ASDEX Upgrade (AUG) entwickelt. Diese ermöglicht die simultane Messung der Elektronendichte n_e und -temperatur T_e mit hoher räumlicher und zeitlicher Auflösung. Die Diagnostik beruht auf der Messung verschiedener Linienemissionsintensitäten von neutralem Helium, welches lokal in das Plasma eingebracht wird. Mit Hilfe eines Stoß-Strahlungs-Modells werden Verhältnisse gemessener Linienintensitäten in die zugrunde liegenden Plasmaparameter übersetzt. Linienintensitätsverhältnisse aus zwei spingleichen Übergängen von Helium erlauben hierbei die Berechnung der Elektronendichte, während Verhältnisse aus einer Singulett-Line und einer Triplett-Line hauptsächlich sensitiv auf Temperaturänderungen reagieren.

Um die geeignetsten Linienverhältnisse zur Diagnostik der Plasmarandregion in AUG zu identifizieren, wurde die wellenlängenaufgelöste Emission von sieben He I-Linien für verschiedene Plasmaszenarien gemessen. Die resultierenden n_e- und T_e-Profile ermöglichen den Vergleich mit anderen Diagnostiken in AUG sowie die Validierung verschiedener Stoß-Strahlungs-Modelle.
Die hierbei erlangten Erkenntnisse flossen in die Entwicklung spezialisierter Hardwarekomponenten für die thermische Heliumstrahldiagnostik ein. Ein spezielles piezoelektrisches Ventil, das nahe am Plasma im Inneren der Vakuumkammer angebracht wurde, ermöglicht die schnell gepulste Injektion eines thermischen Gasstrahls. Aufgrund kurzer Schaltzeiten sowie der hohen Variabilität der verwendeten Gassorte und des einstellbaren Gasflusses von $10^{18} - 10^{21}$ Teilchen pro Sekunde ist das Ventil vielseitig einsetzbar.
Die erreichte räumliche Auflösung der Heliumstrahldiagnostik von bis zu 3 mm beruht auf der lokalisierten Helium-Injektion, kombiniert mit einer speziellen Beobachtungsoptik. Diese verfügt über 53 Sichtlinien, welche am Beobachtungsort parallel zum Magnetfeld ausgerichtet sind und einen radialen und poloidalen Bereich von 8 cm in der Plasmarandregion abdecken.

Die Linienemission von vier He I-Linien wird mit einem neu entworfenen Polychromatorsystem gemessen. Dieses verfügt über 32 Kanäle und ist aus dichroischen Spiegeln, schmalbandigen Interferenzfiltern und Zeilenphotomultipliern aufgebaut. Die hohe Signalstärke ermöglicht eine zeitliche Auflösung von 900 kHz.

Ermöglicht durch die neu entwickelten Hardwarekomponenten wurde im Rahmen dieser Arbeit zum ersten Mal eine aktive Heliumstrahldiagnostik an AUG eingesetzt. Diese bietet räumlich und zeitlich hoch aufgelöste Messungen der Elektronentemperatur und -dichte, welche einen breiten Randbereich des Plasmas abdecken. Randlokalisierte Moden (ELMs), Filamente und andere turbulente Strukturen können aufgelöst werden, was erstmals die Messung der Plasmaparameter innerhalb einzelner Strukturen ermöglicht. Demonstriert wurde die Leistung der Diagnostik durch ausgewählte Messungen während Regimeübergängen von der L-Mode über die I-Phase hin zur H-Mode sowie zwischen I-Mode und H-Mode. Es wurde gezeigt, dass Bursts in der I-Phase zu einer Abflachung der Plasmaprofile führen. Darüber hinaus ermöglicht die neue Heliumstrahldiagnostik die radiale Lokalisation schnell-oszillierender Moden sowie die Bestimmung deren Einflusses auf Dichte und Temperatur. Zudem wurde demonstriert, dass die Propagationsgeschwindigkeit intermittierender Störungen im Plasmarand bestimmt werden kann. In Übereinstimmung mit bisherigen Veröffentlichungen wurde gezeigt, dass die radiale Geschwindigkeit von Filamenten zwischen ELMs mit 340 m/s deutlich geringer ist als die radiale Propagationsgeschwindigkeit von ELM-Filamenten mit 1.4 km/s.

Contents

1. Introduction and basics

1.1. Nuclear fusion

Nuclear fusion constitutes the basis for all life. All atoms heavier than hydrogen have been created by nuclear fusion. Only the resulting variety of elements makes life possible. Moreover, all life on earth depends on the energy from the sun. The sun is radiating due to the nuclear fusion processes in its core. On earth, radiation of the sun is converted into biochemical energy by photosynthesis, which enables plant growth and led over millions of years to the generation of fossil fuels as oil, coal and gas. Till this day the increasing energy demand of modern societies is mainly fed by burning these fossil fuels [IEA17], which leads to CO_2 release and the devastating consequences for our climate. Therefore more and more effort is put into the development of renewable energies, which themselves mostly rely directly or indirectly on the energy of the sun. Most of the renewable concepts struggle with geographical restrictions and the fluctuations of the driving sources as wind or direct sun irradiation [Wag14]. Therefore it seems desirable to build power plants which use controlled fusion on earth directly as a primary energy source. Such base load power plants could combine the reliability of current fossil and nuclear fission power plants with a long term safe and CO_2 emission free operation, which are the advantages of renewable concepts.
As fuel for nuclear fusion on earth, the hydrogen isotopes deuterium and tritium, which fuse via the reaction

$$ {}^{2}_{1}\mathrm{D} + {}^{3}_{1}\mathrm{T} \longrightarrow {}^{4}_{2}\mathrm{He} + \mathrm{n} + 17.6\,\mathrm{MeV} \tag{1.1} $$

to helium, are the most promising candidates. This reaction has the highest reaction cross section for the conditions achievable in fusion power plants. Furthermore, both fuels are available in great quantity. Deuterium can be extracted from water after electrolysis, as 0.015 % of hydrogen is deuterium [Gat70]. Tritium, however, is unstable with a decay time of 12.3 years, so no relevant amount of natural tritium can be found on earth. But it can be generated from lithium by directly using the fusion neutrons (cf. Eq. 1.1) and the reactions

$$ {}^{6}_{3}\mathrm{Li} + \mathrm{n} \longrightarrow {}^{4}_{2}\mathrm{He} + {}^{3}_{1}\mathrm{T} $$
$$ {}^{7}_{3}\mathrm{Li} + \mathrm{n} \longrightarrow {}^{4}_{2}\mathrm{He} + {}^{3}_{1}\mathrm{T} + \mathrm{n}. $$

The energy which is released in the fusion process (cf. Eq. 1.1) is distributed among the alpha particle and the neutron inversely proportional to their respective mass.

To enable the fusion reaction from Eq. 1.1 in a thermalized environment, i.e. to perform thermonuclear fusion, high temperatures are needed. At these high temperatures, atoms are ionized and therefore form a plasma consisting of positively charged ions and negatively charged electrons. To fuse, ions have to overcome the Coulomb barrier to get close enough for interactions of the short-ranged strong nuclear force. The required temperature where the D-T reaction cross section has its maximum is around 15 keV, corresponding to 175 MK, hotter than the core of our sun.
If this temperature can be sustained only by the released energy from the fusion α particles, i.e. without external heating, the plasma is called ignited. To achieve this, the plasma density n as well as the energy confinement time τ_E has to be sufficiently high as already described in 1955 by the so-called Lawson criterion[1] [Law57]. The energy confinement time is a measure for the thermal insulation of the plasma, i.e. the decay time of the plasma temperature once all heating systems are switched off instantly. In the experiment it is defined in equilibrium as

$$\tau_\mathrm{E} = \frac{W_\mathrm{MHD}}{P_\mathrm{heat}}, \tag{1.2}$$

with the total stored energy in the plasma W_MHD and the heating power P_heat. For the D-T reaction at 15 keV the Lawson criterion

$$n \cdot \tau_\mathrm{E} > 2 \times 10^{20}\,\mathrm{s/m^3} \tag{1.3}$$

has to be fulfilled for a self burning plasma. To achieve this criterion in steady state, it is obvious that good confinement of the plasma is needed. In the sun, the burning plasma is confined by gravity due to the huge mass (cf. section A.1). On earth, magnetic confinement using the Lorentz force acting on the charged plasma particles seems to be the most promising way for a fusion power plant (cf. section 1.2).

1.2. Magnetic confinement fusion

The long history of magnetic confinement fusion research began in the 1940s [Isa10]. In 1960, the Max Planck Institute for Plasma Physics (IPP) was founded in Garching. As in these times the way toward a fusion power plant was not as clear as today [Fed14], the research activities were spread over a broad range of linear pinch devices. These machines should heat up the plasma adiabatically by magnetic compression, achieved by a fast increase of the magnetic field strength. Plasma instabilities, short confinement times and impurities, however, prevented the ongoing success of these machines. The impurities were mainly produced by the direct contact of the plasma with the two ends of the confining column.
More promising configurations overcome this problem by using toroidal devices for the confinement, which are studied at IPP since 1968. Two main concepts with static magnetic fields are

[1] Multiplication of the Lawson criterion with the temperature T yields the triple product $n \cdot T \cdot \tau_\mathrm{E}$, which is also often used as ignition criterion.

especially successful, the tokamak and the stellarator. The stellarator uses only external coils to produce the magnetic field cage, whereas the tokamak relies on a strong, transformer driven plasma current, which creates the resulting field structure. Both concepts are pursued at IPP, with the experiments ASDEX Upgrade (AUG) in Garching (cf. [Zoh15b] and Tab. A.1) and Wendelstein 7-X (W7-X) in Greifswald [Kry16]. As the tokamak ASDEX Upgrade is the machine at which this thesis is executed, the following part of the section is focused on the tokamak principle.

1.2.1. Magnetic confinement in a tokamak

The magnetic configuration of the toroidally symmetric tokamak is sketched in Fig. 1.1, together with the most important coil types. To describe the coordinates of a tokamak, the toroidal direction Φ, the poloidal direction Θ and the major plasma radius R are introduced as pictured in Fig. 1.2.

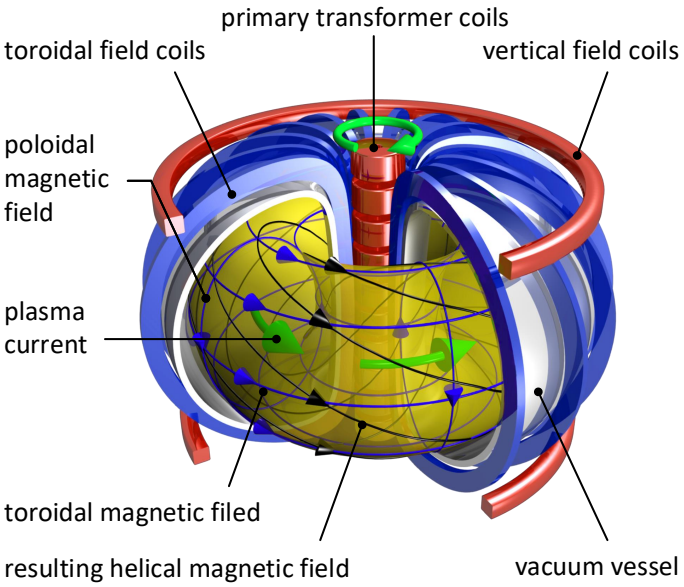

Figure 1.1.: Schematic drawing of a tokamak including the toroidal and vertical field coils as well as the primary transformer coils [adapted from Christian Brandt, IPP].

The main magnetic field B_Φ in toroidal direction is generated by the toroidal field coils. The field strength is not homogeneous and decays with increasing radius with $1/R$ due to the lower distance of the coils for smaller R. Therefore the inner side of the tokamak is called magnetic high field side (HFS), whereas the outer side is called magnetic low field side (LFS).
For a purely toroidal field both, the inhomogeneity of the magnetic field and the curvature of the field lines lead to particle drifts described by (cf. [Str11, Chapter 2])

$$\boldsymbol{v}_{\nabla B+\mathrm{curv}} = \left(\frac{mv_\perp^2}{2} + mv_\parallel^2\right)\frac{\boldsymbol{B}\times\nabla B}{qB^3}. \tag{1.4}$$

Both terms depend on the mass m and the charge q of the particles. The first term of Eq. 1.4 depends on the perpendicular velocity[2] and is called grad-B drift whereas the second term, which depends on the parallel velocity, is called curvature drift. The absolute drift velocity of ions and electrons is approximately the same, but it points in different directions due to the different signs of the charge. The consequential vertical charge separation builds up an electric field (see Fig. 1.2 a)), which itself leads to the electric-drift velocity

$$\boldsymbol{v}_{\boldsymbol{E}\times\boldsymbol{B}} = \frac{\boldsymbol{E}\times\boldsymbol{B}}{B^2}. \tag{1.5}$$

This drift velocity points radially outwards with the same sign for both species and leads to prompt particle losses. Therefore a purely toroidal field is not sufficient to confine a plasma effectively.

To overcome the charge separation, a poliodal magnetic field B_Θ can be added. This field is superposed with the toroidal field and leads to a twisting of the field-lines which subsequently form a helical pattern. Described by the Biot-Savart law, B_Θ is created by a strong current flowing in the plasma (cf. Fig. 1.2 b)). This current is inductively coupled into the plasma by the central solenoid which builds the primary transformer coil. The plasma acts as secondary coil. Due to the low resistance of the plasma (cf. subsection 2.1.1), loop voltages of several volts are sufficient to drive plasma currents $I_\mathrm{p} > 1\,\mathrm{MA}$.

The poliodal field however, has on account of the torus symmetry, a stronger vertical component in the center of the torus (HFS) compared to the LFS[3]. This leads to hoop stress (cf. Fig. 1.2 b)) which can be compensated by adding a homogeneous vertical field B_vert. It lowers the vertical component of the magnetic field in the inner, while strengthening the vertical component on the outer side of the torus. The vertical field, which can also be used for plasma positioning, is generated by the two large vertical field coils. Thus, the resulting magnetic field structure of a tokamak is able to confine the plasma in steady state.

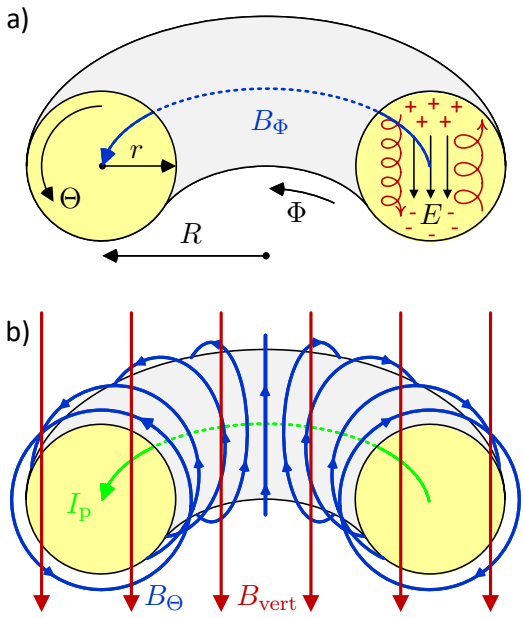

Figure 1.2.: Illustration of the tokamak coordinate system and the $\boldsymbol{v}_{\nabla B+\mathrm{curv}}$ drift a) and the poloidal and vertical fields in b).

[2] Perpendicular with respect to the magnetic field.

[3] As mentioned before, the term HFS and LFS originates on the radial gradient of the toroidal magnetic field, but it is also correct for the vertical component of the poloidal field.

The ratio between the plasma pressure[4] $p = nT$ and the magnetic pressure $p_{\mathrm{mag}} = B^2/2\mu_0$ is defined as the normalized plasma pressure

$$\beta = \frac{p}{p_{\mathrm{mag}}} = \frac{nT}{B^2/2\mu_0}. \tag{1.6}$$

For confined plasmas, β is always smaller than one and typically lies in the lower percent range for tokamaks. For nuclear reactors, a high β is required on the one hand to increase the plasma pressure in favour of a high fusion triple product (cf. Eq. 1.3) and on the other hand to keep the magnetic field strength as low as possible as the costs of large magnets increase with increasing B.

1.2.2. Magnetic flux surfaces

Flux surfaces are labeled with the so-called normalized poloidal flux radius ρ_{pol} [Zoh15a, Chapter 2]. It is defined as

$$\rho_{\mathrm{pol}} = \sqrt{\frac{\Psi - \Psi_{\mathrm{axis}}}{\Psi_{\mathrm{sep}} - \Psi_{\mathrm{axis}}}}, \tag{1.7}$$

A stationary magnetically confined plasma has to fulfill the equilibrium condition

$$\nabla p = \boldsymbol{j} \times \boldsymbol{B}. \tag{1.8}$$

By calculating the scalar product of Eq. 1.8 with $\boldsymbol{B}$, one can see[5] that $\boldsymbol{B} \cdot \nabla p = 0$. This means that the pressure is constant along the field lines, i.e. constant on surfaces with the same magnetic flux Ψ. The scalar product of Eq. 1.8 with $\boldsymbol{j}$ delivers on the same way $\boldsymbol{j} \cdot \nabla p = 0$. As also the current density is constant for a fixed Ψ, the term magnetic flux surface is developed.

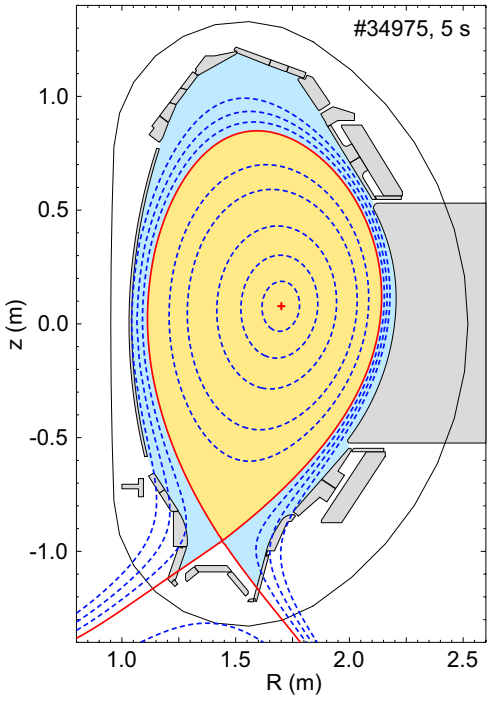

Figure 1.3.: Poloidal cross section of AUG in the lower single null magnetic configuration. The confined region (yellow area) is separated by the separatrix (red line) from the SOL (blue area).

The concept of toroidally symmetric flux surfaces $\Psi(R, z)$ allows the transition from the 3-D space into a 2-D plane (cf. Fig. 1.3), which is sufficient to describe the plasma properties in most cases. Because the heat conductivity parallel to field-lines, i.e. in the flux surfaces, is much higher compared to the radial one[6] [Pit97], i.e. perpendicular to the flux surfaces, the

[4] Pressure in general is given by $p = nk_{\mathrm{B}}T$. As the unit of temperature in fusion is commonly given in eV, the relation changes to $p = nT$.

[5] The scalar triple product $(\boldsymbol{j} \times \boldsymbol{B}) \cdot \boldsymbol{B} = 0$.

[6] The radial heat transport is described by the term "cross-field thermal conduction".

temperature can also be assumed to be constant on a flux surface. Connected over $p = nT$, this applies also for the plasma density n.
with the poliodal magnetic fluxes Ψ_{sep} and Ψ_{axis} at the separatrix and on the magnetic axis, respectively. It yields $\rho_{\text{pol}} = 0$ at the magnetic axis of the equilibrium and $\rho_{\text{pol}} = 1$ at the last closed magnetic flux surface, the so-called separatrix. The separatrix separates the confined region of the plasma with closed field lines ($\rho_{\text{pol}} < 1$; Fig. 1.3, yellow region), from the so-called scrape-off layer (SOL) where the field lines touch the wall ($\rho_{\text{pol}} > 1$; Fig. 1.3, blue region). The magnetic axis is marked in Fig. 1.3 with a red cross in the middle, the separatrix with the red line which closes at the so-called x-point.

1.2.3. The divertor concept

The region where the separatrix and the field lines in the near SOL touch the wall is called divertor. It was invented by IPP and for the first time installed in the year 1980 at the **A**xially **S**ymmetric **D**ivertor **Ex**periment (ASDEX), the precursor experiment of ASDEX Upgrade [Isa10].
With a peak of around $50\,\text{MWm}^{-2}$ [Her02], the divertor heat load is comparable to the power passing the suns surface. Short time scale transient events increase the power load even further (cf. section 2.2). Whereas the power load for present-day devices can be handled, the material limits for future devices and fusion power plants would clearly be exceeded without adapted plasma scenarios.

1.2.4. Next step devices and challenges

To realize a nuclear fusion power plant, the plasma confinement time appears to be one of the key factors. A measure for this is the so-called fusion energy gain factor Q which is the ratio of fusion power to auxiliary heating power injected into the plasma [Aym02]. As described in section 2.1, present-day devices as AUG are already equipped with sufficient heating systems to achieve the desired temperature of $10^8\,\text{K}$. Nevertheless, the confinement efficiency for medium sized tokamaks as AUG is by far too low, which results in a calculated $Q \ll 1$.
It has been shown that the energy confinement time of tokamaks as well as stellarators increases with increasing machine size, described by scaling laws (cf. [Str96, Edi99] and [Str11, Chapter 4 and 10]). Therefore an international collaboration is building a machine with approximately four times the size of AUG (cd. Tab. A.1), the **I**nternational **T**hermonuclear **E**xperimental **R**eactor, **ITER**. ITER, Latin for "the way", is built in Cadarache in southern France and should pave the way toward nuclear fusion power plants. Aiming for $Q = 10$ and fuelled with deuterium and tritium, a fusion power of 500 MW should be achieved with 50 MW of auxiliary heating [Aym02]. The subsequent step is the construction of a demonstration fusion power plant called **DEMO** [Fed14]. With an approximate size 50 % larger compared to ITER it should fulfill the requirements for commercial electricity production.

Increasing the size and magnetic field strength of fusion reactors improves the confinement time, but leads in the same way to new engineering and operational challenges. One already discussed issue is the power load on the first wall, which is limited to $10\,\mathrm{MWm^{-2}}$ in the divertor for next step devices [Her02, Edi99]. The resulting power load onto plasma facing components depends strongly on plasma edge parameters which are therefore discussed in the following section.

1.3. Plasma edge transport processes

The plasma edge region strongly determines the overall plasma behaviour as well as the resulting wall loads as illustrated in Fig. 1.4. Transport barriers which might build up close to the separatrix in the confined region lead to different confinement regimes as discussed in section 2.2. This underlying confinement regime determines the power and particle flux crossing the separatrix and entering the scrape-off layer (SOL). In the SOL heat and power are transported to the divertor via transport parallel to the magnetic field. The fraction of parallel and perpendicular heat flux leads to a distinct power fall-off length on the divertor target, which has a typical width of a few millimeters.

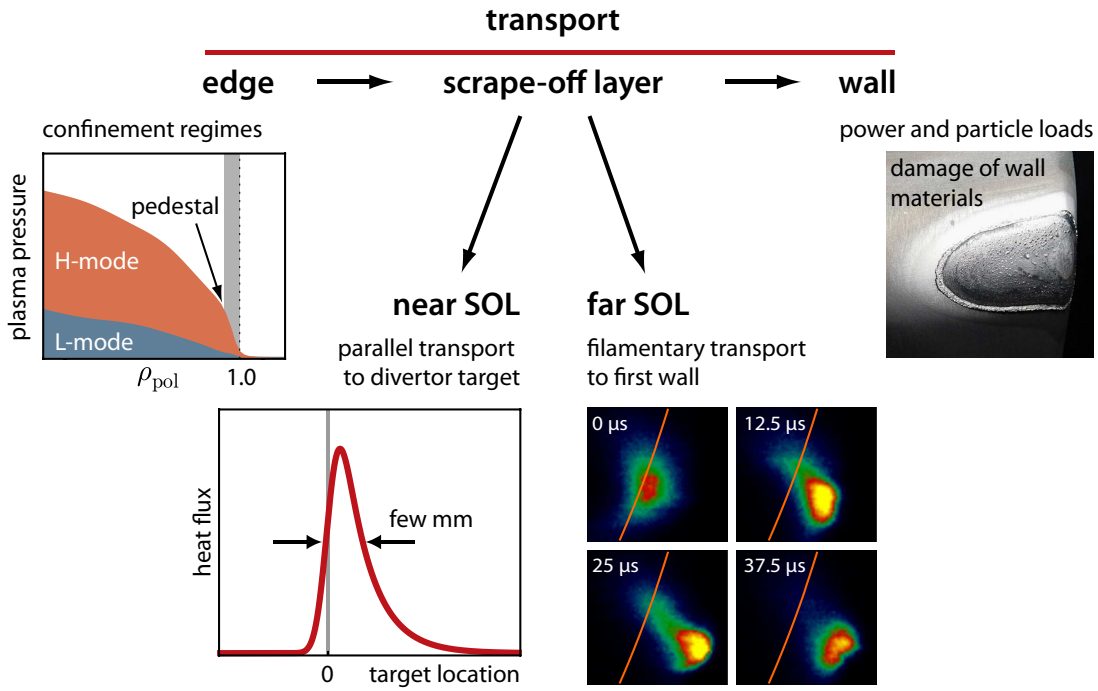

Figure 1.4.: Schematic representation of transport processes in the plasma edge and SOL, measurable with the thermal helium beam diagnostic. The transport is determine by the underlying confinement regime in the plasma edge region, the effective power fall of length in the near SOL [adapted from Michael Faitsch, IPP] and by turbulent filaments in the far SOL. These transport processes can lead to high power loads onto the wall materials as demonstrated exemplarily with a molten tungsten surface.

For ITER high parallel power loads of $2000\,\mathrm{MWm^{-2}}$ are expected to enter the near SOL (cf. [Pit97]). If this power is fully deposited on the divertor plates, the plasma configuration is called attached. As this would clearly exceed the material limits, a detached configuration has to be

used where the power flux to the divertor is limited by a high neutral pressure in the divertor, which leads to power dissipation by radiation.
To determine the power deposited on the divertor, infrared measurements (cf. [Fai17]) or probe measurements (cf. subsection 2.3.2) can be performed in the divertor target for attached plasma conditions. As the power enters the SOL across the separatrix, density and temperature profile measurements at the mid-plane also allow the calculation of the expected divertor loads, as the divertor and mid-plane measurements are connected via fast parallel transport, described by the so-called "two-point" model[7]. These mid-plane measurements also work for detached plasma scenarios and allow the calculation of the fraction of the power which directly reaches the first wall via radial transport.
In the far SOL the portion of perpendicular transport is mainly driven by short time scale filamentary turbulence, as illustrated in Fig. 1.4 by measurements from the gas-puff imaging diagnostic.

For the success of a fusion power plant it is indispensable to adapt the plasma scenarios itself in order to increase the confinement efficiency as well as to decrease the material loads. A precise understanding of the underlying processes can be gained by theoretical predictions and modelling bench-marked with high quality experimental data.
Adequate diagnostics are probe measurements, lithium beam emission spectroscopy, the Thomson scattering diagnostic, reflectometry, charge exchange recombination spectroscopy as well as line ratio spectroscopy on helium as discussed in chapter 2.

1.4. Scope of the thesis and outline

With the goal of gaining a better understanding of steady-state as well as fast transport processes, this thesis describes the design and implementation of a thermal helium beam as plasma edge diagnostic for the ASDEX Upgrade (AUG) tokamak. This diagnostic provides simultaneous measurements of the electron density n_e and electron temperature T_e with superior spatiotemporal resolution. As introduced in the following section the thermal helium beam is capable of covering the whole plasma edge region to address the aforementioned transport phenomena.
The main part of this thesis covers the planning, development, optimization, construction, testing, bench-marking and installation of the required hardware components of the new thermal helium beam diagnostic as well as the improvement and validation of the required collisional radiative models for data evaluation. Beside the examination of a suitable measurement concept in initial experiments, the data of the newly installed helium beam are used in this thesis for first physical studies of regime transitions.

This thesis is organized as follows. In chapter 2, the plasma heating systems, confinement regimes and different plasma edge diagnostics from ASDEX Upgrade are introduced. Strengths and weaknesses of each diagnostic are compared and possible applications of the thermal helium beam are highlighted.

[7] For a comprehensive review about experimental divertor physics see [Pit97].

Fundamentals of beam emission spectroscopy and the basics of collisional radiative models are introduced in chapter 3, leading to the physical basics of helium line ratio spectroscopy. The developed hardware components for active thermal helium beam emission spectroscopy at AUG comprise a piezoelectric gas injection system as well as optical components for light collection and detection. The new and versatile piezoelectric valve for the injection of a collimated thermal He beam into the plasma is shown in chapter 4. The light which is emitted by the injected helium during the plasma discharge is collected by a new optical head which is presented in section 5.1. The light is split into four spectral components in order to measure the line radiance of four neutral helium lines simultaneously for 32 channels. This is enabled by the newly developed polychromator system which is introduced in section 5.2.
In chapter 6 multiple line ratios are investigated in order to identify suitable combinations showing a strong dependence on electron temperature and density changes. This chapter also discusses the application of different collisional radiative models, rating the importance of selected processes. The results are brought together in presented radial n_e and T_e profiles, in comparison to other diagnostics.
Selected measurement results of the diagnostic are presented in chapter 7. T_e and n_e profiles are compared in L-mode, I-phase and H-mode as well as in I-mode. The high spatiotemporal resolution of the new system allows the determination of the propagation velocity of fast transient events such as bursts and blobs. While such measurements of the electron density have been available for quite some time, the simultaneous determination of critical transport quantities in n_e and T_e is unique.

2. Description and diagnostics of the plasma edge

To achieve the required temperatures in magnetic confinement fusion devices, adequate heating systems are required. These systems which are presented in section 2.1 allow the access of reactor relevant confinement regimes (cf. section 2.2). As illustrated in Fig. 1.4, the underlying confinement regime directly determines the transport parameters at the plasma edge. Furthermore, characteristic intermittent processes, which lead to an increased radial transport, often accompany with particular confinement regimes.
To understand these short time scale filamentary structures as well as the power fluxes across the LCFS, powerful plasma edge diagnostics are required. ASDEX Upgrade was already well equipped with a broad set of different diagnostics. But there was still a lack of fast and spatially highly resolved electron temperature measurements which cover the plasma edge and SOL region. This as well as the simultaneous measurement of the electron density is provided by the new thermal helium beam diagnostic, which supplements the AUG edge diagnostics introduced in section 2.3.

2.1. Plasma heating

ASDEX Upgrade is equipped with a total heating power of over 30 MW [Str03]. Considering the plasma volume of $14\,\mathrm{m}^3$, AUG has the highest heating power density of all current magnetic confinement devices. It is sufficient to enable the study of reactor relevant divertor plasma conditions as needed for the next step devices (cf. subsection 1.2.4), where also alpha-particle heating will be present.
As explained in the following, AUG is equipped with three heating mechanisms which are ohmic heating by the plasma current, wave heating for electrons (ECRH) and ions (ICFH) as well as heating by injection of highly energetic neutral particles (NBI).

2.1.1. Ohmic heating

The necessary plasma current I_P of up to 1.6 MA, is produced by the primary transformer coils (OH coils, cf. section 1.2). In AUG, these coils are also used for the plasma breakdown which is regularly achieved with $V_\mathrm{OH} < 10\,\mathrm{V}$ [Str03].

Due to the non-zero resistance R_{plasma} of the plasma, the ohmic losses by the plasma current are given by

$$P_{\text{OH}} = R_{\text{plasma}} \cdot I_{\text{P}}^2. \tag{2.1}$$

In AUG the ohmic heating power is around 1 MW. As the resistance of the plasma decreases with temperature and ionization fraction, ohmic heating is suitable for the plasma breakdown and low temperature L-mode discharges, but not for achieving higher temperatures.

2.1.2. Wave heating

Charged particles, i.e. ions and electrons of the confined plasma, gyrate around the field lines with a frequency of

$$\omega_{\text{c}} = \frac{eB}{m}, \tag{2.2}$$

which depends on the charge, the magnetic field strength and the inverse of the particle mass. The radiation which is emitted by the gyrating electrons can be used for diagnostic purposes (cf. subsection 2.3.4). Furthermore, the energy of the particles can be increased specifically by irradiating electromagnetic waves in multiples of their gyro-frequency. Due to the magnetic field dependence on the radius and the dependence on the particle mass, this heating technique can be used for local and particle species specific heating. Together with the ability to use wave heating for current drive, this tool establishes a broad range of different operation scenarios.
With a typical magnetic field of several tesla, the gyro-frequencies are allocated to the microwave spectrum for the electron cyclotron resonance heating (**ECRH**) and to the radio spectrum for the ion cyclotron resonance heating (**ICRH**). At AUG, the ICRH covers a frequency range of 30–120 MHz, which corresponds to wavelengths of 2.5–10 m. Radiation with a power of maximum 8 MW is injected by up to four antennas into the plasma [Str03]. ECRH can either be used at 140 GHz or 105 GHz (2.1 mm and 2.8 mm) corresponding to the X2, O2 or X3 scheme with a total heating power of 6.5–7 MW [Wag16].

2.1.3. Neutral beam injection

The most powerful heating system in AUG is the neutral beam injection (**NBI**) with a total power of 20 MW, where highly energetic neutral particles are injected into the plasma. Two injectors with four ion sources each are used to accelerate deuterium ions to energies of 60 keV and 93 keV [Str03]. Before the electrostatic acceleration phase the ions are produced by an arc source in one and by a radio-frequency driven plasma source in the other injector. To be able to enter the magnetic field cage without being deflected, the fast positive ions have to be neutralized by passing neutral gas where electrons are collected.
The eight ion sources, with an equal power of 2.5 MW respectively, can be switched on and off separately. A quasi-continuous variation of the beam power can be achieved by pulse width modulation of the single sources [Str03].

2.2. Confinement regimes: L-, H-, and I-mode

In the year 1982, it was seen for the first time at ASDEX that the particle and energy confinement time suddenly increased during NBI heated plasma discharges [Wag82]. This led to a higher value of β (cf. Eq. 1.6) and the term high confinement mode (**H-mode**) for this type of confinement. Because of the lower values of β for comparable preceded discharges, they are classified as low confinement type (**L-mode**) scenarios.
In H-mode, the so-called edge transport barrier (ETB) is formed where the fluctuation level which drives the turbulent transport is strongly reduced. This leads to a simultaneous improvement of energy, particle and momentum confinement at the plasma edge [Wag07]. The reduced transport leads to strong gradients of plasma pressure in the ETB region, forming the so-called pedestal. This can be seen in Fig. 2.1 where typical edge profiles of a) n_e, b) T_e and c) plasma pressure are compared between L-mode (blue) and H-mode (red). The ETB can be identified by the steep gradient of the plasma pressure shown in Fig. 2.1 d).
It was empirically found that the transition from L- to H-mode requires a minimum heating power, called the L–H transition power threshold [Sni96]. But up to now it is not fully resolved what exactly leads to the phase transition. However, a good overview of different theories is given in [Con00]. In many theories it is supposed that two steps lead to the phase transition. First, a radial electric field E_r is formed which exhibits a strong gradient in the separatrix region. This electric field leads in the second step to an $\boldsymbol{E} \times \boldsymbol{B}$ velocity shear (cf. Eq. 1.5) which suppresses the edge turbulence [Cav16].
In the transition phase, this $\boldsymbol{E} \times \boldsymbol{B}$ flow which triggers the H-mode may build up and decay periodically, i.e. a limit cycle oscillation between L- and H-mode is performed [Kim03]. This phase is called **I-phase** and can be seen as a competition between a high turbulence level and the shearing flow [Cav17b].
In section 7.2 experimental results of a transition from L-mode over an I-phase to H-mode are discussed.

Once H-mode is fully established, a common phenomenon going along with it are the so-called edge localized modes (**ELMs**). They are magnetohydrodynamic (MHD) instabilities which periodically release energy across the separatrix into the SOL. This leads to a periodic relaxation of the steep edge temperature and density and hence the pressure profile of the plasma. Among different types of ELMs, the most prominent one is classified as type-I ELM as this type carries the most energy per event. Type-I LMs occur in H-mode with a frequency between 10 and 150 Hz, which increases with the heating power. ELMs can be detected by magnetic or spectroscopy signals like divertor D_α signal or divertor shunt current measurements (cf. subsection 2.3.1). For a review of ELMs see the article by H. Zohm [Zoh96] or more recently by A. Kirk [Kir14].
ELMs carry burst-wise high amounts of energy and particles into the SOL. From there particles and energy are transported to the divertor or directly to the first wall which leads to large peak power fluxes onto the plasma facing components. In the divertor, 30 % of the total deposited energy is caused by type-I ELMs in an ELMy H-mode [Her02]. This may limit the usability and

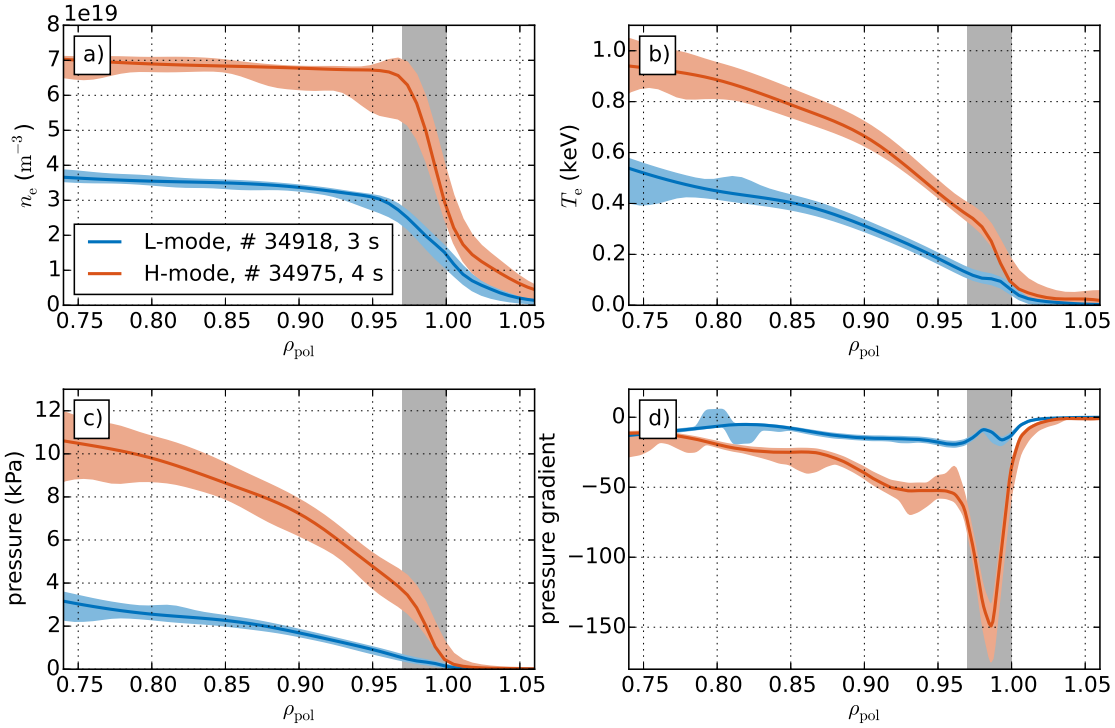

Figure 2.1.: L-/H-mode comparison of plasma profiles of a) electron density, b) electron temperature, c) electron pressure and d) pressure gradient along ρ_{pol}. The region of the edge transport barrier (ETB) is shaded in gray.

lifetime of wall materials for future fusion devices (cf. subsection 1.2.4) so that ELM mitigated scenarios are favorable [Sut11].

One possible candidate for a future fusion reactor operation scenario is the "improved energy confinement mode", short **I-mode** [Why10]. In this improved L-mode confinement regime, energy and particle transport channels are decoupled. In contrast to H-mode, an edge transport barrier in I-mode is only observed in heat but not in particle transport. Therefore I-mode does not show any ELMs [Hap17, Ryt17].
The confinement improvement of I-mode compared to the ordinary L-mode is produced by a deepening of the edge radial electric field well and a subsequent reduction of turbulence. The I-mode is usually accompanied by a plasma edge instability, called the weakly coherent mode (WCM) [Czi13, Man15a]. Due to the reduced turbulence level in I-mode compared to L-mode, the weakly coherent mode (WCM) is clearly visible in the turbulence spectrum, typically measured by reflectometry. Sawtooth-induced temperature pulses increase the stored energy in the plasma step-wise by increasing temperature but not density in the pedestal region. This process might lead to an increase of the WCM frequency.
Linked to the pronounced WCM, strongly intermittent high-amplitude density bursts are characterizing the I-mode [Hap16]. They are visible in the plasma edge region inside the separatrix. Strong bursts are expelled from the plasma as they appear in the divertor current or bolometry signal with a time delay with respect to direct measurements in the confined regions.

As motivated in section 7.4, the thermal helium beam is an excellent diagnostic for further studies of the I-mode regime. It allows the precise radial determination of the impact of the WCM as well as a simultaneous temperature and density determination of the I-mode bursts for the first time.

2.3. Plasma diagnostics

This section gives an overview of the most common diagnostics used within this thesis. In subsection 2.3.7 helium line ratio spectroscopy is introduced. With its high spatiotemporal resolution it is unique in measuring the critical transport quantities in n_e and T_e simultaneously.

2.3.1. Divertor current

A simple and useful diagnostic in divertor tokamaks is the measurement of the so-called divertor shunt current. It is neither a direct measurement of the temperature nor of the density of the plasma. The physical quantity which is measured is the electrical current which flows in the SOL between the inner and outer divertor. This current is mainly driven by the temperature difference between the hotter outer and colder inner divertor. This causes a thermoelectric voltage between the two field-lines ends connecting the inner and outer divertor. The current $j_{\parallel}$ is limited by the resistivity of the plasma along the connection path, which is with $L_{\mathrm{con}} \approx 60\,\mathrm{m}$ longest close to the separatrix and shortens to $L_{\mathrm{con}} \approx 35\,\mathrm{m}$ in the far SOL [Kal01].
The robust and cheap shunt current diagnostic obtains the total current which is flowing through one divertor tile by measuring the voltage drop over the so-called shunt which connects the divertor tile with its mechanical support. The shunt itself is basically a hollow screw containing a copper rod with a known electrical resistance [Pau11]. The total current which flows to the divertor can be calculated by multiplying the measured current of one tile by the total number of divertor tiles assuming toroidal symmetry. This is checked by measurements at several toroidal positions and holds basically for the thermocurrent, but not for halo currents caused by disruptions[1].
The measured divertor current at the inner divertor is called $I_{\mathrm{i-DIV}}$, whereas the current at the outer divertor is named $I_{\mathrm{a-DIV}}$. These signals are qualitatively mainly identical, but of different sign. As ELMs in H-Mode cause a drastic increase of the divertor current, these signals are excellent tracers for ELMs, usable to determine the ELM onset times for ELM synchronization as well as to classify the ELM itself.

[1] The halo current, caused by disruptions, is magnitudes stronger than the thermocurrent. As it flows in the SOL, it can also be measured by the shunt technique. Halo currents are in general not toroidally symmetric so that the shunt measurements are extended to a broad set of toroidal and poliodal locations [Pau11].

2.3.2. Langmuir probes

The most traditional diagnostic providing n_e as well as T_e information are Langmuir probes (1926) [MS26], which are in physical contact with the plasma [Hud65]. But it is obvious that this measurement technique might disturb the plasma itself, due to the direct contact of the probes with the plasma. Furthermore Langmuir probe measurements are limited to low electron temperature regimes in the SOL, best suitable in the divertor or regions close to a limiter [Mat94].
In addition to a broad set of divertor Langmuir probes, the mid-plane manipulator of ASDEX Upgrade can be equipped with different types of probe heads. The so-called quadruple ball-pen probe (BPP) head, for example, combines four BPPs with four graphite Langmuir probes [Ada10]. This allows fast measurements (up to 1 µs) of the electron density, the electron temperature and the plasma potential at the mid-plane in the far SOL. By the fast reciprocating probe shaft, radial profiles can be measured with a radial resolution of 2–4 mm [Hor10].

2.3.3. Thomson scattering diagnostic

Another option for n_e and T_e measurement is the Thomson scattering (TS) diagnostic (1962) [Hug62]. Within this technique, the light of a strong monochromatic laser beam which is scattered by the free electrons in a plasma is analyzed. Due to the thermal motion of the electrons, the frequency of the back-scattered light is Doppler broadened allowing temperature reconstruction. The electron density can be deduced from the intensity of the scatted light as described in [Hut05, Chapter 7].
In the early years of this diagnostic [Fün63] low signal levels caused by low laser powers and low electron densities were limiting the application. In ASDEX Upgrade a dedicated TS system is available for the edge region. 10 channels with a spatial resolution of 3 mm offer a temporal resolution of 120 Hz in steady state, built by 6 lasers with 20 Hz respectively. A pulsed higher time resolution is available in the burst mode [Kur11]. This diagnostic covers electron temperatures starting at 3 eV and densities down to $1 \times 10^{18}\,\mathrm{m}^{-3}$. However, the continuous measurement of highly temporally resolved profiles or the resolution and tracing of single plasma perturbations is not possible with this diagnostic.

2.3.4. Electron cyclotron emission

By analyzing the electron cyclotron emission (ECE), electron temperatures can be measured. The radiation is caused by electrons gyrating along the magnetic filed lines with the cyclotron frequency (cf. [Str11, Chapter 2])

$$\omega_{ce} = \frac{eB}{m_e}. \tag{2.3}$$

The emitted radiation in multiples of the cyclotron frequency is absorbed by the optically thick plasma only in a thin radial layer around the emission point due to the $1/R$ dependence of

the magnetic field strength in a tokamak. Assuming the electron energy distribution to be thermalized, the multiple absorption and re-emission processes of the cyclotron radiation lead to an effective spectral radiance $L(\omega)$ similar to a black body described by Planck's law. As the emission energy is much lower than the thermal energy of the electrons ($\hbar\omega < \mathrm{meV} \ll k_\mathrm{B}T$), the Rayleigh-Jeans approximation can be used to express the spectral radiance[2] $L(\omega)$ as

$$L(\omega) = \frac{\omega^2}{4\pi^3 c^3} k_\mathrm{B} T. \tag{2.4}$$

With this formula, the underlying temperature can be determined and allocated to a specific radial position due to the $B(R)$ dependence. In regions of low electron densities and for steep temperature gradients however, the assumption of an optically thick plasma does not hold anymore [Rat12]. By applying a forward model for the T_e evaluation (cf. [Rat12]), good measurement results can be achieved within the confined region up to the separatrix. In the SOL, however, where the measured radiation stems mostly from further inward, the ECE diagnostic application is limited.
AUG is equipped with a 60-channel heterodyne radiometer receiver [Har97], capable of measuring the second harmonic (X-mode) cyclotron emission in a spectral range of 2–18 GHz. The system provides a spatial resolution of around 5 mm [Rat12] and a temporal resolution of 1 MHz .

2.3.5. Microwave reflectometry

Microwave reflectometry can be used for electron density but not for electron temperature measurements in plasmas. It is based on the reflection of microwaves in the plasma for probe frequencies ω_probe smaller than the cut-off frequency ω_cut of the plasma.
As the plasma is confined by a magnetic field $\boldsymbol{B}$ and the irradiated microwave is directed perpendicularly to the flux surfaces, the orientation of the electric field $\boldsymbol{E}$ of the microwave with respect to $\boldsymbol{B}$ is important. One has to distinguish between two different linear polarization directions of the microwave beam, the ordinary mode (O-mode, $\boldsymbol{E} \parallel \boldsymbol{B}$) and the extraordinary mode (X-mode, $\boldsymbol{E} \perp \boldsymbol{B}$). For the O-mode, the cut-off frequency equals the local plasma frequency [Str11, Chapter 5]

$$\omega_\mathrm{p} = \sqrt{\frac{e^2 n}{\epsilon_0 m_\mathrm{e}}}, \tag{2.5}$$

whereas two frequencies are existing for the X-mode. They are separated by the electron cyclotron frequency ω_ce [Bot87].
The electron density can be reconstructed by measuring the phase shift between the incident and the reflected wave. Profile measurements are enabled by sweeping the frequency of the incident microwave.
Microwave reflectometry was first used in the 1960s for measurements on ionospheric plasmas and applied in 1985 for reconstructing electron density profiles in tokamaks [Sim85, Bot87]. In AUG, microwave antennas are placed on the LFS as well as on the HFS of the torus. The

[2] $[L(\omega)] = \frac{\text{photons}}{\text{s m}^2 \text{ sr Hz}}$

usage of frequencies between 18 GHz and 110 GHz enables the coverage of a density range of $0.32\text{–}12 \times 10^{19}\,\mathrm{m}^{-3}$. The system achieves a sub centimetre spatial resolution and a time resolution of up to 250 µs [Sil96]. Density fluctuations can be studied by means of Doppler reflectometry with a sampling frequency of 25 MHz [Hap15].

2.3.6. Lithium beam emission spectroscopy

One of the most common active spectroscopy methods for density evaluation in the plasma edge region of magnetically confined plasmas is the beam emission spectroscopy of lithium (cf. [Bra84, Igu85] and references therein). For the measurement, a collimated beam of high energetic lithium atoms (^{7}Li) is injected into the plasma in order to measure the lithium line radiance $\epsilon_{2p,2s}$ of the $2p \rightarrow 2s$ transition at 670.8 nm.
In order to calculate the electron density based on the measured line radiance, a full collisional radiative model (cf. section 3.2) for lithium has been developed. It describes the population density $n_i(t)$ of the considered excited states of lithium, balancing all the relevant population and depopulation processes. For the lithium model in AUG (cf. [Fis08]) the main state changing processes are ion and electron collisions, spontaneous emission, ionization and charge-exchange processes.
For the n_e reconstruction at AUG, the full radial emission profile of lithium is considered. The beam axis z of the injected lithium beam is directed with an angle of 10° to the flux surfaces. To describe the population distribution of lithium at the different measurement points along the axis, one can preform a transformation of the reference frame of the beam atoms. Taking the known beam velocity v into account, the temporally changing population density of the injected particles can be transformed to a spatial dependence as a function of z along the beam axis [Sch92b]:

$$\frac{\mathrm{d}n_i(t)}{\mathrm{d}t}\frac{1}{v} = \frac{\mathrm{d}n_i(t)}{\mathrm{d}t}\frac{\mathrm{d}t}{\mathrm{d}z} = \frac{\mathrm{d}n_i(z)}{\mathrm{d}z}. \tag{2.6}$$

Assuming that all the injected lithium atoms are in the ground state when entering the plasma, the lithium emission at the position z can be forward modelled when the electron density profile $n_e(z)$ and the electron temperature profile $T_e(z)$ are given. The modelled line radiance profile can be compared to the measured one and the initial density profile can thus be adapted repetitively. This technique is implemented in AUG to obtain the underlying density profile, using a probabilistic approach based on the Bayes' theorem [Fis08].
By comparing the total shape of the modelled and measured emission curve, the shape and absolute value of the underlying density profile can be reconstructed with high accuracy. This technique, however, is very susceptible to changes of the emission profile shape caused by technical uncertainties. These are changes in the efficiency of the detectors and the transmission path and in particular in the alignment of the narrow lithium beam with respect to the observation region. To handle this, the emission profile is calibrated in AUG at the end of each plasma discharge by injecting the beam in the torus which is filled with deuterium at low pressure. This leads to light emission due to molecule-impact excitation of the fast lithium atoms with only a

very weak attenuation of the beam along its path. These "beam in gas" measurements are used for the relative calibration of all channels.
State of the art applications of lithium beam emission spectroscopy like in AUG use beams with up to 60 keV and 3 mA and achieve a time resolution of the measurements of 200 kHz. Here, in total 60 lines of sight (LOS) are installed in three rows, each with an elliptical cross section with axes of 6 mm radial and 12 mm perpendicular to the lithium beam which itself has a FWHM of 12 mm at the observation point [Wil14]. The collected light is transferred to the lab by optical fibers. Each fiber is connected to one photomultiplier tube which is equipped with a 1 nm-FWHM interference filter.
To summarize, the Li-beam diagnostic delivers both, high accuracy density profiles as well as density fluctuation information. Electron temperature information cannot be reconstructed with this technique.

2.3.7. Helium line ratio spectroscopy

Line ratio spectroscopy on He I emission lines is another active spectroscopy method. It enables electron temperature and density evaluation simultaneously out of at least three measured optical transitions. The first idea of using helium line ratio spectroscopy for diagnostic purposes came up in the nineteen-fifties [Coo58]. The main barriers for application were the poor knowledge of the excitation cross-sections needed for the collisional radiative model (CRM) as well as low experimental light intensities. Big progress on the CRM had been made by Brosda and co-authors [Bro93], leading to the first application of a thermal helium beam in a fusion plasma in the TEXTOR experiment in 1992 [Sch92a].
Helium line ratio spectroscopy can be applied on background helium as done in MST [Ahn06], NAGDIS-II [Kaj06], ASDEX Upgrade [Sie10], heliac devices [Boi01, Ma12] and the FT-2 tokamak [Las12]. For bigger devices, improved spatial resolution (cf. section 3.1) can be achieved by actively injecting helium into the plasma. This can be done by a supersonic beam [Nam06] which was used in TEXTOR [Bri98] and TJ-IU [Tab97] and is currently operated in TJ-II [Tab10]. An effusive as well as a thermal helium source was also used at TEXTOR [Bri98, Sch08b]. Further, a thermal helium beam was used in JET [Dav97], the RFX reversed field pinch [Car99], RFX-mod [Ago10, Ago15], W7-X [Bar16] and it is planned for WEST [Jon16].
The total emission intensity of He I lines can be measured with a spectrometer which covers the desired wavelength region (e.g. [Boi01]) by integrating over the emission profiles of the selected He I lines. Another method is splitting the light into several paths e.g. by dichroic or semipermeable mirrors and then selecting the specific He I lines with small band interference filters [Unt12, Kru12].

As active spectroscopy, this technique relies on an injected helium beam to achieve a localized measurement in the region where the helium beam and the lines of sight intersect (cf. Fig. 3.2). This leads to a spatial resolution of 3.5 mm. A sufficient signal level of the measured helium emission requires two boundary conditions. On the one hand the neutral helium density has to be high enough. This limits the application to the plasma edge and SOL region, as the neutral

helium gets rapidly ionized in the pedestal region by high temperature and density H-modes. On the other hand, neutral helium emission depends strongly on a sufficiently high temperature and density. Especially for temperatures $< 10\,\mathrm{eV}$, as in the far SOL, the helium excitation and therefore the signal is very low. The accessible radial region is experimentally demonstrated in section 7.1.

In AUG, the lithium beam compared to the helium beam diagnostic covers a broader radial range and is more suitable for investigations of the pedestal region due to the highly accelerated lithium atoms with a higher penetration depth than thermal helium. Local density fluctuations can be determined by the lithium diagnostic only by taking into account the lifetime of the excited state, which leads to a radial smearing[3] of the signal [Wil14]. The helium line ratio spectroscopy, however, excels in the near SOL region. Here the high signal level compared to other optical diagnostics allows fast measurement (900 kHz at AUG) and thus the investigation of high frequency and small amplitude fluctuations in n_e and T_e.

In AUG, the helium beam diagnostic covers the gap of n_e and T_e measurements between probe measurement in the far SOL and Thomson scattering and ECE data in the pedestal and confined region. Due to the physical contact to the plasma, the mid-plane manipulator (cf. subsection 2.3.2) cannot access regions around the separatrix for high power discharges. Due to the sweeping technique of the probe head, continuous profile measurements are also not possible. The Thomson scattering diagnostic suffers from low signal levels and does not allow continuous fluctuation studies due to the low acquisition rate of 120 Hz (cf. subsection 2.3.3). Due to shine through effects (cf. subsection 2.3.4), the ECE diagnostic is also not suitable for T_e measurements in the SOL.

This highlights active line ratio spectroscopy on helium as an excellent complement of plasma edge diagnostics at AUG which allows the precise investigation of hitherto not accessible phenomena. Therefore a thermal helium beam diagnostic as been built and installed in AUG within this thesis. The exact functional principle of the diagnostic is introduced in the following chapter, before the developed hardware components are introduced in chapter 4 and chapter 5.

[3] Radial smearing is the distance beam atoms move after excitation before emitting a photon. This effect is especially considerable for the Li-beam as the lithium atoms with $\approx 1300\,\mathrm{km/s}$ are thousand times faster compared to the thermal atoms of the helium beam.

3. Diagnostic basics of helium beam emission spectroscopy

Parts of this chapter are published in M. Griener, et al., "Qualification and implementation of line ratio spectroscopy on helium as plasma edge diagnostic at ASDEX Upgrade", PPCF, 60, 25008 (2018) [Gri18a].

In this chapter, the fundamental terms of photometry are introduced to describe the measured quantities of spectroscopic diagnostics. For the purpose of beam emission spectroscopy, neutral particles are injected into the plasma. These neutrals are excited by collisions with plasma particles, which leads to the diagnosed volume radiation. To gain back the underlying plasma parameters, collisional radiative models (CRMs) can be applied. The main features of light collection for active spectroscopy are introduced in section 3.1 and the concept of CRMs in section 3.2. The specific application for line ratio spectroscopy of helium is illustrated in section 3.3.

3.1. Photometry and active spectroscopy

For active helium line ratio spectroscopy, neutral helium is locally injected into the plasma. It is excited mainly by collisions with the plasma electrons, leading to spontaneous emission. Due to the low helium densities, re-absorption of the emitted light or stimulated emission can be neglected, i.e. the helium cloud forms an optically thin volume radiator. The radiation is emitted isotropically, when the individual lines which appear due to the Zeemann effect (cf. Fig. 6.4) are not resolved. The emitted photon rate per volume and solid angle is called emission coefficient ϵ in the unis photons/m^3/s/sr.
The emitted radiation is partially captured by an optical head which leads the light to the detection system by optical fibers. The optical head (cf. chapter 5, Fig. 5.4) consists of a lens with area A_{lens} and optical fibers with a cross-section area A_{f} placed at a distance g behind the lens. The lens produces a sharp image of the fiber ends at the measurement location in the plasma with a distance b to the lens where the area of the image is $A_{\mathrm{LOS}} = A_{\mathrm{f}}(b/g)^2$.
A characteristic parameter describing an optical system is its etendue $\mathcal{E}$. It is the product of area $A_\perp$ and solid angle Ω (cf. Fig. 3.1) and determines the sensitivity with which the radiation can be measured. It is given by

$$\mathcal{E} = A_\perp \cdot \Omega = \frac{A_{\mathrm{f}} A_{\mathrm{lens}}}{g^2} = \frac{A_{\mathrm{LOS}} A_{\mathrm{lens}}}{b^2}. \tag{3.1}$$

The focal length of the lens is chosen such that the image area does not vary a lot within the measurement area, i.e. the helium cloud for active line ratio spectroscopy on helium. Furthermore the variation of emission perpendicular to the optical axis shall be weak such that it can be assumed to be constant over the imaged area. Within this assumption the radiance L is given by a single integration of the emission coefficient along the optical axis, which is called the line of sight (LOS). With the coordinate l along the LOS the radiance is given by

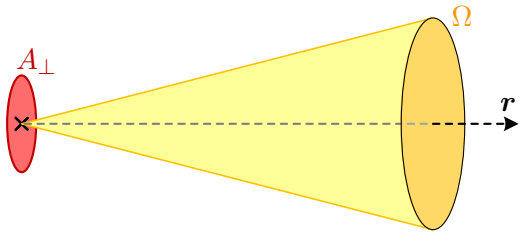

Figure 3.1.: The etendue is the product of the solid angle $\mathrm{d}\Omega$ and the area $\mathrm{d}A_\perp$.

$$L = \int_{\mathrm{LOS}} \epsilon \, \mathrm{d}l. \tag{3.2}$$

The spectraly resolved radiance L_λ can be determined by using dispersive elements like gratings or interference filters before the light is detected. Integration of the spectral radiance over a selected wavelength interval leads again to the term radiance as listed in Tab. 3.1.
The product of the radiance with the system specific etendue yields the radiant flux Φ, i.e. the photon rate on the detector.

$$\Phi = \mathcal{E} \int_{\mathrm{LOS}} \epsilon \, \mathrm{d}l = \mathcal{E} \cdot L \tag{3.3}$$

With an emitting surface of known radiance as provided by an integrating sphere, the etendue of the optical setup including the detector response can be calibrated. Doing this, the integrating sphere can be placed anywhere on the optical axis, since the etendue does not depend on l. The output of detectors like charge coupled devices (CCD) [Vie12, Cav17a], photomultiplier tubes (PMT) or avalanche diodes (APD) [Dun10] is a current or voltage signal. With the known wavelength dependent calibration factor it is expressible in units of photons per second for the radiant flux as summarized in Tab. 3.1.

Table 3.1.: Fundamental terms of photometry and corresponding units.

term	symbol	unit
radiant flux	Φ	photons/s
radiance	L	photons/m^2/sr/s
spectral radiance	L_λ	photons/m^2/sr/nm/s

In passive spectroscopy for a non local emission source, the signal is integrated along the whole line of sight as illustrated in Fig. 3.2 a). Active spectroscopy limits the region of the active emission signal to the overlap of the LOS and the injected beam (cf. Fig. 3.2, b)). This increases the spatial resolution of the measurement drastically.
Under certain circumstances a passive signal contributes to the overall measurement. This mostly non localized emission can arise from an intrinsic content in the plasma of the injected species, emission lines form other elements in the same wavelength region or contributions by

bremsstrahlung. This passive background can be eliminated by subtracting the measured signal in beam-off phases from the active signal of a fast chopped particle beam. This technique is applied for lithium and helium beam (cf. chapter 4) emission spectroscopy.

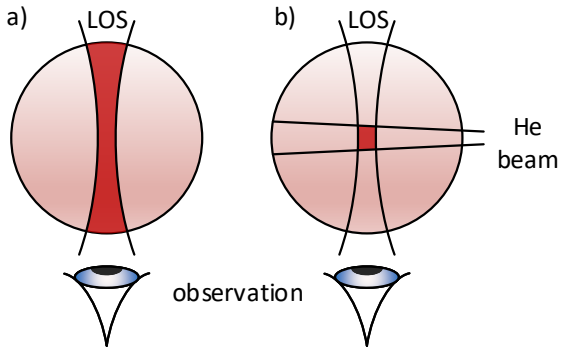

Figure 3.2.: Passive spectroscopy a) integrates the signal along the whole line of sight (LOS). In active spectroscopy b) the signal is only collected at the overlap of the LOS and the beam region.

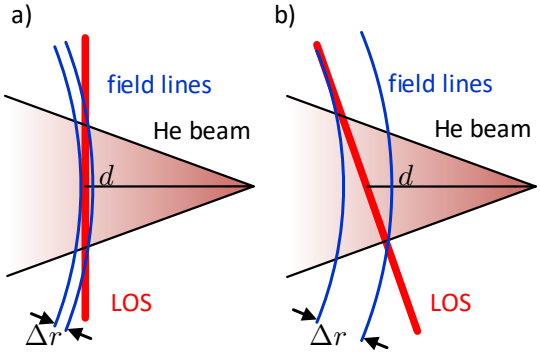

Figure 3.3.: Radial resolution Δr at the distance d to the beam injection point for a parallel alignment a) and non parallel alignment b) of the LOS with respect to the field lines.

In magnetic confinement devices, the effective spatial resolution Δr depends on the magnetic field configuration. The curvature of the field lines together with the diameter of the injected beam determine the achievable resolution. Furthermore the resolution is limited by the chosen diameter of the LOS in which a higher diameter increases the signal strength (cf. Eq. 3.1) in favour of a high temporal and at the cost of spatial resolution.
For an optimal result within these given boundary conditions, the alignment of the LOS and the injected particle beam with respect to the flux surfaces is crucial. As pictured in Fig. 3.3 a), the best spatial resolution can be achieved for lines of sight which are tangential to the flux surfaces in the beam region. Moreover, the central beam axis should be aligned perpendicular to the flux surfaces. For this perfect alignment, the resolution in AUG is dominated by the contribution of the LOS diameter (cf. subsection 5.1.2). If the LOS is not tangential to the flux surfaces in the region of the central beam axis, the spatial resolution is decreased because the active signal comes from regions at different radii. This is shown in Fig. 3.3 b) at the same measurement position d as in a), according to the beam injection point.

3.2. Basics of collisional radiative models

In beam emission spectroscopy, the spectral radiance is the measured quantity which carries information about the light source, i.e. the population density n_i of the atomic energy states i. The emission coefficient $\epsilon_{i,j}$ of a specific transition from the state i to the state j is equal to the population density[1] n_i of the considered upper state, multiplied by the corresponding Einstein coefficient $A_{i,j}$ for spontaneous emission:

$$\epsilon_{i,j} = \frac{1}{4\pi} n_i A_{i,j}. \tag{3.4}$$

To connect the measured line radiance over the population density n_i with the underlying plasma parameters, a collisional radiative model (CRM) has to be applied (cf. [Bri98, MB12]). It models the evolution of the population density taking all the relevant state changing processes into account:

- Spontaneous photonic decay $A_{i,j}$
- Electron-impact excitation and de-excitation $q^{\mathrm{e}}_{j,i}$ and $q^{\mathrm{e}}_{i,j}$
- Ion-impact excitation and de-excitation $q^{\mathrm{I}}_{j,i}$ and $q^{\mathrm{I}}_{i,j}$
- Electron-impact ionization S^{e}_i
- Ion-impact ionization S^{I}_i
- Radiative recombination[2] ,[3] $\alpha^{(\mathrm{r})}_i$
- Dielectronic recombination[4] $\alpha^{(\mathrm{d})}_i$
- Three-body recombination[3,5] $\alpha^{(3)}_i$
- Charge-exchange processes q^{CX}_i

The possible processes are not limited to the list above. However it was found (cf. [MB16a, MB12]) that the most dominant processes for modelling a thermal helium beam are the spontaneous emission as well as the electron excitation, de-excitation and ionization.
The calculation of the rate coefficients $q^{\mathrm{e}}_{i,j}$ is based on the collisional cross-sections $\sigma_{i,j}$ weighted with the thermal velocity distribution of the electrons as

$$q^{\mathrm{e}}_{i,j} = \langle \sigma_{i,j} v_{\mathrm{e}} \rangle. \tag{3.5}$$

[1] The population number density n_i in cm^{-3} is the density of atoms in the energy state i. The relative population density of the state i is given by the fraction n_i/n_{He}, where n_{He} is the total density of neutral atoms.
[2] Radiative recombination leads to photon emission at the moment when a positive ion captures an electron, e.g. $\mathrm{He}^+ + \mathrm{e}^- \longrightarrow \mathrm{He} + \mathrm{photon}$.
[3] Radiative and dielectronic recombination is the inverse of photo-ionization which only plays a role in optically thick environments.
[4] Dielectronic recombination is a resonant process where the energy gained from electron capture leads to the excitation of an already bound electron and a subsequent photon emission as $\mathrm{He}^+ + \mathrm{e}^- \longrightarrow \mathrm{He}^* \longrightarrow \mathrm{He} + \mathrm{photon}$.
[5] Three-body recombination is the inverse of electron-impact ionization and occurs at high electron densities.

Taking the relevant state changing processes into account, the time evolution of the population density n_i can be described as

$$\begin{aligned}
\frac{\mathrm{d}n_i}{\mathrm{d}t} = &+ \underbrace{\sum_{j>i} A_{j,i} n_j}_{\text{spontaneous emission}} - \underbrace{n_i \sum_{j<i} A_{i,j}}_{\text{spontaneous emission}} \\
&+ \underbrace{\sum_{j\neq i} q^{\mathrm{e}}_{j,i} n_{\mathrm{e}} n_j}_{\text{electron-impact}} - \underbrace{n_i \sum_{j\neq i} q^{\mathrm{e}}_{i,j} n_{\mathrm{e}}}_{\text{electron-impact}} \\
&+ \underbrace{\sum_{j\neq i} q^{\mathrm{I}}_{j,i} n_{\mathrm{I}} n_j}_{\text{ion-impact}} - \underbrace{n_i \sum_{j\neq i} q^{\mathrm{I}}_{i,j} n_{\mathrm{I}}}_{\text{ion-impact}} \\
&+ \underbrace{n^+ n_{\mathrm{e}} \alpha^{(\mathrm{r})}_i}_{\text{radiative recombination}} + \underbrace{n^+ n_{\mathrm{e}} \alpha^{(\mathrm{d})}_i}_{\text{dielectronic recombination}} + \underbrace{n^+ n_{\mathrm{e}}^2 \alpha^{(3)}_i}_{\text{three-body recombination}} \\
&- \underbrace{n_i n_{\mathrm{e}} S^{\mathrm{e}}_i}_{\text{electron-impact ionization}} - \underbrace{n_i n_{\mathrm{I}} S^{\mathrm{I}}_i}_{\text{ion-impact ionization}} \\
&+ \underbrace{n^+ n'_{\mathrm{D}} q^{\mathrm{CX}}_{\mathrm{D}',i}}_{\text{charge-exchange gain}} - \underbrace{n_i n'_{\mathrm{I}} q^{\mathrm{CX}}_{i,I'}}_{\text{charge-exchange loss}}.
\end{aligned} \tag{3.6}$$

Here n_{e} and n_{I} are the electron and ion densities, n_i is the helium population density of the state i and n_j the density of the state $j \neq i$. The He^+ density of the singly ionized helium is named n^+. The free arbitrary ion density n'_{I} may remove a charge exchange electron from n_i, whereas the arbitrary neutral density[6] n'_{D} may contribute an electron to neutralize n^+.

For a CRM it is crucial how many excited states are considered. For a number of N states, a differential equation system of N equations as Eq. 3.6 with N unknown population densities n_i has to be solved.

For active beam emission spectroscopy, this leads in general to a time dependent problem where the lifetime of the excited state with respect to the propagation velocity of the neutrals has to be considered. For solving the time dependent equations, a coordinate transform as in Eq. 2.6 can be performed.

In many cases (cf. chapter 6), a static approach is possible which facilitates the solution. One CRM which assumes a local equilibrium regarding the atomic state population is implemented in the atomic data and analysis structure (ADAS, cf. [Sum04]). The resulting photo emissivity coefficients (PEC, cf. ADAS data set 'pec96#he_pju#he0.dat') for each excited level allow the connection between the driving population and depopulation processes and the line radiance to

$$\epsilon_{i,j} = \frac{1}{4\pi} n_i A_{i,j} = \frac{1}{4\pi} n_{\mathrm{e}} n_{\mathrm{He}} \mathrm{PEC}_{i,j}, \tag{3.7}$$

where n_{He} is the total density of neutral atoms which can be excited by the electrons with density n_{e}.

[6] Non fully ionized ions may also contribute to the charge-exchange processes, but with a significantly lower rate.

This section gave an overview of the processes which have to be considered when the interaction of neutrals with a plasma is quantified. It showed how the excited energy states n_i of neutrals are populated and depopulated and that the resulting population density is directly connected to the measured line radiance $\epsilon_{i,j}$. The following section explains how exactly this measurement together with collisional radiative modelling can be used to determine the underlying electron density and temperature for helium beam emission spectroscopy.

3.3. Diagnostic principle of helium line ratio spectroscopy

For neutral helium the electronic system is divided into singlet (s) and triplet (t) states as shown in the Grotrian diagram of He in Fig. 3.4. The simplicity of this two electron system, which is more easily described than that of other noble gases for which the optical transitions are also split into singlet and triplet states, is one advantage of helium as spectroscopy gas. This led to further improvements in the CRM for helium [MB12] which is crucial for data evaluation. The second advantage lies in the ionization energy of 24.6 eV, which is the highest first ionization energy of all atoms. Therefore, neutral helium atoms injected as a thermal or supersonic beam can penetrate relatively deep into the plasma.

The possibility of measuring T_e with helium line ratio spectroscopy is based on the different behavior of the singlet and triplet state population density following changes of n_e and T_e. While the triplet state population density peaks at a temperature of $T_e \approx 25$ eV, the singlet states have their maximum of the population density at $T_e \approx 300$–500 eV (cf. section A.2 and [Bri98, Kru06]). Therefore, for high temperatures, the population density of singlet states is increased relative to that of the triplet states.

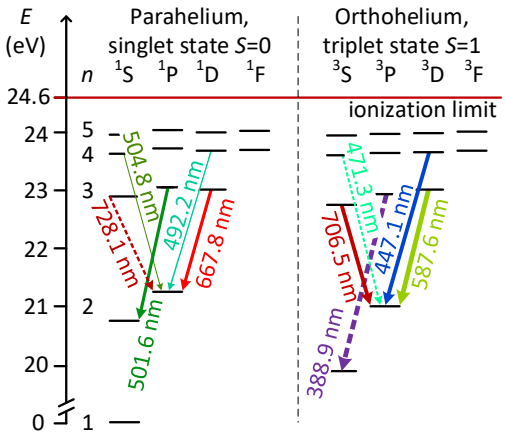

Figure 3.4.: He I Grotrian diagram, divided into singlet and triplet states. All lines are listed in Tab. 6.1.

The density dependence can by explained by the different types of the dominant depopulation processes. States with a main quantum number $n \geq 3$ are mainly populated by electron collisions ($\sim n_e$), whereas the excited state is either dominantly depopulated by radiation (independent of n_e) or by electron collisions ($\sim n_e$). Consequently, the line ratio of such two states is electron density sensitive.

In general this means that the line intensity ratios[7] of two suitable singlet or triplet lines combined with a collisional radiative model (CRM) enable the reconstruction of the underlying values for the electron density, whereas singlet/triplet ratios yield T_e values.

Two suitable line ratio pairs for a simultaneous n_e and T_e determination are presented in Fig. 3.5. Fig. 3.5 a) uses the ratio combination of the 501.6 nm (s), the 504.8 nm (s) and the 587.6 nm (t) lines which was found in this thesis to show good n_e and T_e dependencies in the relevant parameter region (cf. section 6.3). Fig. 3.5 b) presents the traditionally used triple of the 667.8 nm (s), the 706.5 nm (t) and the 728.1 nm (s) lines (cf. [Sch08b]). This plot is shown for a broader n_e and T_e parameter range in Fig. A.2, in comparison to a ratio plot including the 587.6 nm triplet line.
In both plots of Fig. 3.5 it can be seen that the ratios of two singlet lines (black, solid) mainly changes with changing electron temperature, whereas the s/t ratios (red, dashed) depend more on the electron temperature.

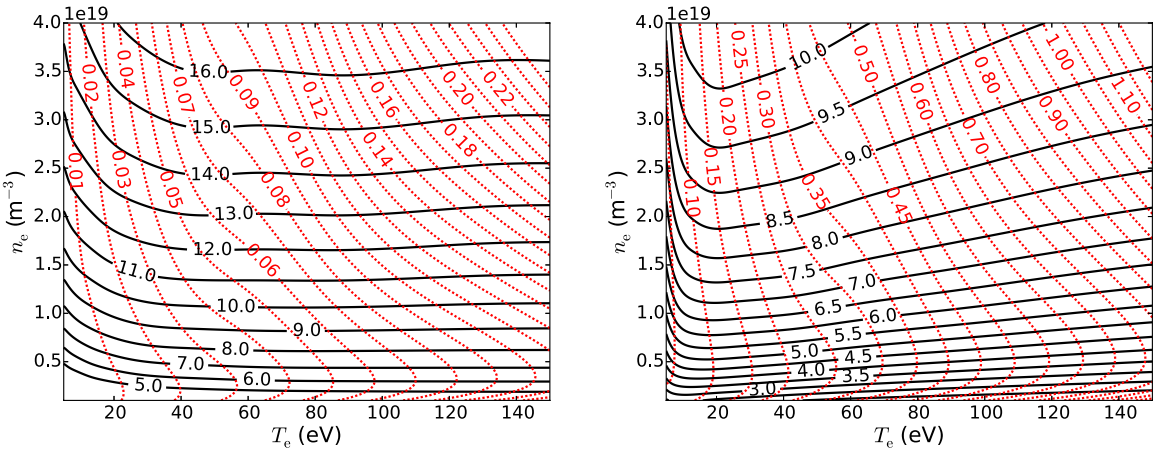

(a) T_e 501/587 (red) and n_e 501/504 (black) ratio.

(b) T_e 728/706 (red) and n_e 667/728 (black) ratio.

Figure 3.5.: Electron temperature and density dependence of two sets of line ratios, the T_e dependent s/t line ratios 501/587 a) and 728/706 b) in red-dashed as well as the n_e dependent s/s line ratios 501/504 a) and 667/728 b) in black-solid. The data are based on the ADAS data set 'pec96#he_pju#he0.dat' [Sum04].

A simultaneous measurement of three suitable lines allows the calculation of the two required ratios and thus the n_e and T_e determination using Fig. 3.5 as a look-up table in the simplest case. A more advanced approach considers time dependent effects for the evaluations as described in chapter 6, where different line combinations together with different CRMs are compared.
An overview about the necessary hardware components to perform active beam emission spectroscopy on helium is given in chapter 4 for the helium injection system and in chapter 5 for the optical components of the experimental setup.

[7] When the line ratio of two emission lines is calculated, the total number of atoms (cf. Eq. 3.4) is canceled out. Therefore the CRM does not change with the number of injected atoms which thus can be varied.

4. Piezoelectric valve for controlled gas injection

Parts of this chapter are published in M. Griener, et al., "Fast piezoelectric valve offering controlled gas injection in magnetically confined fusion plasmas for diagnostic and fuelling purposes", Rev. Sci. Instrum. 88, 33509 (2017) [Gri17].

As active beam emission spectroscopy on thermal helium is a completely new diagnostic at AUG, a set of dedicated hardware components had to be developed. The optical system and detectors are discussed in chapter 5. This chapter presents a new and versatile piezoelectric valve for the local injection of thermal gases.
In devices for magnetic confinement of fusion plasmas as tokamaks or stellerators as well as linear machines, controlled gas injection is crucial for plasma fueling and diagnostic applications. Special piezo based valves offer fast response and switching times for a wide range of applications. Typically valves are placed far away from the plasma periphery as the systems are not constructed to withstand the harsh environment of strong magnetic fields and high thermal loads. The resulting dead volume in the vacuum system and the pipe conductance leads to long response times of the gas flux, although the valves themselves provide faster responses [Bat84]. Therefore several specialized systems for different applications have been developed to compensate this disadvantage. At AUG, e.g., a spring driven piezoelectric valve [Dib17] for disruption mitigation enables the injection of high amounts of gases in a short time.
A supersonic piezo based gas valve [Kru12] was used in TEXTOR for line ratio spectroscopy on helium (cf. [Sch92a, Sch08b, Unt12] and references therein). However, because the supersonic system is very expensive in terms of setup and maintenance, simpler but still flexible valves for both, fueling and diagnostic applications are desirable. Such a versatile piezo valve system for thermal gas beams has been developed within this thesis, based on the TEXTOR system [Kru12]. The valve can be placed inside the vacuum vessel close to the plasma periphery, compensating the higher divergence angle of the thermal beam compared to supersonic beams with a small distance of the gas injection point to the observation point. A thin and short capillary is used for gas injection, enabling a collimation of the beam and fast formation and decay times of the gas cloud.
Three of the presented piezo valves are installed in AUG, two on the magnetic low field side at sector 13 and sector 16 and a newly installed valve on the high field side at sector 1. The valves in sector 13 and 16 were successfully tested within over 250 plasma discharges for gas-puff imaging [Fuc14], line ratio spectroscopy on helium [Sch08b] as well as for thermal charge exchange recombination spectroscopy (CXRS) on non fully ionized impurities in the scrape-off

layer [Chu13]. Another similar piezo system with a cascade of five inlet tubes is implemented in the stellerator W7-X in Greifswald [Kry16] used as thermal helium beam [Bar16] and fueling valve as well as for impurity transport studies [Ste16].

In the following the valve properties are discussed part by part: In section 4.1 an overview and the design details of the piezo valve are presented, the gas supply system for the piezo valve is described in section A.3. In section 4.2 the physical basics of gas flows through a capillary are summarized. This leads to a prediction of the achievable flowrates. The flow measurements for different operation regimes are presented in section 4.3. In section 4.4 the achievable switching times are discussed. Measurements of the shape of the gas beam are presented in section 4.5, which is important for the achievable spatial resolution of diagnostic applications.

4.1. Overview and design details of the piezo valve

The piezo electric valve is based on a modular concept of several custom made parts (stainless steel 1.4301, total mass 3 kg (cf. Fig. 4.1)). The central element is the commercially available piezo actor "PX 500"[1] (dimensions: $52 \times 20 \times 8\,\mathrm{mm}^3$) with a total stroke of 700 µm in a voltage range from −20 to 130 V. It is directly placed in the gas pressure chamber with dimensions[2] $10 \times 7 \times 7\,\mathrm{cm}^3$ and a volume of $100\,\mathrm{cm}^3$. This gas chamber is connected to the ground plate with eight M6x20 screws and sealed with a HELICOFLEX[3] metal sealing. This enables, as stress calculations for leak tests show, filling pressures up to 100 bar.

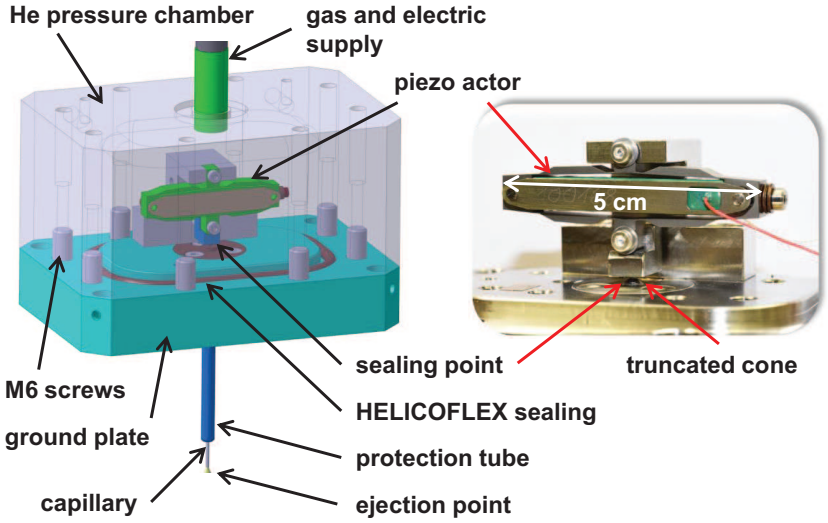

Figure 4.1.: CAD drawing (left) and photo (right) of the piezoelectric valve as installed in ASDEX Upgrade.

[1] Piezosystem Jena GmbH, Stockholmer Straße 12, 07747 Jena, Germany
[2] These dimensions are referred to the original design dedicated for the installation at the LFS. To be able to install this valve on the HFS behind the heat shields, the arbitrary dimensions of the gas chamber were reduced without changing the sealing mechanism.
[3] Technetics Group, Falkenweg 1, 41468 Neuss, Germany

The leak rate was determined in a laboratory setup using an Adixen ASM 310[4] helium leak tester to 3.7×10^{-9} mbar l/s at a background of 3.6×10^{-9} mbar l/s. This fulfils the vacuum criteria for the application in AUG.
To adjust the gas flowrate, variable pressures (tested from 10 mbar up to 7 bar) can be applied using the gas supply system which is described in section A.3. This enables the tuning of the gas flux at fully opened valve over a wide range in a precise way (cf. section 4.3).
For a fully opened valve the gas flow is only limited by the diameter and length of the capillary used for gas injection. Depending on the application of the valve, different diameters can be used. Capillaries with a length of 66 mm and diameters of 400 and 700 µm were tested within this thesis.
The gas pressure chamber is sealed toward the capillary by a Viton plate pressed on a truncated cone with an orifice of 400 µm diameter[5] in the middle. The sealing area is around 1 mm^2. When applying no voltage, the contact pressure force is 3 N. For a fully opened valve the Viton plate is lifted by 500 µm. Details on this sealing mechanism as well as the comparison with another sealing concept can be found in Griener et al. [Gri17].
The design with the thin and short capillary combined with the presented sealing mechanism has two major advantages. First, the capillary yields a small divergence of the injected beam with a half opening angle of 20°. Second, it minimizes the enclosed volume between the sealing and gas ejection point ($\sim 9\,\mathrm{mm}^3$), ensuring a very fast response of the valve which enables fast chopping of gas beams (cf. section 4.4). This has been shown to be a valuable technique for background subtraction as realized with the helium line ratio spectroscopy at TEXTOR [Unt12] and AUG [Gri17, Gri18a] as well as the lithium beam [Fis08, Wil12] and charge exchange recombination spectroscopy (CXRS) [Vie12] at AUG.
As the valve is placed close to the plasma periphery in AUG (cf. section 5.1), thermal loads can increase the valve temperature significantly as shown in section A.4. To protect the thin capillary from these high thermal loads, it is embedded in a tungsten coated carbon tile (pictured in Fig. 4.7). The operation temperature of the valve is restricted by the piezo actor between −20 and 80 °C. In this range the maximum piezo stroke decreases with increasing temperature by (4.0 ± 1.5) µm/K for $25\,^\circ\mathrm{C} < T < 80\,^\circ\mathrm{C}$, cf. [Gri17] and section A.4. To be sure to not exceed the operation limits of the piezo, a Pt100 sensor is installed to measure its temperature. If not operated, the piezo can withstand higher temperatures which also occur during the baking process of the of AUG vacuum chamber with 150 °C.
The gas as well as the electric supply for the piezo actor and the thermocouple is provided through the pipe of the gas supply. Behind the vacuum feed through of the supply pipe, a T-fitting is connected. One connection is used for gas supply, the other is connected to a 5-pin instrumentation feed through[6] which is welded into a VCR face seal fitting. A 4-pin LEMO[7] connector with a custom made case is used in the pressure box to connect the cable from the supply pipe with the electrical parts placed on the ground plate, when the gas box is closed.

[4] Pfeiffer Vacuum GmbH, Berliner Strasse 43, 35614 Asslar, Germany
[5] For high gas fluxes at low pressures (e.g. $> 1.6 \times 10^{21}$ particles/second at 1 bar pressure) this valve diameter has to be enlarged thus it becomes the flux limiting part (cf. subsection 4.2.2).
[6] IPT-Albrecht GmbH, Waldweg 37, 7963 Schwanau, Germany
[7] LEMO Elektronik GmbH, Hanns-Schwindt-Str. 6, 81829 München, Germany

The gas supply system which provides the desired pressure for valve operation is described in section A.3. This section also introduces the calibration procedure used to determine the gas flax through the valve. Some fundamentals of gas kinetics are introduced in section 4.2 which are needed to discuss the calibration measurements as done in section 4.3.

4.2. Theoretical basics of gas flow

To be able to interpret the measured valve properties, especially the dependencies of the gas flowrate, this section presents some basics of gas flow in subsection 4.2.1 and valve theory in subsection 4.2.2. This allows the prediction and verification of the measured gas flowrate in section 4.3. The measured flowrate is calculate with ideal gas equation

$$pV = Nk_{\mathrm{B}}T \tag{4.1}$$

out of the pressure increase Δp in a vacuum chamber after gas injection with the piezo valve. In Eq. 4.1 p is the pressure in the volume V, T is the temperature, N is the number of gas particles and $k_{\mathrm{B}} = 1.38 \times 10^{-23}\,\mathrm{J/K}$ is the Boltzmann constant. Because the number of injected particles is at least three orders of magnitude higher than the initial number of particles in the vacuum chamber, the initial pressure in the vacuum chamber can be approximated to be zero. Thus the number of injected particles is given by

$$N = \frac{pV}{k_{\mathrm{B}}T}. \tag{4.2}$$

To achieve comparable results, the particle flowrate $\dot{N}$ (particles per second, pps) is used in the following.

4.2.1. Flow regimes

Because the piezo valve can be operated at pressures across 2–3 orders of magnitude and different capillary diameters, different equations have to be used to describe the resulting flow rate which depends on the obtained flow regime.
An important parameter to describe gas kinetics is the **mean free path** of particles in a gas, which is the average distance particles can travel between two collisions. It is given by [Joh98, eq. (21.101)]

$$\lambda = \frac{k_{\mathrm{B}}T}{\sqrt{2}\pi p(2r)^2} = \frac{1}{\sqrt{2}\pi n(2r)^2}, \tag{4.3}$$

where r is the hard shell radius of the gas particle which lies on the order of a few Å. Fig. 4.2 shows the mean free path of helium as well as the particle density plotted versus the gas pressure at 300 K.

The **Knudsen number** Kn puts the mean free path length λ in relation to the characteristic length scale D of the system, e.g. the diameter of a tube:

$$\mathrm{Kn} = \frac{\lambda}{D}. \tag{4.4}$$

The Knudsen number is an indicator for the probability of particle-particle collisions compared to particle wall interactions. For $\mathrm{Kn} \ll 1$, fluid equations can be used to describe the viscous flow regime, where the mean free path of particles is much smaller than the dimension of the system. For $\mathrm{Kn} \gg 1$, the interaction between particles can be neglected compared to particle wall interactions. Here, the stochastic process of particles passing a barrier in form of an orifice or small tube has to be considered, leading to the concept of molecular flow. The intermediate regime is called Knudsen flow.

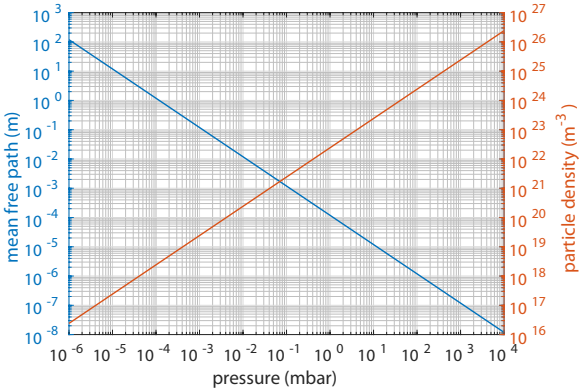

Figure 4.2.: Mean free path and particle density of He at 300 K plotted versus the gas pressure.

For the valve geometry with a nozzle diameter of 400 µm the Knudsen number is 3.4×10^{-4} for 1 bar pressure (mean free path for He is 1.2×10^{-7} m) and $\mathrm{Kn} = 0.034$ for 10 mbar (mean free path for He is 1.2×10^{-5} m). In both cases the flow can be described using a fluid approach.
For a detailed analysis of the problem, compressible (in general all kinds of gases) and non compressible flow regimes (e.g. liquids or dilute gases with very low pressure differences) have to be distinguished.
In the non compressible case, the **Hagen-Poiseuille** equation [Dem08, p.237, eq. (8.31)] can be applied for a Newtonian fluid with the dynamic viscosity η to describe the particle flux through a round capillary with radius r_c and length L_c:

$$\dot{N} = \frac{\pi \cdot r_\mathrm{c}^4}{8\eta} \frac{p^2}{L_\mathrm{c} \cdot k_\mathrm{B} T}. \tag{4.5}$$

In subsection 4.3.2 it is shown that the particle flowrate exhibits this quadratic pressure dependence (cf. Fig. 4.4 b)) for low pressures and small capillary diameters. In this case, the capillary decreases the flowrate by friction, which decreases the pressure gradient, making compressible effects less important. This region of laminar flow can be described using the Hagen-Poiseuille equation.
For higher pressures the flowrate changes into a linear function of the system pressure (cf. Fig. 4.4) as compressible effects become important. Therefore, equations for compressible fluids are applied as described in the following.

4.2.2. Valve and friction limited flow

For compressible gases, the flux through a valve is first calculated without attached capillary so that the flux in this **valve limited case** is only limited by the diameter D_v of the orifice. For a mathematical treatment of this process, the orifice connects two reservoirs, separated by an infinitesimal thin barrier. The first reservoir contains particles with the density n_0, the second reservoir is assumed to be empty. As the barrier is thin, friction can be neglected when particles pass the orifice.
The resulting particle flux $\dot{N}_\mathrm{max}$ through the orifice can be calculated by the **nozzle equation**[8]

$$\dot{N}_\mathrm{max} = n_0 c_\mathrm{s} A_\mathrm{v} \left(\frac{\gamma+1}{2}\right)^{-\frac{\gamma+1}{2(\gamma-1)}}, \tag{4.6}$$

where $A_\mathrm{v} = \pi D_\mathrm{v}^2/4$ is the cross section area of the orifice. The gas type dependency is caused by the specific heat ratio[9] γ, which also contributes to the adiabatic sound speed[10]

$$c_\mathrm{s} = \sqrt{\frac{\gamma\, p}{\varrho}} = \sqrt{\frac{\gamma\, k_\mathrm{B} T}{m}}. \tag{4.7}$$

The mass density ϱ of the gas used can be expressed by the particle mass m as $\varrho = m n_0$. Using the ideal gas equation to set $n_0 = p_0/(k_\mathrm{B}T)$, Eq. 4.6 changes to

$$\dot{N}_\mathrm{max} = p_0 \frac{\pi}{4\sqrt{k_\mathrm{B}T}} \frac{D_\mathrm{v}^2}{\sqrt{m}} \sqrt{\gamma} \left(\frac{\gamma+1}{2}\right)^{-\frac{\gamma+1}{2(\gamma-1)}}. \tag{4.8}$$

At constant temperature, this equation shows a linear dependence on pressure. It can be used to describe the flux of compressible gases in the frictionless, i.e. valve limited case for thermal and supersonic expansions as described in the work of Kruezi [Kru06, eq. (3.11), p. 32].

When now a capillary is attached to the orifice, friction effects can become important. The resulting flux with attached capillary cannot be higher than the maximum flux $\dot{N}_\mathrm{max}$ in the valve limited case. In the **friction limited case** the length and diameter of the capillary become important. The flow is still treated as adiabatic, but it is not frictionless any more. Since friction increases the entropy, the flow is not isentropic, i.e. adiabatic and frictionless, and a friction factor has to be introduced.
Dependent on the diameters D_v of the valve, D_c of the capillary, the capillary length and a surface friction factor (cf. [Par11]), one can detect the flow limiting element, as big capillaries attached to small orifices may have no influence on the gas flux. Then the exact capillary length and diameter do not play a role.

[8] A derivation of the nozzle equation can be found in Shapiro [Sha53, Chapter 4] and the equation used in the paper by Parks et al. [Par11, eq. (1a)].

[9] $\gamma = \frac{c_\mathrm{p}}{c_\mathrm{v}} = \frac{f+2}{f}$, where c_v is the heat capacity at constant volume, c_p the heat capacities at constant pressure and f the number of degrees of freedoms of the gas.

[10] $c_\mathrm{s} = 1.02\,\mathrm{km/s}$ for helium at 300 K.

Parks et al. [Par11] show a way to calculate the critical diameter $D_{\mathrm{v,trans}}$ for which the capillary becomes the flux limiting element.

- If $D_{\mathrm{v,trans}} \leq D_{\mathrm{v}}$, the tube does not limit the particle flux so that Eq. 4.8 is used to describe the system.
- If $D_{\mathrm{v,trans}} > D_{\mathrm{v}}$, a set of parametric equations as described in [Par11] has to be used to calculate the resulting gas flux.

In the considered case the orifice diameter is fixed to $D_{\mathrm{v}} = 400\,\mu\mathrm{m}$, independent of the attached capillary diameter. Following [Par11] and solving the set of parametric equations leads to $D_{\mathrm{p,trans}} = 760\,\mu\mathrm{m}$. For bigger or removed capillaries only the thinnest part in the nozzle with $D_{\mathrm{v}} = 400\,\mu\mathrm{m}$ limits the flowrate. Fig. 4.4 shows that the 700 µm capillary slightly decreases the flowrate, since the friction limited regime becomes dominant.

4.3. Measured flowrates

In the following, the measured properties of the valve are explored. Starting with the flow rate dependence on the piezo voltage, the role of nozzle diameter for various pressures is discussed. The errorbars of the performed measurement with helium as working gas include the following uncertainties:

- Volume of the vacuum chamber: ±5 l
- Temperature of the vessel: ±2 K
- Baratron: $\pm 1 \times 10^{-4}$ mbar, relative ±1 %
- Gas filling pressure: ±15 mbar for $p > 1$ bar and ±2 mbar for $p < 1$ bar

4.3.1. Voltage regulation

Fig. 4.3 shows the gas flux as a function of the piezo voltage for three different filling pressures (helium). For a voltage $U < U_{\mathrm{open}}$ the valve is closed. The value of U_{open} depends on the initial tension of the sealing and denotes the voltage where the gas flux begins. A temperature increase leads to a shift of the opening voltage U_{open} toward higher values as discussed in Fig. A.6 and [Gri17]. U_{sat} is the minimal required voltage at which the gas flux is limited by the capillary (or the orifice diameter) and does not change with voltage for $U > U_{\mathrm{sat}}$. For $U_{\mathrm{open}} < U < U_{\mathrm{sat}}$, the flux is limited by the distance of the sealing point to the Viton element.
A simple estimation of the necessary distance for a full opening can be achieved by equalizing the orifice cross section with the shell area of a hypothetical cylinder. This cylinder has the same ground area as the orifice, its height is defined as the distance between the Viton element and the orifice. This leads to a minimum distance of 0.25 times the diameter of the orifice for a full opening of a valve. For the 400 µm sealing perforation this gives a minimal distance of 100 µm.
The opening and saturation voltage as well as the shape of the curves stay constant for all

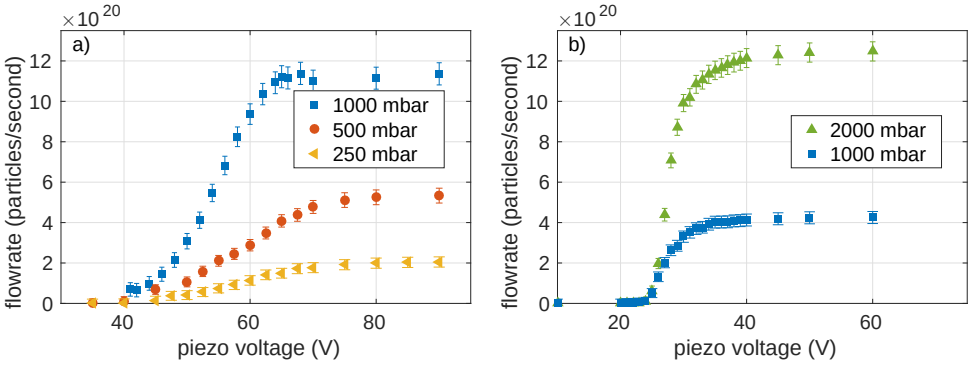

Figure 4.3.: Voltage dependent gas flux for different pressures. a) Viton plug sealing with 700 µm capillary, b) Viton plate sealing with 400 µm capillary.

pressures. The level of saturation is dependent on the pressure as shown in Fig. 4.4.
The voltage span between U_{open} and U_{sat} depends on the stiffness of the system, which is much higher for the Viton plate sealing (cf. [Gri17]). Fig. 4.3 shows that this voltage span for the Viton plug a) is 30 V compared to 10 V for the Viton plate b). The smaller voltage span needed for a full opening decreases the switching time for the Viton plate sealing b) by a factor of 3 compared to the Viton plug a).

The slope at the steepest point of the voltage dependent flowrate curve for 1000 mbar in Fig. 4.3 a) is $(6.9 \pm 0.4) \times 10^{19}$ pps/V. 1 V piezo voltage corresponds to a distance change of 4.77 µm. This shows that small changes in the distance between the Viton sealing and the orifice (e.g. caused by oscillations of the piezo, cf. Fig. 4.6 a)) have an enormous influence on the flowrate in this region.
For a more robust behavior of the valve it is therefore recommended to use the maximum piezo voltage, yielding a complete opening of the valve. As described in the following, the gas flow is then regulated by pressure variation, e.g. at a rate of $(1.333 \pm 0.015) \times 10^{18}$ pps/mbar for the 700 µm capillary (cf. subsection 4.3.2).

4.3.2. Pressure variation

Variation of the pressure at fully opened valve has shown to be the most precise way to regulate the gas flux. As shown in Fig. 4.4, for sufficiently high pressures, the dependence of the flowrate on the pressure is linear and can be described by Eq. 4.8. The regressions lead to

$$\begin{aligned}
\dot{N}(p)|_{298\,\text{K,no cap.}} &= (1.635 \pm 0.003) \times 10^{18}\text{pps/mbar} \cdot p - (5.2 \pm 1.6) \times 10^{19}\,\text{pps} \\
\dot{N}(p)|_{298\,\text{K,700 µm}} &= (1.333 \pm 0.015) \times 10^{18}\text{pps/mbar} \cdot p - (1.5 \pm 0.3) \times 10^{20}\,\text{pps} \\
\dot{N}(p)|_{298\,\text{K,400 µm}} &= \quad (7.66 \pm 0.12) \times 10^{17}\ \ \text{pps/mbar} \cdot p - (2.9 \pm 0.5) \times 10^{20}\,\text{pps},
\end{aligned}$$

where $\dot{N}$ is the particle flowrate per second and p is the gas pressure (He) in mbar. The theoretical description of the flowrates (cf. section 4.3) achieves an excellent agreement with the measured slope of the linear pressure dependence. This is shown in Fig. 4.4 for three different cases. How-

ever, it is necessary to set a friction factor ($\sim$ 0.01–0.02, cf. [Par11]) for the calculation, which is hard to determine exactly and which strongly depends on the chosen capillary. In contrast to the measurements, Eq. 4.8, which describes the gas flow through an orifice, does not predict an offset for the linear regime. However, this is reasonable, since the dependence becomes quadratic for low pressures, where compressibility effects become negligible due to smaller pressure differences. Fig. 4.4 b) shows that the smaller capillary limits the expansion by frictional processes and hence reduces the pressure gradient, which leads to a wider range of quadratic dependence. Without attached capillary the quadratic regime nearly vanishes, since in this case the flux is limited by the orifice diameter, leading to strong pressure gradients (cf. subsection 4.2.2). This is confirmed by the increasing offset of the linear function the more the flow gets friction limited. This offset is demonstrated in Fig. 4.4 for the thinnest capillary by comparing the theory curve (dashed line) which goes through zero with the offset corrected theory values.

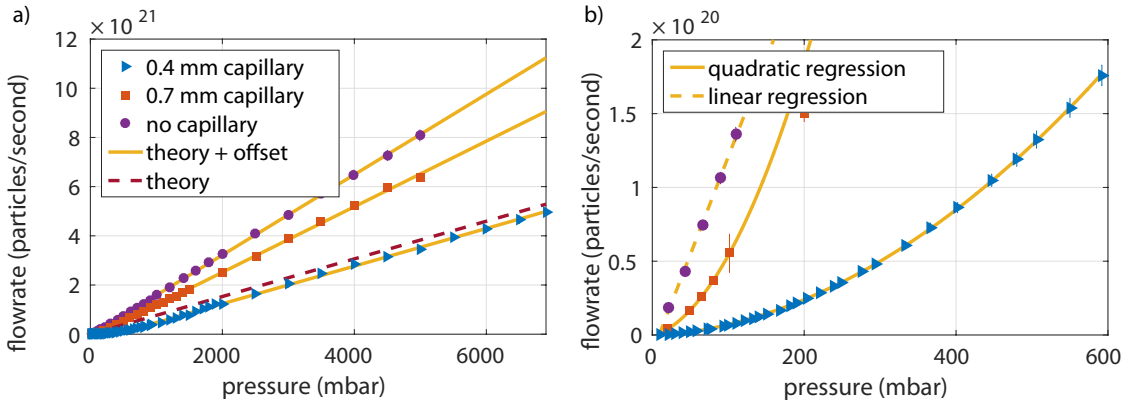

Figure 4.4.: Pressure dependent gas flux for two different capillary diameters and without attached capillary. a) shows the total pressure range measured, b) shows a magnification of the low pressure regime. For the 400 µm capillary, the flux regime with a quadratic pressure dependence is valid up to higher pressures, compared to the 700 µm capillary. With no capillary attached to the sealing point, the flow regime is linear for all measured pressures.

4.3.3. Gas type dependency

The gas flux through a valve depends on the gas type. For low pressures, where Eq. 4.5 holds, the gas type dependent quantity is the dynamic viscosity η of the gas. As the dynamic viscosity at room temperature is with $1.96 \times 10^{-5}\,\mathrm{Pa \cdot s}$ higher for helium compared to hydrogen with $0.88 \times 10^{-5}\,\mathrm{Pa \cdot s}$ (cf. [vI40]), the gas flux of hydrogen is higher compared to helium in the low pressure range.

This changes for higher pressures where the dependence of the flowrate on the pressure is linear. In this regime the flow dependence on the gas type is more complex as can be seen in Eq. 4.6 with the gas dependent quantities c_s and γ, where the dominant effect is mostly the $1/\sqrt{m}$ dependence of the adiabatic sound speed c_s. To demonstrate this influence helium has been compared to other gases as argon, nitrogen (N_2) and deuterium (D_2), which are also common gases used for

diagnostic and fueling in fusion applications. The flux reduction of the heavier gases argon and nitrogen, compared to helium is plotted in Fig. 4.5, measured with the 700 µm capillary.

For deuterium, the flux difference to helium is not very pronounced as both gases have the same mass. In contrast to helium, the nature of deuterium is a two atomic molecule with two additional degrees of freedom. In this case, the heat capacity ratio ($\gamma_{D_2} = 7/5$) is lower than for helium ($\gamma_{He} = 5/3$). The dependence of the flowrate on γ, as it is given by Eq. 4.8, is quite complex, although the square root behavior dominates. So the flowrate is by 5.7 % lower for deuterium.

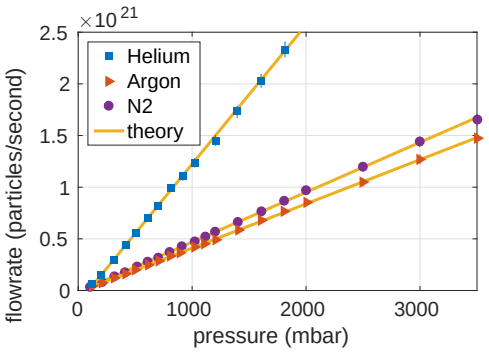

Figure 4.5.: Dependency of the flowrate on the gas type for the two noble gases helium and argon as well as for nitrogen (N_2). Measured with the 700 µm capillary.

Tab. 4.1 shows the influence of the gas type on the resulting flux compared to helium, as measured and also as theoretically calculated. As the measured results are in excellent agreement with the theoretical prediction of the flux reduction, the table is supplemented by additional gases often used in fusion research. The flux changes listed in the table are relative to helium as this is the working gas used in this paper.

Table 4.1.: Influence of the gas type on the resulting flux, compared to helium.

	unified		flux change (%)	
gas type	atomic mass	γ	measured	theory
helium	4	5/3	0	0
hydrogen	2	7/5	–	+33.3
deuterium	4	7/5	-4.1 ± 1.5	−5.7
neon	20.18	5/3	–	−55.5
nitrogen	28	7/5	-64.1 ± 0.3	−64.4
argon	39.95	5/3	-68.2 ± 0.2	−68.4

4.4. Switching times

One advantage of the chosen valve design is the possibility of fast modulation of thermal gas beams. To realize this, the piezo element, which behaves like a capacitor, has to be charged and discharged quickly. A suitable piezo driver is the system "30V300"[11], which provides a maximum current of 300 mA, leading to a switching time of 3.1 ms for a full opening of the piezo from −20

[11] Piezosystem Jena GmbH, Stockholmer Straße 12, 07747 Jena, Germany

to 130 V[12]. Fig. 4.6 a) shows the piezo voltage as a function of time after the control signal change. The piezo voltage is proportional to the expansion of the piezo ceramic whereas the total movement of the piezo actor corresponds to the ceramic movement amplified by a spring system surrounding the ceramic (stiffness: 0.06 N/µm).

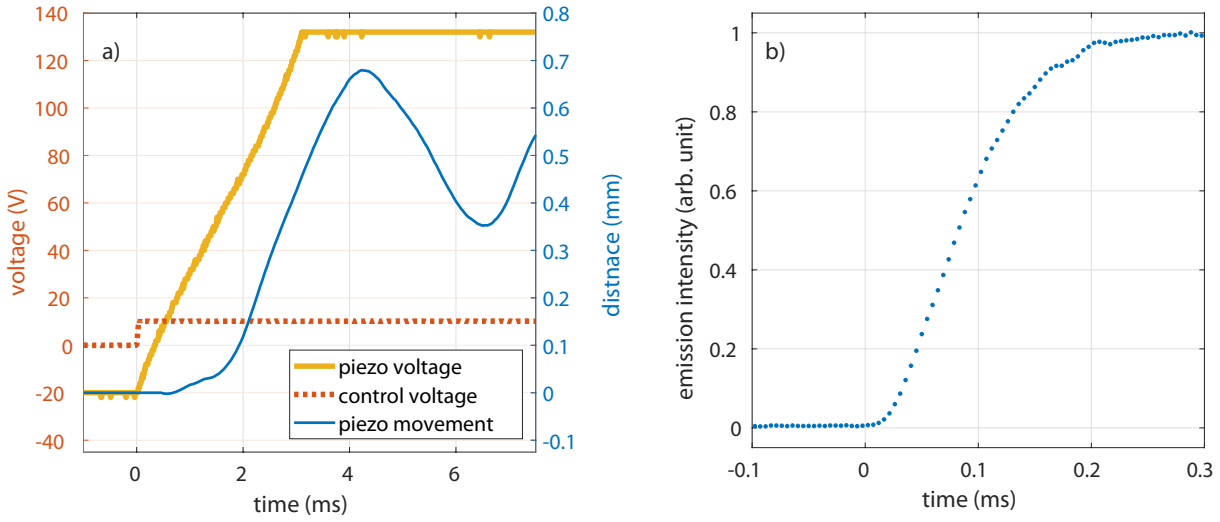

Figure 4.6.: Switching time of the piezo valve. a) shows the total movement of the sealing plate (blue) compared to the piezo voltage (yellow) as a function of time together with the control signal (red). b) shows the intensity timetrace of the 587 nm helium line measured with gas puff imaging as the overall intensity of the 2-D image during AUG discharge #34 227 as a marker for the gas cloud formation time. The 10 to 90 % rise-time is 0.15 ms, whereas the 2 to 98 % rise-time is 0.2 ms. Measured with 210 kfps and 4.3 µs exposure time. The zero points of the x axes are arbitrary.

The total movement of the piezo actor is traced with a fast camera (model "Phantom v711"[13]). The resulting trajectory, plotted in Fig. 4.6 a) (blue), shows that the piezo movement closely follows the applied voltage (yellow). The delay between the trigger and the start of the movement is caused by the initial tension of the piezo-spring system as well as the elasticity of the Viton plate. The main part of the piezo movement begins at the point, when the Viton plate detaches from the orifice at around 40 V piezo voltage (dependent on the initial tension, cf. Fig. 4.3). At 3.1 ms the piezo is fully charged with 120 V, corresponding to a stroke of 500 µm. Inertia causes an overshooting of the piezo of about 180 µm, leading to a damped oscillation with a resonance frequency of 250 Hz. This resonance frequency depends on the movable mass connected to the piezo, in this case 2.84 g.
For the operation with fully opened piezo valve this oscillation is not influencing the particle flux because the minimal distance during oscillation between the sealing plate and the orifice is always larger than the maximum distance (100 µm, cf. subsection 4.3.1) limiting the particle flux.

The buildup time of the injected gas beam is even faster than the full opening time of the piezo from −20 to 130 V. This can be seen in Fig. 4.3 a) where only the voltage change between 40 and

[12] The control voltage for the piezo drivers is produced with Siemens SIMATIC, which also controls the valves for the gas inlet system.
[13] Vision Research, 100 Dey Road, Wayne, New Jersey 07470, USA

70 V influences the gas flux. This reduces the relevant time by 80 %. With the Viton plate as sealing mechanism, the system is more stiff so that only a voltage change of 10 V is required for a full opening (cf. Fig. 4.3 b)), leading to gas formation times < 0.2 ms. An experimental proof for the fast buildup of the thermal beam is the temporally resolved measurement of the total emission of the injected helium cloud during an AUG discharge, using a fast camera. Fig. 4.6 b) shows that the emission intensity rise-time from 2 to 98 % is 0.2 ms. Thus, sharp gas pulses with short interruptions for background subtraction can be produced as shown in section 7.1.

4.5. Gas cloud shape

The beam geometry influences the achievable spatial resolution of active spectroscopy. To measure the beam geometry[14], the valve is placed in a helium glow discharge (cf. Fig. 4.7), current controlled at 500 mA and a background pressure of 3×10^{-3} mbar. When additional helium or other gases are injected into the glow discharge by the piezo valve, the injected neutral gas is excited mainly by the plasma electrons and therefore emits light. This emission is brighter[15] compared to the background, due to the higher local gas density.

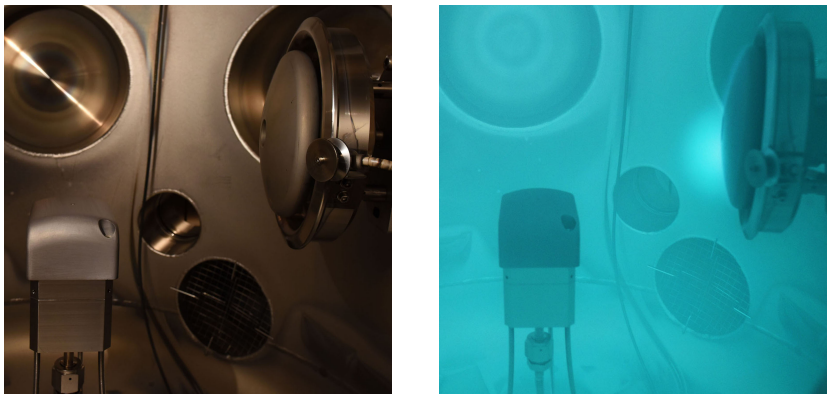

(a) Piezo valve (left) and glowing anode (right) in the vacuum chamber.

(b) Photo of the helium glow discharge (580 V, 500 mA).

Figure 4.7.: Experimental setup in the vacuum chamber for beam shape measurements without (a) and with (b) a glow discharge.

As shown in Fig. 4.8, a fast camera (model "Phantom v710") was used to measure the total line integrated 2-D emission intensity. The result of such a measurement can be seen in Fig. 4.9 for injected deuterium after background subtraction. It has to be remarked that an inverse Abel

[14] Here the unperturbed beam geometry, i.e. without ionization effects of the neutral beam in the plasma, is measured. As discussed in section 6.1 these effects have to be included to model the neutral beam geometry in the SOL of tokamaks.

[15] A too high local density leads to local cooling of the plasma and therefore to a decrease of the light emission intensity.

transformation is not necessary to reconstruct the 3-D emission distribution from the measured line integrated data in case of a Gaussian emission profile as shown in section A.5.

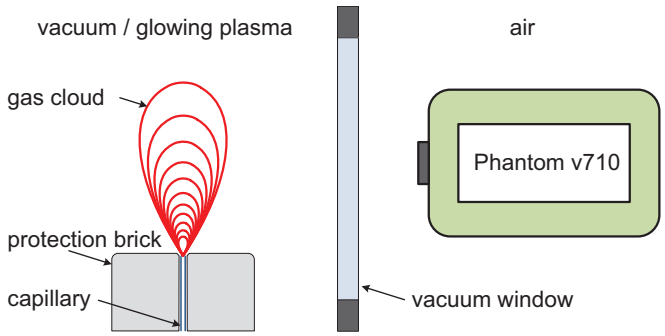

Figure 4.8.: Scheme of optical measurement of the gas beam shape. The fast camera "Phantom v710" was used with a frame rate up to 10 000 Hz.

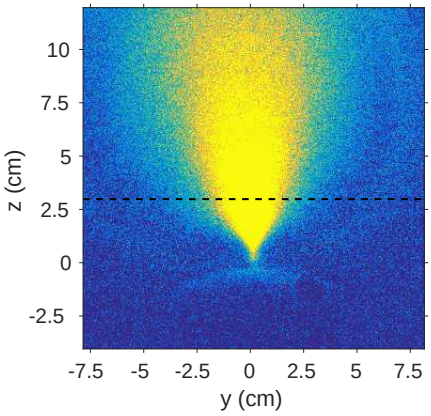

Figure 4.9.: 2-D emission of a deuterium cloud in a helium glow discharge. A 1-D profile for the dashed line is shown in Fig. 4.10.

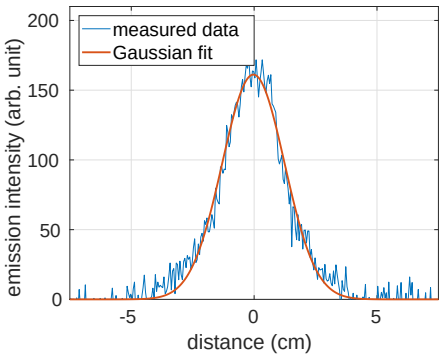

Figure 4.10.: 1-D line integrated emission profile at 3 cm distance to the valve.

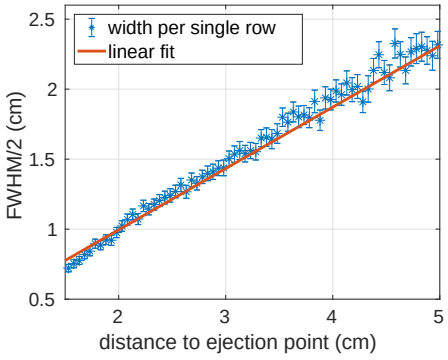

Figure 4.11.: Width of the Gaussian fits for different distances to the gas ejection point.

We can assume a symmetric 2-D Gaussian distribution (cf. Fig. 4.10) of the gas density $n(x, y, z)$ in planes perpendicular to the capillary which is aligned in z-direction[16].

$$n(x, y, z) = \frac{1}{2\pi\sigma(z)^2} \cdot \exp\left(-\frac{x^2 + y^2}{2\sigma(z)^2}\right) \tag{4.9}$$

The gas expands in a cone shaped cloud, where the radius of the cone, dependent on the distance to the injection point, is defined as the full width at half maximum (FWHM) of the Gaussian distribution. It is given by

$$\mathrm{FWHM} = 2\sigma\sqrt{2\ln 2}. \tag{4.10}$$

[16] This is the normalized gas area density so that $\int_{-\infty}^{\infty}\int_{-\infty}^{\infty} n(x, y, z)\,\mathrm{d}x\,\mathrm{d}y = 1$. The total 3-D gas density is $n(x, y, z) \cdot \dot{N}/v$ with the particle flowrate $\dot{N}$ and the mean particle velocity v.

The FWHM increases linearly with rising distance like

$$\mathrm{FWHM} = 2z \cdot \tan\alpha, \tag{4.11}$$

where α is the half angle of beam spread. Combining Eq. 4.10 and Eq. 4.11 leads to the relation

$$\sigma(z) = \frac{z \cdot \tan\alpha}{\sqrt{2\ln 2}}. \tag{4.12}$$

To evaluate the measured data in order to calculate the angle of beam spread 2α, Gaussian functions were fitted to the background subtracted camera data line by line, as shown exemplarily in Fig. 4.10. The FWHM of each line were combined for all distances z to the nozzle as long as the fit was good enough ($R^2 > 0.92$, cf. Fig. 4.11). A linear fit through the data allows the calculation of α as listed in Tab. 4.2 for three different gas types.

Table 4.2.: Comparison of the half angle of beam spread α for different combinations of gas type and pressure.

gas type	pressure (mbar)	α (degree)
helium	5000	20.0 ± 1.5
deuterium	600	25.4 ± 0.5
argon	400	18.9 ± 0.5

4.6. Summary of the gas injection system

This chapter presented a versatile gas injection system, developed within this thesis for active beam emission spectroscopy on helium. As the compact system withstands the harsh environment of fusion devices, it is placed directly inside the vacuum chamber close to the plasma periphery. The valve system is based on a piezo element and a thin capillary through which the gas expands. This leads to an opening angle of the injected gas beam of about 20° for helium. Dependent on the filling pressure of the valve and the chosen capillary diameter, gas fluxes are accessible from 10^{18} up to 10^{23} part/s. The valve offers high duty cycles and fast switching times which enables background subtraction for the spectroscopic signal. This makes the piezo system an excellent device to provide gas injection for fueling or various diagnostic applications as active line ratio spectroscopy on helium. The optical components which are necessary to perform the measurements are presented in the following chapter.

5. Optical hardware components

Parts of this chapter are published in M. Griener, et al., "Helium line ratio spectroscopy for high spatiotemporal resolution plasma edge profile measurements at ASDEX Upgrade (invited)", Rev. Sci. Instrum. 89, 10D102 (2018). [Gri18b].

This chapter presents the dedicated optical system for the thermal helium beam diagnostic at AUG. Two components are of particular importance. The first one is the optical head which collects the light from the experiment, presented in section 5.1. The second main development is the polychromator system presented in section 5.2.

5.1. In-vessel components

In the following, the in-vessel components for the implementation of active helium line ratio spectroscopy at AUG are presented. All components must be vacuum compatible and have to withstand the harsh environment of fusion devices, i.e. high thermal and radiation loads as well as high magnetic fields. The in-vessel components are pictured in Fig. 5.1, which shows a CAD-based view of AUG sector 13 in the toroidal direction. Furthermore the components are pictured in Fig. 5.2, which shows a photography of the low field side of the AUG vacuum chamber in sector 13.

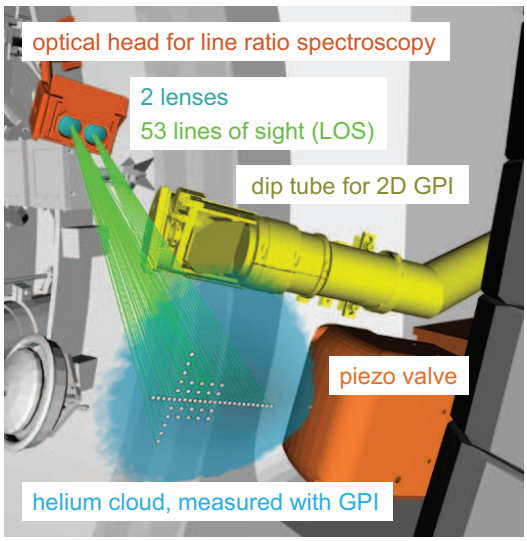

Figure 5.1.: View in the toroidal direction, representing the helium beam and GPI diagnostics at AUG. A detailed representation of the LOS is given in Fig. 5.6.

The **piezoelectric valve** for helium injection (cf. chapter 4) is placed at the magnetic low field side of AUG (radius $R = 2.19\,\mathrm{m}$ and height $z = -0.16\,\mathrm{m}$ with respect to the midplane, cf. Fig. 5.6). The emitted light is collected by the optical head or a **dip tube** which provides a 2-D image of the gas cloud. The 2-D image is transmitted to the fast camera "Phantom v711" by an image conductor. This camera can be equipped with a filter for one specific wavelength or record the total emission of the cloud. The information extracted from a full 2-D image can e.g. be used for gas-puff imaging (GPI) (cf. [Zwe17, Fuc14]).

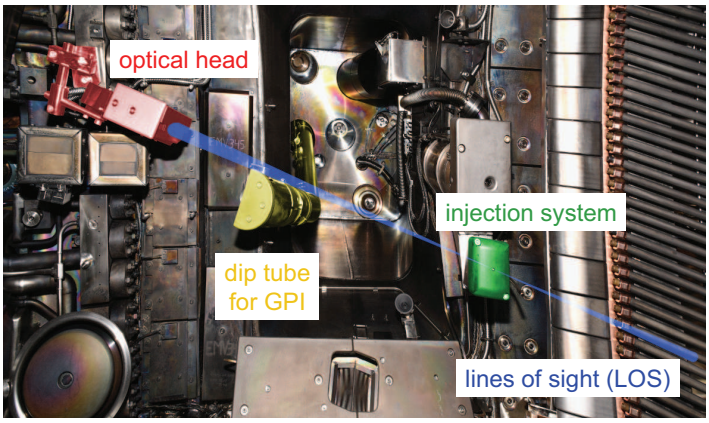

Figure 5.2.: In-vessel components of the thermal helium beam and the GPI system at the low field side of sector 13 in AUG. Helium is injected by the valve (highlighted in green) perpendicular to the image plane. The optical head for the helium beam diagnostic (red) and the corresponding LOS orientation (blue) as well as the mirror system GPI (yellow) are shown. All components are placed close the the plasma periphery and therefore protected by tungsten coated carbon tiles.

5.1.1. Optical head for light collection

The newly developed **two-lens optical head** for the helium beam diagnostic provides 52 LOS (cf. Fig. 5.3) which intersect with the helium cloud. The optical head is equipped with an innovative clamping system for optical fiber ends (cf. subsection 5.1.3). With this technique an arbitrary distribution pattern of LOS can be achieved to gain radial and poloidal profiles. In this, two perpendicular 1-D arrays yield profiles in the radial and poloidal directions, whereas a 2-D matrix distribution of 5×5 fibers allows the tracing of turbulent blob structures in the scrape-off layer (SOL) [Fuc14]. These points can be superposed with the 2-D image of gas-puff imaging (cf. Fig. 7.18).

The optics achieves a spatial resolution of up to 3 mm (cf. subsection 5.1.2) and covers a radial region of 8.5 cm, starting at the limiter radius and ranging into the confined region beyond the separatrix. The high spatial resolution is achieved by aligning the LOS tangentially to the magnetic field lines in the measurement region.

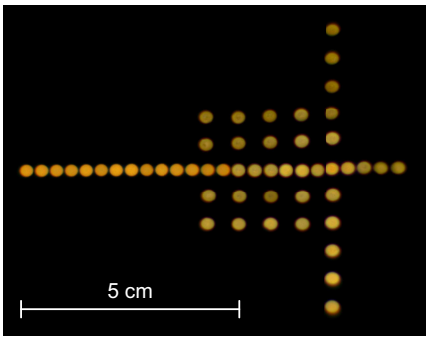

Figure 5.3.: Image of the backward illuminated optical fibers at the observation plane.

In the vacuum chamber, the optical head is tilted by 17° with respect to the horizontal plane (cf. Fig. 5.9). The lenses have a distance of $d = 0.69\,\mathrm{m}$ to the helium injection point. With a clear aperture of 34 mm (area $A_{\mathrm{lens}} = 9.1 \times 10^{-4}\,\mathrm{m}^2$), one lens covers a solid angle of $\Omega = A/d^2 = 1.9 \times 10^{-3}\,\mathrm{sr}$.

The light which is collected by the lenses is coupled to in-vessel fibers, placed at a distance of 88 mm behind the lenses. The numerical aperture (NA) of the fibers is 0.22. NA is defined as

$$\mathrm{NA} = n_0 \sin \alpha, \tag{5.1}$$

where n_0 is the refraction index of the surrounding medium (vacuum or air) and α is the light acceptance angle, measured toward the optical axis. For NA = 0.22, the angle is 12.7°, such that all light which is collected by the lenses is accepted by the optical fibers. This as well as the schematic structure of the optical head is presented in Fig. 5.4.

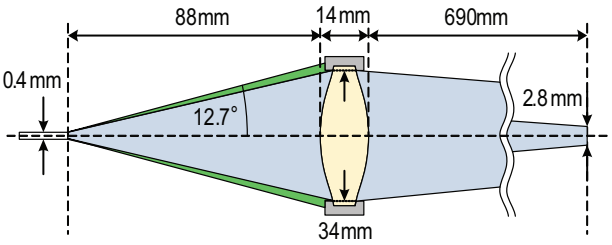

Figure 5.4.: Schematic representation of the optical head. The lens (shaded in yellow) collects the light along the LOS (shaded in blue) with a diameter of 2.8 mm at the narrowest point. The light is bundled into the bare end of optical fibers with a 0.4 mm core diameter and an NA of 0.22. The NA, which determines the acceptance angle of the fiber is illustrated as the green-shaded area.

A detailed view of the optical head is given in Fig. 5.5. The fiber ends in the interior of the optical head are placed as a 2-D-pattern in a wire-eroded holder as described in subsection 5.1.3. The head is equipped with two aspherical lenses, "AFL50-80-S-A2"[1], with a nominal focal length of 80 mm (effective focal length, EFL = 85 mm) and a diameter of 35 mm (cf. section A.6). The lenses are protected by a magnetic shutter (cf. subsection 5.1.4), which is closed in between discharges. Two lenses are used to increase the spatial resolution of the diagnostic, since this reduces the maximum angle between the LOS and the field lines at the observation point as explained in subsection 5.1.2.

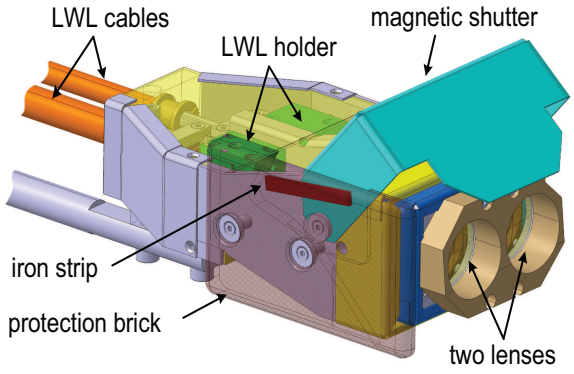

Figure 5.5.: CAD drawing of the two-lens optical head including the magnetic shutter in an open position with iron strip (red) and optical fiber (LWL) holders in the head's interior. The two LWL cable bundles are connected to a vacuum feed through.

[1] Asphericon GmbH, Stockholmer Straße 9, 07747 Jena , Germany

5.1.2. Spatial resolution

The spatial resolution of active beam emission spectroscopy depends on three major factors; the beam width, the alignment of the LOS and the beam orientation with respect to the magnetic field lines as well as the diameter of the LOS at the observation point. The latter one influences also the amount of collected light so that a diameter of 3 mm is chosen (cf. section 3.1). This sets the lower limit for the spatial resolution, as measured in units of mm. The best resolution can be achieved if the beam is directed perpendicularly to the flux surfaces and the LOS are tangential to the flux surfaces in the region of intersection with the beam. This perfect alignment is, of course, only possible for one LOS per lens. The angle between the remaining LOS and the flux surfaces increases with the radial region covered by one lens. To achieve a good resolution over a radial distance of 8.5 cm, which covers the whole scrape-off layer, two lenses are used in the optical head. Furthermore the usage of two lenses minimizes aberrations of the optics due to a reduced off-axis distance as described in section A.6.

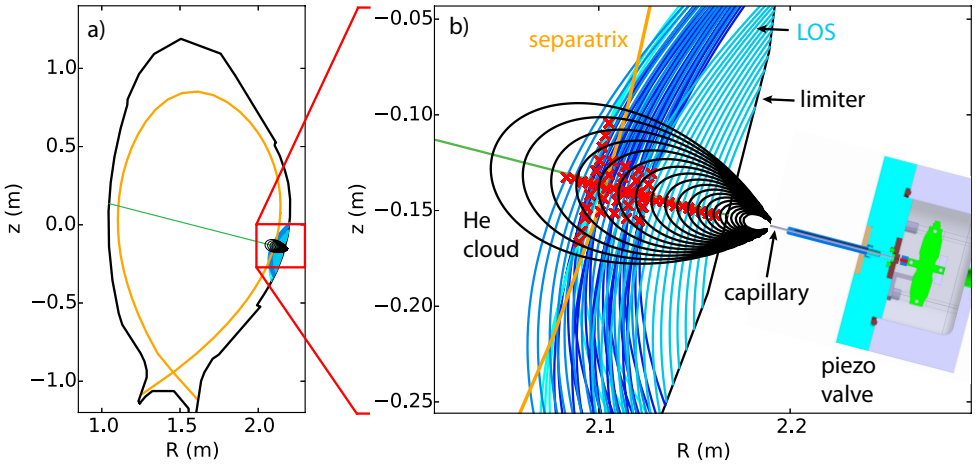

Figure 5.6.: Poloidal cross section of AUG. The LOS (blue), the piezo valve and a contour plot of the helium density (black), as well as the separatrix (orange) and limiter position (black) are illustrated. The green line shows the central axis of the helium cloud, which is situated perpendicular to the flux surfaces and the LOS at the measurement region. The red crosses mark the points of highest emission along each LOS.

The achieved resolution of each LOS is calculated in a forward model. This model calculates the emission of the helium cloud and overlaps it with each LOS as illustrated in Fig. 5.6. This yields the emission along the LOS as a function of ρ_{pol} along each LOS, which is plotted in Fig. 5.7 for three LOS with the worst a), the mean b), and the best c) resolution. The names of the LOS in the plot follow the system "HEBxy", where x is the position of the LOS in radial direction ($x = 0$ corresponds to the standard separatrix position, higher numbers correspond to higher radii) and y is the position in poloidal direction ($y > 0$ above the central axis of the beam).
The worst resolution in Fig. 5.7 corresponds to the innermost LOS, where the helium beam is broadest and the LOS has the steepest angle toward the field lines. This broadening corresponds to a spatial range of 3 mm, which has to be added to the 3 mm resolution minimum given by the LOS diameter. The broadening for the best aligned LOS is negligible and the mean value is 0.9 mm.

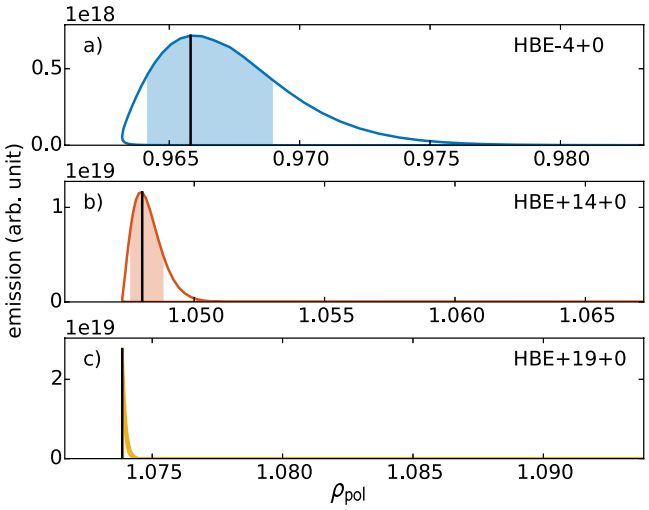

Figure 5.7.: Photon emission along three lines of sight as a function of ρ_{pol} along the LOS for the a) worst, b) mean and c) best resolution of all 52 LOS. The black vertical line denotes the radius of maximum emission, whereas the shaded area shows the region where 67 % of the total emission comes from.

5.1.3. Fiber holder

The most innovative part of the optical head is the mechanism that fixes the fiber ends in the head's interior. The clamping mechanism allows the production of arbitrary LOS patterns, which are images of the fiber distribution. The optical head is a modular system, such that the fiber-equipped fiber holder for each lens can be placed separately in the head's interior. This is necessary for installing the optical head in the vacuum chamber as the fibers have to fit through small vacuum ducts. The two fiber holders are not symmetric. Holder 1 is equipped with a 2-D array, while holder 2 contains only a single row of fibers to increase the measurement range for the radial profiles (cf. Fig. 5.8 a)).

Both fiber holders are based on a clamping system, which fixes the fiber ends reversibly. Without using of any glue, the system is well suited to usage in vacuum chambers, including the baking procedure at 150 °C.

The high-OH (high concentration of hydroxyl groups) "UV400-440-480P"[2] fibers with NA = 0.22 and an outer diameter of 0.480 mm were used in-vessel. The holders (cf. Fig. 5.8) were wire-eroded from an aluminum block with the "Sodick AG400L" eroding machine equipped with a 0.15 mm brass wire. This enabled the cutting of single wire channels for the optical fibers. The 3-D arrangement of the fibers is built in such a way that every fiber is aligned toward the center of the corresponding lens (cf. Fig. 5.8 b)). This minimizes the maximum angle of light incidence with respect to the fiber and enables an optimal light incoupling.

The reversible fixing of the fibers in the 2-D pattern is achieved by shearing the inner part of the holder with respect to its front and back sides by simultaneously pressing the holder's upper and

[2] Art Photonics GmbH, Rudower Chaussee 46, 12489 Berlin, Germany

lower parts together, as illustrated in Fig. 5.8 with red arrows. For the 1-D pattern, clamping by pressing both holed parts together is sufficient.

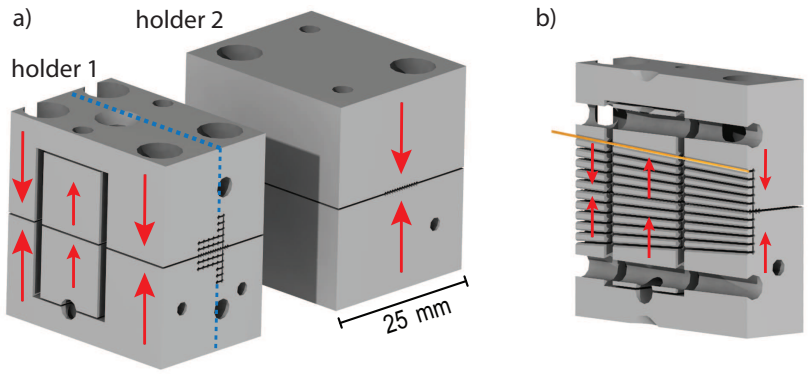

Figure 5.8.: CAD drawing of the fiber holders manufactured by wire eroding out of an aluminum block. The arrows represent the direction of tension used to fix the fibers mechanically in their positions. Each block is positioned behind one lens in the optical head. A cross-sectional view of the dashed marked plane in a) is given in b). It demonstrates the arrangement of fiber channels in the block's interior. One fiber is illustrated in the uppermost channel.

5.1.4. Magnetic shutter

To prevent the lenses of the optical head to be coated during boronisation (cf. [Roh07]), a magnetic shutter is installed in front of the lenses. It is normally closed and only opened during the operation time of the toroidal magnetic field. The shutter is lifted by magnetic force which is applied to two ferromagnetic strips ($46 \times 6 \times 2\,\mathrm{mm}^3$) with a relative permeability of $\mu_\mathrm{r} = 220$. The ferromagnetic strips are attached to the shutter and become aligned to the magnetic field during operation. The resulting torque for the closed shutter, leading to this alignment, is 6 Nm for an AUG standard discharge with a toroidal field of $B_\mathrm{tor} = -2.5\,\mathrm{T}$ and a plasma current of 1 MA. The shutter was experimentally tested in a magnetic test stand with 0.5 T, which was strong enough to fully open the shutter.
The torque produced by the magnetic field is given by $D = l \cdot F$, where l is the length of the iron strip. The force F depends on the field strength, the relative permeability of the ferromagnetic material as well as its geometry and the alignment with respect to the magnetic field. A parallel translation of the iron strip with respect to the rotation axis of the shutter does not influence the magnetic torque. For the location of the strip, only a precise angular alignment with respect to the shutter and the magnetic field lines is important.
The slope of the field lines at the low field side, where the optical head is located, is around 10° for normal operation and −10° if the plasma current is reversed. During both scenarios the shutter should be opened. The mechanically maximum possible opening angle of the shutter is 67°, related to the optical head, which itself is tilted by −17° toward the horizontal plane. An opening angle of at least 38° is necessary for the shutter to avoid a partial blocking of light. These boundary conditions determine the geometrical alignment of the ferromagnetic stripe on

the shutter, which is represented in Fig. 5.9 a) for the closed and in b) for the opened shutter. For normal operation, the shutter rotates by 50° which fulfills the requirements. For B_{rev}, the opening angle would even be higher, but it is restricted by a mechanical stop.

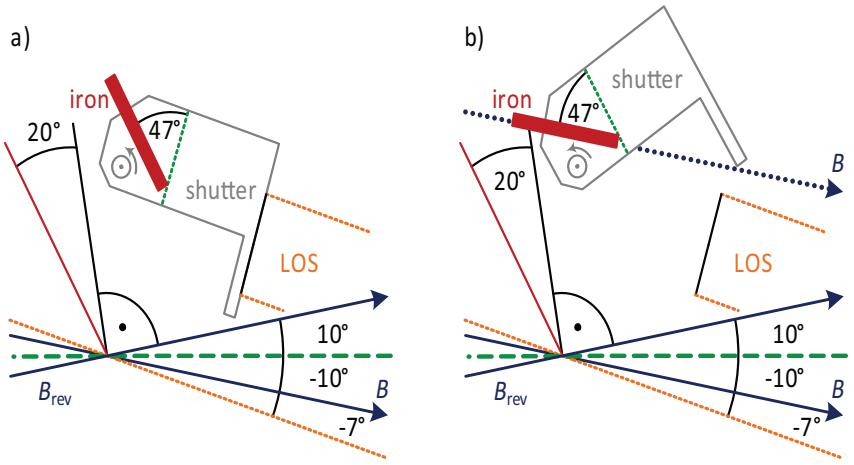

Figure 5.9.: Alignment of the ferromagnetic iron strip of the magnetic shutter with respect to the horizontal axis (green, dashed), the viewing angle of the LOS (orange, dashed), the magnetic field B for AUG standard configuration and B_{rev} for reversed plasma current (blue, solid). a) shows the shutter in closed and b) in open position, rotated by 50° such that the iron strip aligns to B. In b) the LOS region (between the two short orange lines) is fully cleared.

5.2. Polychromator system and data acquisition

This section handles the light sensors and data acquisition hardware for line ratio spectroscopy, where the simultaneous measurement of several He I line intensities is required. This can be achieved with a broad band spectrometer as used in [Bar16], which enables also the observation of other spectral lines which may disturb the exclusive measurement of He I lines. The disadvantage of this approach is that the typical spectrometers provide a poor time resolution on the order of 1–100 ms. To measure thousand times faster, a system based on photomultiplier tubes (PMT) [Col03, Kaj06] or avalanche diodes [Dun10] has to be used.

Two approaches are common for the spectral selection of He I lines, namely, either the usage of a spectrograph [Ago15] or the combination of beam splitters and filters. Within the filter approach, the light from each fiber is split with semipermeable mirrors [Kaj06] or dichroic mirrors [Col03] into different optical paths where the desired He I line is selected with a small band interference filter. Typically, such polychromator systems[3], which are often called filterscopes [Col03, Unt12], are designed to measure the light from only one optical fiber. This results in a large number of required filter systems, every single one of which has to be modified if another wavelength should be measured.

More flexibility can be obtained by combining all spatial channels within one device using PMT arrays. This is realized in the setup described in reference [Kru12], for which a direct optical

[3]Commonly used synonyms for polychromators are multichromators or multicolor systems.

access to the measurement region as a 2-D image is required. Within this thesis, a four-color, 32-channel polychromator system was developed which offers the simultaneous measurement of four wavelengths for 32 optical fibers by one device for the first time. The optical part of this system is described in subsection 5.2.1 and the following.

5.2.1. Four-color thirty-two channel polychromator

The light collected by the optical head in the torus is transmitted from the experimental hall to the laboratory by optical fibers[4] of 52 m length, 0.4 mm core diameter and an NA of 0.22. The light is coupled to a fiber bundle with an included taper (cf. subsection 5.2.2). Its 32 round end caps are optically mapped by a telecentric lens to the photomultiplier arrays. As illustrated in Fig. 5.10, the four detectors are therefore all placed at the same distance of 20.5 cm with respect to the end lens of the objective.

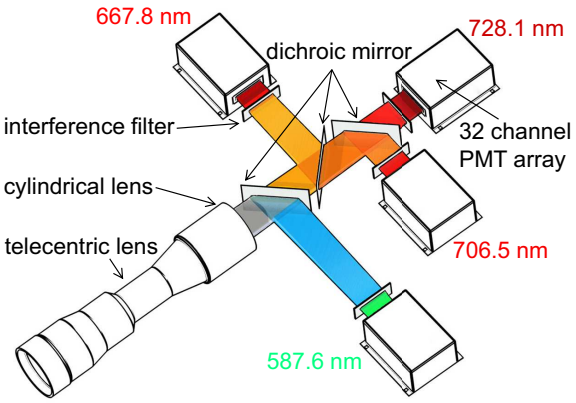

Figure 5.10.: Schematic representation of the 32-channel polychromator system, which includes imaging optics (left) that relay the light from the fiber array (left of the objective, not pictured) to the detectors. The light of each channel is divided into four wavelengths and measured separately.

On the way to the detector, the light of each fiber is split into four wavelength parts to measure the 587, 667, 706 and 728 nm helium lines simultaneously. The splitting of the spectral components is achieved using dichroic mirrors and the subsequent filtering is done with high-transmission interference filters (cf. subsection 5.2.3) placed directly in front of the detector plane. To match the elongated sensitive area of the detectors (cf. subsection 5.2.4), a cylindrical lens is placed behind the end lens of the objective to elongate the image of the fibers. The complete setup is enclosed by a blackened aluminum box to protect the detectors from other light sources. An active cooling of the setup is not necessary as the temperature increase within the protection box, caused by the lost heat of the detectors, is measured to be $< 4\,\mathrm{K}$.

The combination of high-transmission optics in combination with fast-responding PMT detectors and appropriate analog digital converters for the PMT output voltage allow a temporal resolution of 900 kHz. This makes the newly designed setup an excellent device for high resolution helium line ratio spectroscopy, also offering a compact design and a high flexibility in changing the selected wavelengths.

[4] Fiber type "UV400-440-470-830HT". Art photonics GmbH, Rudower Chaussee 46, 12489 Berlin, Germany

5.2.2. Fiber bundle and telecentric lens

Fiber bundle The fibers delivering light from the experimental hall are connected by fiber-optic connectors (FC) to a bundle[5] of 32 fibers. At the end of the bundle, the fibers with a core diameter of 0.8 mm are placed next to one another with a spacing of 1 mm in a linear array. This geometry matches the detector geometry (cf. subsection 5.2.4), such that a one to one mapping is possible. Each fiber of the bundle is tapered from a 0.4 mm core diameter on the FC side to a 0.8 mm core diameter on the imaging side. This process, which increases the diameter linearly is shown in Fig. 5.11. The red line illustrates the change of the NA for the etendue preserving transition between the diameters. The etendue $\mathcal{E}$ is defined with the fiber diameter d as

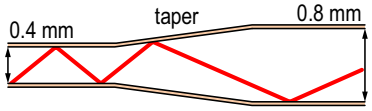

Figure 5.11.: Optical taper connecting a fiber with 0.4 mm diameter to a 0.8 mm fiber.

$$\mathcal{E} = \frac{\pi^2}{4} d^2 \mathrm{NA}^2. \tag{5.2}$$

It can be seen directly that doubling the diameter halves of the NA. The resulting NA of 0.11 corresponds to a light opening angle of 6.3° compared to an angle of 12.7° for NA = 0.22, measured toward the optical axis. This process increases the transmittance of light through the telecentric lens.

Telecentric lens The main boundary condition when designing a filter based system is that the light which passes the filters and mirrors should be as collimated, i.e. parallel, as possible. In general, this can be achieved by placing the fiber ends at the focal distance f_0 of a collimator lens and then focusing the light after wavelength splitting and filtering by an ocular lens to the detectors. Doing this, the light from off-axis fibers with a distance r_0 to the optical axis shows an angle of $\arctan(r_0 \cdot f_0^{-1})$ to the optical axis behind the collimator lens. The high distance between the collimator and ocular lenses needed to split the four wavelength parts would lead to high diameters for the ocular lenses. Therefore, most systems are designed to handle only a small number of fibers close to the optical axis. With the disadvantage of losing light, this problem can be solved using a telecentric lens as presented below.
Telecentric lenses produce an orthographic view of the subject. This is relevant because, with this technique, the distance between the off-axis rays and the optical axis stays constant. This major advantage comes at the cost of loss of light at the built-in aperture of the lens, which can only be passed by beams that make a small angle with the optical axis.
In the simplest case, a telecentric lens consists of two lenses with the same focal length f, separated by a distance of $2f$ with an aperture placed between them. This is illustrated in Fig. 5.12. Light passing through the lens at an angle higher than the teletricity angle toward the optical axis is blocked by this aperture. Therefore, more light is transmitted through the lens when small-NA fibers compared to high-NA fibers are used.

[5] Ceram Optec SIA, Skanstes iela 7, 1013 Riga, Latvia

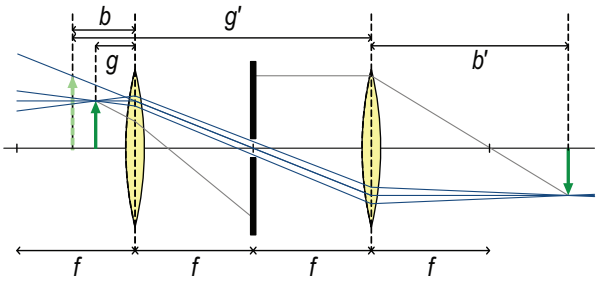

Figure 5.12.: Illustration of a telecentric objective with an equal focal distance f of both lenses, separated by an aperture. The effective object distances to the lenses are called g and g', the image distances b and b'. The objective produces a one to one image, the leftmost arrow is the imaginary intermediate image used for the construction of the light path.

If both objective lenses have the same focal length, a one-to-one image is produced. In the case of a telecentric lens, the position of the lens between the object and its image does not influence the image. This can be seen by using the lens equation of a thin lens which is given by

$$\frac{1}{b} + \frac{1}{g} = \frac{1}{f} \tag{5.3}$$

with the image distance b and the object distance g. For a telecentric lens where two lenses are placed at a distance of $2f$ and the distances of the second lens are named b' and g', one can write the lens equation for the second lens as

$$\frac{1}{2f - b} + \frac{1}{b'} = \frac{1}{f}. \tag{5.4}$$

Eliminating b by plugging in Eq. 5.3 and solving for f yields

$$2f = b' + g. \tag{5.5}$$

To achieve a sharp image, the distance between the object and the image plane is given by two times the effective focal length of the telecentric lens plus the distance of it's end lenses. The latter one is $2f$ according to Fig. 5.12, but can differ if a more complex setup for e.g. chromatic corrections is used for the imaging. This is the case for the telecentric lens TC16M036 from Opto Engineering [6] which is used for this setup. The diameter of the symmetric end lenses with a distance of 250 mm is 51 mm. The effective focal length of the objective is $f = 102.6\,\text{mm}$. According to Eq. 5.5 this is the half distance between the exit lens of the objective and the detectors if the fibers are placed directly at the surface of the entrance lens.
To enable the exact positioning of the fiber bundle close to the first lens, the delivered F-mount of the telecentric lens was unscrewed and replaced by a custom made fiber adapter.

[6] Opto Engineering Deutschland GmbH, Agnes-Pockels-Bogen 1, 80992 München, Germany

5.2.3. Interference filters and dichroic mirrors

The polychromator system is based on splitting the light from each fiber into four separated wavelength regimes by means of dichroic mirrors and selecting the required wavelength for each photomultiplier array with a small band interference filter[7] (cf. section A.7 Tab. A.3 and Tab. A.4). Both, dichroic mirrors as well as interference filters rely on stacked Fabry-Perot resonant cavities. The cavity consists of multiple thin layers of dielectric materials having different refractive indices. The layer thickness d is a multiple of the central wavelength λ_0 which is transmitted under normal incidence of collimated light. The transmitted wavelength λ is given by [Mal89, p.31]

$$\lambda = \frac{2n_{\text{eff}} d \cos\phi}{m}, \tag{5.6}$$

where m is the order of interference, n_{eff} is the effective reflection index of the filter and ϕ is the angle of incident light inside the spacer. Replacing $\lambda_0 = 2n_{\text{eff}} d \cdot m^{-1}$ and $\cos\phi$, after conversion, with the refraction law $\sin\theta = n_{\text{eff}} \sin\phi$, where θ is the incident angle of light in air, leads to the formula

$$\lambda_\theta = \lambda_0 \sqrt{1 - \frac{\sin^2\theta}{n_{\text{eff}}^2}}. \tag{5.7}$$

Eq. 5.7 is valid for angles up to some tens of degrees. The used filters were experimentally

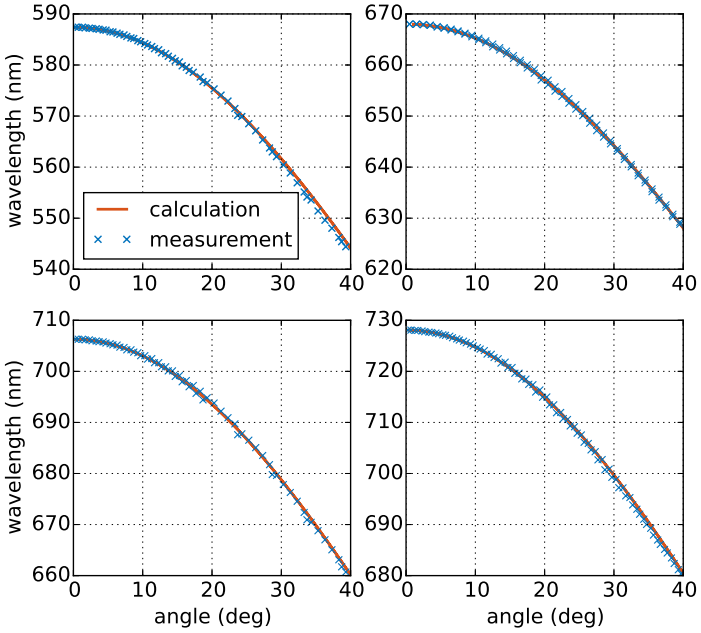

Figure 5.13.: Shift of the central wavelength as a function of the light incident angle for the four interference filters used. The measured values are compared to the calculated prediction, applicable for small wavelengths.

validated according to the correct central wavelength and the wavelength shift described by Eq. 5.7. This is done by placing the interference filters between a collimated light source and a

[7] Laser Components GmbH, Werner-von-Siemens-Straße 15, 82140 Olching, Germany

spectrometer[8] which measures the transmittance of the filter for normal incidence. Turning the filters in the beam path leads to the measurements presented in Fig. 5.13. It compares the shift of the central wavelength (CWL) of the interference filters as a function of the incident angle of the light to the predicted values by Eq. 5.7. The central wavelength for normal incidence is given by the maximum wavelength of the measurement as the function is symmetric for negative incident angles.
The knowledge of the angle dependent wavelength shift is of specific interest for estimating the required alignment tolerances in the optical setup. In this case, the wavelength shift is $< 0.5\,\mathrm{nm}$ for an alignment uncertainty of $\pm 4\,\mathrm{degree}$.

The dichroic mirrors are specified for an angle of incidence of 45°, where Eq. 5.7 is no longer valid. Fig. 5.14 shows the wavelength shift of the mirror with a 718 nm cut-on wavelength as a function of the incident angle. The wavelength of maximum transmission in the transmission band was measured (cf. Fig. 5.15). At 45° the transmission reaches its maximum of 98 % at a wavelength of 727.5 nm. Here the wavelength shift is a linear function of the incident angle with a slope of $(1.89 \pm 0.06)\,\mathrm{nm/degree}$ which makes precise alignment of the mirrors crucial.

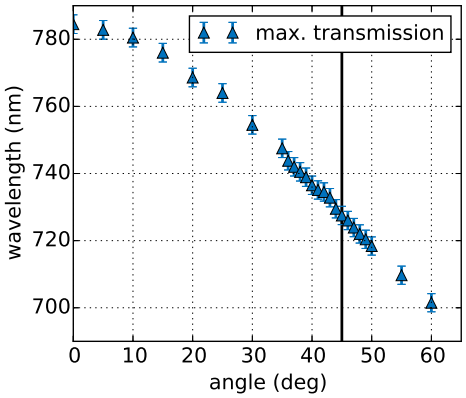

Figure 5.14.: Shift of the onset wavelength for the saturated region of the transmission band for the dichroic mirror with a 718 nm cut-on wavelength.

Fig. 5.15 shows the transmission spectra of the dichroic mirrors compared to the position of the interference filters. The absolute transmission of the filters is not representative because the resolution of the spectrometer used (AvaSpec-2048x14-USB2[8]) is on the order of the FWHM of the filters. In contrast to systems where semipermeable mirrors would lead to a transmittance of light $< 25\,\%$ for each channel, the dichroic mirrors and filters were chosen in a way that guarantees the maximum transmittance for each of the four measured lines. The 587 nm line is reflected by the first mirror with $> 98\,\%$ whereas the remaining three lines are transmitted with $> 98\,\%$ efficiency. The same numbers are valid for the other two mirrors with their corresponding lines, such that 94 % of the 706 nm and 728 nm light which passes the imaging optic reaches the corresponding filters.

[8] Avantes BV, Oude Apeldoornseweg 28, 7333 Apeldoorn, Netherlands

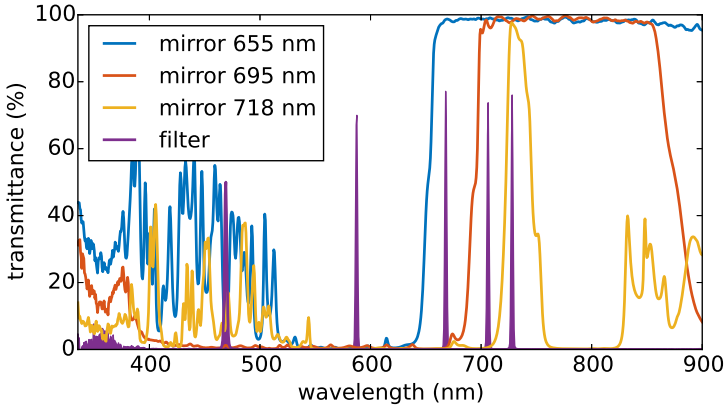

Figure 5.15.: Spectra of the three dichroic mirrors labeled with their cut-on wavelength compared to the transmission region of the interference filters.

The He^+ line at 468.6 nm can be observed alternatively to the 587 nm line by changing the filter in front of the first PMT array. Although the first dichroic mirror is not specially designed for reflecting the 468.6 nm line, the reflection efficiency is still 90 %. The two cavity 468.6 nm filter[9] has the same aperture as the other interference filters. But with 6.4 mm it is thicker compared to the other filters. The FWHM is 1.9 nm and the out-band blocking is 1×10^{-4} from X-ray to far infrared. At zero degrees light incident angle, the transmission reaches its maximum of 54 % at nominal 468.6 nm (measured 469.0 nm). The angle dependent wavelength shift is plotted in Fig. 5.16, compared to the calculated curve with $n_{\text{eff}} = 2.05$.

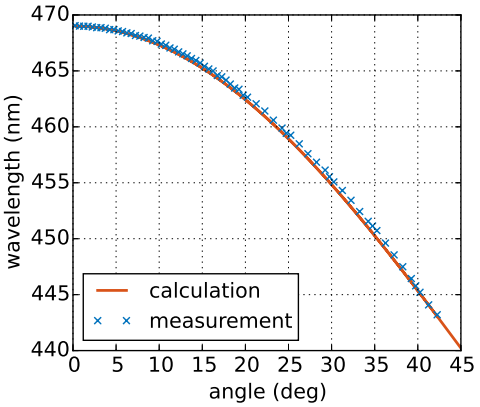

Figure 5.16.: Shift of the central wavelength as a function of the light incident angle for the 468.6 nm interference filters.

The PMT units can be damaged by an overexposure of light. Even at the lowest gain voltage the units would be damaged by room light, though the spectral composition of the room light has only little overlap with the the small band interference filters (cf. Fig. 5.17). To protect the setup from accidentally be damaged by room light, the box which covers the PMTs has a safety switch which shuts down the PMT power supplies when the box is opened.

5.2.4. Detectors and data acquisition

Light intensity is of prime importance in choosing an appropriate detection technique. Taking all transmission losses into account, the estimated photon flux lies in the range between 10^7 and $10^{10}\,\text{s}^{-1}$, depending on the chosen emission line and the underlying plasma temperature and density (cf. subsection 5.2.5). Especially for low photon fluxes, which limit the time resolution

[9] Andover Corporation, 4 Commercial Drive, Salem, NH 03079, USA

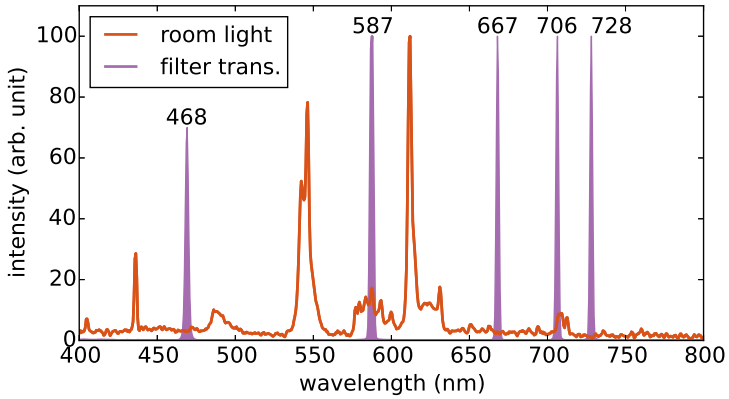

Figure 5.17.: Spectra of room light (fluorescent tubes) compared to the transmission bands of the interference filters used.

of the diagnostic, the best signal-to-noise ratio can be achieved with photomultiplier tubes, as explained in [Dun10].

To enable simultaneous measurement of several channels in one system, PMT array sensors with 32 channels (Hamamatsu[10] type H7260-20) are chosen. The detector is identical to the system previously used in [Kru12]. In contrast to [Kru12], where supply and amplification of the PMT array had to be added externally, linear multianode photosensor modules of the type H11460-20 with built-in high voltage power supplies and amplifiers are used. The compact detectors are shown in Fig. 5.18 with and without an interference filter attached.

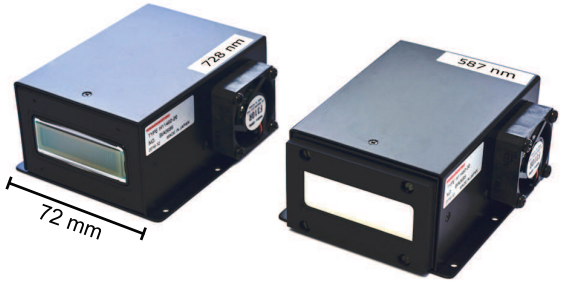

Figure 5.18.: Two Hamamatsu PMT array modules H11460-20 without (left) and with (right) an interference filter attached. The detector area is magnified in Fig. 5.19.

A magnification of the photosensitive area of the detection system is shown in Fig. 5.19. The black vertical stripes are the photosensitive areas of each channel with dimensions of $0.8 \times 7\,\mathrm{mm}^2$. The 32 channels are spaced by 1 mm. The optical system, described in subsection 5.2.2, is used to image the fiber array onto this area in a one to one representation. The elongation of the image of the round 0.8 mm fibers to 5.7 mm is achieved with a cylindrical lens with a $-500\,\mathrm{mm}$ focal length, placed 200 mm in front of the detector plane. This leads to homogeneous illumination of the detector area as represented in Fig. 5.20. It can be seen that the single images of the fibers are well separated on the optical axis, whereas chromatic aberrations of the lens are visible for the side channels. As discussed in subsection 5.2.5, this leads to a small optical crosstalk of the affected channels.
For operation of the PMT modules, power supplies (Kniel: CAD 15.1,6) with $\pm 15\,\mathrm{V}$ and control voltages between 2.0 V and 3.2 V are used. The control voltage regulates the high voltage for the

[10]Hamamatsu Photonics Deutschland GmbH, Arzbergerstr. 10, 82211 Herrsching am Ammersee, Germany

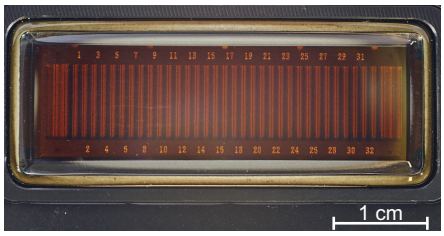

Figure 5.19.: Detector area of the 32-channel PMT array H11460-20. The 32 channels with a spacing of 1 mm have a photosensitive area of $0.8 \times 7\,\mathrm{mm}^2$, recognizable as black vertical stripes.

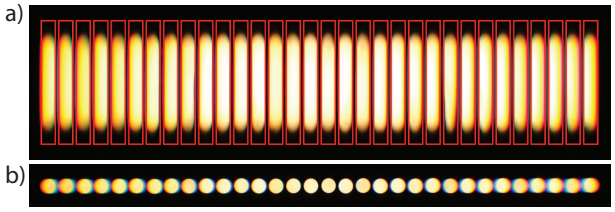

Figure 5.20.: Images of the LWL array at the detector plane measured a) with and b) without an cylindrical lens in the light path. The sensitive areas of the PMT array, spaced by 1 mm, are represented by $0.8 \times 7\,\mathrm{mm}^2$ red rectangles.

PMT dynodes between 500 V and 800 V, leading to a maximum gain of 1×10^6 and a relative amplification of the output voltage by a factor of ≈ 60 between the lowest and highest gains. The target output voltage lies in the range of 0–0.6 V. This voltage is transmitted to the acquisition system by two ribbon cables which are transferred to LEMO[11] cables, one for each channel.
The data were recorded by a SIO-2 (serial input-output, cf. [Beh08, Beh10, Beh12]) data acquisition system using 32 analog-to-digital converter (ADC) cards with four channels, respectively. The maximum sampling rate is 900 kHz with a 14 Bit resolution. The 32 cards are equally distributed over four rack-mount "PIPE" crates, including power supplies. Each crate has a backplane which connects the cards and works like a multiplexer based on the pipeline principle (PIPE V02, cf. [Beh08]). In addition, two digital-to-analog (DAC) units with two channels, respectively, are used to provide the control voltage for the PMT modules. The signal of the ADC cards is transferred through the pipe backplane to the controller cards (PIPE-Ctrl) situated in the first slot of each crate. These PIPE-Ctrl cards further serialize the information and transfer the bit-serial stream by optical fiber (LWL) to the SIO-2 host interface (217.6 MB/s). The SIO-2 host interface card has four LWL channels to communicate with up to four PIPE-Ctrl cards. So for this diagnostic the SIO-2 capacity is fully booked. The SIO-2 interface card has an additional feature providing connectivity to the experiment timing system as described in [Beh08]. This allows time-stamp and trigger functionality for data acquisition. For one plasma discharge with a data acquisition time of 10 s around 2.1 GB of data are recorded.

5.2.5. Calibration of the detection system

To assign the output voltage of each channel of the PMT arrays to the detected line radiance, several calibration steps are necessary. On the one hand, absolute calibration of the system is not necessary, as constant factors like the aperture of the first lens and the LOS diameter cancel out when the ratios between two wavelengths are built. This also eliminates the influence of the helium flux upon the absolute emission strength. On the other hand, the relative calibration between PMTs is crucial. The wavelength specific transmission of all optical elements, as well as

[11] LEMO Elektronik GmbH, Hanns-Schwindt-Str. 6, 81829 München, Germany

the wavelength and channel specific quantum efficiencies of the PMT arrays, have to be corrected and different values of the PMT gain settings have to be compensated.
One uncertainty in the calibration of most spectroscopic diagnostics in fusion research arises from possible coatings on the first lens, which is located close to the plasma in the vacuum chamber. These coatings can change during operational campaign, but in-vessel calibrations are only possible during the maintenance periods of the device. By measuring the transmission before and after the experimental campaign, the influence of surface layers upon lenses can mostly be estimated. However, the data presented in chapter 7 may still contain some remaining uncertainties caused by the calibration process, since calibration prior to the experiments was not possible and thus the post calibration may not be fully reliable[12].
The recorded raw data contain the directly measured PMT output voltages as well as the measurement settings. They are stored in the AUG shotfile system as level zero diagnostic data under the abbreviation **HEB**. From this file an independent data-set, classified as level one and called **HEC**, is generated. It contains the calibrated data as well as the position information of the LOS used. The final level two shotfile is called **HEP** and contains the evaluated n_e and T_e values. The performed calibration steps, explained in the following, are graphically presented in Fig. 5.21.

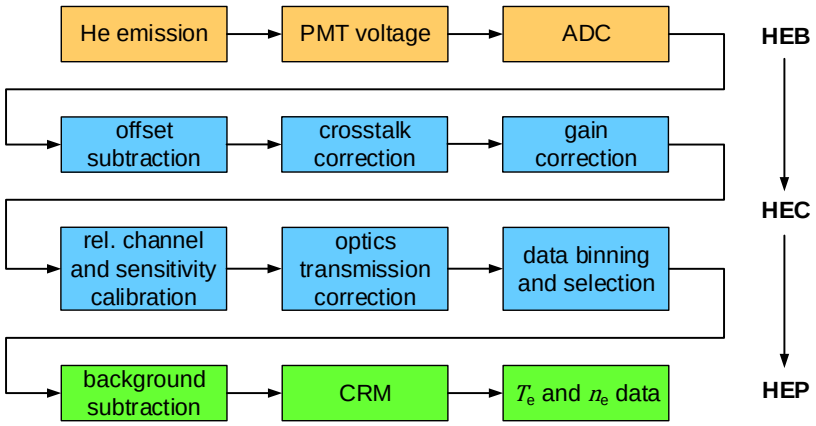

Figure 5.21.: Thermal helium beam data processing and calibration scheme. The upper row shows the conversion of the emitted light into a processible signal, the middle part shows the calibration steps and the lowest row shows the steps of the conversion from the measured line ratios into temperature and density values.

Offset correction Each PMT channel as well as the allocated ADC has a specific offset value, i.e. a dark voltage, which is subtracted in a first step from all measured data. This value stays constant over time.

[12] In this work, a measurement at the beginning of the of the campaign was not possible because the required fibers connecting the torus and the laboratory system were not available at that time. The reliability and applicability of the post experiment calibration is furthermore not fully ensured as a water break-in in AUG at the end of the experiments might have changed the lens surfaces.

Crosstalk correction The crosstalk between the channels of one PMT module can be determined by measuring the signal of all dark channels while only one channel is illuminated. The crosstalk is based on the one hand on the electrical circuit of the PMT module and ranges up to 4 % for neighboring channels. On the other hand, a non perfect optical image of the fibers onto the sensitive areas (cf. subsection 5.2.4) has an additional contribution. This becomes mainly important for channels far away from the optical axis of the objective, as here the spherical and chromatic aberrations become visible (cf. Fig. 5.20). This can be seen in section A.8, which shows matrices representing the crosstalk relation between the channels for all PMT modules.

Gain correction The gain of the PMTs can be controlled via a gain voltage between 2.0 V and 3.2 V. This control voltage is translated in an exponential way into the dynode voltage range of 500–800 V. The increased dynode voltage leads to a higher amplification factor of the photo electrons and therefore to a higher voltage output of the modules. By exploiting the total control voltage range, the amplification can be increased be a factor of sixty with respect to the lowest control voltage. This control voltage dependent gain increase has to be considered in the data calibration. The curves which show this dependency are plotted in Fig. 5.22 for all four PMT array modules, which show slightly different amplifications at the same gain value. Sometimes the gain behavior can depend on the illumination intensity. This was tested and it showed that the curves are valid, independent of the light intensity.

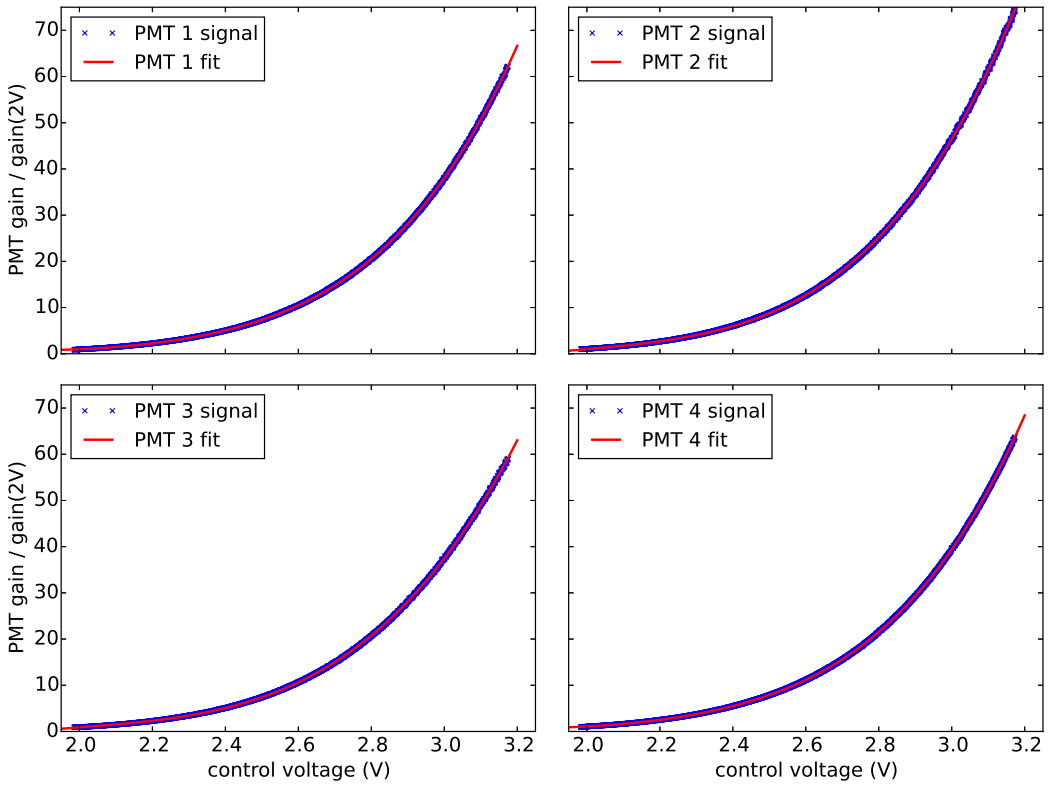

Figure 5.22.: Relative gain increase of the PMT modules 1–4 as a function of control voltage.

Relative channel and sensitivity calibration As the sensitivity of all channels within a PMT module and the transmission of the fibers from the torus to the lab is not equal, this effect has to be considered in the calibration procedure. In the same calibration step the relative transmission and PMT quantum efficiency between the four wavelengths is considered.
To measure the channel dependent sensitivity, all channels are illuminated by an integrating sphere which is placed in the torus at the measurement position. By knowing the spectral radiance of the sphere, the relative signal between the PMTs can be calibrated, too. So this calibration step can cover both, the optical transmission correction and the relative calibration between the PMTs. The resulting correction curves are plotted in Fig. 5.23 for all PMT modules.

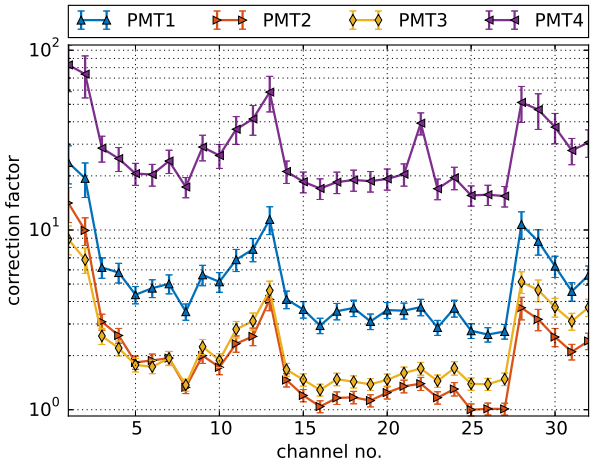

Figure 5.23.: Correction of the relative intensity between all channels; within the PMTs and all PMTs relative to each other.

In contrast to the absolute calibration of the system, the relative sensitivity between the four PMT modules is crucial for the calculation of the line ratios. Using an integrating sphere for this calibration may result in uncertainties of the calibration if the filter width is not exactly known or if the helium lines[13] are cut-off in parts by the narrow filters, which is not detected when a continuum light source is used. The measured spectral shift of the filters for a given alignment uncertainty confirms that this effect should not play a role. Local uncertainties in the filter quality, however, may still lead to an undesired loss of light. This can be tested by cross-calibrating the PMTs with a helium lamp with known[14] line intensities. The comparison of both calibration methods showed for several channels some not yet resolved discrepancies. They may be caused by the transmission of the filters, which is not homogeneous over the whole area, or by uncertainties in the determined helium lamp intensities.

The assignment of 52 lines of sight to 32 polychromator channels can be changed in order to observe different positions with adapted LOS configurations in the plasma. Therefore the transmission of the optical system in the torus including the fibers to the laboratory has to be disen-

[13] Also the Zeeman Splitting of helium lines in the magnetic field (cf. Fig. 6.4) may contribute to a partial loss of intensity for non-optimal filters.
[14] The helium lamp was calibrated with an absolutely calibrated spectrometer.

tangled from the polychromator system. This is done by comparing the signal of the integrating sphere placed in the torus to the signal of the sphere placed in the optics laboratory with the directly connected fiber bundle of the polychromator. Differences in the absolute transmittance of the single fibers are caused by connections and slight differences in the polished fiber ends. Furthermore, spectral dependence of transmittance is even more relevant. It is caused by the absorption characteristics of fibres as explained in the following.

Optics transmission correction The transmittance of the optical fibers used is a strong function of the wavelength as shown in Fig. 5.24. The figure shows the transmittance of an average of 20 fibers with a length[15] of 52 m. These fibers dominate the overall transmission characteristics, where the pronounced transmission dip at 728 nm is caused by an absorption band of hydroxyl groups which are present in so-called high OH fibers. Fibers with a low content of hydroxyl groups show a better transmission behavior at the relevant wavelengths, but they are prone to neutron irradiation [Coo96] so that high OH fibers have to be used.

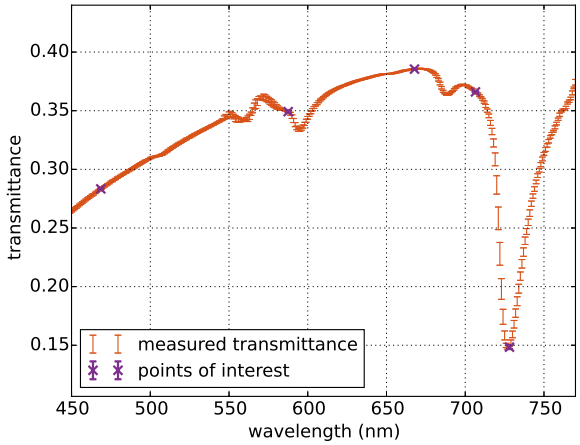

Figure 5.24.: Spectral transmittance of in-vessel optics and the optical fibers connecting the optical head with the polychromator system in the laboratory. The plotted transmission data show the average of 20 fibers.

Data binning and selection For writing the HEC shotfile with the calibrated data, time points of the raw data can be binned together. This is done to reduce the noise and the data size for faster processing. Furthermore only the time span from 200 ms before to 200 ms after the last helium puff is stored in the HEC file.

[15] When only absorption and no bending losses are considered, the absorption of the light intensity I in an optical fiber with the length x and the wavelength dependent absorption coefficient μ can be described as $I(x) = I_0 \cdot \mathrm{e}^{-\mu x}$.

5.3. Summary of the optical hardware components

The newly installed set of optical components for active helium emission spectroscopy comprises in-vessel optics for light collection, optical fibers which transmit the light to the laboratory and a dedicated polychromator system for light detection. The high spatial resolution of up to 3 mm is achieved by combining the locally injected helium beam with lines of sight which are aligned parallel to the field lines at the observation region. To achieve this, 52 lines of sight are distributed over 2 lenses in the optical head. The field of view covers not only a radial, but also a poloidal range of 8 cm. In the lab, the signal of each fiber is split into four spectral components to measure the 587, 667, 706 and 728 nm helium lines simultaneously. This is achieved with the newly developed 32 channel polychromator system based on dichroic mirrors and filter photomultiplier arrays, offering a temporal resolution of 900 kHz.
Before measurement results of this system are presented in chapter 7, chapter 6 presents pioneering experiments which influenced the designing process of the presented optical components.

6. Rating of collisional radiative models and line ratios

Parts of this chapter are published in M. Griener, et al., "Qualification and implementation of line ratio spectroscopy on helium as plasma edge diagnostic at ASDEX Upgrade", Plasma Phys. Control. Fusion 60, 25008 (2018) [Gri18a].

In order to design a dedicated detection system for the thermal helium beam at AUG, the absolute emission intensity of seven He I transitions were initially measured by a spectrometer to validate different line ratio combinations for their diagnostic application.
The conventional approach is to use the singlet/singlet (s/s) ratio of the 667.8 and 728.1 nm lines for density evaluation and the singlet/triplet (s/t) ratio of the 728.1 and 706.5 nm lines for temperature determination [Sch92a, Sch08b]. One reason for this is that these lines are lying relatively close together which facilitates spectroscopic measurements. Although this argument does not hold for filter based systems as described in section 5.2, these lines were used together with the 587.6 nm line for the polychromator system. Compared to other applicable line ratios (cf. section 6.3), they offer the best combination of high intensity and a suitable n_e and T_e dependence.
The temperature and density behavior of He I lines has been investigated in linear plasma test stands [Pos92, Ray16]. Although an extensive overview of possible helium lines was achieved, only a small range of plasma parameters, especially at lower densities, could be covered, which made it difficult to predict the application possibilities for larger devices.
In order to expand the line ratio technique to other helium line ratios, several ratios have been tested to find the ones with the best dependencies in a parameter range of $1 \times 10^{18}\,\mathrm{m}^{-3} < n_e < 4 \times 10^{19}\,\mathrm{m}^{-3}$ and $5\,\mathrm{eV} < T_e < 250\,\mathrm{eV}$, which are typical parameters for the SOL and pedestal region of AUG. The radially resolved emission information of seven helium lines is used to validate a new collisional radiative model (CRM) for helium [MB16b, MB12].
The optical transitions of neutral helium in the visible range are listed in Tab. 6.1 and plotted in Fig. 3.4, where the line thickness represents their relative intensity. The measured relative emission intensities strongly depend on plasma density and temperature as required for this diagnostic. The measured intensities including the error interval which takes these changes into account are compared to the intensity data from NIST [Kra15] in Tab. 6.1.

Table 6.1.: Optical transitions of He I in the visible spectral range, as plotted in Fig. 3.4. The relative intensities from NIST [Kra15] are compared to the mean measured intensities. The standard deviation denotes the range of intensity values for different plasma parameters.

wavelength (nm)	species	transition	rel. int. (NIST)	mean rel. int. (measured)
388.86	triplet	1s3p - 1s2s	500	–
447.15	triplet	1s4d - 1s2p	200	200 ± 100
471.31	triplet	1s4s - 1s2p	30	–
492.19	singlet	1s4d - 1s2p	20	70 ± 30
501.56	singlet	1s3p - 1s2s	100	100 ± 40
504.77	singlet	1s4s - 1s2p	10	10 ± 4
587.56	triplet	1s3d - 1s2p	500	2800 ± 1600
667.81	singlet	1s3d - 1s2p	100	620 ± 250
706.52	triplet	1s3s - 1s2p	200	590 ± 360
728.13	singlet	1s3s - 1s2p	50	–

6.1. Experimental setup

In AUG a piezo valve based system for the injection of thermal gas beams (cf. chapter 4 and [Gri17]) is used to locally inject helium into the plasma SOL. For the first study of different helium lines, the compact valve is placed in sector 16 at the low field side mid-plane of the vacuum chamber at a major radius of $R = 2.23\,\mathrm{m}$. The gas expands through a 700 µm capillary in a cone shaped gas beam with a full opening angle of about 40° for helium.

The position of the valve relative to the plasma and the lines of sight (LOS) is represented in a toroidal cross section of AUG in Fig. 6.1. The endpoint of the capillary for gas inlet is protected by a tungsten coated carbon brick 2 cm behind the limiter contour. The central axis of the gas beam is directed perpendicular to the magnetic flux surfaces. 21 LOS from three optical heads (pictured with three different shades of blue, NA = 0.026), which were optimized for charge-exchange measurements at AUG [Vie12, Cav16], are almost tangential to the field lines in the measurement area over the radial range of 4 cm.

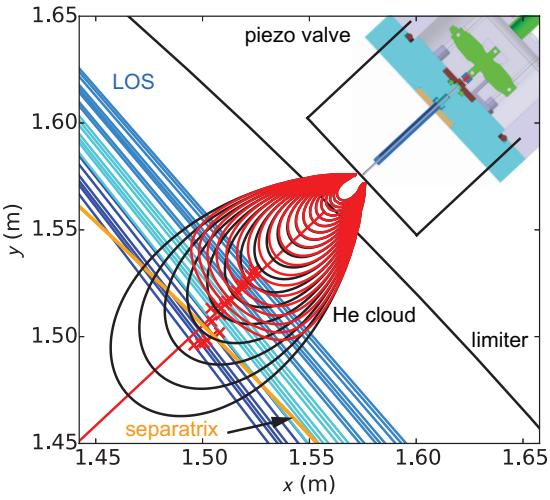

Figure 6.1.: Toroidal cross section of AUG at $z = 0.05\,\mathrm{m}$. The LOS, the piezo valve (top right corner) and a contour plot of the helium density (black: without ionization, red: with ionization) as well as separatrix (orange, $R = 2.12\,\mathrm{m}$) and limiter positions are illustrated (#32 032, $t = 2.2\,\mathrm{s}$, cf. Fig. 6.2).

To map the measured line integrated intensity of each LOS to a radial position, a forward model calculates the spatial origin of helium emission along each LOS. The modeled neutral helium beam expansion is based on measurements with a fast camera in a lab experiment (cf. section 4.5). The shape of the helium cloud corresponds to the expansion of the neutral beam in

vacuum. It reflects the geometrical dilution of the neutral helium density, but it does not contain additional attenuation by ionization losses in the plasma environment. This becomes mainly important in the confined region and the near SOL. These ionization losses were taken into account by adding the ionization cross sections from ADAS [Sum04] and the underlying plasma parameters. The helium cloud without ionization is represented in Fig. 6.1 by black contour lines. The calculated shape of the cloud including ionization processes in the AUG plasma is presented by red contour lines, representing the same density values as the black lines.
The radial positions of maximum emission, marked in Fig. 6.1 by red crosses, and the radial intervals which cover 68 % of the emission along a LOS are set as radial origin and its error of the signal, respectively. The radial resolution ranges from 3 mm (outermost LOS, closest to the gas injection point) to 7 mm (innermost LOS). The maximum resolution of the system is limited by the diameter of the LOS at the measurement positions which is 3 mm. The achievable poloidal resolution is calculated the same way. As the LOS are aligned tangentially to the field lines, the poloidal resolution is 3–4 mm for all LOS.

For the analysis of helium emission, the collected light is transmitted from the optical heads by 400 µm optical fibers (NA = 0.22) to a high through-put $f/4$ Czerny-Turner spectrometer with a variable spectrometer slit of typically 50 µm, two objective lenses and a turnable grating with 2400 grooves/mm. The imaging is based on a Princeton Instruments[1] "ProEM" charge coupled device (CCD) camera with a 512×512 16 µm pixel chip. This limits the temporal resolution to 2.3 ms (cf. [Vie12, Cav17a]). The covered wavelength range for one spectrometer setting lies between 14 nm for the lowest and 7 nm for the highest measured wavelength. So the resolution of the spectrometer ranges from 36 to 73 pixel/nm.
This spectrometer did not cover the highest (728.1 nm) and lowest (388.9 nm) wavelengths of the discussed He I lines which is the reason for the lack of experimental data there. The 447.3 nm line was skipped due to the limited number of available plasma discharges.

6.2. Measurement results of helium line intensities

6.2.1. Experimental sequence

In the 2015 AUG campaign, six comparable discharges (#32 029−32 032, #32 046, #32 047) were performed to measure the intensity profiles of seven He I transitions. Due to the high resolution of the spectrometers (cf. subsection 6.2.2), one helium line was measured per discharge, besides the 501.56 and 504.77 nm lines which are close enough to be measured within one discharge at the same spectrometer setting.
One of the identical discharges is presented in Fig. 6.2. They are designed in a way to cover a wide range of typical SOL parameters, $1 \times 10^{18}\,\mathrm{m}^{-3} \leq n_\mathrm{e} \leq 4 \times 10^{19}\,\mathrm{m}^{-3}$ and $5\,\mathrm{eV} \leq T_\mathrm{e} \leq 130\,\mathrm{eV}$. This is enabled by a step-wise increase of electron cyclotron resonance heating power P_ECRH, neutral beam heating power P_NBI (see Fig. 6.2 b)) and plasma fueling (Fig. 6.2 c) and d)) during

[1] Princeton Instruments, New Jersey, 3660 Quakerbridge Road, Trenton, NJ 08619 USA

the discharge. The discharges start in L-mode with a transition to H-mode at about 3 s, which is accompanied by the appearance of edge localized modes (ELMs). ELMs are identified by peaks in the divertor shunt current signal $I_{\mathrm{i-DIV}}$ (Fig. 6.2 e)).
The position of the separatrix at the mid-plane is given by the parameter R_{aus} (Fig. 6.2 f)). This position is periodically shifted five times (marked by the vertical black lines) to cover different regions in the plasma with diagnostics which are spatially fixed such as the Li- or He-beam or the Thomson scattering diagnostic.
For the helium beam measurements, the piezo valve was operated with 50 mbar helium. This leads to a gas flux of 1.68×10^{19} part/s through the 700 µm capillary. This is around 600 times less than the continuously injected deuterium for plasma fueling (Fig. 6.2 d)).
The helium beam was pulsed with 10 Hz, leading to puffs with 50 ms duration, where the down-time was used for background subtraction. The emission time trace of the helium 667.8 nm line is shown in Fig. 6.2 g) with two signals from two different radial positions, i.e. the inner- and outermost LOS as shown in Fig. 6.1. The emission behavior is discussed in subsection 6.2.4.

6.2.2. Spectral profiles of He I transitions

The experimental equipment used offers a wavelength resolved emission profile for each line of sight. Although this is not crucial for the helium line ratio technique, the detailed analysis of the spectral lines helps to identify other emission lines which might disturb helium measurements. Elements which are often found in a nuclear fusion device are hydrogen and its isotopes as main plasma species, carbon and tungsten as plasma wall materials, boron for wall conditioning, nitrogen and oxygen as impurities from air, or as nitrogen, neon and argon injected on purpose for seeding experiments or as diagnostic gases [Bar16].

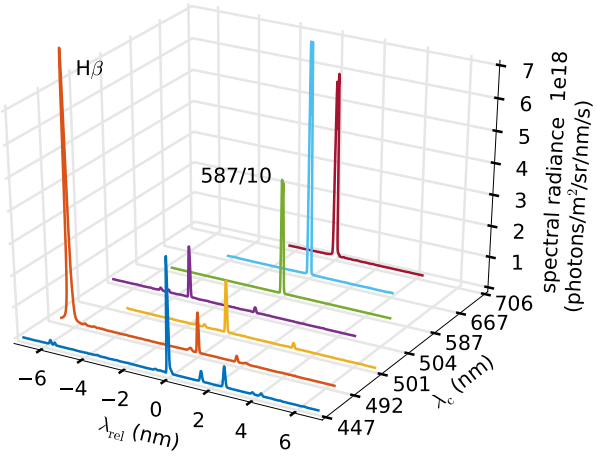

Figure 6.3.: Measured spectra λ_{rel} of He I lines where the central wavelength λ_{c} of the transitions corresponds to $\lambda_{\mathrm{rel}} = 0$. The data are the time averaged mean of all LOS during the He puffs. The strongest signal which corresponds to the 587 nm line is divided by ten.

In the experiments performed, all He I lines could be clearly resolved from other transitions in the measurement region. The exact wavelengths and measurement ranges are summarized in Tab. 6.2 and Fig. 6.3. Besides the very strong H_β line (as deuterium was used, it is actually the D_β line), all additional peaks found are weaker than the helium lines and can be allocated to W I emission as ASDEX Upgrade is equipped with a full tungsten wall.

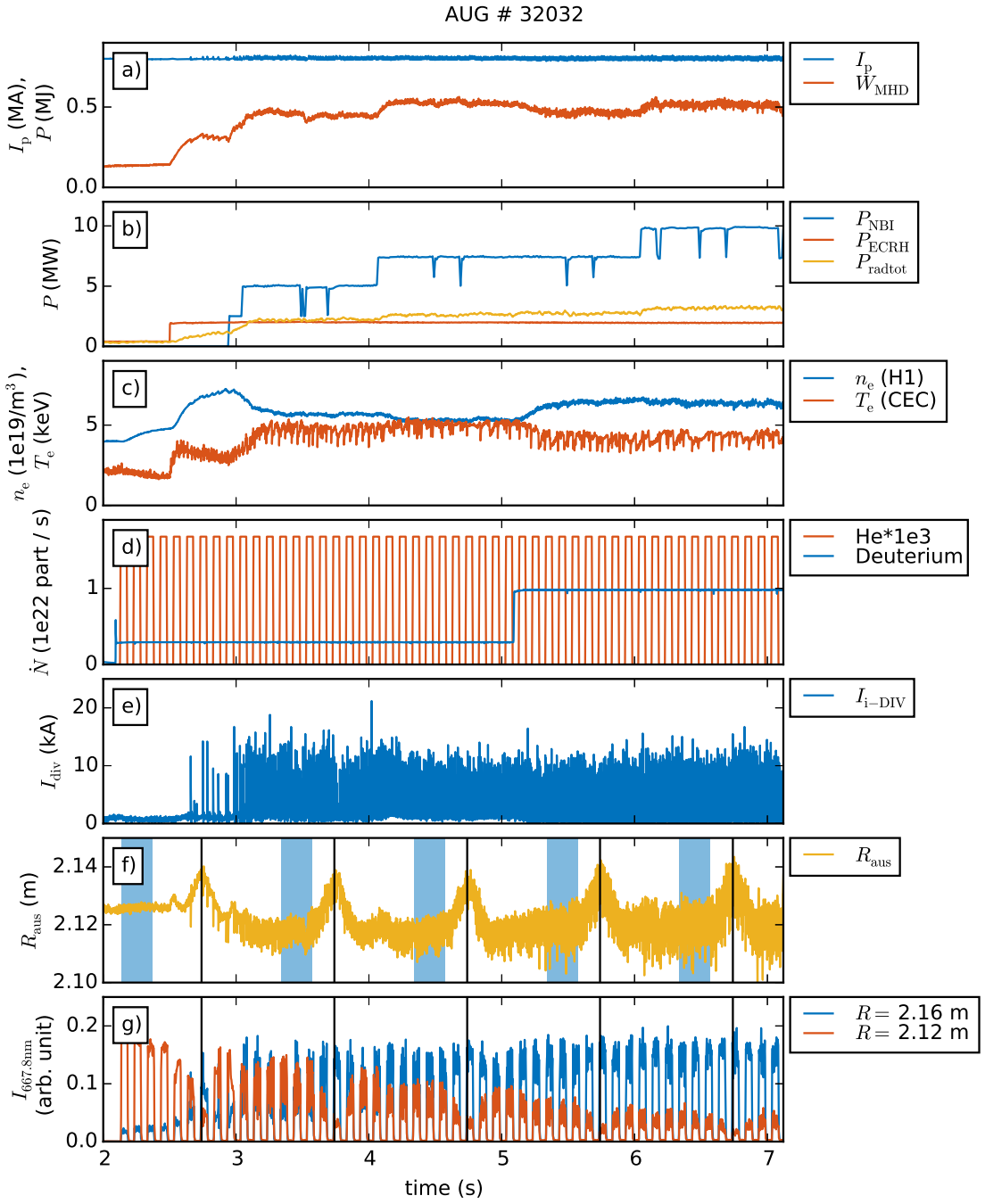

Figure 6.2.: Experimental time traces of AUG discharge #32 032. The time traces show plasma current I_P, total stored energy in the plasma W_{MHD}, neutral beam injection and electron cyclotron resonance heating power P_{NBI} and P_{ECRH}, total radiated power P_{radtot}, line integrated electron density n_e and core electron temperature T_e, total plasma fueling with deuterium compared to the diagnostic He inlet, shunt current of the inner divertor I_{i-DIV}, separatrix position at the mid-plane R_{aus} (shifted five times which is marked by the vertical black lines) and the measured emission $I_{667.8nm}$ at 667.8 nm of injected helium at two radial positions (cf. subsection 6.2.4). The blue shaded time intervals with constant plasma parameters indicate the five different scenarios which were investigated.

Table 6.2.: Emission lines close to He I transitions. Beside the very strong H_β line, all peaks found in the measurement range can be allocated to W I emission. The presence of neon (Ne I-II) would mostly interfere with the He I lines.

transition	wavelength (nm)	discharge number	measurement range (nm)	perturbation lines measured (nm)	closest Ne line [Kra15]
$3^3P \rightarrow 2^3S$	388.86	–	–	–	388.94
$4^3D \rightarrow 2^3P$	447.15	32 046	703–710	441.4, 441.6, 446.4, 448.6, 449.7, 451.0, 451.4	447.15
$4^3S \rightarrow 2^3P$	471.31	–	–	–	471.30
$4^1D \rightarrow 2^1P$	492.19	32 047	485–498	486.1(H_β), 491.8, 494.1, 494.5	492.82
$3^1P \rightarrow 2^1S$	501.56	32 030	496–509	500.1, 500.5	501.52
$4^1S \rightarrow 2^1P$	504.77	32 030	496–509	504.5	504.66
$3^3D \rightarrow 2^3P$	587.56	32 031	582–594	none	587.28
$3^1D \rightarrow 2^1P$	667.81	32 032	663–671	none	667.82
$3^3S \rightarrow 2^3P$	706.52	32 029	703–710	none	706.47
$3^1S \rightarrow 2^1P$	728.13	–	–	–	724.52

The presence of nitrogen would not disturb the measurements. When a filter based system instead of spectrometers is used for the measurements, it is of particular interest that all nitrogen lines for $\lambda \geq 587\,\text{nm}$ are separated more than 1.1 nm from the He I lines, respectively.

In contrast to nitrogen, the presence of noble gases like neon and argon would mostly interfere with the exclusive measurement of He I lines. The highest distance (in brackets) of He I lines to Ne lines shows the 728.1 nm line (3.6 nm), followed by 492 nm (0.6 nm), 587 nm (0.3 nm), 504 nm (0.1 nm) and 388 nm (0.08 nm) lines. These could still be resolved with a high resolution spectrometer. Nevertheless the Zeeman splitting of the lines has to be taken into account so that some of these lines cannot be distinguished anymore.

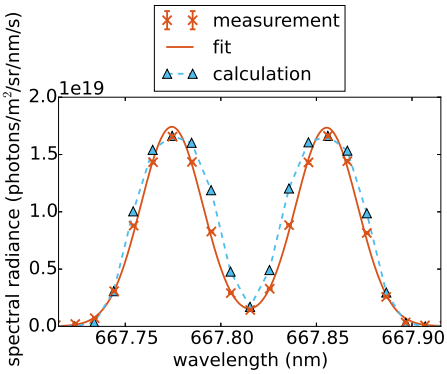

Figure 6.4.: Zeeman splitting of the He I 667.8 nm line, measured in the AUG discharge #32 167 with the outermost LOS, compared to a forward modeling taking the spectrometer function and the Zeeman splitting into account.

The Zeeman splitting for example splits the $3^1D \rightarrow 2^1P$ transition into 9 allowed transitions where the σ^+ and σ^- lines are separated by 0.08 nm at a magnetic field of 2 T at the measurement position (cf. Fig. 6.4). The angle between the magnetic field and the observation direction was around 5° which makes the π lines nearly vanish. Fig. 6.4 shows that the measured spectral profile fits the predictions by a forward modeling taking the spectrometer function and the Zeeman splitting into account.

6.2.3. Effects of diagnostic gas puffs on the plasma helium content

The impact of the pulsed helium beam with a flux of 1.68×10^{19} part/s on the helium content of the plasma is exemplarily shown for an experiment with ten 50 ms He puffs with a periodicity of 100 ms as performed in AUG discharge #32 167.

The absolute helium content of the plasma can be measured in the confined region with charge exchange recombination spectroscopy [Ath14]. Fig. 6.5 shows the absolute helium concentration during ten helium puffs at three different radial positions, located toroidally close to the helium injection point. Whereas at the outermost position the single helium puffs are directly visible, the puffs lead only to a slight increase of the helium concentration in the plasma core ($\rho_{\mathrm{pol}} = 0.2$) of the order of 0.1 %.

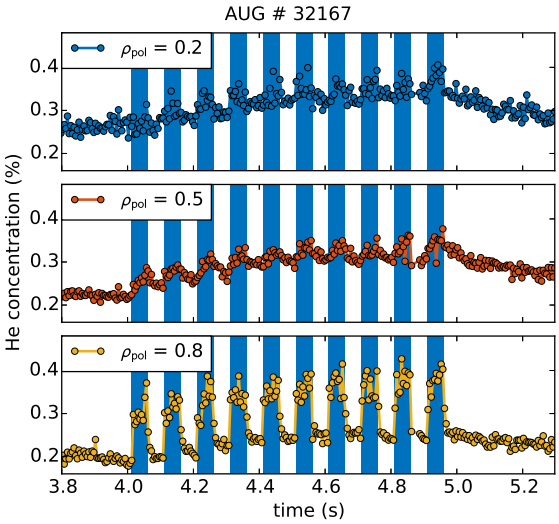

Figure 6.5.: Absolute helium concentration at three different radial positions in the confined region of the plasma. Measured with the helium charge exchange recombination spectroscopy at AUG discharge #32 167 for ten 50 ms He puffs with 1.68×10^{19} part/s [Gri17].

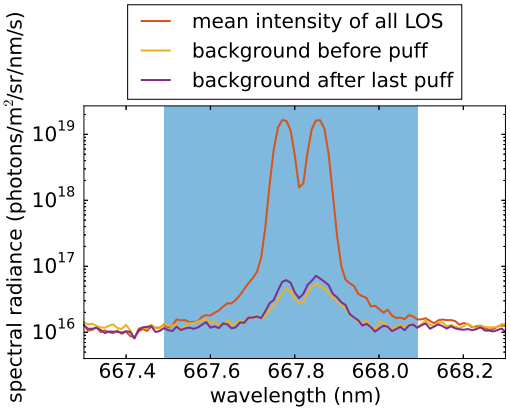

Figure 6.6.: Active and passive signal of the He I 667.8 nm line in logarithmic scale as a mean of all LOS (AUG #32 167). The signal is compared before, during, and directly after ten 50 ms He puffs.

The intrinsic helium content of the plasma shows that helium itself is also an impurity which is present in fusion devices. Only the locally injected helium should be considered for active line ratio spectroscopy, as only actively injected helium grants a good spatial resolution and enables time dependent modeling. Thus, the background helium signal is subtracted by chopping the active helium beam. This method of background subtraction is also used to eliminate background by bremsstrahlung.

The helium background signal before the first and after the last helium puff is compared to the active signal during the puffs in Fig. 6.6. It shows on the one hand the very good signal-to-noise ratio during helium puffs and on the other hand the fast depletion of neutral helium in the SOL as the background is not significantly increased by the diagnostic puffs.

Furthermore a detailed analysis of the inner divertor shunt current $I_{\mathrm{i-DIV}}$ (cf. Fig. 6.2 e) for an overview time trace) shows that the helium puffs had no influence on the ELM behavior, although ELMs react very sensitively to perturbations of the plasma edge region. This is an additional indicator that the operation of the piezo valve with low helium fluxes causes negligible disturbance.

6.2.4. Helium emission intensity time traces from L- to H-mode

The intensity time trace of the examplarily chosen He I singlet transition at 667.8 nm is shown in Fig. 6.2 g) for two different radial positions. The first is the separatrix position at $R = 2.12\,\mathrm{m}$ (at the height $z = 0.05\,\mathrm{m}$, where the valve is located), the second is lying in the far scrape-off layer at $R = 2.16\,\mathrm{m}$, with 6 cm distance to the helium injection point. The fifty 50 ms helium puffs with a duty cycle of 100 ms are clearly visible for all measurement locations.
Note that the emission intensity in L-mode (at the beginning of the discharge) is highest in the confined region of the plasma ($R \leq 2.125\,\mathrm{m}$), although the neutral helium density is higher in the far SOL. The reason for this is that the excitation of the neutral helium is much more efficient at the temperatures in the separatrix region, compared to that at the low temperatures in the far SOL.
In H-mode this effect is compensated by increasing SOL temperatures[2] on the one hand, which lead to an increased emission at $R = 2.16\,\mathrm{m}$, and by the increasing amount of ionization of the injected helium in the confined region on the other hand, which decreases the number of neutral helium atoms.
As temperature and density are increased step-wise during the discharge, the ionization losses gain more and more importance, as the emission drop in the separatrix region shows. The high ionization in the confined region is pronounced by the R_{aus} scans which are indicated by the five vertical lines in the subplots f) and g) of Fig. 6.2. At these times, the position of the separatrix is shifted closer to the wall so that the measurement points are shifted more toward the plasma center, where the density of neutral helium is strongly decreased by ionization and thus the total emission intensity is decreased, too.
During H-mode, the R_{aus} scans do not influence the emission intensity in the far SOL. The reason for this is that the electron density and temperature profiles (cf. section 6.4) do not show steep gradients in this region. Furthermore, ionization does not influence the neutral density strongly in the far SOL as shown in Fig. 6.1.

Regarding the emission time traces, it is clear that the intensity variation within the single puffs is strongly increased in H-mode with respect to L-mode. This emission variation is caused by ELMs which directly influence the electron temperature and density in the measurement region and thus lead to a changed helium emission. In contrast to the measurements presented in chapter 7, the time resolution of 2.3 ms of the spectrometer setup is not sufficient to resolve single ELMs. To achieve comparable results, only measurement points in between ELMs were taken into account for the time averaged signals which are used for the radial profiles as shown in subsection 6.2.5.
For the analysis of the different He I line intensities only the total line emission is of interest so that the integral value of the helium peaks was taken from spectrally resolved measurements. This region of interest is exemplarily shown as the highlighted region in Fig. 6.6 for the 667.8 nm line.

[2] In the far SOL the signal is generated by warm intermittent filaments which cannot be resolved with this setup. These filaments can be clearly seen with the upgraded diagnostic as presented in chapter 7.

6.2.5. Radial profiles of He I transitions in L- and H-mode

The information from each line of sight can be mapped to a radial position as shown in section 6.1. Taking all LOS together leads to radial profiles as shown in Fig. 6.7a for the L-mode phase and in Fig. 6.7b for an H-mode phase with high deuterium fueling and high heating power. The intensity values of all optical transitions are background subtracted and time averaged over the ELM free points in the denoted time spans with constant plasma parameters. The separatrix position ($\rho_{\mathrm{pol}} = 1.0$) is given by the vertical black lines. These lines divides the confined region (to the left of the line) and the SOL (to the right of the line) of the plasma. Helium is injected from right to left starting at a radius of $R = 2.23\,\mathrm{m}$.

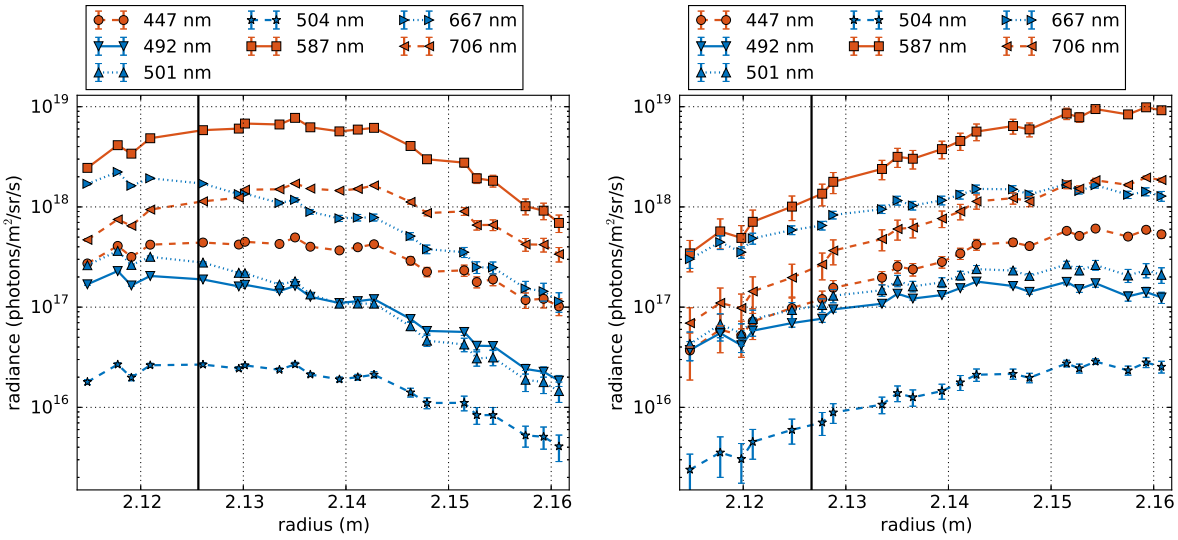

(a) L-mode profiles, $t = 2.17$–$2.37\,\mathrm{s}$.

(b) H-mode profiles, $t = 6.34$–$6.57\,\mathrm{s}$.

Figure 6.7.: Radial profile of the absolute emission intensity of He I transitions in logarithmic scale (blue: singlet, red: triplet) for L- and H-mode in the AUG discharges #32 029–32 032, #32 046 and #32 047 (cf. Fig. 6.2). The separatrix position ($\rho_{\mathrm{pol}} = 1.0$) is given by the vertical black line.

Also the neutral helium density decreases from right to left due to geometrical dilution and ionization losses, the total emission intensity in L-mode increases toward the plasma center. This is explained by the more efficient excitation at higher temperatures. In H-mode, however, beam attenuation via ionization dominates toward the center leading to a decreased total emission, as discussed earlier.

In L-mode the singlet line emission profiles (blue) are mainly increasing continuously toward the plasma center whereas the triplet lines (red) peak already in the SOL region. The reason for this difference is the different temperature behavior of the population density of singlet and triplet lines as explained in section 3.3. The population density of singlet lines peaks at $T_{\mathrm{e}} \approx 300$–$500\,\mathrm{eV}$ which is far in the confined region, whereas the population density of triplet lines peaks at $T_{\mathrm{e}} \approx 25\,\mathrm{eV}$ which lies in the SOL [Bri98]. This also causes the steeper decrease in the H-mode of triplet line emission compared to singlet line emission. By taking the intensity ratio of two lines, the absolute intensity, which is proportional to the neutral helium density, cancels out. The line ratio thus only reflects the changes of T_{e} and n_{e}.

6.3. Feasible He I line ratios for n_e and T_e measurements

From four measured He I singlet line intensities and three measured triplet intensities one can calculate 21 different ratios, distributed into 12 singlet/triplet, 6 singlet/singlet and 3 triplet/triplet ratios. These ratios were tested regarding their suitability for n_e and T_e evaluation for five different plasma scenarios in AUG as described in subsection 6.2.1.
As the temperature as well as the density of the plasma strongly decay in the scrape-off layer, the measured ratios should show a strong dependence on the plasma radius. Furthermore, a high intensity of both transitions of the ratio would be preferable to enable fast measurements.

To rate the ratios according to these criteria, their relative variation in the investigated radial range, i.e. max/min, is compared. This value, together with the absolute maximum and minimum values of all ratios along the radius are given in Tab. A.9 for the L-mode and first H-mode timespan. The given relative intensity is averaged over the radius and corresponds to the intensity of the weaker line of the ratio with respect to the weakest intensity of all lines for all measured plasma scenarios.
Furthermore, the relative variation of all ratios is plotted in the left subfigure of Fig. 6.8 for all singlet/triplet (s/t) ratios and in the right subfigure for s/s and t/t ratios for five different plasma scenarios. The ratios are ordered by the intensity of the weaker line of the ratio.

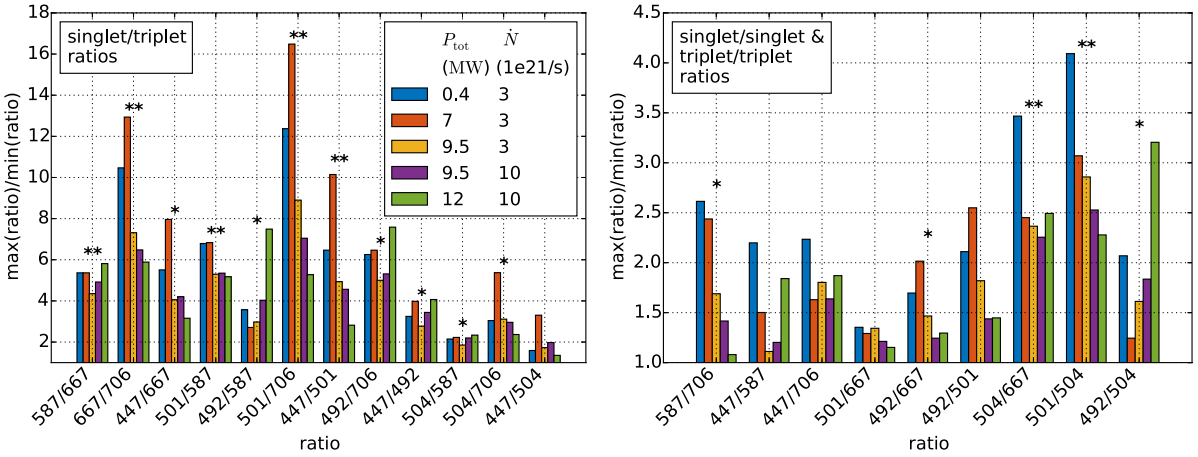

Figure 6.8.: Comparison of the radial dependence of T_e sensitive line ratios (left) and n_e sensitive line ratios (right) for five dedicated time periods during the AUG discharge (cf. Fig. 6.2, blue shaded areas). The legend shows the total heating power P_{tot} as well as the plasma fueling $\dot{N}$ with deuterium. The ratios are ordered by decreasing intensity of the weaker line of the ratio. Two asterisks denote the usability of the ratio for n_e or T_e evaluation, one asterisk denotes a general segregate n_e or T_e dependence.

In general the values of s/t ratios show a stronger change along the radius compared to s/s or t/t ratios. Furthermore, the change of the ratio along the radius is highest for the first H-mode timespan for most of the T_e dependent ratios (cf. Fig. 6.8, left). The reason for that is that the temperature decrease around the separatrix is stronger in H-mode compared to L-mode, which leads to a higher temperature range. With increasing plasma heating and fueling this effect is compensated as the temperatures are still high in the far SOL (cf. [Sun15]), which leads to a smaller variation of the ratios.

Beside the radial dependence of the ratio, an additional criterion for application as diagnostic is that the ratio depends on changes in T_e or in n_e but only weakly on both simultaneously. Moreover, the translation into T_e and n_e values is only possible, if the measured ratio can be predicted with the collisional radiative model (CRM).
The fulfilment of these two criteria is denoted with asterisks in Fig. 6.8. The ratio is rated with one asterisk if the T_e and n_e dependencies are separated in the CRM and with two asterisks if in addition the absolute value of the measured ratio matches roughly the predictions of the CRM.

Traditionally the 667/728 (s/s) ratio is used for density measurements [Sch08b]. Fig. 6.8 (right) shows that especially the 504.8 nm transition is well suited to replace the 728.1 nm line. Both transitions change the total orbital momentum by $\Delta L = +1$ (and start at $L = 0$) and both corresponding upper states are mainly depopulated by electron collisions. In contrast to that, the upper states of singlet transitions with $\Delta L = -1$ are mainly depopulated by radiation [Bri98]. So it can be concluded that s/s ratios are best suitable for density evaluation if one transition shows $\Delta L = +1$ and the other $\Delta L = -1$. However, also the 4^1D state, which is the upper state of the 492.2 nm line, is partially depopulated by electron collisions. This could also make this transition applicable for n_e reconstruction in combination with the 667.8 nm line.
To translate the measured ratios into density and temperature values, three different CRMs are compared. One CRM is based on ADAS using the 'pec96#he_pju#he0.dat' data set [Sum04] and an equilibrium assumption regarding the atomic state population. The other two CRMs rely on the so-called hybrid code by Muñoz Burgos et al. [MB12]. The code is called hybrid because it couples both, the time-dependency of the atomic states with respect to the plasma conditions and the equilibrium solution when electron collisions dominate due to high electron densities so that the time-dependency of the state population can be neglected. When electron densities are low, time-dependent relaxation times become significant and must be considered.

To compare the three CRMs for an example of an n_e dependent ratio, the T_e and n_e dependent value of the 501/504 (s/s) ratio is plotted in Fig. 6.9. The left subplot shows the predictions of the CRM included in ADAS, the middle and right subplots show two equilibrium grids from the hybrid model, as the time-dependent profile cannot be shown without a given relaxation time (cf. section 6.4). The middle subplot includes high Rydberg state contributions while the right does not.
In ADAS, the single excited levels are treated as individual up to $n = 4$. Before the ionization state which is treated as loss term, one bundled state is added. This state gets populated by collisions from lower states and itself can populate lower states again, described by the so-called bundle-n approach [Sum06].
The predicted values of the ADAS CRM are in agreement with the predictions of the hybrid code which includes high Rydberg (Ry) states up to $n = 500$, although this high number of states is physically not possible. The spikes of the line ratios at low temperature can be explained by the resonances of the electron-impact excitation cross-sections calculated using both the R-Matrix, and R-Matrix with Pseudo-States (RMPS) methods. When electrons scatter from complex targets such as atoms or molecules, resonance features occur often at energies where the target has many excited electronic states. These resonances occur below the ionization threshold, therefore

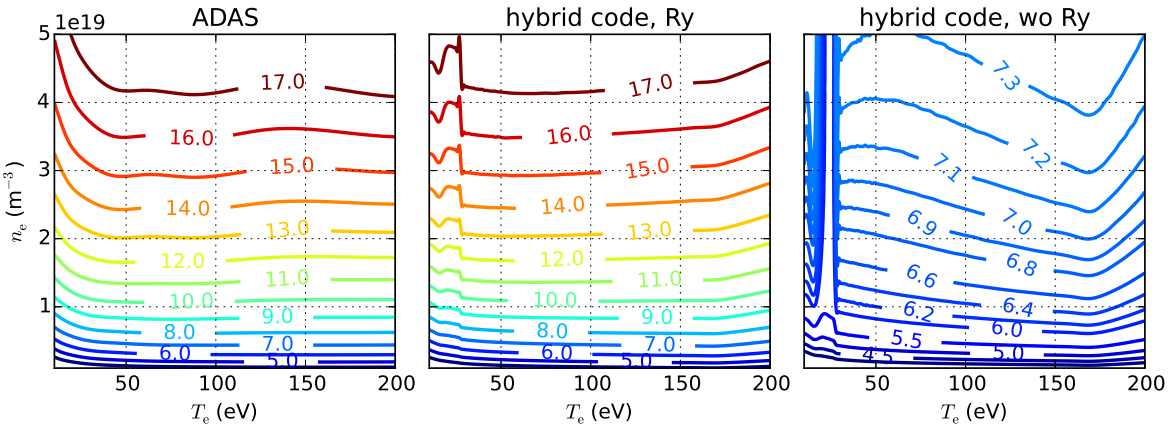

Figure 6.9.: Comparison of the T_e and n_e behavior of the 501/504 (s/s) ratio for three different CRMs. The left is the CRM implemented in ADAS [Sum04], the middle is the hybrid code from [MB12] with high Rydberg states included, the right is the same code from [MB12], but without the high Rydberg states. The absolute number of these predicted values for the ratio can be compared to the experimental values in Tab. A.9 and Fig. 6.12.

when calculating rate coefficients using cross-sections that include resonances, the effect of the resonances become significant for low electron temperatures and the bulk of the Maxwellian is located over these resonances. A very detailed analysis of the importance and the effects of these resonances in line-ratio diagnostics is presented by Muñoz Burgos et al. in [MB09].
The same hybrid code without high Rydberg states included stops at $n = 4$ and directly considers every higher excitation as ionization. The predictions without high Rydberg states deliver significantly lower numbers of the ratio, which means that the population of the 4^1S state is overestimated with respect to the 3^1P state. Therefore an n_e reconstruction is not possible without the high Rydberg states as the measured values of the ratio up to 16 would lead to unreasonably high densities.
Nevertheless, the ADAS model as well as the hybrid code with Rydberg states lead to well suitable density profiles if the 504.8 nm lines is used, as shown in section 6.4. The disadvantage of the 504.8 nm line is that it is the weakest of all He I lines and therefore not suitable for fast measurements. For a time resolution of 2.3 ms however, the absolute emission intensity was sufficient for all measured helium lines.

Beside s/s ratios, t/t ratios should also show a distinct n_e dependence. The 587/706 (t/t) ratio is the triplet counterpart to the classically used s/s ratio. Its advantage is the strong emission of both involved lines. Although this t/t ratio shows a general n_e dependence, the overall value of the measured ratio does not match the predictions of the CRMs which are shown in Fig. 6.10. The predictions without high Rydberg states deliver significantly higher numbers of the ratio, which means that the population of the 3^3D state is overestimated with respect to the 3^3S state. The discrepancy between the models becomes higher with rising density. Also the separation of the lines with the same number for the ratio grows with rising temperature. This means that the ratio becomes less sensitive to n_e changes. Reversed this means that small changes of the measured ratio now yield higher changes of the calculated density. Nevertheless, the overall

measured values of the ratio (cf. Tab. A.9) are smaller than the predictions, which leads to significantly too low electron densities (cf. Fig. 6.14).

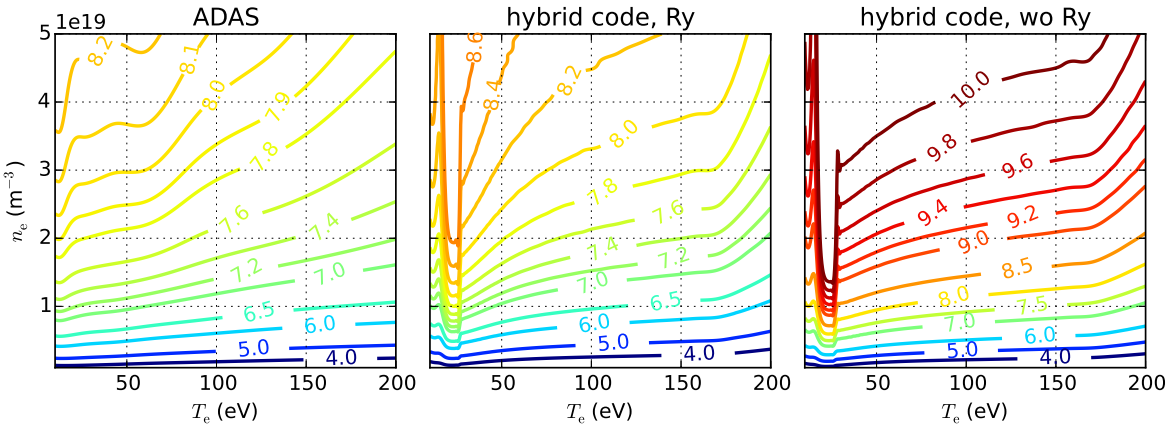

Figure 6.10.: Comparison of the T_e and n_e behavior of the 587/706 (t/t) ratio for three different CRMs.

To achieve a strong temperature dependence, ratios between singlet and triplet lines are used, with the classical combination being the 706/728 (t/s) ratio. This general T_e dependence leads in most of the (s/t) ratios to a strong change of their value along the plasma radius as shown in Fig. 6.8 (left). As an example for a clearly separated T_e dependence, the 501/587 (s/t) ratio is plotted in Fig. 6.11 as a comparison of the three CRMs. Again the discrepancy between the ADAS code and the hybrid code with Rydberg states is the smallest, although the differences are more prominent than in the comparison of ratios from the same species. Together with the absolute value of the measured ratio from Tab. A.9 and Fig. 6.12 which lies in the range of 0.01–0.11, one can see that in this case the hybrid code without high Rydberg states is best suitable to describe the data (cf. Fig. 6.13) when separatrix temperatures between 30 and 50 eV for L-modes and 100 eV for the H-mode are assumed [Sun17].

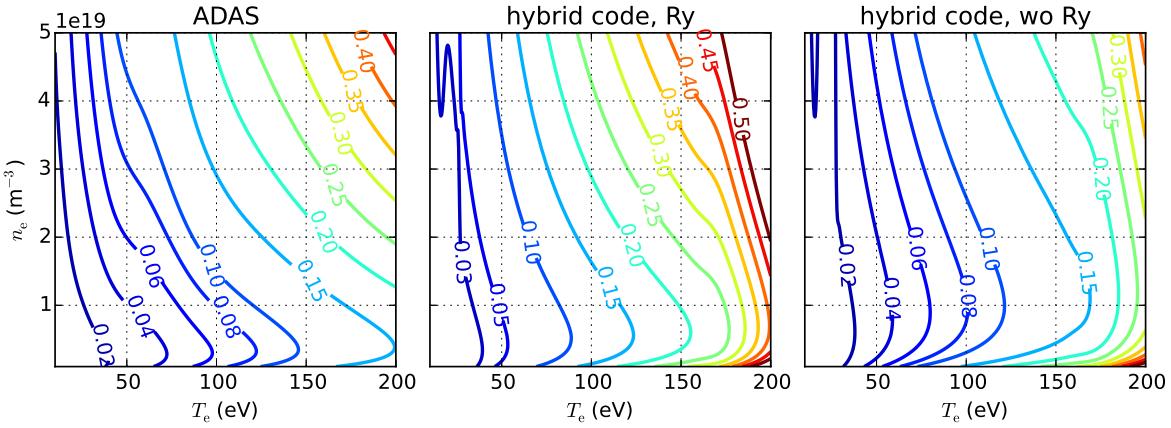

Figure 6.11.: Comparison of the T_e and n_e behavior of the 501/587 (s/t) ratio for three different CRMs.

The discrepancy of the results with respect to the number of considered Rydberg states strongly depends on the n_e and T_e range as well as on the chosen ratio. A direct comparison of the

photon emission coefficient of all states shows that especially all lines starting from a $n = 4$ level are highly affected by the treatment of the Rydberg states. On the one hand, the photo emission coefficient and thus the population density of all $n = 4$ states is overestimated by the hybrid code without high Rydberg states with respect to the ADAS results. On the other hand the inclusion of states up to $n = 500$ leads to a lower population density compared to ADAS. From this general result one cannot directly conclude which model is best. In fact one has to assume that dependent on electron density different treatments of the Rydberg states may be necessary, especially because highly excited Rydberg states in the high n_e range may be physically impossible [MB12].
Beside the $n = 4$ states also other states are affected by the Rydberg state treatment (cf. Fig. 6.10). Mostly the population density of all states is overestimated without the high Rydberg states, although the amount depends strongly on the specific state and the n_e and T_e region. This can be seen in Fig. 6.9 and Fig. 6.10 where the results are closest for small n_e values.

In addition to the treatment of high Rydberg states it can be seen that the predicted emission intensities within one model are not consistent for different line ratios. Temperature evaluation where ratios between singlet and triplet lines are formed and thus the singlet-triplet mixture is of highest importance is especially problematic. In addition to the underlying temperature and density itself, several parameters as the initial energy of helium atoms, species dependent ionization or charge-exchange (CX) losses may affect the s/t mixture. In [MB16a] it is shown that ion-impact ionization as well as helium-deuteron CX losses can be neglected compared to electron-impact ionization. However, species dependent rate coefficients for CX between He^+ and hydrogen isotopes (cf. [Lor11]) may contribute as additional population channel which favours triplet state population and would mostly lead to higher evaluated temperatures. The content of this effect depends on the local He^+ and neutral hydrogen concentration. Implementing this CX process to the hybrid code has shown that for SOL conditions in AUG, contributions of this CX process to the total emission are several orders of magnitude lower than electron recombination contributions. However, measurements or detailed modeling of He^+ and neutral hydrogen profiles may be necessary to validate this result.

Based on measurements, this section discussed the capability of several He I line ratios to be used for diagnostic purposes. It allowed the identification of several processes which influence the ratio behavior. Emphasized on the treatment of highly excited Rydberg sates, three modeling approaches are compared. Their influence on the evaluated n_e and T_e profiles as well as the consistency of several ratios within one model are shown in the following section.

6.4. Comparison of n_e and T_e profiles

As one of the best suitable examples for line ratio pairs, the contour plot in Fig. 3.5a exemplarily shows the values of the 501/504 (s/s) n_e and the 501/587 (s/t) T_e sensitive ratios, as result of the static CRM based on ADAS data and routines [Sum04].

In the simplest approach for profile evaluation, this n_e - T_e grid can be used as a look up table to translate the measured value pairs of the ratios from Fig. 6.12 in a static approach, assuming local equilibrium, into n_e and T_e data.

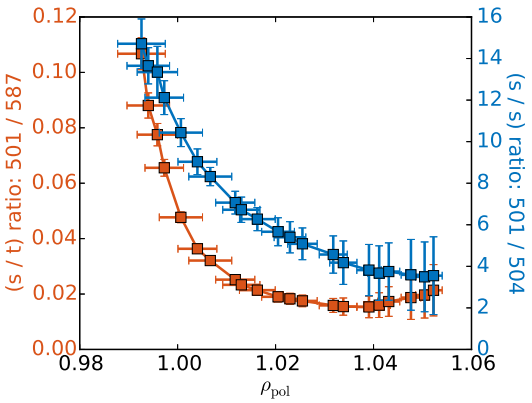

Figure 6.12.: Radial profile of the 501/504 (s/s) n_e and the 501/587 (s/t) T_e sensitive ratio. Data from AUG discharges #32 030 and #32 031 for L-mode, in the time span of 2.14–2.37 s.

In some cases this method is limited by the relatively long relaxation times of the triplet ^{3}S metastable term of helium which populates the triplet spin system. To handle this effect, a time dependent analytical solution, called the hybrid code, was developed by Muñoz Burgos et al. [MB12] which models the time dependent population density of the two spin systems. The time dependent electron temperature and density are calculated by starting the propagation of the neutral beam in the ground state at an initial radial position r_0, where the thermal beam is first introduced into the vacuum chamber. By knowing the initial radial position r_0, the radial position of the first measurement location r_1, and the average velocity of the thermal beam v_b, the relaxation time is obtained and used to calculate a mesh profile of line ratios as function of electron temperatures and densities for that specific time. Once the local value of electron temperature and density is determined, the new initial atomic level population is calculated and used to calculate the new initial conditions for the following measurement point r_2. A new relaxation time is calculated by using the radial distance between r_1 and r_2 and the average thermal propagation speed so that a new set of local temperatures and densities for r_2 can be determined (cf. [MB12]). These time dependent effects mainly affect the electron temperature sensitive line ratios.

Looking at the T_e sensitive line ratio in Fig. 6.12 one can see that the ratio rises again for higher radii, caused by the long relaxation times for low electron densities. Translating this measured ratio in a static way into electron temperature values as done in Fig. 6.13 with the ADAS data set leads to a temperature profile which rises also again at higher radii. This effect is not physical because the time-dependent effects become important in the edge region and if they are not taken into account there will be an overestimation of electron temperature. The hybrid model handles these effects, leading to slightly lower values of T_e in the far SOL compared to the ADAS equilibrium model. These features of the time dependent modeling are also demonstrated in [MB12].

The hybrid code with Rydberg states delivers comparable electron densities to the ADAS model in both, L- and H-mode cases (cf. Fig. 6.15). The results are in both cases in excellent agreement

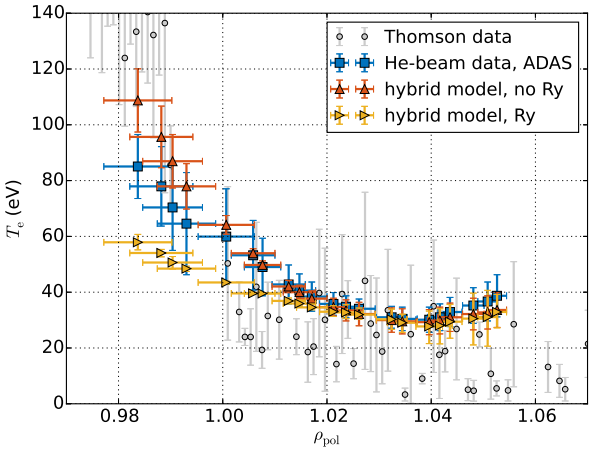

Figure 6.13.: L-mode temperature profile in AUG discharge #32 030, $t = 2.14$–$2.37\,s$. The values from the measured 501/587 ratio are translated into T_e profiles by the hybrid model with and without high Rydberg states and the ADAS CRM. The profiles are compared to data from the Thomson scattering diagnostic.

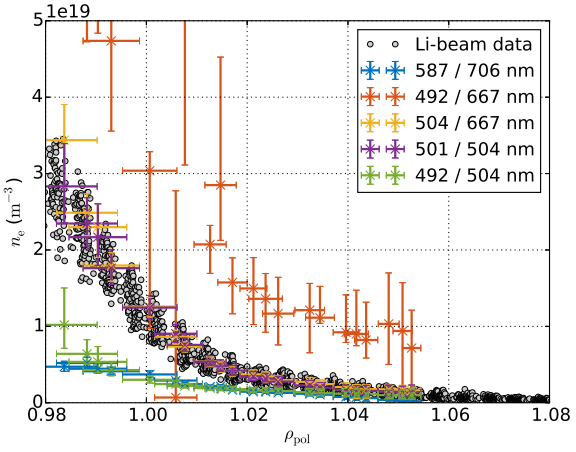

Figure 6.14.: L-mode density profile at AUG. The results from the hybrid model with high Rydberg states are compared for several ratios with general n_e dependence (cf. Fig. 6.8, right, marked with asterisks). The T_e ratio used for the self-consistent analysis is always the 501/587 ratio from Fig. 6.13.

with the Li-beam data as a reference. Nevertheless, this good agreement is only achieved with the 504/667 and the 501/504 ratios as plotted in Fig. 6.14 for the evaluation with the hybrid model with Rydberg states. The remaining three ratios with a general n_e dependence deliver significantly too low or too high values. This shows that different ratios are not described in a self-consistent way, although the two models deliver consistent results within one chosen ratio for the density.

For electron temperature sensitive line ratios, the results are consistent for the models and a fixed ratio within the error bars and under consideration of time dependent effects in the far SOL for small n_e and T_e values, as shown in Fig. 6.13. In regions of high temperature and density however, a significant discrepancy between the models is found. This discrepancy arises from the different number and treatment of Rydberg states in the models. To handle this effect, a revised handling of the Rydberg states is necessary as discussed in section 6.3. Compared to the data of the Thomson scattering diagnostic, the model without the high Rydberg states delivers the best agreement in the high temperature region as the highest T_e values are achieved. The ADAS results are also reasonable, however the temperature may be underestimated for high values as described in [Sch08b].

Nevertheless, only the ADAS results are suitable to describe the n_e and T_e profiles within one model to deliver self-consistent results. In contrast to that, the hybrid code without high Rydberg states is well suitable for T_e evaluation whereas the inclusion of the high Rydberg states is necessary for the electron density reconstruction.

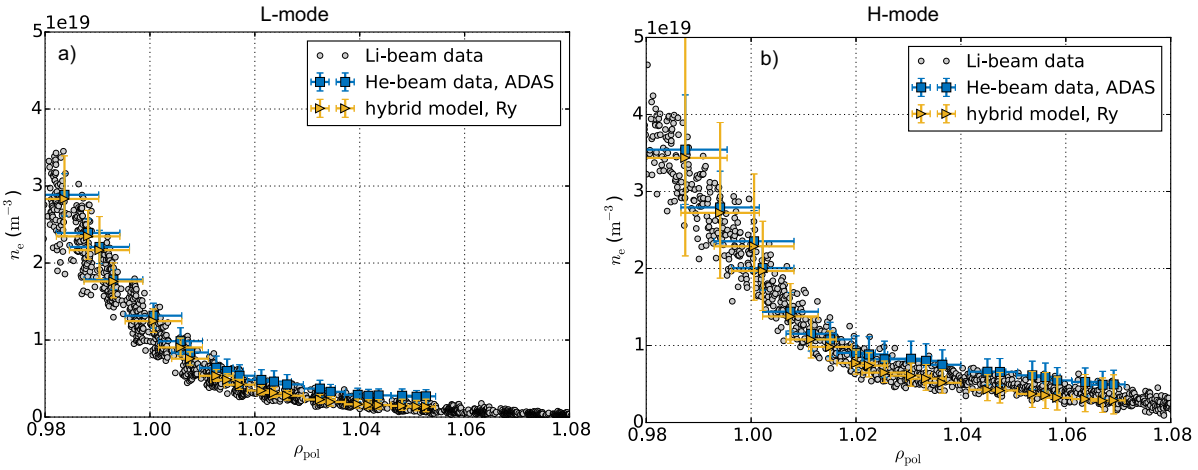

Figure 6.15.: Density profile in AUG discharge #32 030, for a) the L-mode at $t = 2.14$–2.37 s, and b) the H-mode at $t = 3.34$–3.57 s. The profiles reconstructed out of the 501/504 ratio with the hybrid model with Rydberg states and the ADAS code are compared to Li-beam data.

6.5. Conclusion of the line ratio analysis

Comprehensive measurements of spatially resolved He I emission lines in the edge region of AUG were performed. The aim of this study is the selection of suitable line ratios in combination with a proper collisional radiative model (CRM) to describe electron density and temperature profiles. Seven measured lines and thus 21 different ratios allowed a comparison of different CRMs and their underlying processes and assumptions. It is shown that the state of art CRMs are not able to describe all measured lines in a consistent way and that the calculated temperature and density profiles strongly depend on the chosen ratio. Especially a better treatment of highly excited Rydberg states might be necessary to achieve more consistent results. The comparison of line ratios based on experimental values has built an excellent basis for improvements of the CRM.

Consistently within the existing CRMs and in addition to the established 667/728 line ratio, especially the 504/667 and the 501/504 (s/s) ratios are best suitable for electron density evaluation with an excellent agreement to density profiles from the lithium beam diagnostic at AUG. For electron temperature the 501/587 (s/t) ratio can replace the 728/706 (s/t) ratio, although the discrepancy between the CRMs is not fully resolved. Nevertheless, the current ADAS model for these lines leads to self-consistent results which are usable for the diagnostic application.

Furthermore it was shown that the small amount of gas necessary for the diagnostic does not lead to a measurable disturbance of the plasma. The high signal level allows faster measurements without increasing the amount of injected helium. As the detailed analysis of the plasma background verified, the application of a filter based system as described in section 5.2 is suitable. The subsequently upgraded diagnostic with a superior spatial and temporal resolution enables the study of turbulent transport in the edge region of AUG. With continuous and simultaneous measurements of electron temperature and density, the resolution of filaments in the plasma edge region is possible as shown in chapter 7.

7. High resolution measurements

Parts of this chapter are published in M. Griener, et al., "Helium line ratio spectroscopy for high spatiotemporal resolution plasma edge profile measurements at ASDEX Upgrade (invited)", Rev. Sci. Instrum. 89, 10D102 (2018). [Gri18b].

This chapter presents some selected measurement examples performed with the newly developed thermal helium beam diagnostic. It demonstrates the ability of measuring in different plasma scenarios with excellent spatial and temporal resolution. This already becomes apparent when looking at raw emission intensities of injected helium which is presented in section 7.1. Focusing on regime transitions, it is shown that the thermal helium beam enables the measurement of SOL profiles (cf. section 7.2) with a high temporal resolution. The versatile diagnostic enables the localization of modes (cf. section 7.4) and the determination of the propagation velocities of fast transient events such as bursts and blobs (cf. section 7.5). These measurements can be combined directly with the gas-puff imaging technique.

7.1. Temporal resolution and radial measurement range

This section presents selected examples demonstrating the high spatiotemporal resolution of the diagnostic as well as the accessible measurement range. The application of thermal helium beam measurements underlies two major constraints as introduced in subsection 2.3.7. First, neutral helium is required for line ratio emission spectroscopy. Second, the underlying plasma parameters have to lead to sufficient excitation of the neutral helium (cf. section A.2). In the far SOL from where the neutral helium is injected, the neutral helium content is highest. Here the emission is limited by a too low excitation rate at low temperatures. Further inside, the neutral helium content decreases with increasing temperature and density due to ionization and thus limits the application at higher n_e and T_e values.
A discharge which covers different plasma scenarios is presented in Fig. 7.1 to demonstrate the accessible measurement range of the thermal helium beam diagnostic. The discharge starts in L-mode with a transition to H-mode caused by the increase of heating power, as shown in subplot b). Subplot d) shows the performed fueling ramp which leads to an increase of plasma density over time. During the L-mode phase, the separatrix position is moved as indicated with the signal R_{aus} in subplot f). Two signals of the 667.8 nm helium emission are shown in subplot g), where the temporal evolution of the signals reacts on separatrix position as well as changes in heating and fueling level.

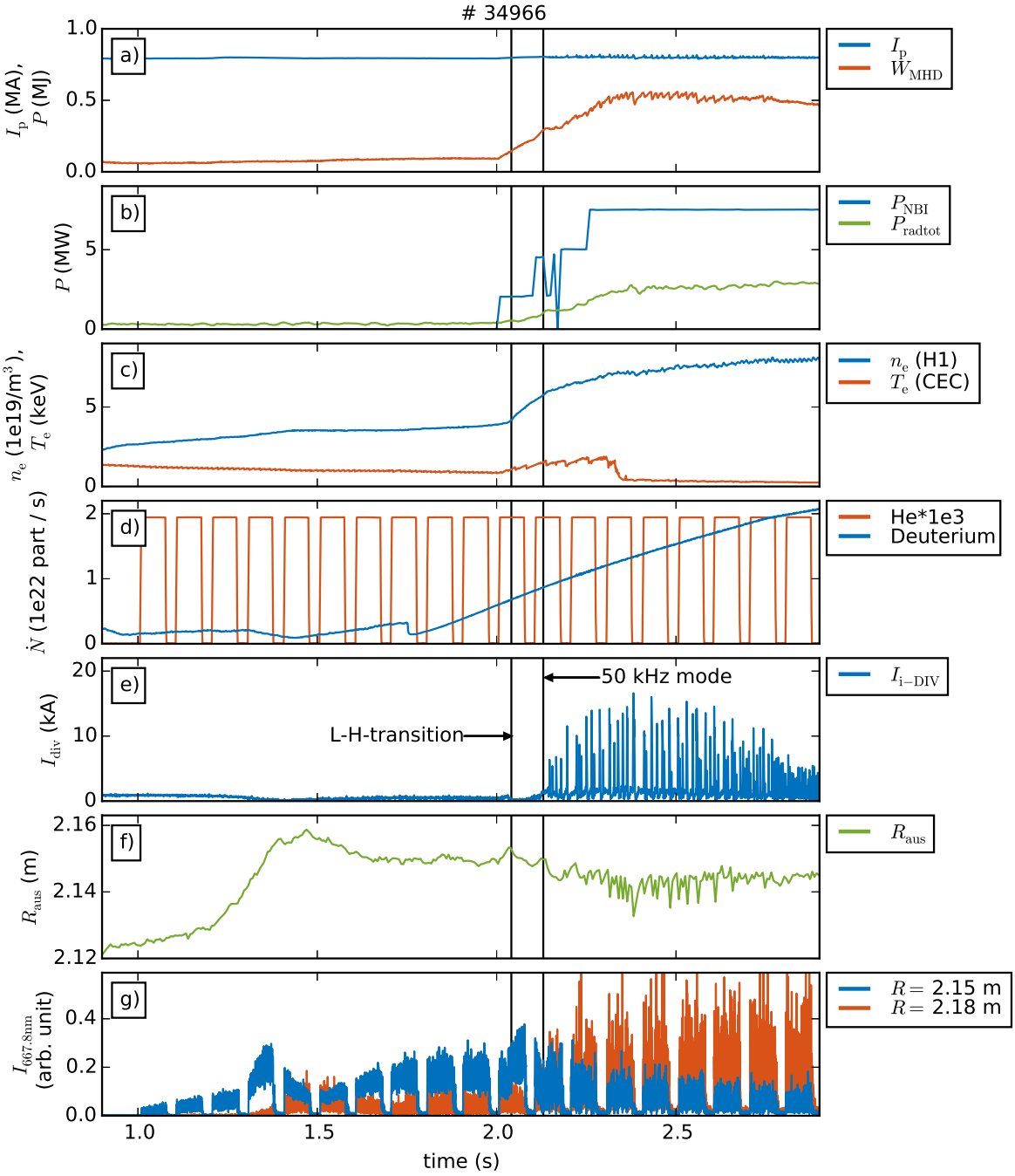

Figure 7.1.: Experimental time traces of AUG discharge #34 966. The time traces show plasma current I_P, total stored energy W_{MHD}, neutral beam injection heating power P_{NBI}, total radiated power P_{radtot}, line integrated electron density n_e and core electron temperature T_e, total plasma fueling with deuterium compared to the diagnostic He inlet, shunt current of the inner divertor I_{i-DIV}, separatrix position at the midplane R_{aus} and the measured emission $I_{667.8nm}$ at 667.8 nm of the injected helium at two radial positions. A zoom of the L-H transition is shown in Fig. 7.4.

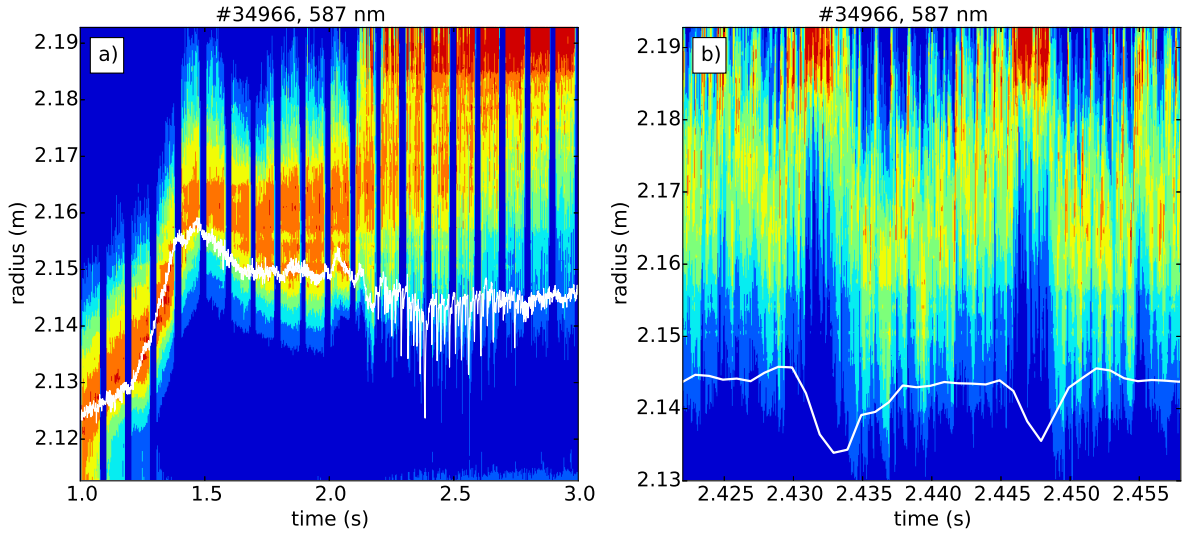

Figure 7.2.: Contour plot showing the 587.6 nm helium emission along radius over time during a discharge. The shift of the separatrix position (white line) and a density ramp (cf. Fig. 7.1) shifts the point of maximum emission along the radius a). Subplot b) shows a zoom into the H-mode phase showing how ELMs and inter-ELM filaments influence the emission profile.

The change of emission of the 587.6 nm helium line during this discharge is illustrated in Fig. 7.2 as a function of time and plasma radius. The radial region with pronounced helium emission has a width of 4–5 cm, following precisely the separatrix position, marked as white line in Fig. 7.2 a). This pronounced response of the signal shows the high radial resolution of the measurement. Furthermore, the emission region is influenced by the increase of the density which leads to a outwards shift of the emission.

Fig. 7.2 b) shows a temporal zoom of the H-mode phase in Fig. 7.2 a). The high temporal resolution clearly shows that the signal in the far SOL is mostly produced by intermittent events such as turbulence driven filaments or filaments generated by edge localized modes (ELMs), which lead to increased radial transport of temperature and density. Whereas these events increase the signal in the far SOL, they lead to a decrease of the signal further inside due to the increased ionization rate[1].

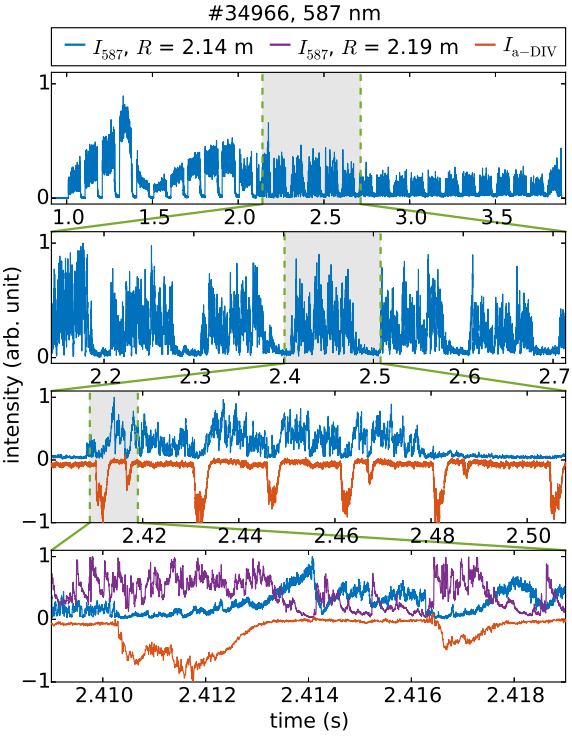

Figure 7.3.: Helium emission time trace with increasing temporal resolution, measured at $R = 2.14\,\mathrm{m}$. This emission is compared in the lower subplots to the divertor current signal (red). The bottom plot shows an additional channel at $R = 2.19\,\mathrm{m}$ (purple).

[1] Note that the radial outwards shift of the signal during ELMs is not caused by the separatrix shift during these events. In fact, the perturbation of the equilibrium during ELMs shift the separatrix inwards, which shows that the increased radial transport is the reason for the outwards shift of the signal maximum.

This can also be seen in Fig. 7.3 which demonstrates the high temporal resolution of the signal. The plot shows four zoom levels of the signal time trace of one channel located at a fixed spatial position at $R = 2.14\,\mathrm{m}$. For $t \gtrapprox 2.1\,\mathrm{s}$, this location corresponds roughly to the separatrix position. For $t \lessapprox 1.7\,\mathrm{s}$, the response of the signal to the aforementioned separatrix shift can be seen.
The overview signal reflects the chopping of the helium beam and fluctuations caused by plasma phenomena. The lower two plots compare the helium emission at the separatrix and the far SOL to the divertor current signal (red), which indicates the occurrence of ELMs. The bottom plot shows an additional radial channel at $R = 2.19\,\mathrm{m}$ (purple). As mentioned above, the signal strengths for the two plotted channels behave inversely to each-other. Besides the response to dominant ELMs (which are visible in the divertor current signal), the helium emission is also sensitive to inter-ELM filaments. This sensitivity can be used to calculate radial propagation velocities as done in section 7.5.

7.2. Regime transition from L-mode over I-phase to H-mode

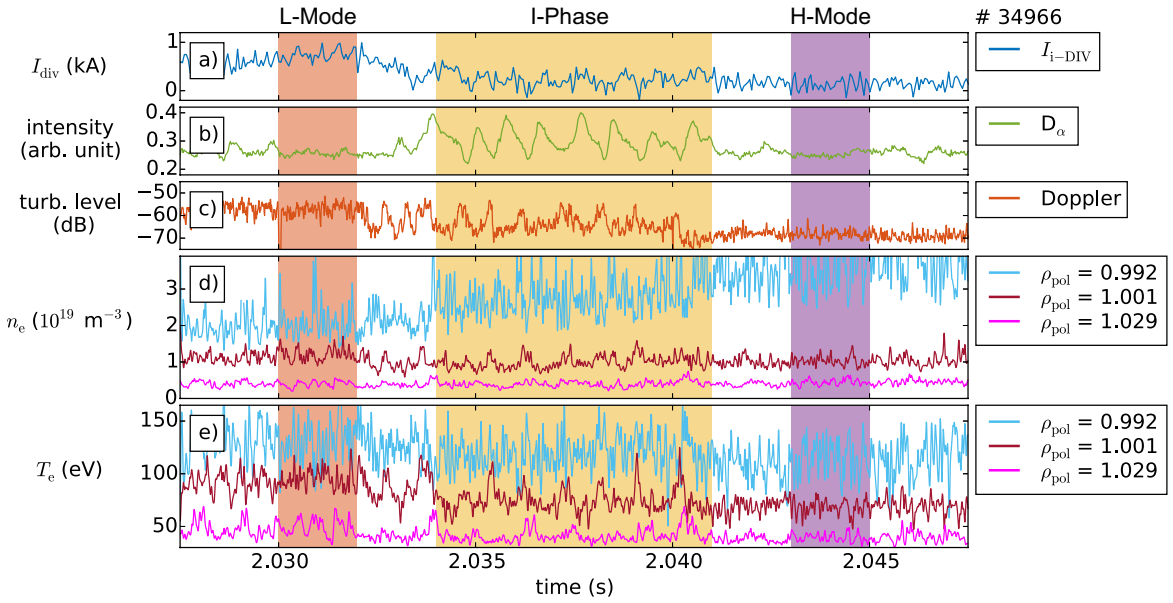

Figure 7.4.: Time traces of AUG discharge #34966, showing a transition from L-mode over an I-phase to H-mode. Characteristic for the I-phase are bursts visible in the divertor D_α signal b) and the Doppler reflectometry signal c). Electron density measurements by the helium beam at three different positions are shown in d) and electron temperature measurements in e). Full radial profiles of the three marked areas can be found in Fig. 7.5.

This section demonstrates how the helium beam diagnostic can be used to investigate the aforementioned regime transitions and their underlying phenomena. In general the n_e and T_e data evaluated with the helium beam have to be treated with reservations of possible calibration discrepancies of the helium beam optics as discussed in subsection 5.2.5. It has been found that the density profiles agree very well with other diagnostics for a variety of plasma scenarios. The temperature profiles, however, are not always consistent with Thomson scattering measurements

and further investigations of their reliability in different scenarios is planned. The calibration uncertainties do not affect the studied fluctuation phenomena, the relative comparison between profiles or the calculated propagation velocities.

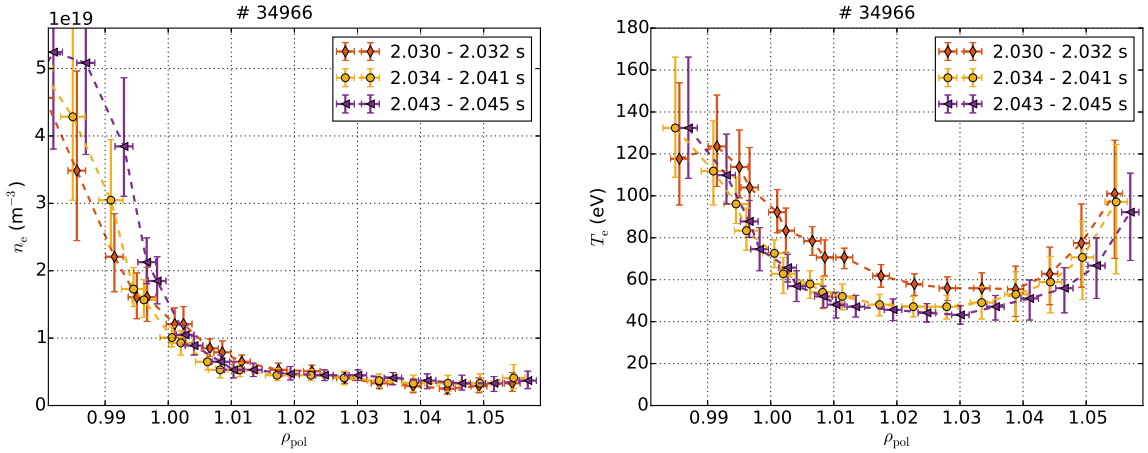

Figure 7.5.: Radial profiles for electron density and temperature for the three time intervals marked in Fig. 7.4. The data are evaluated with the helium beam diagnostic, using the static ADAS model. Burst-resolved profiles for the I-mode phase are shown in Fig. 7.7.

The discharge which was already examined in section 7.1 is a suitable example to study the transition from L-mode over an I-phase to H-mode. A magnification of the time span around the regime transition in Fig. 7.4 shows how the divertor current signal a), the D_α emission b) and the turbulence level c) react. The turbulence level is measured using Doppler reflectometry around the position of $\rho_{pol} = 0.98$, with a perpendicular wavenumber of $k_\perp = 6.5\,\mathrm{cm}^{-1}$. The signals in a) and c) show a reduction in the turbulence level in H- compared to L-mode. As introduced in section 2.2, the characteristic I-phase bursts are visible in all signals, most prominent in subplot b). The bursts can also be seen in temperature and density time traces, evaluated with the helium beam diagnostic and presented in the subplots d) and e).
Radial edge profiles of n_e and T_e from the helium beam diagnostic are shown in Fig. 7.5 for the three phases highlighted in Fig. 7.4. The electron density shows a strong increase in the confined region after the transition from L- to H-mode. The electron temperature profiles also steepen in the confined region in H-mode compared to L-mode. The increase of T_e in the far SOL is a known effect and can be explained by the static collisional radiative model used for evaluation. As shown in Fig. 7.6, this effect can be compensated by the time dependent approach[2] (the time dependent hybrid code) as described in section 6.4 and [MB12]. For n_e, the hybrid code delivers the same results compared to the ADAS code, whereas electron temperature is 15 eV lower for the hybrid code, independent of the time dependency. The time dependent hybrid code reduces the rise of T_e in the far SOL.

[2] As explained in section 6.4, the velocity of injected helium atoms is used to calculate the relaxation time for given n_e and T_e values. However a ten times higher velocity of the beam atoms than the expected thermal velocity of 1.24×10^3 m/s has to be set in the code to compensate the time dependent effect as shown in Fig. 7.6.

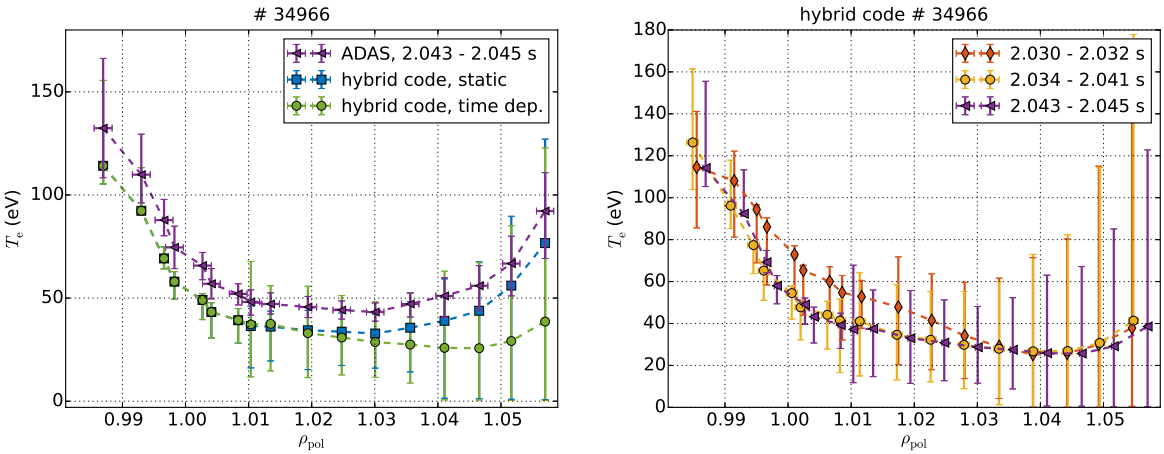

(a) Comparison of T_e profiles evaluated with the ADAS and the hybrid model with and without time dependency.

(b) Time dependent evaluation of T_e as comparison the the static ADAS evaluation which is shown in Fig. 7.5.

Figure 7.6.: Effect of the time dependent evaluation process performed with the hybrid code. Considering the time dependent relaxation effects reduces the increase of T_e in the far SOL. The electron density is not affected by the time dependency.

It can be seen that the electron temperature in L-mode is higher in the near SOL compared to the early H-mode case, with and without compensation of the time dependent relaxation effect. The drop in SOL T_e at the onset of H-mode can be explained with the established transport barrier and the pedestal formation, which leads transiently to a reduced power flux across the separatrix since the total stored energy increases.

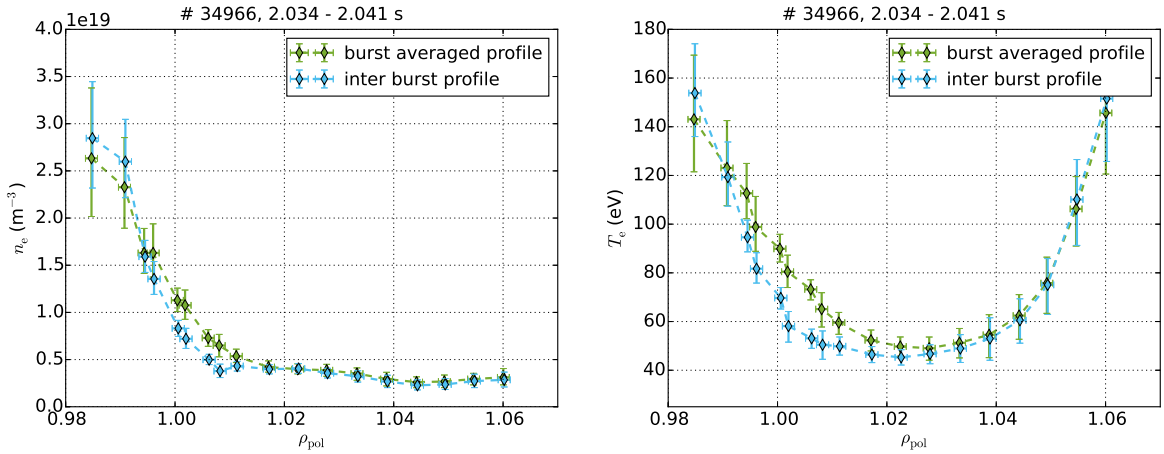

Figure 7.7.: Burst-resolved profiles for n_e and T_e during I-phase in #34966 (cf. Fig. 7.4), evaluated with the static ADAS model. It can be seen that both, the profiles for n_e and T_e flatten during bursts.

During I-phase bursts the pedestal relaxes. This is illustrated in Fig. 7.7, where plasma profiles are not averaged over the whole I-phase but plotted burst-resolved. The plot shows profiles of n_e and T_e, averaged over bursts and burst-free timepoints of the I-phase, respectively. It can be

seen that during bursts both, n_e and T_e increase at the separatrix and in the near SOL region. This reverses toward the pedestal, leading to a flattening of the profiles as described in [Cav17b]. The turning point where the values of n_e and T_e are not changing, called Pivot point, is located at $\rho_{pol} \simeq 0.992$.

7.3. Fluctuation analysis

7.3.1. Assessment of experimental results

In Fig. 7.1, the occurrence of a 50 kHz mode during the early H-mode phase at $t = SI2.13s$ is noted. This mode can clearly be seen in the intensity of the measured helium emission lines and the corresponding spectra as shown in Fig. 7.8. As the mode is barely visible with magnetic pick-up coils it might be an electrostatic phenomenon. Fig. 7.8 shows time traces of a channel allocated to $\rho_{pol} = 1.00$ in the left column and the corresponding Fourier spectra [3] in the right column. The upper row shows the emission data of the four lines, whereas the middle row shows four calculated ratios. As stated in section 3.3, ratios calculated from lines of the same spin species should react sensitively to electron density changes, whereas spin-mixed ratios should show electron temperature changes.
As the observed mode is only visible in both spin-mixed ratios and not in ratios of lines from the same spin system (middle row in Fig. 7.8), one would assume that the mode only affects temperature but not density. The calculated values of n_e and T_e are plotted in the lower row of Fig. 7.8, where the mode is not clearly pronounced, neither in n_e nor in T_e. This impression is caused by the strong fluctuation of both signals due to the noise of the measurement. In the simplest case, the resulting noise of a ratio of two quantities x and y with uncertainties Δx and Δy is given by

$$\Delta\left(\frac{x}{y}\right) = \frac{x}{y}\left(\frac{\Delta x}{x} + \frac{\Delta y}{y}\right), \tag{7.1}$$

which is the sum of both relative fluctuations. Therefore ratios of channels with a weak signal level show strong fluctuations which leads to high spikes or unevaluable points in n_e and T_e. As n_e and T_e are typically evaluated simultaneously out of two measured line ratios, a strong fluctuation of one ratio translates in a high noise of both quantities.
Spin-mixed ratios show the mode more clearly compared to s/s and t/t ratios. As treated in section 6.3, the absolute change of the value of spin-mixed ratios is higher compared to s/s or t/t ratios, for comparable changes in n_e and T_e, respectively. Thus spin-mixed ratios suffer less from a given noise level.

[3] For Fourier transformation, a time interval of 22 ms is used, with a time resolution of 5.6 µs. The shown spectra are averaged from windows with 512 timepoints, multiplied by a Hanning window, and an overlap of 50 %, respectively.

7.3.2. Forward modeling of line radiance and ratios

The following example demonstrates how changes of specific ratios have to be interpreted correctly and what can be learned from spectra of line intensities in regard of plasma fluctuations. Synthetic n_e and T_e traces are used as input for a forward model, which shows the reaction of emission intensities and ratios onto a given perturbation in T_e.
As input, the density is considered to be constant at $n_e = 2.5 \times 10^{19}\,\mathrm{m}^{-3}$, with a noise level of 1 %. With the same noise level, T_e is given to show a sinusoidal fluctuation with an amplitude of 10 % and a frequency of 20 kHz around the mean value of 59 eV.
Input and results of the modeling are shown in Fig. 7.9, where the left column represents the data as time traces and the right column as Fourier spectra. The spectra of the input data clearly indicate 20 kHz fluctuations in T_e but not in n_e. The given fluctuation in T_e can be seen in the emission time traces of all emission lines, plotted in the second row of Fig. 7.9. Singlet lines show a fluctuation with the same frequency as the given T_e perturbation. The two triplet lines, however, fluctuate with double frequency, i.e. 40 kHz. This appears, because T_e is chosen to fluctuate around a local maximum of triplet emission as it can be seen in Fig. A.1. In the corresponding triplet spectra, the 20 kHz part totally vanishes or it is less pronounced compared to the 40 kHz fluctuation. This doubling of the frequency for triplet lines is not always present and only occurs when T_e fluctuates around the respective emission maxima. So this example shows that one cannot necessarily conclude on the fluctuation frequency of a plasma perturbation by only looking at the spectra of one emission line.
As can be seen in the lowest row of Fig. 7.9, this doubling of the frequency cancels out as soon as ratios are formed. Here it is to remark that all ratios and not only the spin-mixed ones react on the given T_e fluctuation. So it can also be seen directly that from observing a change in a certain ratio one cannot conclude if the change is caused by n_e or T_e fluctuations. The reason for this is that the values of the ratios do not purely depend on n_e or T_e (cf. Fig. 3.5) and thus also the s/s ratio has to adapt to keep the density constant when the s/t ratio is changed (and vice versa).

7.3.3. Conditional averaging

To investigate the impact of the observed mode on n_e and T_e, despite of strong fluctuations in the directly evaluated signal, a conditional averaging technique can be applied. As the period of the fluctuation is known, a sample interval of two periods can be chosen from the ratio which represents the fluctuation best (667/587). By means of correlation analysis, the starting positions of similar fluctuation periods can be searched for in the time trace. The minimal distance between the matches is the length of the sample interval, ensuring that no redundant information are generated. In the time interval of $t = 2.122$–2.144 s, where the mode appears with constant frequency, 345 matches of the sample are found. Taking the gained time intervals to average the data, n_e and T_e evaluation is possible. The results are shown in Fig. 7.10, which represents the averaged impact of two periods of the 50 kHz mode on the electron temperature

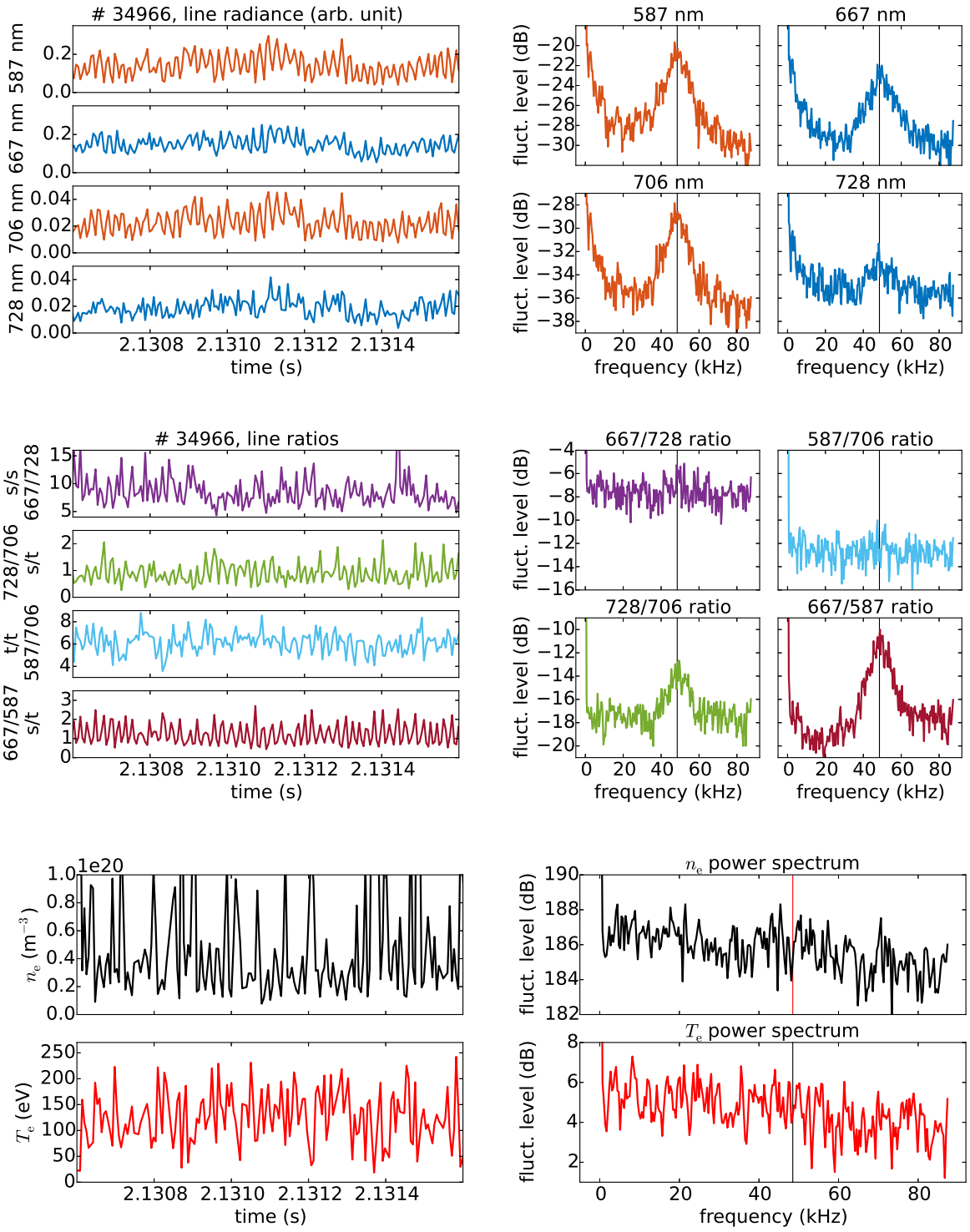

Figure 7.8.: Appearance of a 50 kHz mode in #34966 (cf. Fig. 7.1). Helium emission is shown in the top, four different ratios in the middle, and the evaluated n_e and T_e data in the bottom row. The left column shows the signal over time, wheres the right column shows the frequency spectra of the signals, respectively. The plotted channel is located at the separatrix at $\rho_{pol} = 1.00$, the total time interval used for the spectra is 2.122–2.144 s.

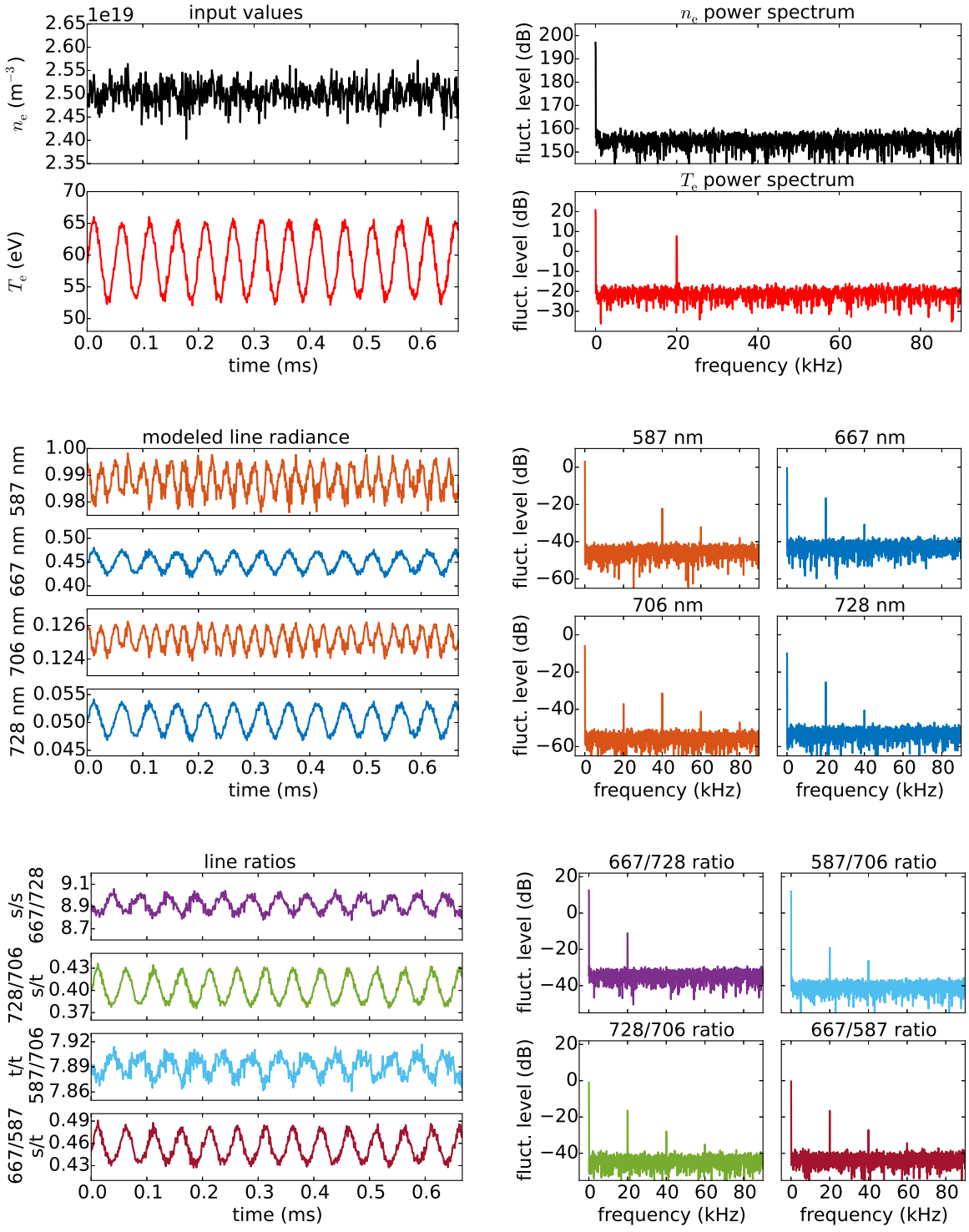

Figure 7.9.: Forward modeling of helium emission and calculated ratios with a given input for n_e and T_e. Both input quantities have a relative fluctuation level of 1 %. The electron density is set to be constant at $2.5 \times 10^{19}\,\mathrm{m}^{-3}$, the electron temperature fluctuates with 20 kHz and an amplitude of ±10 % around the base value of 59 eV.

and density profiles. It can be seen that the impact of the mode in the measurement range of $\rho_{\mathrm{pol}} = 1.00$–$1.05$ is highest at the separatrix and vanishes completely in the far SOL.

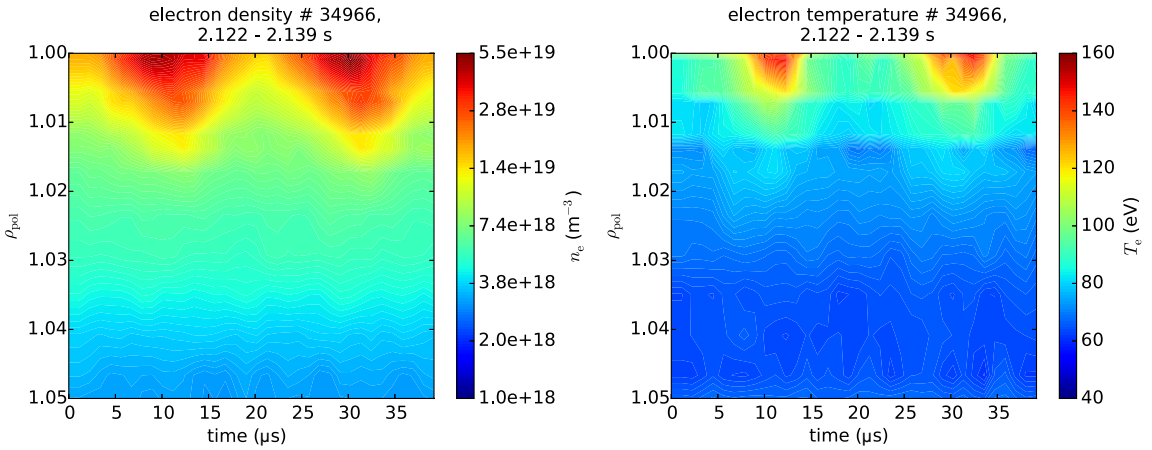

Figure 7.10.: Contour plots of n_e and T_e as function of time and radius, showing the impact of the 50 kHz mode for two fluctuation periods. The data are conditionally averaged over 345 intervals in #34 966 at $t = 2.122$–2.144 s.

7.4. Regime transition from I-mode to H-mode

A further example where the investigation of modes is of highest interest is the I-mode as described in section 2.2. A plasma experiment with a pronounced I-mode phase is shown in Fig. 7.11. For this experiment, a constant plasma current of $I_P = 1$ MA, and a separatrix position of $R_{\mathrm{sep}} = 2.138$ m where used in upper single null geometry, i.e. the upper but not the lower divertor of AUG is used. As depicted in subplots e) and f), the helium beam is used for a continuous time interval of 300 ms to perform line ratio spectroscopy. Whereas the discharge is still in L-mode when the helium puff starts, I-mode is achieved at $t = 3.535$ s. As visible in subplot a), the NBI heating power is slowly increased by pulse width modulation of a single source (cf. section 2.1). Whereas in L-mode temperature decreases after step-wise jumps, the slope of this decrease is reduced during I-mode so that T_e becomes stationary between sawteeth as can be seen in c). This increases the stored energy in the plasma step-wise [Hap17, Ryt17]. At $t = 3.778$ s the plasma jumps into H-mode, visible by the steep increase of plasma density b) and the stored energy in the plasma d).

The characteristic weakly coherent mode can be clearly seen in spectra of helium emission time traces[4] at a specific radial location as shown in Fig. 7.12. At $\rho_{\mathrm{pol}} = 0.986$, the WCM with the sawtooth induced frequency increase is visible at frequencies around 50 kHz. Especially in the late phase of the I-mode, vertical stripes can be seen in the frequency spectra, denoting typical I-mode bursts. Sharply defined at the I-mode to H-mode transition, the WCM vanishes and a mode at 150 kHz is generated.

[4] As the same frequencies occur in four measured wavelengths and in the calculated ratios, they directly show the WCM and not a double frequency as shown in Fig. 7.9.

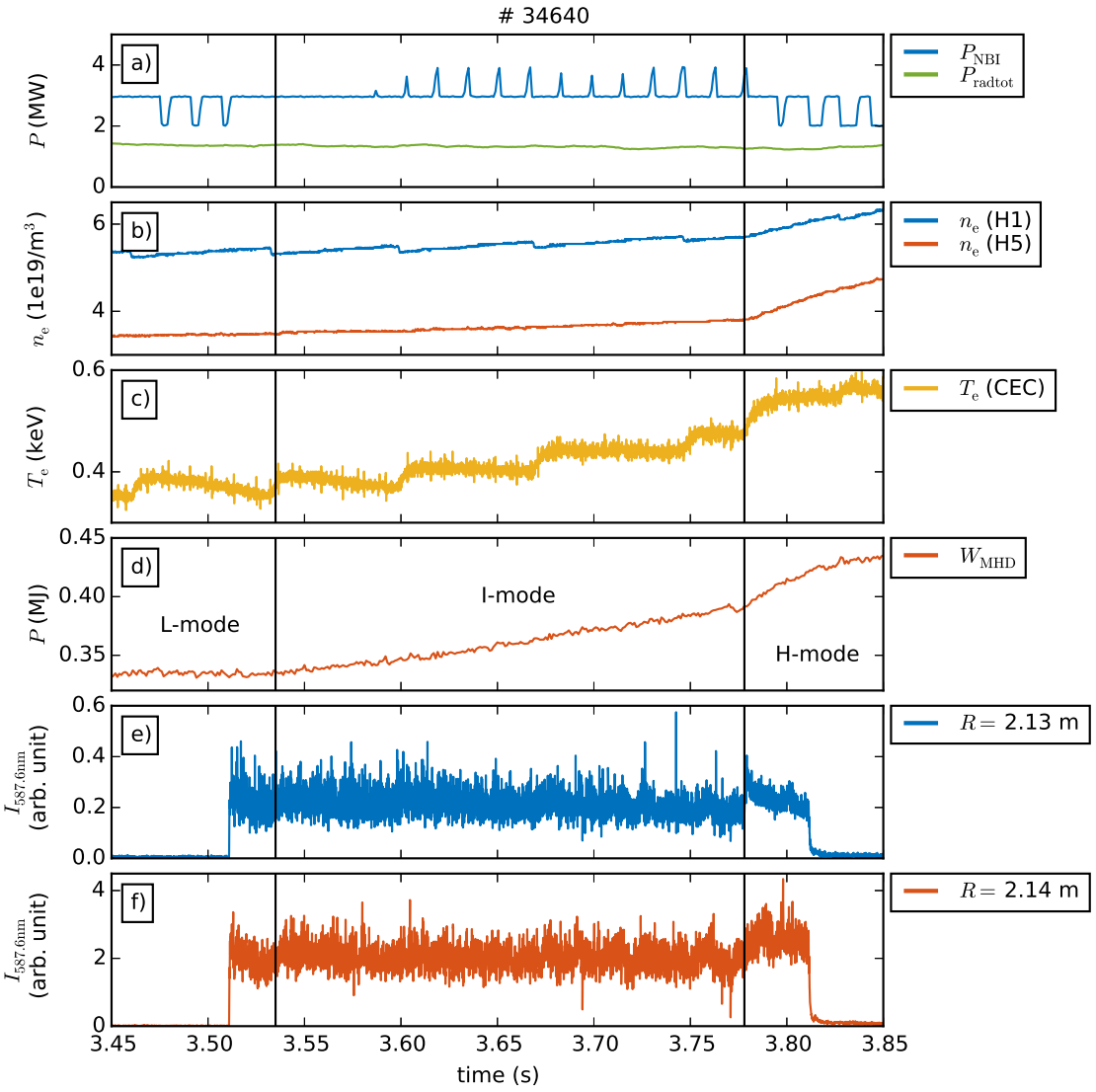

Figure 7.11.: Experimental time traces of AUG discharge #34 640, showing the transition from L- to I-mode and from I- to H-mode. Chopped neutral beam heating power P_{NBI} as well as total radiated power P_{radtot} are shown in a). Line integrated electron density n_e is shown for an interferometer core (H1) and edge channel (H5) in b). Core electron temperature T_e c) is clearly affected by sawtooth crashes. The total stored energy in the plasma W_{MHD} d) responds on the marked phase transitions (vertical black lines). The measured emission $I_{587.6\mathrm{nm}}$ at 587.6 nm of the injected helium is shown for two radial positions e), f), the corresponding frequency spectra are plotted in Fig. 7.12.

Because the WCM is not visible in the spectra of all channels, e.g. at $\rho_{\mathrm{pol}} = 1.002$, it can be radially localized. To determine the radial impact of the WCM on n_e and T_e, conditional averaging of five fluctuation periods, occurring ahead of bursts, is performed (cf. section 7.3). The resulting time traces for the fluctuations in n_e and T_e at four radial positions are shown in Fig. 7.13. The maximum impact of the WCM in the measurement range lies at $\rho_{\mathrm{pol}} = 0.992$ with a 18 % fluctuation amplitude in n_e and a 12 % fluctuation amplitude in T_e. The fluctuation amplitude increases toward the bursts in the selected sample, which is consistent to previous investigations done by Happel et al. [Hap16]. Whereas n_e seems to fluctuate around a mean value, T_e shows a slight increase over the averaged time span. For $\rho_{\mathrm{pol}} > 1.01$ the WCM impact seems to vanish completely.

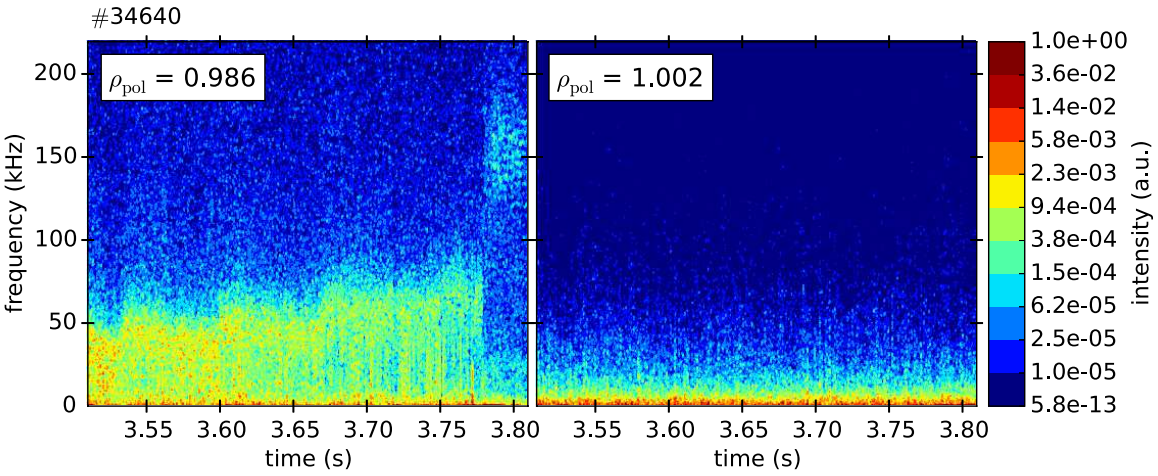

Figure 7.12.: Spectrogram of the 587.6 nm helium line at two radial positions for the I-mode discharge #34 640. Whereas the weakly coherent mode (WCM) is clearly visible in the confined region, its impact cannot be seen in the spectra at $\rho_{pol} = 1.002$. At $\rho_{pol} = 0.986$ disappearance of the WCM and the appearance of a mode around 150 kHz clearly indicates the transition from I- to H-mode.

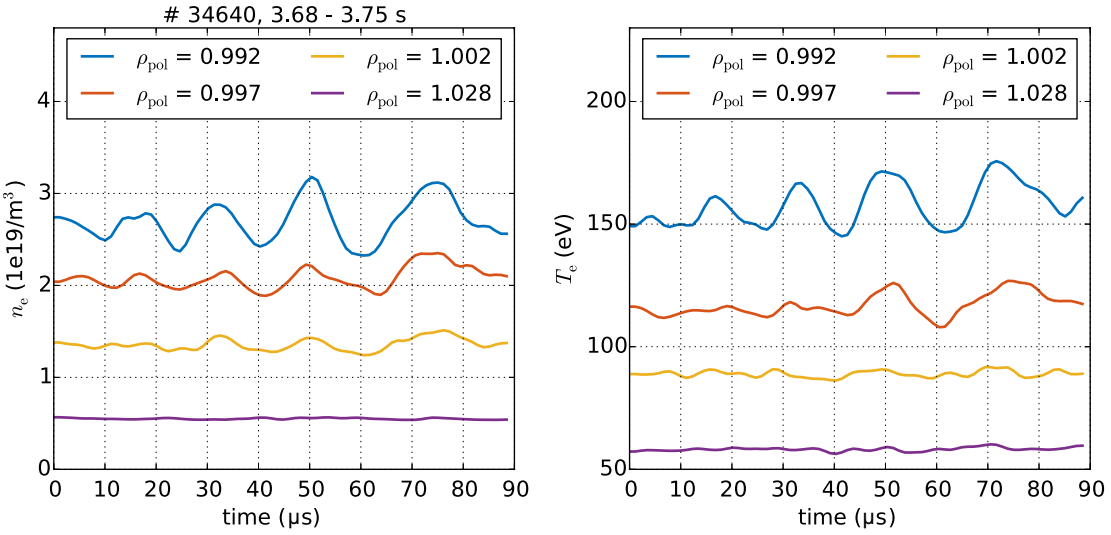

Figure 7.13.: Conditionally averaged sequence of the WCM (54 kHz) occurring before I-mode bursts. 153 matches are found in the time interval of 70 ms. a) shows the electron density and b) the electron temperature at four different radial locations.

7.5. Propagation velocities of filaments in the SOL

As mentioned in section 7.1, the impact of filaments on the emission intensity of the detected helium lines can be seen in the far SOL, even in regions where the inter-filament emission vanishes (cf. Fig. 7.2 b)). Therefore and because of the high spatiotemporal resolution and broad measurement range, the thermal helium beam is an excellent diagnostic to measure filament propagation velocities. As done in [Bir14] with raw data of lithium emission, this analysis can directly be performed based on measured line intensities.

The radial outwards propagation of a single filament is presented in Fig. 7.14, which shows the 587.6 nm signal intensity of the radially distributed channels over time. The channels are presented in a way that their zero level of the normalized intensity corresponds to the radial location of the channel. The separatrix position is marked by a purple horizontal line. The vertical line in the plots guides the eye to notice the radial outwards propagation of the perturbation in the signal time traces. As mentioned before, the impact of events on the emission intensity of a certain helium line depends on the underlying n_e and T_e values and on the neutral helium content. Whereas the signal drops close to the separatrix, the radially outwards propagated filament increases the signal intensity in the far SOL with a certain time delay with respect to the signal drop of the inner channels.

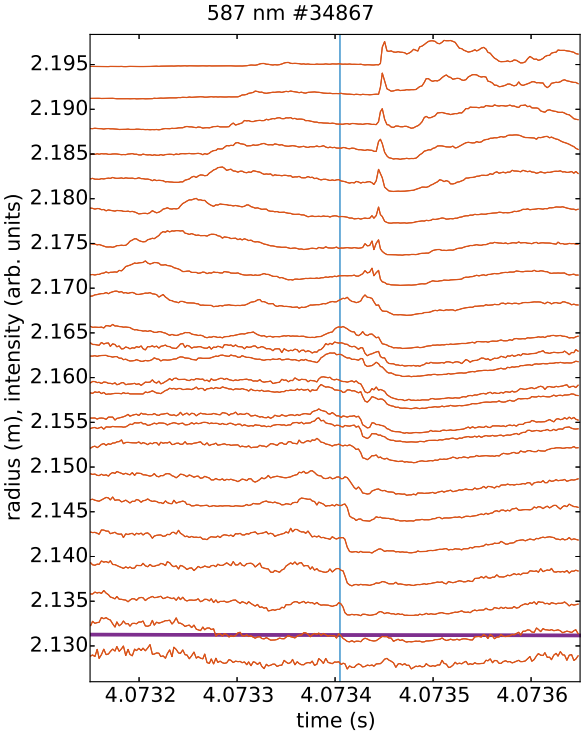

Figure 7.14.: Radial propagation of a single inter-ELM event in the H-mode phase of #34 867, visible in the intensity perturbation of radially distributed lines of sight detecting the emission of the 587.6 nm helium line. The time shift between the channels determined by correlation analysis is plotted in Fig. 7.15.

It is a common method to use correlation analysis between channels to detect their specific time delays. Typically the time shift between one reference channel and all remaining channels is calculated. To take the change of the signal shape of the helium emission along the radius into account, the correlation between two neighbouring channels is calculated subsequently in this work. The total time shift between the innermost and the outermost channel that shows a pronounced response to the filament is then given by the sum of the pairwise calculated time shifts. The result of this analysis for the presented filament in Fig. 7.14 is shown in Fig. 7.15. It depicts the time shift of the signals between the radially distributed channels, enabling the calculation of the radial velocity[5]. Assuming the propagation velocity for each filament to be constant along the radius, a linear fit can be used to determine the resulting mean radial velocity. The tendency for higher velocities at smaller radii is shown in Fig. 7.16.

A systematic analysis[6] of radial propagation velocities is performed for discharge[7] #34 867, separately for the L-mode phase (t = 1.0–2.5 s, 148 detected events) and the inter-ELM H-mode phase (t = 2.6–5.0 s, 302 detected events) as well as for ELM filaments (135 detected events). The results of the analysis are shown in histograms in Fig. 7.17.

[5] As filaments map along field lines (cf. [Ter09]), radial velocity depends on the magnetic field configuration, i.e. the flux broadening in the SOL. The values for the radial velocity in this case are referred to the measurement position of the helium beam as presented in Fig. 5.6.

[6] The filament tracing delivers comparable results, independent of the wavelength used. Only the signal to noise ratio of the 728.1 nm line is too low in the presented discharge to be used for the analysis.

[7] This discharge, which ends at $t = 5$ s, is a shorter version of #32 032, cf. Fig. 6.2.

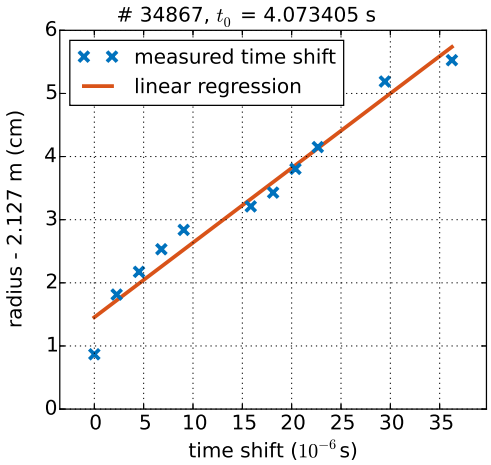

Figure 7.15.: Time delay between the signals of radially distributed channels for a single inter-ELM event (cf. Fig. 7.14). The linear regression through all points delivers a velocity of (1180 ± 90) m/s.

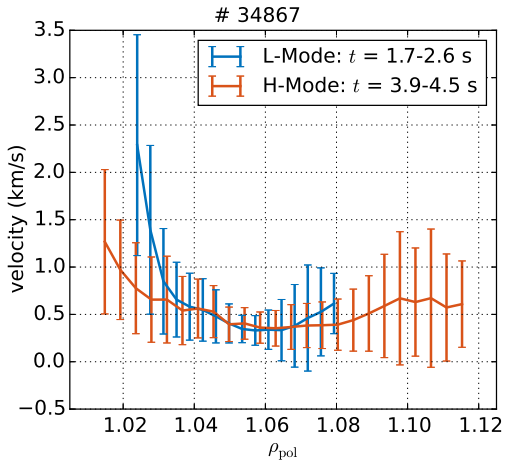

Figure 7.16.: Radial velocity of inter-ELM events as a function of ρ_{pol} in L-mode compared to H-mode. The data are obtained by locally calculating the velocity of each event.

The distribution of radial velocity is similar in L-mode and H-mode. Both velocity distributions tend to be asymmetric with a tail of detected events toward higher velocities. Whereas the median velocity in L-mode (343 m/s) is similar to H-mode (338 m/s) it is noticeable that the mean velocity is with 415 m/s higher in H-mode compared to L-mode with 365 m/s, caused by the stronger pronounced high velocity tail in H-mode. The inter-ELM velocities are in good agreement to [Fuc14] where gas-puff imaging is used to determine the radial velocity to 300–400 m/s. The observation that the averaged radial velocity in L-mode is slightly higher than in H-mode is not seen in the presented discharge.

For selecting inter-ELM periods, ELMs are removed by a threshold criterion in the divertor current signal so that small ELMs may not be detected. Events which lie slightly under the detection threshold for ELMs are bigger compared to typical inter-ELM filaments, which are barely visible in the divertor current. These bigger events which occur in H- but not in L-mode are thus also characterized by higher propagation velocities, explaining the more pronounced high velocity tail in H-mode.

The radial ELM filament velocity is with a mean value of 1572 m/s and a median velocity of 1418 m/s significantly higher than the inter-ELM filament velocity. This agrees with [Sch08a], where a most probable velocity of 1.1 km/s was determined for ELM filaments.

Depending on the plasma conditions where filaments connect to the wall, there are two models which correlate the propagation velocity of filaments with their size a (cf. [Gar06, Myr06, Bir14]). In the sheath connected regime the velocity is proportional to a^{-2}, in the inertial regime, where no electrical connection to the wall is possible, the velocity is proportional to $\sqrt{a}$. Assuming that ELM filaments are larger than inter-ELM filaments, which was, however, not investigated with the thermal helium beam diagnostic, the higher velocity would be in agreement with the inertial filament propagation model. The fact, that ELM filaments are clearly visible in the divertor current (cf. Fig. 7.3), does not support the assumption of an inertial regime in the divertor. Therefore, further studies, especially regarding the radial size of ELM filaments are envisaged.

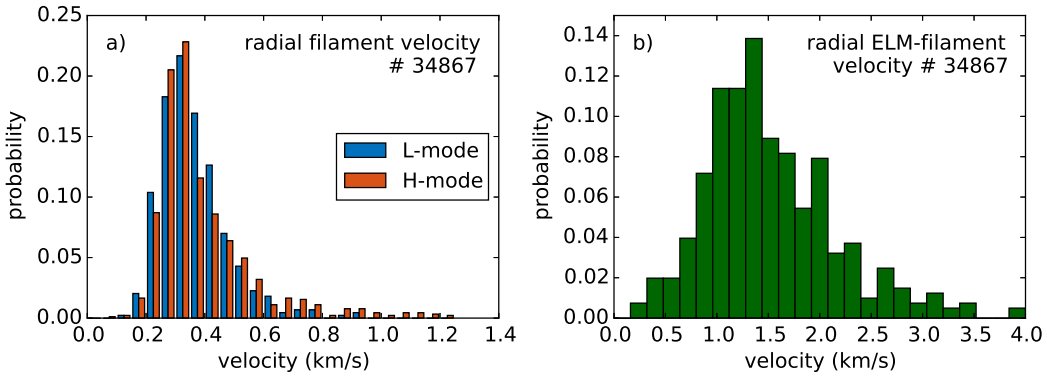

Figure 7.17.: Distribution of the radial velocity of events in AUG discharge #34 867. In a) the radial velocity of inter-ELM events is compared between L- and H-mode. A histogram of ELM velocities is given in b).

The local radial velocity as a function of ρ_{pol} is shown in Fig. 7.16, averaged for filaments in L-mode and inter-ELM H-mode, separately. The different radial coverage in L- compared to H-mode is caused by a changed magnetic configuration. In L-mode as well as in H-mode, the local radial velocity is higher in the separatrix region and decreases toward the SOL. This is in agreement with observations in [Fuc14]. In contrast to [Fuc14] the velocity in the far SOL stays constant within the errorbars instead of decreasing continuously.

7.6. Combination of line ratio and gas-puff imaging measurements

The presented example in section 7.5 shows that the direct observation of helium emission with the newly installed hardware is a powerful tool for the calculation of radial velocities. Compared to probe measurements or gas-puff imaging, the helium beam optics covers a broader measurement range[8]. By using vertically distributed lines of sight (LOS) or the LOS grid (cf. Fig. 5.1) also poloidal velocities can be determined. The combination of the helium beam with a full 2D image of GPI, as shown in Fig. 7.18, allows the determination of radial and poloidal velocity components. Furthermore with the line ratio technique, n_{e} and T_{e} values can be assigned to single filaments as in Fig. 7.18, which shows probably a density blob which is translating radially outwards.

[8] By using PMTs as detectors, the helium beam optics is more sensitive to small signal intensities compared to GPI, where a CCD camera is used. This increases the accessible measurement range.

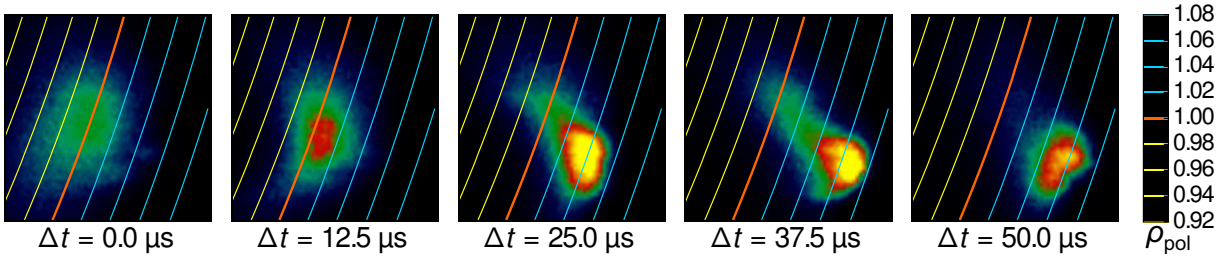

Figure 7.18.: Total emission intensity of the He I 587.6 nm line, measured with the gas-puff imaging (GPI) technique at AUG #34 266, $t_0 = 6.907\,78$ s and a frame rate of the fast camera "Phantom v711" of 400 kfps.

7.7. Summary of high resolution measurements

This section demonstrated the powerful diagnostic capabilities of the new thermal helium beam at AUG which was built within this thesis. The accessible measurement range was demonstrated by looking at the radial emission distribution of the injected helium. It showed that the diagnostic excels typically at the designated region at the separatrix and the near SOL. Here, perturbations of electron temperature and density can be measured in microsecond times scales.
Such high resolution measurements are shown during regime transitions, proving that during I-phase bursts the plasma profiles flatten which confirms previous findings that I-phase bursts are similar to ELM-like events. Furthermore, it is shown that the high spatiotemporal resolution of the measurements allows radial localization of fast oscillating modes. By means of conditionally averaging, the impact of a 50 kHz mode in H-mode as well as the impact of the weakly coherent mode in I-mode is shown. Not least, it is demonstrated that direct measurements of propagation velocities of filaments are possible during L- and H-mode. In compliance to literature, measured radial velocities of inter-ELM filaments are determined to 340 m/s, whereas filaments during ELMs are much faster with 1.4 km/s.

8. Summary and conclusion

The lifetime of first wall materials in nuclear fusion devices may be limited by high power loads. Coming from the confined region of the plasma, where the magnetic field lines are closed within the vacuum chamber, particles and power cross the last closed magnetic flux surface and enter the so-called scrape-off layer (SOL), where the field lines touch the wall. From here, particles and power are either transported parallel to the magnetic field lines to the divertor or directly reach the plasma facing components by turbulence driven transport perpendicular to the magnetic flux surfaces. Besides the steady state power flux, in particular intermittent phenomena like plasma instabilities, edge-localized modes (ELMs) or filamentary turbulence yield a significant contribution to the overall load of plasma facing components.
To gain a better understanding of these steady-state as well as fast transport processes, a thermal helium beam has been implemented as plasma edge diagnostic at ASDEX Upgrade (AUG) within this thesis. It provides simultaneous measurements of the electron density n_e and electron temperature T_e. Due to the achieved high spatial and temporal resolution of this diagnostic, it is not only capable of resolving ELMs with a duration of milliseconds. Also ELM and inter-ELM filaments with a lifetime on the order of 10 µs, velocities of up to several km/s and a typical structure size of 5–10 mm can be investigated.

For thermal helium beam spectroscopy, neutral helium is locally injected into the plasma. The helium is mainly excited by collisions with plasma electrons, leading to spontaneous emission of photons. The intensity ratio from lines of the same spin species are used for electron density reconstruction, whereas spin-mixed ratios are sensitive to electron temperature changes. The reconstruction of n_e and T_e from measured ratios is done with a collisional radiative model (CRM). It takes all relevant interactions between plasma and neutral helium into account in order to predict the n_e and T_e dependent population density of helium.

In order to perform active line ratio spectroscopy on helium at AUG, a set of new hardware components was developed within this thesis. They comprise a piezo valve based system for local helium injection, a dedicated optical head for light collection as well as a polychromator system for the simultaneous acquisition of four helium lines.
The valve system is placed in the vacuum chamber close to the plasma periphery. It uses a 400 µm thin capillary to create a collimated thermal He beam with a half opening angle of 20°. This local gas injection offers, in combination with properly aligned lines of sight, a high spatial resolution of the measurement. The fast responding piezo element and the short capillary enable sharply defined gas pulses down to 10 ms, with a creation time of the gas cloud of 0.2 ms. Interrupting longer pulses by short beam-off times enables background subtraction

from the active signal. Tuned by the filling pressure of the valve, precise adjustable gas fluxes are accessible from 10^{18} particles/s up to 10^{23} particles/s. This makes the piezo system an excellent device to provide gas injection for fueling and diagnostic applications.
For spectroscopic measurements, light is collected by a dedicated two-lens optical head. With lines of sight aligned in parallel to the magnetic field lines at the observation region, a spatial resolution of up to 3 mm is achieved. 52 lines of sight cover not only a radial, but also a poloidal range of 8 cm. This enables the measurement of highly resolved radial profiles, the determination of radial and poloidal propagation velocities and furthermore the combination of measured n_e and T_e values with 2-D images measured by the gas-puff imaging system.
The developed polychromator system is placed in an optics laboratory and connected to the optical head by fibers. It provides 32 channels, the signal of each is split into four spectral components by dichroic mirrors. The 587.6 nm, 667.8 nm, 706.5 nm and 728.1 nm helium lines are detected by photomultiplier arrays after they were filtered by small band interference filters. The achieved high signal level allows a data acquisition rate of 900 kHz. Furthermore it is shown within this thesis that the small amount of necessary diagnostic gas for line ratio spectroscopy on helium does not lead to a measurable disturbance of the plasma.

In pioneering experiments, using a spectrometer setup, the line resolved emission intensities of seven He I lines were measured for different plasma scenarios. This allowed to test which line ratio combinations are best suitable for diagnostic purpose in the plasma edge region of AUG as the suitability of specific line combinations depends on the investigated n_e and T_e ranges. Calculated from seven measured lines, radial profiles of 21 different ratios enabled the comparison and validation of different CRMs and their underlying processes and assumptions. The resulting n_e and T_e profiles were compared to other available diagnostics at AUG.
It is shown that the state of art CRMs are not able to describe all measured lines in a consistent way and that the calculated temperature and density profiles strongly depend on the chosen ratio. Especially a better treatment of highly excited Rydberg states might be necessary to achieve more consistent results. The gained information and experimental dataset constitutes an excellent basis for the ongoing further development of CRMs.
Consistently within the existing CRMs and in addition to the established 667/728 line ratio, especially the 504/667 and the 501/504 (s/s) ratios are best suitable for electron density evaluation with an excellent agreement to density profiles from the lithium beam diagnostic at AUG. For the electron temperature, the 501/587 (s/t) ratio can replace the 728/706 (s/t) ratio, although a discrepancy between the CRMs regarding the Rydberg states was found. Nevertheless, the current ADAS model for these lines leads to self-consistent results which are usable for diagnostic application.

As the outcome of the comprehensive hardware development within this thesis, selected examples demonstrated the powerful diagnostic capabilities of the new thermal helium beam at AUG. It is shown that in agreement to predictions, the accessible measurement range typically lies in the separatrix and the near SOL regions. It is given by the radial emission distribution of the injected helium, limited by a weak excitation rate in the far SOL and a high ionization rate of

neutral helium in the confined region. In the region where the diagnostic excels, perturbations of electron temperature and density can be measured on microsecond times scales.
Such high resolution measurements were shown for selected examples during regime transitions. The measurement of high spatiotemporally resolved plasma profiles in n_e and T_e show that during I-phase bursts the profiles flatten, which confirms previous findings that I-phase bursts are similar to ELM-like events. Furthermore, it is shown that fast oscillating modes can be radially localized with the new diagnostic. As an example for this, the impact on n_e and T_e of a 50 kHz mode in H-mode as well as the impact of the weakly coherent mode in I-mode is shown by means of conditional averaging. Finally, it is demonstrated that direct measurements of radial propagation velocities of turbulent filaments during L- and H-mode lead to inter-ELM filament velocities of 340 m/s, whereas ELM filaments are much faster with 1.4 km/s.

Outlook

Future physical studies will focus mainly on the aforementioned scenarios which will comprise the following: The helium beam diagnostic can be used to investigate the near SOL temperature fall-of length λ_{T_e}. It reflects the ratio of transport parallel and perpendicular to the flux surfaces and is a key parameter of power exhaust, depending on discharge parameters as the divertor configuration, the gas puffing level and the heating power. In the far SOL, the influence of the sheath [Sta00, p. 61 ff.] on T_e can be analyzed, the high temporal resolution provides ELM resolved data. This allows the investigation of:

- Connection between λ_{T_e}, λ_{n_e} and $\lambda_{q_\parallel}$ in the conduction limited high recycling regime as described in [Sta00, p. 159] to be $\frac{1}{\lambda_{q_\parallel}} = \frac{1}{\lambda_{n_e}} + \frac{1}{\lambda_{T_e}}$ and comparison to the results of Sun et al. [Sun15] and divertor infrared measurements.
- Behavior of SOL n_e and T_e profiles during the ELM cycle.
- Perpendicular transport coefficient for different SOL conditions.

As shown in this thesis, the helium beam diagnostic is capable of measuring propagation velocities of plasma perturbations in a broad radial region. The importance of blobs, i.e. filamentary turbulence transport perpendicular to the flux surfaces, is known concerning the power load onto the first wall. However, the point of origin as well as the propagation properties of filaments are still not fully understood [Fuc14, Man15b]. A more detailed characterization of inter-ELM fluctuations in combination with further simulations may help to understand their origin and importance. Therefore, helium beam measurements will be combined with gas-puff imaging and the retarding field analyzer. Measured quantities as size, poloidal velocity and direction of propagation, ion and electron temperature, electron density, plasma potential, ion saturation current and the Mach number of the parallel plasma flow velocity will be combined. The underlying instabilities of inter-ELM high-frequency fluctuations can thus be characterized, focusing on the following points:

- Determine the radial position of the origin of filament formation.

- Characterize SOL instabilities by frequency spectra and electron density/ temperature cross-phase measurements, estimate relative fluctuation amplitudes in density and temperature.
- Estimate the radial and poloidal propagation velocities of plasma filaments as well as their size.

The presented measurements during I-mode are intended to be continued. The helium beam can be used together with correlation reflectometry and correlation electron cyclotron emission to measure both, electron temperature and density as well as a possible phase delay between them. This might bring insight to the decoupling of particle and heat transport in I-mode. Furthermore, the collisionality dependence of I-mode turbulence bursts should be investigated in order to identify whether they play an important role in the avoidance of the density pedestal formation in I-mode. Amplitudes, occurrence rates, and kurtosis of I-mode bursts should be addressed. Thus, important information will be gained to rate the assumption that the bursts are intrinsically linked to the weakly coherent mode.

The performance of the presented gas injection system qualifies the valve to be used for impurity transport studies, in this case the exhaust of helium. Helium exhaust is a critical requirement of fusion devices as without effective exhaust, no fusion reactor can run continuously. A measure for the efficiency of helium exhaust is the helium confinement time. After dedicated helium injection by the piezo valve the confinement time can be extracted from He-I and He-II line intensities using the new polychromator system. This information is combined with plasma density measurements and absolute helium density measurements from charge-exchange recombination spectroscopy.

Bibliography

[Ada10] J. Adamek, J. Horacek, H. Müller, et al. Ball-Pen Probe Measurements in L-Mode and H-Mode on ASDEX Upgrade. *Contributions to Plasma Physics*, 50(9):854–859, 2010. URL http://dx.doi.org/10.1002/ctpp.201010145.

[Ago10] M. Agostini, P. Scarin, R. Cavazzana, et al. Optical measurements for turbulence characterization in RFX-mod edge. *Review of Scientific Instruments*, 81:10D715, 2010. URL http://dx.doi.org/10.1063/1.3478679.

[Ago15] M. Agostini, P. Scarin, R. Cavazzana, et al. Fast Thermal Helium Beam diagnostic for measurements of edge electron profiles and fluctuations. *Review of Scientific Instruments*, 86:123513, 2015. URL http://dx.doi.org/10.1063/1.4939003.

[Ahn06] J.-W. Ahn, D. Craig, G. Fiksel, et al. Development of fast helium beam emission spectroscopy on MST. *Review of Scientific Instruments*, 77:10F114, 2006. URL http://dx.doi.org/10.1063/1.2236279.

[Ath14] Athina Kappatou. *Investigations of helium transport in ASDEX Upgrade plasmas with charge exchange recombination spectroscopy*. Dissertation, Technische Universiteit Eindhoven, 2014.

[Aym02] R. Aymar, P. Barabaschi, and Y. Shimomura. The ITER design. *Plasma Physics and Controlled Fusion*, 44(5):304, 2002. URL http://dx.doi.org/10.1088/0741-3335/44/5/304.

[Bar16] T. Barbui, M. Krychowiak, R. König, et al. Feasibility of line-ratio spectroscopy on helium and neon as edge diagnostic tool for Wendelstein 7-X. *Review of Scientific Instruments*, 87(11):11E554, 2016. URL http://dx.doi.org/10.1063/1.4962989.

[Bat84] S. C. Bates and K. H. Burrell. Fast gas injection system for plasma physics experiments. *Review of Scientific Instruments*, 55(6):934–939, 1984. URL http://dx.doi.org/10.1063/1.1137845.

[Beh08] K. Behler, H. Blank, H. Eixenberger, et al. Real-time diagnostics at ASDEX Upgrade—Architecture and operation. *Fusion Engineering and Design*, 83(2–3):304–311, 2008. URL http://dx.doi.org/http://dx.doi.org/10.1016/j.fusengdes.2008.01.015.

[Beh10] K. Behler, H. Blank, A. Buhler, et al. Real-time standard diagnostic for ASDEX Upgrade. *Fusion Engineering and Design*, 85(3–4):313–320, 2010. URL http://dx.doi.org/http://dx.doi.org/10.1016/j.fusengdes.2010.03.001.

[Beh12] K. Behler, H. Blank, H. Eixenberger, et al. Deployment and future prospects of high performance diagnostics featuring serial I/O (SIO) data acquisition (DAQ) at ASDEX Upgrade. *Fusion Engineering and Design*, 87(12):2145–2151, 2012. URL http://dx.doi.org/http://dx.doi.org/10.1016/j.fusengdes.2012.09.020.

[Bir14] G. Birkenmeier, F. M. Laggner, M. Willensdorfer, et al. Magnetic field dependence of the blob dynamics in the edge of ASDEX upgrade L-mode plasmas. *Plasma Physics and Controlled Fusion*, 56(7):075019, 2014. URL http://dx.doi.org/10.1088/0741-3335/56/7/075019.

[Boi01] R. F. Boivin, J. L. Kline, and E. E. Scime. Electron temperature measurement by a helium line intensity ratio method in helicon plasmas. *Physics of Plasmas*, 8:5303–5314, 2001. URL http://dx.doi.org/10.1063/1.1418020.

[Bot87] H. Bottollier-Curtet and G. Ichtchenko. Microwave reflectometry with the extraordinary mode on tokamaks: Determination of the electron density profile of Petula-B. *Review of Scientific Instruments*, 58(4):539–546, 1987. URL http://dx.doi.org/10.1063/1.1139266.

[Bra84] A. Brazuk, H. Winter, D. Dijkkamp, et al. Absolute emission cross sections for detection of plasma impurity ions with active neutral lithium beam diagnostics. *Physics Letters A*, 101(3):139–141, 1984. URL http://dx.doi.org/https://doi.org/10.1016/0375-9601(84)90509-7.

[Bri98] M. Brix. *Messung von Elektronentemperatur und -dichte mittels Heliumstrahldiagnostik im Randschichtplasma eines Tokamaks.* Dissertation, Ruhr-Universität Bochum, 1998.

[Bro93] B. Brosda. *Modellierung von Helium-Atomstrahlen und ihr Einsatz zur Plasmadiagnostik der Tokamakrandschicht.* Dissertation, Ruhr-Universität Bochum, 1993.

[Car99] L. Carraro, G. D. Pol, M. E. Puiatti, et al. Edge temperature and density measurements with a thermal helium beam in the RFX reversed field pinch. *Plasma Physics and Controlled Fusion*, 42:1–14, 1999. URL http://dx.doi.org/10.1088/0741-3335/42/1/301.

[Cav16] M. Cavedon. *The role of the radial electric field in the development of the edge transport barrier in the ASDEX Upgrade tokamak.* Dissertation, Technical University Munich, 2016.

[Cav17a] M. Cavedon, T. Pütterich, E. Viezzer, et al. A fast edge charge exchange recombination spectroscopy system at the ASDEX Upgrade tokamak. *Review of Scientific Instruments*, 88(4):43103, 2017. URL http://dx.doi.org/10.1063/1.4979801.

[Cav17b] M. Cavedon, T. Pütterich, E. Viezzer, et al. Interplay between turbulence, neoclassical and zonal flows during the transition from low to high confinement mode at ASDEX Upgrade. *Nuclear Fusion*, 57(1):014002, 2017. URL http://dx.doi.org/10.1088/0029-5515/57/1/014002.

[Chu13] R. M. Churchill, C. Theiler, B. Lipschultz, et al. Development of the gas puff charge exchange recombination spectroscopy (GP-CXRS) technique for ion measurements in the plasma edge. *Review of Scientific Instruments*, 84(9):93505, 2013. URL http://dx.doi.org/10.1063/1.4821084.

[Col03] R. J. Colchin, D. L. Hillis, R. Maingi, et al. The Filterscope. *Review of Scientific Instruments*, 74(3):2068–2070, 2003. URL http://dx.doi.org/10.1063/1.1537038.

[Con00] J. W. Connor and H. R. Wilson. A review of theories of the L-H transition. *Plasma Physics and Controlled Fusion*, 42(1):R1–R74, 2000. URL http://dx.doi.org/10.1088/0741-3335/42/1/201.

[Coo58] T. Coor, S. Cunningham, R. Ellis, et al. Experiments on the Ohmic Heating and Confinement of Plasma in a Stellarator. *Physics of Fluids*, 1(5):411, 1958. URL http://dx.doi.org/10.1063/1.1724358.

[Coo96] D. Cooke, B. Bennett, and E. Farnum. Optical absorption of neutron-irradiated silica fibers. *Journal of Nuclear Materials*, 232(2-3):214–218, 1996. URL http://dx.doi.org/10.1016/S0022-3115(96)00405-9.

[Czi13] I. Cziegler, P. H. Diamond, N. Fedorczak, et al. Fluctuating zonal flows in the I-mode regime in Alcator C-Mod. *Physics of Plasmas*, 20(5):55904, 2013. URL http://dx.doi.org/10.1063/1.4803914.

[Dav97] S. Davies, P. Morgan, Y. Ul'Haq, et al. Parallel electron temperature and density gradients measured in the JET MkI divertor using thermal helium beams. *Journal of Nuclear Materials*, 241-243:426–432, 1997. URL http://dx.doi.org/10.1016/S0022-3115(97)80076-1.

[Dem08] W. Demtröder. *Experimentalphysik 1: Mechanik und Wärme*. Springer, Berlin, Heidelberg, New York, 4 edition, 2008. URL https://www.springer.com/de/book/9783662464151.

[Dem09] W. Demtröder. *Experimentalphysik 4: Kern-, Teilchen- und Astrophysik*. Springer, Berlin, Heidelberg, New York, 3 edition, 2009. URL https://books.google.de/books?id=juNemAEACAAJ.

[Dib17] M. Dibon, G. Pautasso, M. Griener, et al. Piezo-driven valve for disruption mitigation studies in tokamaks. *Fusion Engineering and Design*, 2017. URL http://dx.doi.org/http://dx.doi.org/10.1016/j.fusengdes.2017.04.080.

[Dun10] D. Dunai, S. Zoletnik, J. Sarközi, et al. Avalanche photodiode based detector for beam emission spectroscopy. *Review of Scientific Instruments*, 81(10), 2010. URL http://dx.doi.org/10.1063/1.3488458.

[Edi99] I. P. B. Editors, I. P. E. G. C. an Co-Chairs, I. J. C. T. Unit, et al. Chapter 1: Overview and summary. *Nuclear Fusion*, 39(12):2137–2174, 1999. URL http://dx.doi.org/10.1088/0029-5515/39/12/301.

[Fai17] M. Faitsch, B. Sieglin, T. Eich, et al. Divertor heat load in ASDEX Upgrade L-mode in presence of external magnetic perturbation. *Plasma Physics and Controlled Fusion*, 59(9):095006, 2017. URL http://dx.doi.org/10.1088/1361-6587/aa75e7.

[Fed14] G. Federici, R. Kemp, D. Ward, et al. Overview of EU DEMO design and R&D activities. *Fusion Engineering and Design*, 89(7):882–889, 2014. URL http://dx.doi.org/https://doi.org/10.1016/j.fusengdes.2014.01.070.

[Fis08] R. Fischer, E. Wolfrum, and J. Schweinzer. Probabilistic lithium beam data analysis. *Plasma Physics and Controlled Fusion*, 50(8):085009, 2008. URL http://dx.doi.org/10.1088/0741-3335/50/8/085009.

[Fuc14] G. Fuchert, G. Birkenmeier, D. Carralero, et al. Blob properties in L- and H-mode from gas-puff imaging in ASDEX upgrade. *Plasma Physics and Controlled Fusion*, 56(12):125001, 2014. URL http://dx.doi.org/10.1088/0741-3335/56/12/125001.

[Fün63] E. Fünfer, B. Kronast, and H.-J. Kunze. Experimental results on light scattering by a θ-pinch plasma using a ruby laser. *Physics Letters*, 5(2):125–127, 1963. URL http://dx.doi.org/http://dx.doi.org/10.1016/S0375-9601(63)91940-6.

[Gar06] O. E. Garcia, N. H. Bian, and W. Fundamenski. Radial interchange motions of plasma filaments. *Physics of Plasmas*, 13(8):82309, 2006. URL http://dx.doi.org/10.1063/1.2336422.

[Gat70] J. R. Gat and I. Carmi. Evolution of the isotopic composition of atmospheric waters in the Mediterranean Sea area. *Journal of Geophysical Research*, 75(15):3039–3048, 1970. URL http://dx.doi.org/10.1029/JC075i015p03039.

[Gri17] M. Griener, O. Schmitz, K. Bald, et al. Fast piezoelectric valve offering controlled gas injection in magnetically confined fusion plasmas for diagnostic and fuelling purposes. *Review of Scientific Instruments*, 88(3):33509, 2017. URL http://dx.doi.org/10.1063/1.4978629.

[Gri18a] M. Griener, J. M. Muñoz Burgos, M. Cavedon, et al. Qualification and implementation of line ratio spectroscopy on helium as plasma edge diagnostic at ASDEX Upgrade. *Plasma Physics and Controlled Fusion*, 60(2):025008, 2018. URL http://dx.doi.org/10.1088/1361-6587/aa97e8.

[Gri18b] M. Griener, E. Wolfrum, M. Cavedon, et al. Helium line ratio spectroscopy for high spatiotemporal resolution plasma edge profile measurements at ASDEX Upgrade (invited). *Review of Scientific Instruments*, 89(10):10D102, 2018. URL http://dx.doi.org/10.1063/1.5034446.

[Hap15] T. Happel, A. B. Navarro, G. D. Conway, et al. Core turbulence behavior moving from ion-temperature-gradient regime towards trapped-electron-mode regime in the ASDEX Upgrade tokamak and comparison with gyrokinetic simulation. *Physics of Plasmas*, 22(3):32503, 2015. URL http://dx.doi.org/10.1063/1.4914153.

[Hap16] T. Happel, P. Manz, F. Ryter, et al. Turbulence intermittency linked to the weakly coherent mode in ASDEX Upgrade I-mode plasmas. *Nuclear Fusion*, 56(6):064004, 2016. URL http://dx.doi.org/10.1088/0029-5515/56/6/064004.

[Hap17] T. Happel, P. Manz, F. Ryter, et al. The I-mode confinement regime at ASDEX Upgrade: global properties and characterization of strongly intermittent density fluctuations. *Plasma Physics and Controlled Fusion*, 59(1):014004, 2017. URL http://dx.doi.org/10.1088/0741-3335/59/1/014004.

[Har97] H. J. Hartfuss, T. Geist, and M. Hirsch. Heterodyne methods in millimetre wave plasma diagnostics with applications to ECE, interferometry and reflectometry. *Plasma Physics and Controlled Fusion*, 39(11):1693–1769, 1997. URL http://dx.doi.org/10.1088/0741-3335/39/11/001.

[Her02] A. Herrmann. Overview on stationary and transient divertor heat loads. *Plasma Physics and Controlled Fusion*, 44(6):883, 2002. URL http://stacks.iop.org/0741-3335/44/i=6/a=318.

[Hor10] J. Horacek, J. Adamek, H. Müller, et al. Interpretation of fast measurements of plasma potential, temperature and density in SOL of ASDEX Upgrade. *Nuclear Fusion*, 50(10):105001, 2010. URL http://dx.doi.org/10.1088/0029-5515/50/10/105001.

[Hud65] R. H. Huddlestone and S. L. Leonard. *Plasma diagnostic techniques*. Pure and applied physics. Academic Press, 1965. URL https://books.google.de/books?id=Eb08AAAAIAAJ.

[Hug62] T. P. Hughes. A New Method for the Determination of Plasma Electron Temperature and Density from Thomson Scattering of an Optical Maser Beam. *Nature*, 194(4825):268–269, 1962. URL http://dx.doi.org/10.1038/194268b0.

[Hut05] I. H. Hutchinson. *Principles of Plasma Diagnostics*. Cambridge University Press, 2005. URL https://books.google.de/books?id=pUUZKLR0ORIC.

[IEA17] IEA International Energy Agency. *Key World Energy Statistics 2017*. OECD Publishing, Paris, 2017. URL http://dx.doi.org/10.1787/9789264039537-en.

[Igu85] H. Iguchi, K. Kadota, K. Takasugi, et al. Space and time-resolved measurements of plasma density by a lithium neutral beam probe in NBT-1M. *Review of Scientific Instruments*, 56(5), 1985.

[Isa10] Isabella Milch (Red.). *50 Jahre Max-Planck-Institut für Plasmaphysik : Forschung für die Energie der Zukunft*. Max-Planck-Institut für Plasmaphysik (IPP), Garching/ Greifswald, 2010. URL https://www.ipp.mpg.de/ippcms/de/pr/publikationen/buecher/festschrift.

[Joh98] R. W. Johnson. *Handbook of Fluid Dynamics*. Handbook Series for Mechanical Engineering. Taylor & Francis, 1998. URL https://books.google.de/books?id=J5yXxWGLLfsC.

[Jon16] O. M. Jones, O. Meyer, H. Xu, et al. Development of a thermal helium beam emission diagnostic for WEST. In *43rd EPS Conference Proceedings*, pages 1–4. 2016.

[Kaj06] S. Kajita, N. Ohno, S. Takamura, et al. Comparison of He I line intensity ratio method and electrostatic probe for electron density and temperature measurements in NAGDIS-II. *Physics of Plasmas*, 13:1–9, 2006. URL http://dx.doi.org/10.1063/1.2164461.

[Kal01] A. Kallenbach, A. Carlson, G. Pautasso, et al. Electric currents in the scrape-off layer in ASDEX Upgrade. *Journal of Nuclear Materials*, 290-293(Supplement C):639–643, 2001. URL http://dx.doi.org/https://doi.org/10.1016/S0022-3115(00)00445-1.

[Kim03] E.-j. Kim and P. H. Diamond. Zonal Flows and Transient Dynamics of the L-H Transition. *Phys. Rev. Lett.*, 90(18):185006, 2003. URL http://dx.doi.org/10.1103/PhysRevLett.90.185006.

[Kir14] A. Kirk, D. Dunai, M. Dunne, et al. Recent progress in understanding the processes underlying the triggering of and energy loss associated with type I ELMs. *Nuclear Fusion*, 54(11):114012, 2014. URL http://dx.doi.org/10.1088/0029-5515/54/11/114012.

[Kra15] A. Kramida, Y. Ralchenko, and J. Reader. NIST Atomic Spectra Database (ver. 5.3). Online, 2016, September 12, National Institute of Standards and Technology, Gaithersburg, MD., 2015. URL http://physics.nist.gov/asd.

[Kru06] U. Kruezi. *Entwicklung einer Heliumstrahldiagnostik zur Messung der Elektronendichte und -temperatur mit hoher räumlicher und zeitlicher Auflösung*. Dissertation, Heinrich-Heine-Universität Düsseldorf, 2006.

[Kru12] U. Kruezi, H. Stoschus, B. Schweer, et al. Supersonic helium beam diagnostic for fluctuation measurements of electron temperature and density at the Tokamak TEXTOR. *Review of Scientific Instruments*, 83(6):065107, 2012. URL http://dx.doi.org/10.1063/1.4707150.

[Kry16] M. Krychowiak, A. Adnan, A. Alonso, et al. Overview of diagnostic performance and results for the first operation phase in Wendelstein 7-X. *Review of Scientific Instruments*, 87(11):11D304, 2016. URL http://dx.doi.org/10.1063/1.4964376.

[Kur11] B. Kurzan and H. D. Murmann. Edge and core Thomson scattering systems and their calibration on the ASDEX Upgrade tokamak. *Review of Scientific Instruments*, 82(10), 2011. URL http://dx.doi.org/http://dx.doi.org/10.1063/1.3643771.

[Las12] S. I. Lashkul, a. B. Altukhov, V. V. D'yachenko, et al. Use of additional helium puffing for the diagnostics of plasma parameters at the FT-2 tokamak. *Plasma Physics Reports*, 38(11):851–862, 2012. URL http://dx.doi.org/10.1134/S1063780X12110062.

[Law57] J. D. Lawson. Some Criteria for a Power Producing Thermonuclear Reactor. *Proceedings of the Physical Society. Section B*, 70(1):6–10, 1957. URL http://dx.doi.org/10.1088/0370-1301/70/1/303.

[Lor11] J. Loreau, S. Ryabchenko, A. Dalgarno, et al. Isotope effect in charge-transfer collisions of H with He+. *Phys. Rev. A*, 84(5):52720, 2011. URL http://dx.doi.org/10.1103/PhysRevA.84.052720.

[Ma12] S. Ma, J. Howard, B. D. Blackwell, et al. Measurements of electron density and temperature in the H-1 heliac plasma by helium line intensity ratios. *Review of Scientific Instruments*, 83(3):033102, 2012. URL http://dx.doi.org/10.1063/1.3692756.

[Mal89] D. Malacara. *Physical Optics and Light Measurements*. Methods in Experimental Physics. Elsevier Science, 1989. URL https://books.google.de/books?id=bQaUi07ZXOAC.

[Man15a] P. Manz, P. Lauber, V. Nikolaeva, et al. Geodesic oscillations and the weakly coherent mode in the I-mode of ASDEX Upgrade. *Nuclear Fusion*, 55(8):083004, 2015. URL http://dx.doi.org/10.1088/0029-5515/55/8/083004.

[Man15b] P. Manz, T. T. Ribeiro, B. D. Scott, et al. Origin and turbulence spreading of plasma blobs. *Physics of Plasmas*, 22(2), 2015. URL http://dx.doi.org/10.1063/1.4908272.

[Mat94] G. F. Matthews. Tokamak plasma diagnosis by electrical probes. *Plasma Physics and Controlled Fusion*, 36(10):1595–1628, 1994. URL http://dx.doi.org/10.1088/0741-3335/36/10/002.

[MB09] J. M. Muñoz Burgos, S. D. Loch, C. P. Ballance, et al. Electron-impact excitation of Ar 2+. *Astronomy and Astrophysics*, 500(3):1253–1261, 2009. URL http://dx.doi.org/10.1051/0004-6361/200911743.

[MB12] J. M. Muñoz Burgos, O. Schmitz, S. D. Loch, et al. Hybrid time dependent/independent solution for the He I line ratio temperature and density diagnostic for a thermal helium beam with applications in the scrape-off layer-edge regions in tokamaks. *Physics of Plasmas*, 19(1):012501, 2012. URL http://dx.doi.org/10.1063/1.3672230.

[MB16a] J. M. Muñoz Burgos, M. Agostini, P. Scarin, et al. Evaluation of thermal helium beam and line-ratio fast diagnostic on the National Spherical Torus Experiment-Upgrade. *Physics of Plasmas*, 23(5):053302, 2016. URL http://dx.doi.org/10.1063/1.4948554.

[MB16b] J. M. Muñoz Burgos, T. Barbui, O. Schmitz, et al. Time-dependent analysis of visible helium line-ratios for electron temperature and density diagnostic using synthetic simulations on NSTX-U. *Review of Scientific Instruments*, 87(11):11E502, 2016. URL http://dx.doi.org/10.1063/1.4955286.

[MS26] H. M. Mott-Smith and I. Langmuir. The theory of collectors in gaseous discharges. *Physical Review*, 28(4):727–763, 1926. URL http://dx.doi.org/10.1103/PhysRev.28.727.

[Myr06] J. R. Myra, D. A. Russell, and D. A. D'Ippolito. Collisionality and magnetic geometry effects on tokamak edge turbulent transport. I. A two-region model with application to blobs. *Physics of Plasmas*, 13(11):112502, 2006. URL http://dx.doi.org/10.1063/1.2364858.

[Nam06] S. Namba, D. Andruczyk, K. Takiyama, et al. Development of supersonic metastable helium pulsed beam source for plasma diagnostics. *Japanese Journal of Applied Physics, Part 1: Regular Papers and Short Notes and Review Papers*, 45:8099–8103, 2006. URL http://dx.doi.org/10.1143/JJAP.45.8099.

[Par11] P. Parks and W. Wu. Limitations of extended gas delivery tubes used for fuelling mitigated plasma disruptions, and a unique injection concept for prompt gas delivery. *Nuclear Fusion*, 51, 2011. URL http://dx.doi.org/10.1088/0029-5515/51/7/073014.

[Pau11] G. Pautasso, L. Giannone, O. Gruber, et al. The halo current in ASDEX Upgrade. *Nuclear Fusion*, 51(4):043010, 2011. URL http://dx.doi.org/10.1088/0029-5515/51/4/043010.

[Pit97] C. S. Pitcher and P. C. Stangeby. Experimental divertor physics. *Plasma Physics and Controlled Fusion*, 39(6):779–930, 1997. URL http://dx.doi.org/10.1088/0741-3335/39/6/001.

[Pos92] A. Pospieszczyk, G. Chevalier, Y. Hirooka, et al. Helium line emission measurements in PISCES-B as a tool for Te-profile determinations in tokamak boundary plasmas. *Nuclear Inst. and Methods in Physics Research, B*, 72(2):207–223, 1992. URL http://dx.doi.org/10.1016/0168-583X(92)95236-K.

[Rat12] S. K. Rathgeber, L. Barrera, T. Eich, et al. Estimation of edge electron temperature profiles via forward modelling of the electron cyclotron radiation transport at ASDEX Upgrade. *Plasma Physics and Controlled Fusion*, 55(2):025004, 2012. URL http://dx.doi.org/10.1088/0741-3335/55/2/025004.

[Ray16] H. B. Ray, T. M. Biewer, D. T. Fehling, et al. Spectral survey of helium lines in a linear plasma device for use in HELIOS imaging. *Review of Scientific Instruments*, 87(11):11E711, 2016. URL http://dx.doi.org/10.1063/1.4959796.

[Roh07] V. Rohde, R. Dux, A. Kallenbach, et al. Wall conditioning in ASDEX Upgrade. *Journal of Nuclear Materials*, 363–365:1369–1374, 2007. URL http://dx.doi.org/http://dx.doi.org/10.1016/j.jnucmat.2007.01.200.

[Ryt17] F. Ryter, R. Fischer, J. Fuchs, et al. I-mode studies at ASDEX Upgrade: L-I and I-H transitions, pedestal and confinement properties. *Nuclear Fusion*, 57(1):016004, 2017. URL http://dx.doi.org/10.1088/0029-5515/57/1/016004.

[Sch92a] B. Schweer, G. Mank, and A. Pospieszczyk. Electron temperature and electron density profiles measured with a thermal He-beam in the plasma boundary of TEXTOR. *Journal of nuclear ...*, 198:174–178, 1992. URL http://www.sciencedirect.com/science/article/pii/S0022311506800267.

[Sch92b] J. Schweinzer, E. Wolfrum, F. Aumayr, et al. Reconstruction of plasma edge density profiles from Li I (2s-2p) emission profiles. *Plasma Physics and Controlled Fusion*, 34(7):1173–1183, 1992. URL http://dx.doi.org/10.1088/0741-3335/34/7/001.

[Sch08a] A. Schmid, A. Herrmann, and H. W. Müller. Experimental observation of the radial propagation of ELM induced filaments on ASDEX Upgrade. *Plasma Physics and Controlled Fusion*, 50(4):045007, 2008. URL http://dx.doi.org/10.1088/0741-3335/50/4/045007.

[Sch08b] O. Schmitz, I. L. Beigman, L. A. Vainshtein, et al. Status of electron temperature and density measurement with beam emission spectroscopy on thermal helium at TEXTOR. *Plasma Physics and Controlled Fusion*, 50(11):115004, 2008. URL http://dx.doi.org/10.1088/0741-3335/50/11/115004.

[Sha53] A. H. Shapiro. *The Dynamics and Thermodynamics of Compressible Fluid Flow*, volume I. WILEY-VCH Verlag, 1 edition, 1953. URL http://www.amazon.com/Dynamics-Thermodynamics-Compressible-Fluid-Flow/dp/0471066915/ref=pd{_}sim{_}b{_}59.

[Sie10] B. Sieglin. *Measurement of the Electron Temperature in the Scrape-Off Layer of ASDEX Upgrade by Line Integrated Helium I Emission Lines.* Diploma thesis, TUM, 2010.

[Sil96] A. Silva, M. E. Manso, L. Cupido, et al. Ultrafast broadband frequency modulation of a continuous wave reflectometry system to measure density profiles on ASDEX Upgrade. *Review of Scientific Instruments*, 67(12):4138–4145, 1996. URL http://dx.doi.org/10.1063/1.1147517.

[Sim85] F. Simonet. Measurement of electron density profile by microwave reflectometry on tokamaks. *Review of Scientific Instruments*, 56(5):664–669, 1985. URL http://dx.doi.org/10.1063/1.1138200.

[Sni96] J. Snipes, R. Granetz, M. Greenwald, et al. H mode power threshold database for ITER. *Nuclear Fusion*, 36(9):1217–1264, 1996. URL http://dx.doi.org/10.1088/0029-5515/36/9/I11.

[Sta00] P. C. Stangeby. *The Plasma Boundary of Magnetic Fusion Devices.* Series in Plasma Physics and Fluid Dynamics. Taylor & Francis, 2000. URL https://books.google.de/books?id=qOliQgAACAAJ.

[Ste16] L. Stephey, G. A. Wurden, O. Schmitz, et al. Spectroscopic imaging of limiter heat and particle fluxes and the resulting impurity sources during Wendelstein 7-X startup plasmas. *Review of Scientific Instruments*, 87(11):11D606, 2016. URL http://dx.doi.org/10.1063/1.4959274.

[Str96] U. Stroth, M. Murakami, R. Dory, et al. Energy confinement scaling from the international stellarator database. *Nuclear Fusion*, 36(8):1063–1077, 1996. URL http://dx.doi.org/10.1088/0029-5515/36/8/I11.

[Str03] B. Streibl, P. T. Lang, F. Leuterer, et al. Chapter 2: Machine Design, Fueling, and Heating in ASDEX Upgrade. *Fusion Science and Technology*, 44(3):578–592, 2003. URL http://dx.doi.org/10.13182/FST03-A400.

[Str11] U. Stroth. *Plasmaphysik: Phänomene, Grundlagen, Anwendungen.* Vieweg+Teubner Verlag, Wiesbaden, 2011. URL https://www.springer.com/de/book/9783834883261.

[Sum04] H. P. Summers. The ADAS User Manual, version 2.6, http://www.adas.ac.uk, 2004. URL http://www.adas.ac.uk.

[Sum06] H. P. Summers, W. J. Dickson, M. G. O'Mullane, et al. Ionization state, excited populations and emission of impurities in dynamic finite density plasmas: I. The generalized collisional–radiative model for light elements. *Plasma Physics and Controlled Fusion*, 48(2):263–293, 2006. URL http://dx.doi.org/10.1088/0741-3335/48/2/007.

[Sun15] H. J. Sun, E. Wolfrum, T. Eich, et al. Study of near scrape-off layer (SOL) temperature and density gradient lengths with Thomson scattering. *Plasma Physics and Controlled*

Fusion, 57(12):125011, 2015. URL http://stacks.iop.org/0741-3335/57/i=12/a=125011.

[Sun17] H. J. Sun, E. Wolfrum, B. Kurzan, et al. Study of near SOL decay lengths in ASDEX Upgrade under attached and detached divertor conditions. *Plasma Physics and Controlled Fusion*, 59(10):105010, 2017. URL http://dx.doi.org/10.1088/1361-6587/aa7777.

[Sut11] W. Suttrop, T. Eich, J. C. Fuchs, et al. First Observation of Edge Localized Modes Mitigation with Resonant and Nonresonant Magnetic Perturbations in ASDEX Upgrade. *Phys. Rev. Lett.*, 106(22):225004, 2011. URL http://dx.doi.org/10.1103/PhysRevLett.106.225004.

[Tab97] F. L. Tabarés, D. Tafalla, V. Herrero, et al. Testing of a pulsed He supersonic beam for plasma edge diagnostic in the TJ-IU torsatron. *Journal of Nuclear Materials*, 241-243:1228–1233, 1997. URL http://dx.doi.org/10.1016/S0022-3115(96)00704-0.

[Tab10] F. L. Tabarés, D. Tafalla, J. A. Ferreira, et al. Toward a full exploitation of the helium beam edge diagnostic. *Review of Scientific Instruments*, 81(10):10D708, 2010. URL http://dx.doi.org/10.1063/1.3464462.

[Ter09] J. L. Terry, S. J. Zweben, M. V. Umansky, et al. Spatial structure of scrape-off-layer filaments near the midplane and X-point regions of Alcator-C-Mod. *Journal of Nuclear Materials*, 390-391:339–342, 2009. URL http://dx.doi.org/https://doi.org/10.1016/j.jnucmat.2009.01.152.

[Unt12] E. A. Unterberg, O. Schmitz, D. H. Fehling, et al. HELIOS: a helium line-ratio spectral-monitoring diagnostic used to generate high resolution profiles near the ion cyclotron resonant heating antenna on TEXTOR. *Review of Scientific Instruments*, 83(10):10D722, 2012. URL http://dx.doi.org/10.1063/1.4739236.

[vI40] A. van Itterbeek and O. van Paemel. Measurements on the viscosity of neon, hydrogen, deuterium and helium as a function of the temperature, between room temperature and liquid hydrogen temperatures. *Physica*, 7(3):265–272, 1940. URL http://dx.doi.org/https://doi.org/10.1016/S0031-8914(40)90115-X.

[Vie12] E. Viezzer, T. Pütterich, R. Dux, et al. High-resolution charge exchange measurements at ASDEX Upgrade. *Review of Scientific Instruments*, 83(10):103501, 2012. URL http://dx.doi.org/10.1063/1.4755810.

[Wag82] F. Wagner, G. Becker, K. Behringer, et al. Regime of Improved Confinement and High Beta in Neutral-Beam-Heated Divertor Discharges of the ASDEX Tokamak. *Phys. Rev. Lett.*, 49(19):1408–1412, 1982. URL http://dx.doi.org/10.1103/PhysRevLett.49.1408.

[Wag07] F. Wagner. A quarter-century of H-mode studies. *Plasma Physics and Controlled Fusion*, 49(12B):B1–B33, 2007. URL http://dx.doi.org/10.1088/0741-3335/49/12B/S01.

[Wag14] F. Wagner. Electricity by intermittent sources: An analysis based on the German situation 2012. *The European Physical Journal Plus*, 129(2):20, 2014. URL http://dx.doi.org/10.1140/epjp/i2014-14020-8.

[Wag16] D. Wagner, J. Stober, F. Leuterer, et al. Status, Operation, and Extension of the ECRH System at ASDEX Upgrade. *Journal of Infrared, Millimeter, and Terahertz Waves*, 37(1):45–54, 2016. URL http://dx.doi.org/10.1007/s10762-015-0187-z.

[Why10] D. Whyte, A. Hubbard, J. Hughes, et al. I-mode: an H-mode energy confinement regime with L-mode particle transport in Alcator C-Mod. *Nuclear Fusion*, 50(10):105005, 2010. URL http://dx.doi.org/10.1088/0029-5515/50/10/105005.

[Wil12] M. Willensdorfer, E. Wolfrum, R. Fischer, et al. Improved chopping of a lithium beam for plasma edge diagnostic at ASDEX Upgrade. *Review of Scientific Instruments*, 83(2), 2012. URL http://dx.doi.org/10.1063/1.3682003.

[Wil14] M. Willensdorfer, G. Birkenmeier, R. Fischer, et al. Characterization of the Li-BES at ASDEX Upgrade. *Plasma Physics and Controlled Fusion*, 56(2):25008, 2014. URL http://stacks.iop.org/0741-3335/56/i=2/a=025008.

[Zoh96] H. Zohm. Edge localized modes (ELMs). *Plasma Physics and Controlled Fusion*, 38(2):105–128, 1996. URL http://dx.doi.org/10.1088/0741-3335/38/2/001.

[Zoh15a] H. Zohm. *Magnetohydrodynamic Stability of Tokamaks*. Wiley, 2015. URL https://www.wiley.com/en-ai/Magnetohydrodynamic+Stability+of+Tokamaks-p-9783527677344.

[Zoh15b] H. Zohm. Recent ASDEX Upgrade research in support of ITER and DEMO. *Nuclear Fusion*, 55(10):104010, 2015. URL http://dx.doi.org/10.1088/0029-5515/55/10/104010.

[Zwe17] S. J. Zweben, J. L. Terry, D. P. Stotler, et al. Invited Review Article: Gas puff imaging diagnostics of edge plasma turbulence in magnetic fusion devices. *Review of Scientific Instruments*, 88(4):41101, 2017. URL http://dx.doi.org/10.1063/1.4981873.

A. Appendix

A.1. Nuclear fusion in the sun vs. magnetic confinement

For fusion on earth with devices relying on magnetic confinement of plasmas, as long confinement times as well as densities as in the core of the sun are by far not possible. Therefore one aims for the D-T reaction and a temperature ten times higher than the temperature in the core of the sun to match the maximum reaction cross section. Different parameters which are characterizing fusion in the sun are summarized in comparison to magnetic confinement fusion on earth in Tab. A.1.

Table A.1.: Characterizing parameters of the sun versus thermonuclear fusion experiments with magnetic confinement on earth (cf. section 1.2 and subsection 1.2.4). As the sun is by far not homogeneous, some parameters are separated for the core and the sun in total.

	sun total / core [Dem09]		ITER [Aym02]	ASDEX Upgrade [Str03]
major radius	6.96×10^8 m	$0.25 R_\odot$	6.2 m	1.65 m
minor radius			2 m	0.5 m
plasma volume	1.3×10^{27} m^3	$1/64 V_\odot$	837 m^3	14 m^3
plasma mass	1.99×10^{30} kg	$0.5 M_\odot$	5×10^{-4} kg	3×10^{-6} kg
plasma current	–		15 MA	1.6 MA
plasma density	$\approx 5 \times 10^{29}$ m^{-3}	$\approx 1.7 \times 10^{31}$ m^{-3}	2×10^{20} m^{-3}	10^{20} m^{-3}
plasma temp.	5.77×10^3 K	1.5×10^7 K	1.5×10^8 K	10^8 K
temp. gradient	21 K/km		7.5×10^7 K/m	2×10^8 K/m
confinement time	10^7 years		3 s	<0.2 s
burn duration	10^{10} years		>400 s	<10 s
external heating	–		73 MW	>30 MW
fusion power	$L_\odot = 3.8 \times 10^{26}$ W		500 MW	–
power density	0.2 mW/kg 62 MW/m^2		1 TW/kg 0.8 MW/m^2	–
plasma species	73 %H, 25 %He		H, D, T, He	H, D, He
fusion reaction	p-p chain, (CNO)		D-T	(D-D)

A.2. Photon emission and line ratio grids

In section 3.3 the principle of line ratio spectroscopy on helium is introduced. The emission of triplet lines (left column in Fig. A.1) peaks at a temperature between 25–70 eV, whereas the emission of singlet lines (right column in Fig. A.1) continuously increases with increasing temperature. This is shown by grayscale contour plots which were calculated with a constant helium density over the total n_e and T_e range. It shows the relative emission between the lines for the given n_e and T_e range as well as the parameter region where the diagnostic is most powerful.

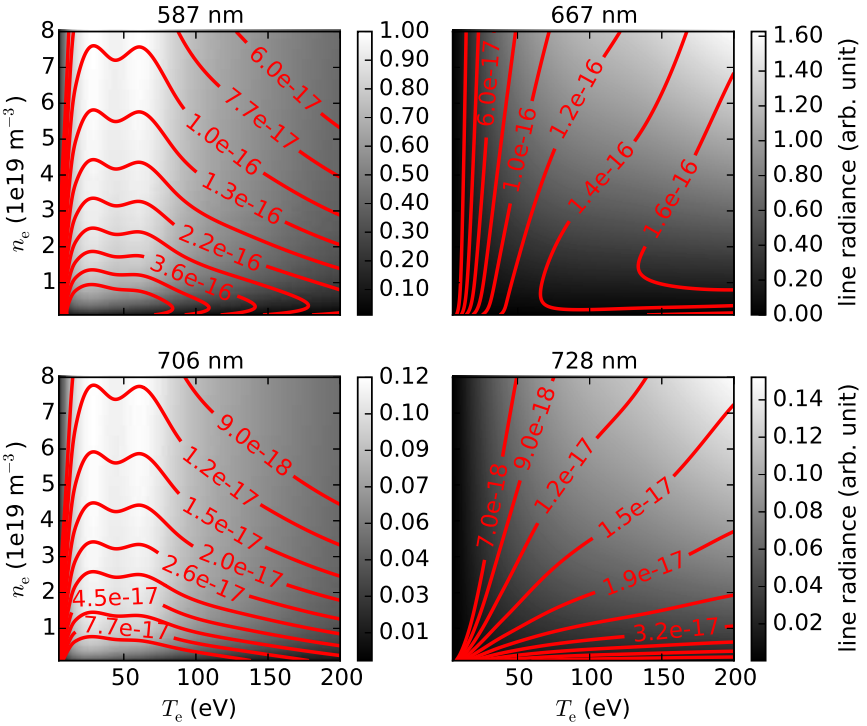

Figure A.1.: Photon emission coefficients (red contour lines in the unit m^3/s) and total photon emission (grayscale) as a function of the electron temperature and density of four different neutral helium lines.

The highest emission signal is achieved where the product of helium density and emission coefficient is highest. One the one hand, the emission of all lines is low at low temperatures. On the other hand, the neutral helium content decreases with increasing temperature and density and thus limits the application of the diagnostic at higher n_e and T_e values.
The resulting line ratios calculated from the photon emission coefficients of the different lines are shown in Fig. A.2, which demonstrates the dependence of the ratios on n_e and T_e.

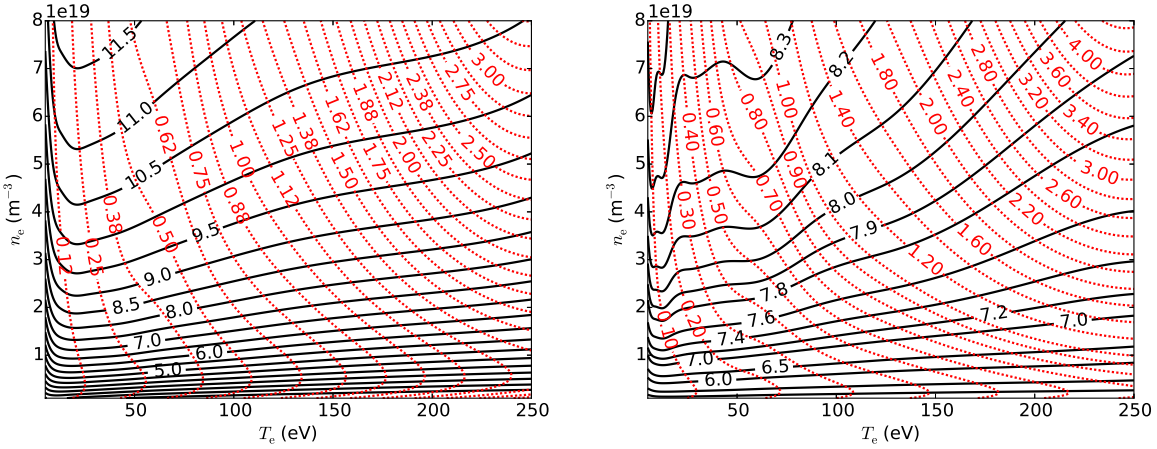

(a) T_e 728/706 (red) and n_e 667/728 (black) ratio.

(b) T_e 667/587 (red) and n_e 587/706 (black) ratio.

Figure A.2.: Electron temperature and density dependence of two sets of line ratios, the T_e dependent s/t line ratios 728/706 a) and 667/587 b) in red-dashed as well as the n_e dependent s/s line ratio 667/728 a) and t/t ratio 587/706 b) in black-solid. The data are based on the ADAS data set 'pec96#he_pju#he0.dat' [Sum04].

A.3. Gas supply system

Fig. A.3 illustrates the gas supply circuit for the piezo valve system (blue) as well as the setup for the gas flux (cf. section 4.3) and beam shape (cf. section 4.5) laboratory measurements (red). The supply system for the piezo is used in the same way for the operation at AUG. It consists of three parts. The gas bottles which are placed outside the building in a skeleton container, the gas supply board which provides the valve with the requested pressure and a pumping system. The gas pipes are galvanically separated at all connection points to the gas supply board. The whole system has been certified by DEKRA[1] regarding the plant safety as it can also be operated with explosive gases like deuterium.

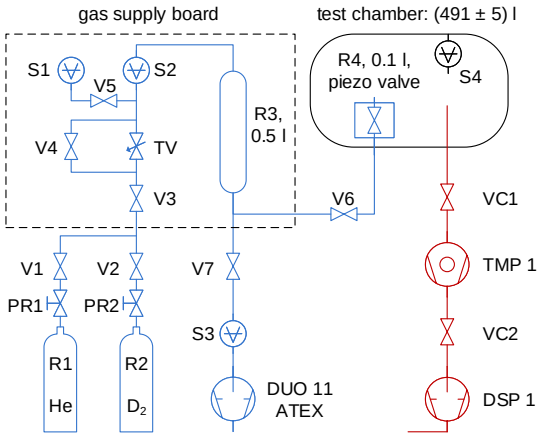

Figure A.3.: Scheme of the gas supply circuit for the piezo valve (blue, left) and vacuum chamber pumping system (red, right) used for the laboratory measurements.

The two gas bottles R1 and R2, equipped with a pressure-relief valve and pressure regulators PR1, PR2, are used to supply the valve with the working gas. They are connected to the gas supply board over the pneumatic valves V1, V2 and V3 to fill the reservoir R3. The requested pressure is adjusted automatically by the electric throttle valve TV. It is bypassed by the valve

[1] DEKRA EXAM GmbH, explosion protection / plant safety, Anton-Ditt-Bogen 1a, 80939 München

V4 to evacuate the system up to V1 and V2 for changing the gas type and ensuring leak tightness. The pressure in the system is measured by two piezoresistive pressure sensors, S1 in the range of 1–500 mbar and S2 in the range of 0.5–20 bar. V5 separates S1 from the system for $p > 500$ mbar. V6 is the safety valve at the flange to the torus and V7 connects the system to the explosion proof rotary vane pump DUO 11 ATEX[2].

To calibrate the mean gas flowrate through the piezo valve, the valve is placed in a laboratory vacuum test chamber. It is pumped with the turbomolecular pump TMP 1, which itself is connected to the rotary vane pump DSP 1. To measure the pressure rise in the chamber after gas injection with a baratron S4, the valve VC1 is closed before the gas pulse. The initial pressure in the vacuum chamber with a volume of (491 ± 5) l is around 1×10^{-7} mbar. The pressure after gas inlet is used to calculate the injected gas quantity and hence the gas flux with the ideal gas equation as described in section 4.2.

A.4. Thermal loads on in-vessel piezo valves

A.4.1. Temperature increase of valves during experiment days

As the piezo valve is designed to be placed close to the plasma periphery, it has to deal with high thermal loads. The amount of the thermal load depends strongly on the position of the valve in the torus and on the plasma scenario. Not only the radial distance of the valve with respect to the limiter contour but also the toroidal placement influences the thermal loads on the protection bricks of the piezo valve.

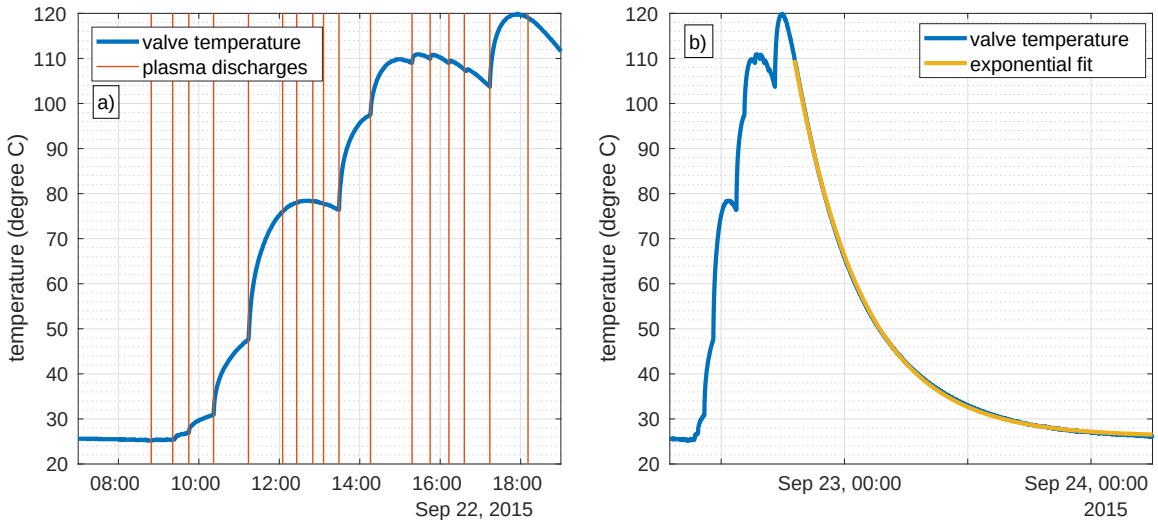

Figure A.4.: Temperature trace of the valve without cooling during an experimental day at AUG. a) shows a magnification for the time during the experiments where the red bars denote the timepoints of plasma discharges. b) shows the subsequent decrease of the valve temperature, which follows an exponential decay with a decay time of (6.4 ± 0.2) hours.

[2]Pfeiffer Vacuum GmbH, Berliner Str. 43, 35614 Aßlar

Especially the valve placed in sector 16 of AUG next to NBI box 1 had to suffer from high thermal loads and a subsequent temperature increase of more than 120 °C. This is shown in Fig. A.4 for one exemplary shot day where the timepoints of the plasma discharges are marked by vertical red lines. The amount of temperature increase after each discharge is strongly correlated with the heating power of NBI box 1. Whereas for non NBI heated discharges no power is deposited on the valve, one high power H-mode (#32 129) with 7.5 MW over 5.9 s from box 1 can cause a temperature increase of over 20 K, equal to a deposited power of 40 kJ. Other clear correlations to the temperate increase as the mean plasma density[3] or specific NBI sources in box 1 could not be found after the investigation of over 300 plasma discharges.
As the heating beam cannot hit the valve directly due to geometrical restrictions, it is assumed that a prompt re-ionization of the beam atoms, already behind the limiter contours, lead to the described high heat loads on the valve.

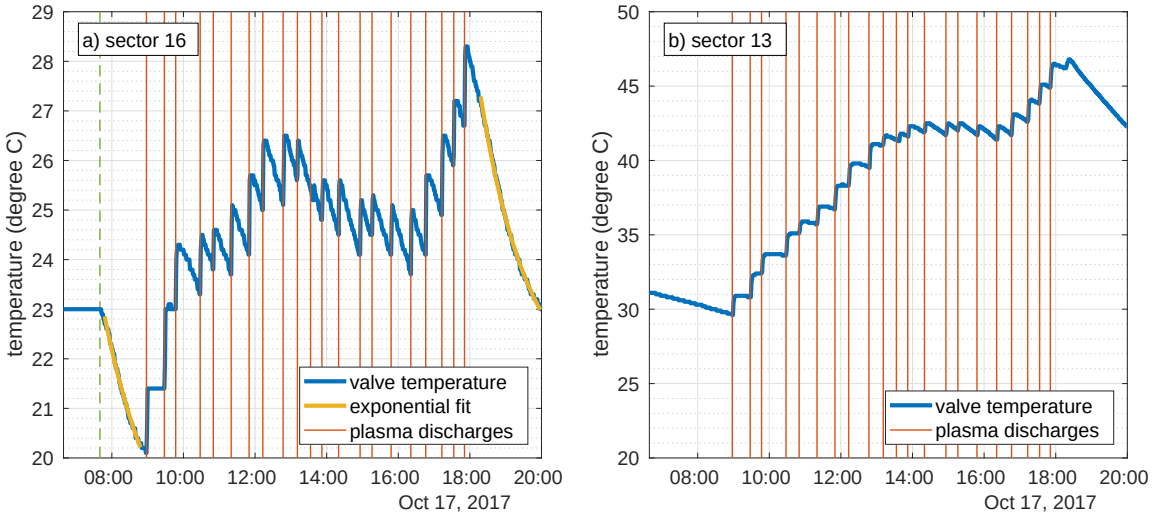

Figure A.5.: Subplot a) shows the temperature trace of the actively cooled valve in sector 16. The red bars denote the timepoints of plasma discharges and the dashed line indicates the timepoint when active cooling is switched on in the morning. The subsequent exponential temperature decrease has a time constant of (1.1 ± 0.2) hours. In b) the temperature of the valve in sector 13 without active cooling is shown. Note the different temperature range of the axes.

In Fig. A.4 a) it can clearly be seen that the temperature increase after a single high power discharge can last more than one hour. This is caused by the low heat conductivity of stainless steal and a small gap between the protection bricks and the valve box. Therefore, after a subsequent number of high power discharges, the valve did not operate anymore.
As shown in Fig. A.4 b) the temperature decrease is very slow, described by an exponential decay with a time constant of (6.4 ± 0.2) hours. Thus, for two subsequent experimental days the initial valve temperature is still not equilibrated. Furthermore, the tungsten coated carbon brick showed melting damages on the surface. To handle this, the geometry of the protection brick was adapted and an active water cooling system was installed, where the actively cooled components separate the valve box from the protection bricks.

[3] It was found that heating power correlates with mean density of the plasma. A correlation of heat influx with different densities at the same heating power could not be found.

The efficiency of the active cooling is shown in Fig. A.5 a), where the temperature increase after high power discharges is strongly reduced. Once the cooling is switched on (vertical dashed line) the time constant for exponential cooling is (1.1 ± 0.2) hours. The valve in sector 13 is not actively cooled as it is not directly affected by the NBI heating. Its temperature development is compared to the one of the valve in sector 16 in Fig. A.5 b).

A.4.2. Influence of temperature on valve properties

The gas flux through the valve is presented in chapter 4 as a function of working pressure p at constant temperature. As the flux depends not directly on the pressure in the valve but on the gas density, this effect has to be considered for measuring the temperature dependency. This normalization to the room temperature T_{room} is done by multiplying the flux at the working temperature T_{work} with the factor $T_{\mathrm{work}}/T_{\mathrm{room}}$ (units of the temperature in Kelvin).
Besides the operation restriction of the piezo for higher temperatures, temperature increase leads to a reduction of the maximum piezo stroke by $\sim (4.0 \pm 1.5)\,\mu\mathrm{m/K}$ for $25\,^{\circ}\mathrm{C} < T < 80\,^{\circ}\mathrm{C}$, as discussed in section 4.1. This shifts the opening voltage (cf. subsection 4.3.1) toward higher values as can be seen in Fig. A.6 b). For the sealing type with the Viton plug (cf. [Gri17]), the shift of U_{open} presented in Fig. A.6 a) is higher compared to b), measured with the advanced Viton plate sealing system.

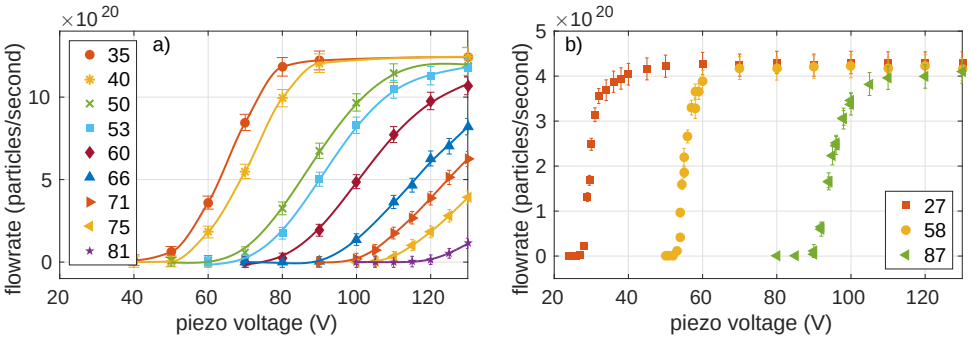

Figure A.6.: Voltage dependent flowrate for different temperatures in °C. a) shows the temperature dependence for the Viton plug sealing (cf. [Gri17], lines to guide the eye) whereas b) shows the temperature behavior of the Viton plate sealing type.

A.5. Effect of line integration on two 2-D profiles

In section 4.5 it is shown how the beam geometry is measured optically, based on the emission of the beam in a plasma glow discharge. The measured 2-D intensity distribution $F(y, z)$ is the projection of the 3-D gas emission[4] $f(x, y, z)$ onto the y, z image plane. The projection along the lines of sight in x-direction can be treated for each x, y plane separately, so that the problem is reduced to one dimension.

[4]It is assumed that the emission profile reflects the density profile.

To calculate the emission distribution $f(x, y)$, the injected gas cloud is treated as optically thin and the emission as axially symmetric to the capillary. The measured signal then is

$$F(y) = \int_{-\infty}^{\infty} f(r)\,\mathrm{d}x, \tag{A.1}$$

where $r = \sqrt{x^2 + y^2}$ denotes the distance to the symmetry axis. Substituting $\mathrm{d}x$ with $\mathrm{d}x = r\,\mathrm{d}r/\sqrt{r^2 - y^2}$ and noticing that $f(r)$ as well as the expression for $\mathrm{d}x$ are even functions yields

$$F(y) = 2\int_{0}^{\infty} \frac{f(r)\,r\,\mathrm{d}r}{\sqrt{r^2 - y^2}}. \tag{A.2}$$

This is the so-called Abel transform[5] of the emission profile. The inverse Abel transform which has to by applied on line integrated measurements to gain back the emission profile is given by

$$f(r) = -\frac{1}{\pi}\int_{r}^{\infty} \frac{\mathrm{d}F}{\mathrm{d}y}\frac{\mathrm{d}y}{\sqrt{y^2 - r^2}}. \tag{A.3}$$

This transform is necessary because in general the line integrated intensity does not represent the shape of the emission profile correctly as illustrated in Fig. A.7.
The upper plot in the left column shows a two dimensional Gaussian distribution, the one on the right shows the emission profile of a homogeneous cylinder. The total emission is the same and the radius of the cylinder equals the FWHM of the Gaussian distribution.
The two middle plots show the intensity distribution $f(0, y)$ along the y axis at $x = 0$, whereas the two lower plots show the line integrated intensity for integration along the x axis. This intensity distribution equals the measured signal $F(y)$.
In contrast to the radiating cylinder, the shape of the intensity profiles (the FWHM) for the Gaussian distribution is the same in both cases. An inverse Abel transform is not necessary here, as the line integration

$$\begin{aligned} F(y,z) &= \int_{-\infty}^{\infty} f(x,y,z)\,\mathrm{d}x \\ &= \int_{-\infty}^{\infty} \frac{1}{2\pi\sigma(z)^2}\cdot\exp\left(-\frac{x^2+y^2}{2\sigma(z)^2}\right)\mathrm{d}x \\ &= \frac{1}{\sqrt{2\pi}\sigma(z)}\cdot\exp\left(\frac{-y^2}{2\sigma(z)^2}\right) \end{aligned} \tag{A.4}$$

only changes the total intensity of the signal which is arbitrary. The FWHM of the function, which exclusively denotes the shape, is preserved.

[5]Named after the Norwegian mathematician Niels Henrik Abel (∗ 5 August 1802 ; † 6 April 1829).

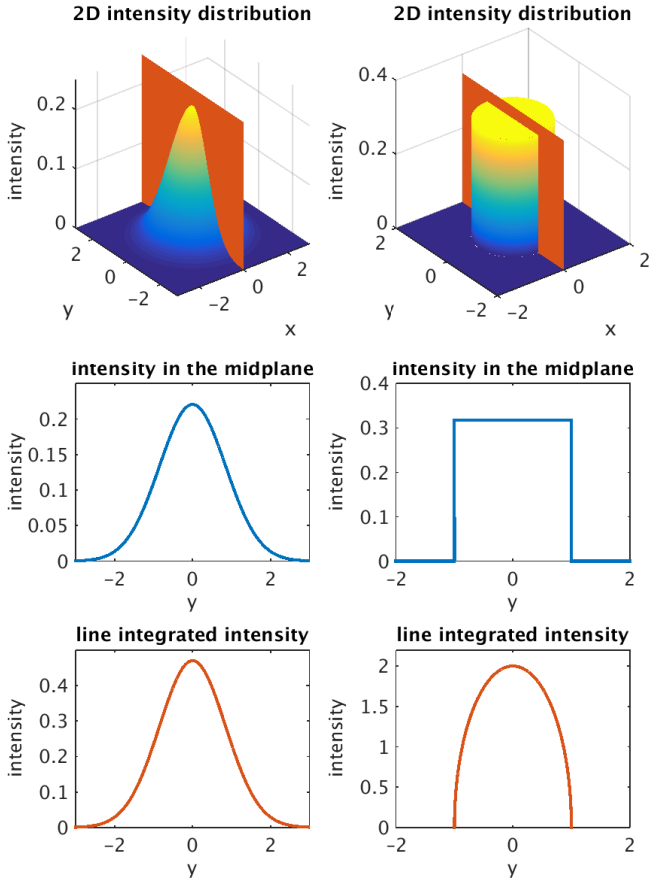

Figure A.7.: Comparison of two emission profiles regarding the effect of an Abel inversion. For a Gaussian distribution (left column), line integration only changes the absolute value, but not the shape of the profile. This does not hold for a general cylinder symmetric profile (right column) where the line integrated values differ from the cross section profile.

A.6. Aspheric lenses

As in vessel lenses, the aspheric lens "AFL50-80-S-A2"[6] with a nominal focal length of 80 mm (effective focal length, EFL = 85 mm) and a diameter of 35 mm is used. Aspheric lenses eliminate spherical aberrations and also reduce other optical aberrations such as astigmatism, compared to a normal spherical lens. This feature is of major importance for off-axis rays in our application. In Fig. A.8, the behavior of the aspheric lens is compared to a conventional lens with 85 mm focal length. For the measurements, an illuminated optical fiber (0.4 mm core diameter) was placed behind the lens (cf. Fig. 5.4). At the image distance of 69 cm, a camera (Nikon D810) without any additional optics was placed and the image was directly produced on the CCD chip of the camera.

For the off-axis measurements, the fiber was displaced off-axis by 8 mm. Fig. A.8 compares the on-axis image (top) to the off-axis image (bottom) of the aspheric lens (left) to the spherical lens (right).

[6] Asphericon GmbH, Stockholmer Straße 9, 07747 Jena , Germany

To estimate the image quality, the width of the fiber image is calculated. 68.3 % of the light lies within a width of σ, whereas a width of 2σ covers 95.4 % of the light. These positions are marked in Fig. A.8 with blue markers. To treat the asymmetric off-axis aberration, the width of the image is calculated separately in x and y direction. It is clearly visible that the aberrations are much smaller in the case of the aspheric lens compared to the standard lens, especially for off-axis applications.

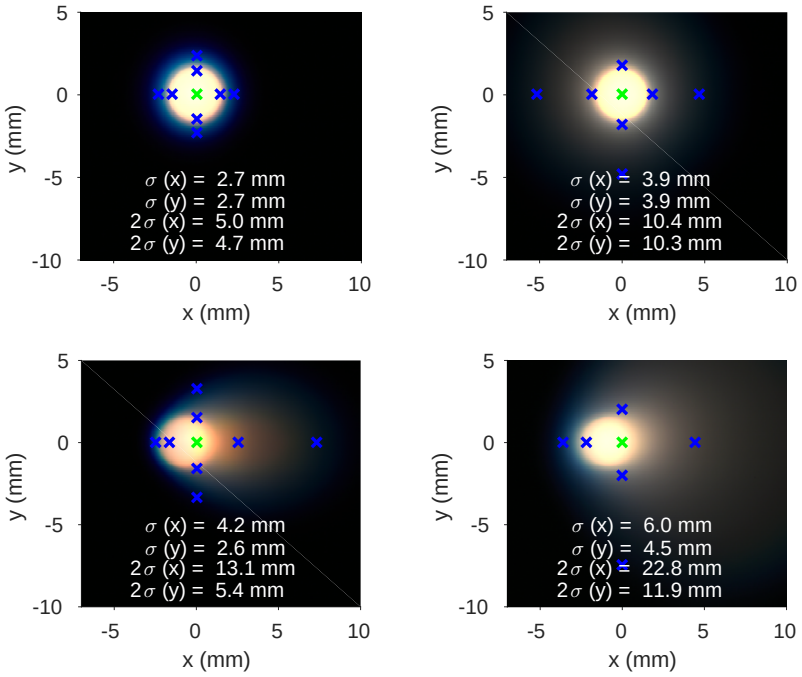

Figure A.8.: Off-axis aberration of aspheric (left) and normal (right) lens. The on-axis images (top) of a fiber are compared to their respective off-axis image (bottom) at an off-axis distance of 8 mm. The green markers denote the point of highest intensity, the blue markers denote the area of 1σ and 2σ (not fully visible) of the total light.

These off-axis aberrations lead to a broadening of the viewing chord in radial direction for the radially distributed LOS. This decreases the spatial resolution of the diagnostic. Therefore the aspheric lens was chosen to minimize this effect. The usage of two lenses leads to a reduction of the off-axis distance which is required to cover the whole SOL. The required distance of 8 mm in the case of a single lens can thus be reduced to 5 mm. This further reduces the off-axis aberrations to $\sigma(x) = 3.1\,\text{mm}$, $\sigma(y) = 2.5\,\text{mm}$ as well as $2\sigma(x) = 6.9\,\text{mm}$ and $2\sigma(y) = 4.7\,\text{mm}$. Because the width in y direction does not significantly change with the off-axis distance (cf. Fig. A.8) it can be used as a comparison to the on-axis image in this context.

The aspherical shape of a lens does not influence the chromatic aberrations compared to a normal single lens. Due to the higher diffraction index for light with a smaller wavelength, the effective focal length of the aspheric lens is 83.8 mm for 400 nm and 86.9 mm for 800 nm light. For an image distance of 69 cm for green light, the focal plane is shifted toward the lens for blue light by 5 cm and away from the lens for red light by 5 cm. These three positions are pictured in Fig. A.9.

The width of the fiber image separated into its blue, green and red components is summarized in Tab. A.2.
The measurement results of both, the chromatic and off-axis aberrations, are in good agreement with predictions of the ray tracing program "WinLens3D Basic".

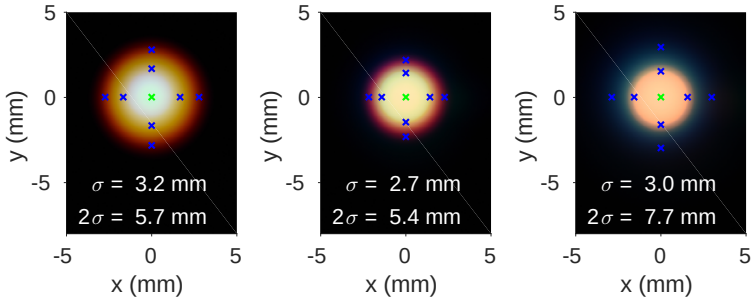

Figure A.9.: Chromatic aberration of the aspheric lens. The focal plane of red light (left) is shifted by 5 cm away from the lens and the focal plans of blue light (right) is shifted by 5 cm toward the lens, with respect to the focal plane of green light (middle). The green markers denote the point of highest intensity, the blue markers denote the area of 1σ and 2σ of the total light.

Table A.2.: Chromatic aberration of the aspheric lens "AFL50-80-S-A2". The table shows the width σ and 2σ of the total image, as well as the width of its blue, green and red part at three positions. The positions are the nominal focal plane at a distance of 69 cm to the lens as well as 5 cm closer and farther away from the lens.

color	diameter	distance to focal plane		
		−5 cm	0 cm	5 cm
blue	σ (mm)	2.3	2.8	3.7
	2σ (mm)	3.5	5.3	7.5
green	σ (mm)	3.1	2.7	3.1
	2σ (mm)	4.9	3.9	5.8
red	σ (mm)	4.2	3.1	3.0
	2σ (mm)	6.1	4.5	4.3
total	σ (mm)	3.2	2.7	3.0
	2σ (mm)	5.7	5.4	7.7

The 10 cm distance between the focal point for blue and red is comparable to the width of the He-cloud in the measurement region. As the aberration is symmetric through the central axis and its radial broadening only influences the wavelength dependent position of the narrowest point along the LOS and not its overall width, the chromatic aberration does not influence the total spatial resolution of the diagnostic.
To compensate chromatic aberration of one single lens, chromatic doublets can be used. They consist of a concave and a convex lens with different diffraction index gradients according to wavelength changes. Typically these two lenses are glued together as in the achromat "AC508-080-A" from Thorlabs. This lens is suitable for vacuum applications as out gassing tests showed.

The tested baking procedure at 150 °C, however, damages the glue between the lenses, excluding this type of lenses from in vessel applications.

A.7. Data of optical components of the polychromator system

Table A.3.: Interference filter specifications including the central wavelength (CWL) of the transmitted light, the angle of incidence (AOI) for the CWL and the full-width half maximum (FWHM) of the transition peak.

	Filter 1	Filter 2	Filter 3	Filter 4
CWL nominal	587.6 nm	667.8 nm	706.5 nm	728.1 nm
CWL measured	(587.4 ± 0.1) nm	(668.0 ± 0.1) nm	(706.3 ± 0.1) nm	(728.1 ± 0.1) nm
AOI		0° collimated		
FWHM		<1.7 nm		
transmission		>90 % abs at CWL		
blocking		>OD6 avg at		
	200–573 nm	200–653 nm	200–691 nm	200–712 nm
	603–1100 nm	683–1100 nm	723–1100 nm	745–1100 nm
dimensions		$49 \times 21\,\text{mm}^2 \pm 0.1$ mm		
substrate thickness		(2.0 ± 0.1) mm		
substrate		gorosilicate glass		
n_{eff}	1.707	1.880	1.808	1.807

Table A.4.: Dichroic mirror specifications.

	Mirror 1	Mirror 2	Mirror 3
50 % cut-on	(655 ± 4) nm	(695 ± 4) nm	(718 ± 4) nm
AOI		45° collimated	
transmission		>95 % avg at	
	661–950 nm	705.5–850 nm	728.1 nm
reflection		>98 % avg at	
	560–649 nm	400–684.5 nm	706.5 nm
dimensions		$50 \times 72\,\text{mm}^2 \pm 0.1$ mm	
substrate thickness		(1.04 ± 0.10) mm	
parallelism		< 3 arcsec	
substrate		fused silica	

A.8. Crosstalk of the PMT arrays

Table A.5.: PMT 1 crosstalk overview with illuminated channels in the vertical axis and crosstalk channels on the horizontal axis. The values are given in percent of the total intensity.

CH	1	2	3	4	5	6	7	8	9	10	11	12	13	14	15	16	17	18	19	20	21	22	23	24	25	26	27	28	29	30	31	32
1	88.9	4.8	0.6	0.1	—	—	—	—	—	—	—	—	—	—	—	—	—	—	—	—	—	—	—	—	—	—	—	—	—	—	—	—
2	4.4	90.0	4.6	0.3	0.2	—	—	—	—	—	—	—	—	—	—	—	—	—	—	—	—	—	—	—	—	—	—	—	—	—	—	—
3	0.5	4.1	90.3	4.4	0.5	0.2	—	—	—	—	—	—	—	—	—	—	—	—	—	—	—	—	—	—	—	—	—	—	—	—	—	—
4	0.1	0.5	3.7	90.9	4.2	0.4	0.1	—	—	—	—	—	—	—	—	—	—	—	—	—	—	—	—	—	—	—	—	—	—	—	—	—
5	0.1	0.2	0.6	2.9	92.8	2.9	0.4	0.1	—	—	—	—	—	—	—	—	—	—	—	—	—	—	—	—	—	—	—	—	—	—	—	—
6	—	0.1	0.2	0.5	4.1	89.2	5.2	0.5	0.2	—	—	—	—	—	—	—	—	—	—	—	—	—	—	—	—	—	—	—	—	—	—	—
7	—	—	0.2	0.1	0.5	2.9	92.7	3.0	0.5	0.2	—	—	—	—	—	—	—	—	—	—	—	—	—	—	—	—	—	—	—	—	—	—
8	—	—	—	0.1	0.2	0.5	3.7	90.5	4.5	0.4	0.2	—	—	—	—	—	—	—	—	—	—	—	—	—	—	—	—	—	—	—	—	—
9	—	—	—	—	0.1	0.2	0.5	3.0	93.1	2.5	0.4	0.2	—	—	—	—	—	—	—	—	—	—	—	—	—	—	—	—	—	—	—	—
10	—	—	—	—	—	0.1	0.1	0.5	3.8	90.5	4.3	0.4	0.2	—	—	—	—	—	—	—	—	—	—	—	—	—	—	—	—	—	—	—
11	—	—	—	—	—	—	0.1	0.2	0.6	3.3	91.3	3.8	0.5	0.2	—	—	—	—	—	—	—	—	—	—	—	—	—	—	—	—	—	—
12	—	—	—	—	—	—	—	0.1	0.2	0.6	3.9	89.7	4.9	0.5	0.2	—	—	—	—	—	—	—	—	—	—	—	—	—	—	—	—	—
13	—	—	—	—	—	—	—	—	0.1	0.2	0.6	2.9	92.6	2.9	0.5	0.2	—	—	—	—	—	—	—	—	—	—	—	—	—	—	—	—
14	—	—	—	—	—	—	—	—	—	0.1	0.1	0.5	3.3	91.7	3.7	0.4	0.2	—	—	—	—	—	—	—	—	—	—	—	—	—	—	—
15	—	—	—	—	—	—	—	—	—	—	0.1	0.2	0.6	3.3	91.7	3.6	0.6	0.1	—	—	—	—	—	—	—	—	—	—	—	—	—	—
16	—	—	—	—	—	—	—	—	—	—	—	0.1	0.1	0.5	3.3	91.8	3.6	0.4	0.2	—	—	—	—	—	—	—	—	—	—	—	—	—
17	—	—	—	—	—	—	—	—	—	—	—	—	0.1	0.2	0.5	3.3	92.1	3.2	0.5	0.2	—	—	—	—	—	—	—	—	—	—	—	—
18	—	—	—	—	—	—	—	—	—	—	—	—	—	0.1	0.2	0.5	4.0	89.7	4.8	0.5	0.2	—	—	—	—	—	—	—	—	—	—	—
19	—	—	—	—	—	—	—	—	—	—	—	—	—	—	0.1	0.2	0.5	2.5	94.0	2.2	0.4	0.2	—	—	—	—	—	—	—	—	—	—
20	—	—	—	—	—	—	—	—	—	—	—	—	—	—	—	0.1	0.2	0.6	4.2	89.9	4.4	0.4	0.2	—	—	—	—	—	—	—	—	—
21	—	—	—	—	—	—	—	—	—	—	—	—	—	—	—	—	0.1	0.2	0.5	3.3	91.8	3.4	0.5	0.2	—	—	—	—	—	—	—	—
22	—	—	—	—	—	—	—	—	—	—	—	—	—	—	—	—	—	0.1	0.2	0.4	3.9	89.4	5.3	0.5	0.2	—	—	—	—	—	—	—
23	—	—	—	—	—	—	—	—	—	—	—	—	—	—	—	—	—	—	0.1	0.1	0.4	2.6	93.5	2.7	0.5	0.1	—	—	—	—	—	—
24	—	—	—	—	—	—	—	—	—	—	—	—	—	—	—	—	—	—	—	0.1	0.1	0.5	3.6	91.1	4.1	0.4	0.1	—	—	—	—	—
25	—	—	—	—	—	—	—	—	—	—	—	—	—	—	—	—	—	—	—	—	0.1	0.1	0.5	3.5	91.1	4.2	0.4	0.1	—	—	—	—
26	—	—	—	—	—	—	—	—	—	—	—	—	—	—	—	—	—	—	—	—	—	0.1	0.2	0.4	3.1	92.1	3.5	0.3	0.3	—	—	—
27	—	—	—	—	—	—	—	—	—	—	—	—	—	—	—	—	—	—	—	—	—	—	0.1	0.1	0.5	3.1	91.9	3.5	0.5	0.1	—	—
28	—	—	—	—	—	—	—	—	—	—	—	—	—	—	—	—	—	—	—	—	—	—	—	0.1	0.2	0.5	3.6	90.1	5.0	0.4	0.2	—
29	—	—	—	—	—	—	—	—	—	—	—	—	—	—	—	—	—	—	—	—	—	—	—	—	0.1	0.1	0.3	2.8	92.7	3.5	0.4	0.1
30	—	—	—	—	—	—	—	—	—	—	—	—	—	—	—	—	—	—	—	—	—	—	—	—	—	0.1	-0.0	0.4	3.4	91.2	4.5	0.4
31	—	—	—	—	—	—	—	—	—	—	—	—	—	—	—	—	—	—	—	—	—	—	—	—	—	—	-0.0	0.1	0.7	2.8	93.1	3.4
32	—	—	—	—	—	—	—	—	—	—	—	—	—	—	—	—	—	—	—	—	—	—	—	—	—	—	—	0.1	0.3	0.5	3.5	95.5

Table A.6.: PMT 2 crosstalk overview with illuminated channels in the vertical axis and crosstalk channels on the horizontal axis. The values are given in percent of the total intensity.

CH	1	2	3	4	5	6	7	8	9	10	11	12	13	14	15	16	17	18	19	20	21	22	23	24	25	26	27	28	29	30	31	32
1	86.1	6.2	0.6	0.1	—	—	—	—	—	—	—	—	—	—	—	—	—	—	—	—	—	—	—	—	—	—	—	—	—	—	—	—
2	1.9	91.1	6.0	0.4	0.1	—	—	—	—	—	—	—	—	—	—	—	—	—	—	—	—	—	—	—	—	—	—	—	—	—	—	—
3	0.1	2.4	91.3	5.4	0.5	0.2	—	—	—	—	—	—	—	—	—	—	—	—	—	—	—	—	—	—	—	—	—	—	—	—	—	—
4	-0.4	0.6	2.5	90.4	6.1	0.5	0.2	—	—	—	—	—	—	—	—	—	—	—	—	—	—	—	—	—	—	—	—	—	—	—	—	—
5	-0.4	0.2	0.5	2.2	92.4	4.5	0.5	0.1	—	—	—	—	—	—	—	—	—	—	—	—	—	—	—	—	—	—	—	—	—	—	—	—
6	—	0.1	0.1	0.6	2.7	90.6	5.2	0.6	0.2	—	—	—	—	—	—	—	—	—	—	—	—	—	—	—	—	—	—	—	—	—	—	—
7	—	—	0.1	0.0	0.4	2.2	91.8	4.8	0.5	0.2	—	—	—	—	—	—	—	—	—	—	—	—	—	—	—	—	—	—	—	—	—	—
8	—	—	—	0.1	0.1	0.5	2.4	91.4	4.8	0.5	0.1	—	—	—	—	—	—	—	—	—	—	—	—	—	—	—	—	—	—	—	—	—
9	—	—	—	—	0.0	0.1	0.4	1.9	93.2	3.8	0.4	0.1	—	—	—	—	—	—	—	—	—	—	—	—	—	—	—	—	—	—	—	—
10	—	—	—	—	—	0.1	0.1	0.5	2.5	91.6	4.7	0.4	0.1	—	—	—	—	—	—	—	—	—	—	—	—	—	—	—	—	—	—	—
11	—	—	—	—	—	—	0.1	0.1	0.5	2.1	92.3	4.2	0.4	0.1	—	—	—	—	—	—	—	—	—	—	—	—	—	—	—	—	—	—
12	—	—	—	—	—	—	—	0.1	0.2	0.6	2.4	91.5	4.7	0.5	0.2	—	—	—	—	—	—	—	—	—	—	—	—	—	—	—	—	—
13	—	—	—	—	—	—	—	—	0.1	0.2	0.6	2.2	92.2	4.1	0.5	0.1	—	—	—	—	—	—	—	—	—	—	—	—	—	—	—	—
14	—	—	—	—	—	—	—	—	—	0.1	0.1	0.5	2.5	91.1	4.9	0.5	0.2	—	—	—	—	—	—	—	—	—	—	—	—	—	—	—
15	—	—	—	—	—	—	—	—	—	—	0.1	0.1	0.5	2.1	92.7	4.0	0.5	0.1	—	—	—	—	—	—	—	—	—	—	—	—	—	—
16	—	—	—	—	—	—	—	—	—	—	—	0.1	0.1	0.5	2.2	92.3	4.1	0.5	0.1	—	—	—	—	—	—	—	—	—	—	—	—	—
17	—	—	—	—	—	—	—	—	—	—	—	—	0.1	0.2	0.5	2.1	92.8	3.8	0.5	0.1	—	—	—	—	—	—	—	—	—	—	—	—
18	—	—	—	—	—	—	—	—	—	—	—	—	—	0.1	0.2	0.6	2.6	91.4	4.7	0.4	0.1	—	—	—	—	—	—	—	—	—	—	—
19	—	—	—	—	—	—	—	—	—	—	—	—	—	—	0.1	0.2	0.6	2.3	91.7	4.5	0.5	0.1	—	—	—	—	—	—	—	—	—	—
20	—	—	—	—	—	—	—	—	—	—	—	—	—	—	—	0.1	0.2	0.5	2.5	91.3	4.7	0.4	0.1	—	—	—	—	—	—	—	—	—
21	—	—	—	—	—	—	—	—	—	—	—	—	—	—	—	—	0.1	0.2	0.6	2.2	92.0	4.3	0.5	0.2	—	—	—	—	—	—	—	—
22	—	—	—	—	—	—	—	—	—	—	—	—	—	—	—	—	—	0.1	0.2	0.5	2.3	91.5	4.7	0.5	0.2	—	—	—	—	—	—	—
23	—	—	—	—	—	—	—	—	—	—	—	—	—	—	—	—	—	—	0.1	0.1	0.5	2.4	91.0	5.2	0.5	0.2	—	—	—	—	—	—
24	—	—	—	—	—	—	—	—	—	—	—	—	—	—	—	—	—	—	—	0.1	0.1	0.5	2.2	91.5	4.9	0.4	0.2	—	—	—	—	—
25	—	—	—	—	—	—	—	—	—	—	—	—	—	—	—	—	—	—	—	—	0.1	0.1	0.5	2.1	92.3	4.2	0.6	0.1	—	—	—	—
26	—	—	—	—	—	—	—	—	—	—	—	—	—	—	—	—	—	—	—	—	—	0.1	0.1	0.6	2.5	90.9	5.1	0.5	0.1	—	—	—
27	—	—	—	—	—	—	—	—	—	—	—	—	—	—	—	—	—	—	—	—	—	—	0.1	0.1	1.3	2.0	92.2	3.7	0.5	0.1	—	—
28	—	—	—	—	—	—	—	—	—	—	—	—	—	—	—	—	—	—	—	—	—	—	—	0.1	0.2	0.7	2.2	91.9	4.3	0.4	0.1	—
29	—	—	—	—	—	—	—	—	—	—	—	—	—	—	—	—	—	—	—	—	—	—	—	—	1.0	0.2	0.7	1.9	91.7	4.0	0.5	0.1
30	—	—	—	—	—	—	—	—	—	—	—	—	—	—	—	—	—	—	—	—	—	—	—	—	—	0.1	0.2	0.7	2.1	92.0	4.4	0.4
31	—	—	—	—	—	—	—	—	—	—	—	—	—	—	—	—	—	—	—	—	—	—	—	—	—	—	0.1	0.2	0.8	2.2	91.9	4.8
32	—	—	—	—	—	—	—	—	—	—	—	—	—	—	—	—	—	—	—	—	—	—	—	—	—	—	—	0.1	0.2	0.8	2.4	96.5

Table A.7.: PMT 3 crosstalk overview with illuminated channels in the vertical axis and crosstalk channels on the horizontal axis. The values are given in percent of the total intensity.

CH	1	2	3	4	5	6	7	8	9	10	11	12	13	14	15	16	17	18	19	20	21	22	23	24	25	26	27	28	29	30	31	32
1	88.7	4.4	0.8	0.4	—	—	—	—	—	—	—	—	—	—	—	—	—	—	—	—	—	—	—	—	—	—	—	—	—	—	—	—
2	20.9	72.6	4.0	0.9	0.4	—	—	—	—	—	—	—	—	—	—	—	—	—	—	—	—	—	—	—	—	—	—	—	—	—	—	—
3	1.0	14.4	78.8	4.3	0.7	0.4	—	—	—	—	—	—	—	—	—	—	—	—	—	—	—	—	—	—	—	—	—	—	—	—	—	—
4	0.3	1.0	12.2	81.3	3.9	0.8	0.4	—	—	—	—	—	—	—	—	—	—	—	—	—	—	—	—	—	—	—	—	—	—	—	—	—
5	0.2	0.3	0.9	9.7	83.9	4.0	0.7	0.3	—	—	—	—	—	—	—	—	—	—	—	—	—	—	—	—	—	—	—	—	—	—	—	—
6	—	0.2	0.2	0.9	7.1	86.9	3.8	0.6	0.3	—	—	—	—	—	—	—	—	—	—	—	—	—	—	—	—	—	—	—	—	—	—	—
7	—	—	0.2	0.3	0.9	9.2	84.6	3.7	0.7	0.4	—	—	—	—	—	—	—	—	—	—	—	—	—	—	—	—	—	—	—	—	—	—
8	—	—	—	0.2	0.2	0.8	6.1	87.9	3.9	0.6	0.3	—	—	—	—	—	—	—	—	—	—	—	—	—	—	—	—	—	—	—	—	—
9	—	—	—	—	0.1	0.3	0.8	5.6	88.6	3.7	0.6	0.2	—	—	—	—	—	—	—	—	—	—	—	—	—	—	—	—	—	—	—	—
10	—	—	—	—	—	0.2	0.3	0.8	5.1	89.6	3.4	0.5	0.2	—	—	—	—	—	—	—	—	—	—	—	—	—	—	—	—	—	—	—
11	—	—	—	—	—	—	0.2	0.3	0.9	5.3	88.4	4.1	0.6	0.2	—	—	—	—	—	—	—	—	—	—	—	—	—	—	—	—	—	—
12	—	—	—	—	—	—	—	0.2	0.3	0.9	4.4	89.0	4.3	0.6	0.3	—	—	—	—	—	—	—	—	—	—	—	—	—	—	—	—	—
13	—	—	—	—	—	—	—	—	0.2	0.3	0.8	3.9	90.1	4.0	0.6	0.2	—	—	—	—	—	—	—	—	—	—	—	—	—	—	—	—
14	—	—	—	—	—	—	—	—	—	0.2	0.3	0.8	3.8	90.0	4.1	0.7	0.3	—	—	—	—	—	—	—	—	—	—	—	—	—	—	—
15	—	—	—	—	—	—	—	—	—	—	0.2	0.2	0.8	3.7	90.6	3.7	0.6	0.3	—	—	—	—	—	—	—	—	—	—	—	—	—	—
16	—	—	—	—	—	—	—	—	—	—	—	0.1	0.2	0.8	3.8	90.7	3.5	0.6	0.3	—	—	—	—	—	—	—	—	—	—	—	—	—
17	—	—	—	—	—	—	—	—	—	—	—	—	0.1	0.2	0.9	3.8	90.1	4.1	0.6	0.2	—	—	—	—	—	—	—	—	—	—	—	—
18	—	—	—	—	—	—	—	—	—	—	—	—	—	0.2	0.3	0.8	3.6	90.1	4.3	0.6	0.2	—	—	—	—	—	—	—	—	—	—	—
19	—	—	—	—	—	—	—	—	—	—	—	—	—	—	0.2	0.3	1.0	3.7	89.2	4.8	0.6	0.2	—	—	—	—	—	—	—	—	—	—
20	—	—	—	—	—	—	—	—	—	—	—	—	—	—	—	0.2	0.3	0.9	3.6	89.4	4.7	0.6	0.2	—	—	—	—	—	—	—	—	—
21	—	—	—	—	—	—	—	—	—	—	—	—	—	—	—	—	0.3	0.4	1.0	3.5	89.3	4.6	0.6	0.2	—	—	—	—	—	—	—	—
22	—	—	—	—	—	—	—	—	—	—	—	—	—	—	—	—	—	0.3	0.4	1.0	3.3	89.6	4.5	0.7	0.3	—	—	—	—	—	—	—
23	—	—	—	—	—	—	—	—	—	—	—	—	—	—	—	—	—	—	0.3	0.4	1.0	3.2	89.7	4.4	0.7	0.3	—	—	—	—	—	—
24	—	—	—	—	—	—	—	—	—	—	—	—	—	—	—	—	—	—	—	0.4	0.5	1.2	2.8	89.9	4.3	0.7	0.3	—	—	—	—	—
25	—	—	—	—	—	—	—	—	—	—	—	—	—	—	—	—	—	—	—	—	0.4	0.5	1.2	3.3	89.0	4.6	0.6	0.3	—	—	—	—
26	—	—	—	—	—	—	—	—	—	—	—	—	—	—	—	—	—	—	—	—	—	0.6	0.8	1.5	3.4	87.6	4.9	0.9	0.3	—	—	—
27	—	—	—	—	—	—	—	—	—	—	—	—	—	—	—	—	—	—	—	—	—	—	0.9	1.0	1.8	3.6	86.4	5.3	0.8	0.3	—	—
28	—	—	—	—	—	—	—	—	—	—	—	—	—	—	—	—	—	—	—	—	—	—	—	1.5	1.5	2.4	4.2	81.6	7.4	1.0	0.5	—
29	—	—	—	—	—	—	—	—	—	—	—	—	—	—	—	—	—	—	—	—	—	—	—	—	1.9	1.8	2.1	4.2	81.4	7.0	1.1	0.4
30	—	—	—	—	—	—	—	—	—	—	—	—	—	—	—	—	—	—	—	—	—	—	—	—	—	2.4	1.8	3.2	4.4	77.9	9.0	1.2
31	—	—	—	—	—	—	—	—	—	—	—	—	—	—	—	—	—	—	—	—	—	—	—	—	—	—	2.0	4.0	3.2	4.9	74.7	11.3
32	—	—	—	—	—	—	—	—	—	—	—	—	—	—	—	—	—	—	—	—	—	—	—	—	—	—	—	4.7	2.9	3.5	5.3	83.6

Table A.8.: PMT 4 crosstalk overview with illuminated channels in the vertical axis and crosstalk channels on the horizontal axis. The values are given in percent of the total intensity.

CH	1	2	3	4	5	6	7	8	9	10	11	12	13	14	15	16	17	18	19	20	21	22	23	24	25	26	27	28	29	30	31	32
1	91.2	3.2	0.9	0.3	—	—	—	—	—	—	—	—	—	—	—	—	—	—	—	—	—	—	—	—	—	—	—	—	—	—	—	—
2	10.7	82.8	3.6	1.1	0.4	—	—	—	—	—	—	—	—	—	—	—	—	—	—	—	—	—	—	—	—	—	—	—	—	—	—	—
3	0.8	8.0	86.2	3.3	1.0	0.4	—	—	—	—	—	—	—	—	—	—	—	—	—	—	—	—	—	—	—	—	—	—	—	—	—	—
4	0.3	0.7	7.4	86.8	3.3	1.0	0.3	—	—	—	—	—	—	—	—	—	—	—	—	—	—	—	—	—	—	—	—	—	—	—	—	—
5	0.2	0.2	0.7	7.1	86.8	3.9	0.9	0.3	—	—	—	—	—	—	—	—	—	—	—	—	—	—	—	—	—	—	—	—	—	—	—	—
6	—	0.1	0.2	0.6	5.1	89.4	3.4	0.8	0.3	—	—	—	—	—	—	—	—	—	—	—	—	—	—	—	—	—	—	—	—	—	—	—
7	—	—	0.2	0.3	0.7	6.0	88.2	3.4	1.0	0.3	—	—	—	—	—	—	—	—	—	—	—	—	—	—	—	—	—	—	—	—	—	—
8	—	—	—	0.2	0.2	0.7	4.8	89.7	3.4	0.8	0.3	—	—	—	—	—	—	—	—	—	—	—	—	—	—	—	—	—	—	—	—	—
9	—	—	—	—	0.2	0.3	0.6	5.1	89.2	3.6	0.8	0.3	—	—	—	—	—	—	—	—	—	—	—	—	—	—	—	—	—	—	—	—
10	—	—	—	—	—	0.2	0.3	0.6	4.8	89.3	3.7	0.8	0.3	—	—	—	—	—	—	—	—	—	—	—	—	—	—	—	—	—	—	—
11	—	—	—	—	—	—	0.2	0.3	0.7	5.0	89.0	3.8	0.9	0.3	—	—	—	—	—	—	—	—	—	—	—	—	—	—	—	—	—	—
12	—	—	—	—	—	—	—	0.2	0.3	0.7	4.8	89.0	3.8	0.9	0.3	—	—	—	—	—	—	—	—	—	—	—	—	—	—	—	—	—
13	—	—	—	—	—	—	—	—	0.2	0.2	0.5	3.8	90.4	3.8	0.8	0.3	—	—	—	—	—	—	—	—	—	—	—	—	—	—	—	—
14	—	—	—	—	—	—	—	—	—	0.2	0.2	0.6	4.2	89.6	4.1	0.9	0.4	—	—	—	—	—	—	—	—	—	—	—	—	—	—	—
15	—	—	—	—	—	—	—	—	—	—	0.1	0.2	0.6	4.5	89.2	4.2	0.9	0.3	—	—	—	—	—	—	—	—	—	—	—	—	—	—
16	—	—	—	—	—	—	—	—	—	—	—	0.2	0.2	0.6	4.9	88.2	4.7	0.8	0.3	—	—	—	—	—	—	—	—	—	—	—	—	—
17	—	—	—	—	—	—	—	—	—	—	—	—	0.2	0.2	0.5	3.6	90.6	3.8	0.8	0.3	—	—	—	—	—	—	—	—	—	—	—	—
18	—	—	—	—	—	—	—	—	—	—	—	—	—	0.2	0.3	0.6	4.1	89.6	4.3	0.8	0.2	—	—	—	—	—	—	—	—	—	—	—
19	—	—	—	—	—	—	—	—	—	—	—	—	—	—	0.2	0.3	0.6	3.8	90.1	4.2	0.7	0.1	—	—	—	—	—	—	—	—	—	—
20	—	—	—	—	—	—	—	—	—	—	—	—	—	—	—	0.2	0.3	0.6	3.3	91.1	4.0	0.4	0.3	—	—	—	—	—	—	—	—	—
21	—	—	—	—	—	—	—	—	—	—	—	—	—	—	—	—	0.2	0.2	0.5	3.4	92.5	2.2	0.8	0.3	—	—	—	—	—	—	—	—
22	—	—	—	—	—	—	—	—	—	—	—	—	—	—	—	—	—	0.3	0.5	1.0	5.4	82.8	8.0	1.4	0.6	—	—	—	—	—	—	—
23	—	—	—	—	—	—	—	—	—	—	—	—	—	—	—	—	—	—	0.2	0.2	0.4	1.7	91.9	4.5	0.8	0.2	—	—	—	—	—	—
24	—	—	—	—	—	—	—	—	—	—	—	—	—	—	—	—	—	—	—	0.1	0.1	0.2	3.2	90.6	4.8	0.6	0.3	—	—	—	—	—
25	—	—	—	—	—	—	—	—	—	—	—	—	—	—	—	—	—	—	—	—	0.1	0.1	0.5	3.2	90.8	4.3	0.7	0.3	—	—	—	—
26	—	—	—	—	—	—	—	—	—	—	—	—	—	—	—	—	—	—	—	—	—	0.1	0.2	0.6	3.7	88.1	6.3	0.8	0.3	—	—	—
27	—	—	—	—	—	—	—	—	—	—	—	—	—	—	—	—	—	—	—	—	—	—	0.1	0.2	0.6	3.0	89.2	6.0	0.7	0.2	—	—
28	—	—	—	—	—	—	—	—	—	—	—	—	—	—	—	—	—	—	—	—	—	—	—	0.1	0.3	0.6	3.5	87.3	7.2	0.7	0.3	—
29	—	—	—	—	—	—	—	—	—	—	—	—	—	—	—	—	—	—	—	—	—	—	—	—	0.2	0.2	0.7	3.4	87.6	6.9	0.7	0.2
30	—	—	—	—	—	—	—	—	—	—	—	—	—	—	—	—	—	—	—	—	—	—	—	—	—	0.2	0.4	0.8	3.8	85.8	8.2	0.8
31	—	—	—	—	—	—	—	—	—	—	—	—	—	—	—	—	—	—	—	—	—	—	—	—	—	—	0.2	0.4	0.6	3.0	86.9	8.8
32	—	—	—	—	—	—	—	—	—	—	—	—	—	—	—	—	—	—	—	—	—	—	—	—	—	—	—	0.3	0.3	0.7	4.4	94.4

A.9. Intensity values for all measured helium line ratios

Table A.9.: Comparison of all measured line ratios for the first two time intervals in Fig. 6.2. The maximum and minimum values of the ratios along the measured radius are given. The column with the value for max/min shows the dependence of the given ratios on changes of T_e and n_e along the radius. The absolute emission intensity of the weaker line of a ratio limits the possible time resolution of measurements. Thus the relative intensity of transitions with respect to the weakest line is given. The intensity is averaged along the radial profile for each time interval.

		L-mode: 2.14–2.37 s				H-mode: 3.34–3.57 s			
line ratio	spin type	max ratio	min ratio	max/ min	rel int	max ratio	min ratio	max/ min	rel int
447/492	t / s	5.24	1.61	3.25	7	4.84	1.22	3.98	8
447/501	t / s	6.64	1.03	6.47	9	6.59	0.65	10.1	10
447/504	t / s	24.1	15.2	1.59	1	34.1	10.3	3.31	1
447/587	t / t	0.14	0.06	2.20	21	0.09	0.06	1.50	25
447/667	t / s	0.87	0.16	5.51	21	0.81	0.10	7.96	25
447/706	t / t	0.58	0.26	2.23	21	0.46	0.28	1.63	25
492/501	s / s	1.31	0.62	2.11	7	1.36	0.53	2.55	8
492/504	s / s	9.42	4.55	2.07	1	8.49	6.82	1.24	1
492/587	s / t	0.07	0.02	3.57	7	0.05	0.02	2.71	8
492/667	s / s	0.17	0.10	1.70	7	0.17	0.08	2.02	8
492/706	s / t	0.36	0.06	6.25	7	0.38	0.06	6.47	8
501/504	s / s	14.8	3.62	4.09	1	15.9	5.18	3.07	1
501/587	s / t	0.11	0.02	6.79	9	0.10	0.01	6.83	10
501/667	s / s	0.16	0.12	1.35	9	0.16	0.12	1.29	10
501/706	s / t	0.56	0.05	12.3	9	0.71	0.04	16.5	10
504/587	s / t	0.01	0.00	2.15	1	0.01	0.00	2.23	1
504/667	s / s	0.04	0.01	3.47	1	0.02	0.01	2.45	1
504/706	s / t	0.04	0.01	3.04	1	0.04	0.01	5.37	1
587/667	t / s	7.79	1.45	5.37	61	8.74	1.63	5.37	66
587/706	t / t	5.57	2.13	2.61	66	7.48	3.07	2.44	75
667/706	s / t	3.64	0.35	10.4	61	4.54	0.35	12.9	66

B. Acknowledgments

Der Bau einer komplett neuen Diagnostik an einem Großprojekt wie ASDEX Upgrade ist eine umfangreiche Aufgabe, welche ohne die vielseitige Hilfe aller Mitarbeiter des Instituts nicht möglich gewesen wäre. Daher gilt mein erster Dank dem **ASDEX Upgrade Team** und insbesondere meinem Doktorvater **Prof. Ulrich Stroth**, der mich in seine Abteilung aufnahm. Die regelmäßigen Treffen, bei welchen wir nicht nur den Fortschritt beim Bau der Diagnostik besprechen, sondern auch über die physikalischen Einsatzbereiche dieser diskutieren konnten, formten maßgeblich diese Arbeit.

Ein besonderes Dankeschön verdient **Dr. Elisabeth Wolfrum**, welche sich mit mir zusammen als meine direkte Betreuerin in das für ASDEX Upgrade neue Diagnostikkonzept der Helium Linienspektroskopie einarbeitete. Durch ihre fundierten Kenntnisse der Plasmarandphysik leistete sie einen erheblichen Beitrag zum Erfolg der Arbeit und der Diagnostik. Sie hatte stets ein offenes Ohr für alle Belange rund um die Doktorarbeit und darüber hinaus. Die persönliche, stets unkomplizierte und enge Zusammenarbeit mit ihr führte zu einem hervorragenden, motivierenden Arbeitsklima.

Die langjährige Erfahrung von **Prof. Oliver Schmitz** mit der Heliumstrahdiagnostik am Experiment TEXTOR legte den Grundstein dafür, eine solche Diagnostik auch an ASDEX Upgrade zu etablieren und gab somit auch den Anstoß für diese Arbeit. Bei meinem Forschungsaufenthalt in Wisconsin und durch die zahlreichen Videokonferenzen konnte ich in großem Maße von seinem Wissen profitieren, welches das gesamte Projekt inspirierte. Insbesondere bei der Weiterentwicklung des Stoß-Strahlungs-Modells möchte ich auch **Dr. Jorge Muñoz Burgos** danken. Ohne diese Kollaboration wäre ein vergleichbarer Fortschritt nicht möglich gewesen.

Motiviert in die Plasmaphysik einzusteigen hat mich **Dr. Thomas Eich**. Durch seine Vorlesung in Ulm konnte er mich für die Fusionsforschung begeistern und mich davon überzeugen, das ebenso spannende Gebiet der experimentellen Quantenoptik zu verlassen. Es hat sich gezeigt, dass sich die Arbeit in beiden Gebieten sehr ähnelte, obwohl 15 Zehnerpotenzen zwischen den untersuchten Temperaturen liegen. Die Vorgehensweisen und Techniken verlangen neben Programmierarbeit in beiden Fällen den Umgang mit Vakuumkomponenten, Optiken, Elektronik und Magnetspulen. Profitieren konnte ich bei all diesen Bereichen durch die Unterstützung von zahlreichen Experten, was zweifelsohne für mich den größten Vorteil an der Arbeit an einem großen Institut wie dem IPP darstellte. Einige der Kollegen, die an sehr wichtigen und auch kritischen Punkten meines Promotionsprojekts mitgewirkt haben, möchte ich besonders hervorheben und mich ebenso bei allen nicht namentlich genannten Kollegen bedanken.

Dr. Ralph Dux war mit seiner Erfahrung als Leiter der Spektroskopiegruppe eine sehr große Hilfe bei diversen optischen Fragen sowie bei der Arbeit mit ADAS. Bei physikalischen Diskussionen, insbesondere über Filamente, konnte ich auf das fundierte Wissen von **Dr. Gregor Birkenmeier** und **Dr. Peter Manz** zurückgreifen. Bei Letzterem möchte ich mich auch insbesondere für die Koordination unserer Graduiertenschule HEPP bedanken.
Dr. Tim Happel danke ich für die Unterstützung bei den umfangreichen Interpretationen meiner Messdaten im Bezug auf I-Mode Phänomene, welche einen zukünftigen Einsatzbereich der neuen Diagnostik darstellen.
Dr. Rainer Fischer möchte ich für die Implementierung des Stoß-Strahlungs-Modells in Fortran und die Einbindung in die Bayessche Umgebung danken. Dieses Vorgehen half beim Verständnis und der Weiterentwicklung der Modelle und wird auch zukünftig die Diagnostikauswertung weiter verbessern. Ferner danke ich Rainer für die Aufnahme in das Volleyballteam, welches einen guten Ausgleich zur Büroarbeit darstellt.

Neben den physikalische Grundlagen und Fragestellungen ist vor allem der Aufbau der Diagnostikhardware von zentraler Bedeutung für meine experimentelle Arbeit. An erster Stelle möchte ich daher **Manfred Sochor** danken, welcher als Konstrukteur beste Arbeit geleistet hat. Er konnte nicht nur meine Vorgaben präzise und schnell umsetzen, sondern hat mit eigenen Ideen bei noch offenen Punkten das Projekt sehr bereichert. Zudem möchte ich **Wolfgang Zeidner** und **Dr. Albrecht Herrmann** danken, welche zusätzliche Ideen lieferten und den reibungslosen Einbau der Teile an ASDEX Upgrade ermöglichten. Danken möchte ich auch **Prof. Arne Kallenbach**, welcher den Einbau und den Betrieb der neuen Diagnostik für ASDEX Upgrade unterstützte.
Beim Aufbau und der Charakterisierung des Piezoventils zur lokalen Heliuminjektion standen Arbeiten im Vakuumlabor im Mittelpunkt. Mein bester Dank geht daher an **Dr. Volker Rohde** und **Detlef Bösser** für die Unterstützung und die gute Zusammenarbeit. Ebenso danke ich **Karola Bald**. Unserem SIMATIC Experten **Dr. Pascal De Marné** habe ich das hervorragend funktionierende Steuerprogramm für das Ventil zu verdanken, welches er kontinuierlich meinen Wünschen anpasste. Ohne dies wäre ein reibungsloser Ablauf der Experimente nicht möglich.
Horst Eixenberger und **Andreas Wöls** danke ich für die Unterstützung bei der Elektronikentwicklung und dem Aufbau der schnellen Datenerfassung SIO-2 sowie der Inbetriebnahme und den Tests der Photomultiplier. **Dr. Karl Behler** sowie **Roland Merkel** und **Helmut Blank** unterstützten die Datenerfassung von programmiertechnischer Seite und standen mir bei allen Problemen während des Betriebes mit Rat und Tat zur Seite.
Maximilian Pichl und **Klaus Sauerer** waren die tragenden Kräfte, wenn es um den Anschluss von Leitungen und die Inbetriebnahme elektrischen Anlagen ging. Sie verloren nie die Geduld, nicht einmal, wenn ein und dasselbe Kabel zum fünften Mal repariert werden musste.
Michael Ebner war die helfende Hand, welche bis spät abends für mechanische Fragen und Hardware Installationen in der Torushalle zur Verfügung stand. Stellvertretend für das gesamte Gefäßteam gilt ihm mein bester Dank. Als Leiter der feinmechanischen Werkstatt möchte ich **Karl Eismann** danken, welcher mit seinen Kollegen stets auch kurzfristig Hilfe ermöglichte.
Da die Sicherheit beim Aufbau neuer Anlagen natürlich auch nicht vergessen werden darf, ins-

besondere wenn man Gasversorgungssysteme für explosionsfähigen Wasserstoff baut, möchte ich **Michaela Uhlmann** danken, welche bei der Kooperation mit der DEKRA eine tragende Rolle einnahm.

Bei **Dr. Bernhard Sieglin** möchte ich mich für die Programmierunterstützung mit Python sowie bei der Initialisierung der Schussfile-header bedanken. **Dr. Golo Fuchert** sowie **Dr. Tilmann Lunt** waren eine große Hilfe beim Betrieb der schnellen Kameras sowie der Auswertung ihrer Daten.
Ein weiterer Dank geht an **Dr. Dirk Wünderlich**, welcher mit seiner Erfahrung bei Stoß-Strahlungs-Modellen hilfreiche Informationen bereitstellte. **Dr. Athina Kappatou** ermöglichte die Auswertung der absoluten Heliumkonzentration im Plasma, was für das Abschätzen des Einflusses meiner Diagnostik auf das Plasma eine große Hilfe darstellt. Vor allem beim Umgang mit dem pinboard und dem logbook war **Dr. Christoph Fuchs** ein ständiger Ansprechpartner.
Ferner danke ich **Dr. Günter Haas** und **Dr. Andrea Scarabosio** für die Einführung in den Umgang mit den ASDEX Manometern, welche mein zukünftiges Aufgabengebiet erweitern werden.
Ich danke **Dr. Marco Cavedon** für die großzügige Unterstützung bei Programmierfragen sowie dem Betrieb der CXRS Spektrometer, für welchen ich auch **Dr. Eleonora Viezzer** und **Ulrike Plank** danken möchte. Danke zudem an **Dr. Mathias Dibon** für die gute Zusammenarbeit bei der Entwicklung der Piezoventile. **Dr. Ian Faust** sowie **Dr. Simon Freethy** danke ich insbesondere für ihre Expertise als Muttersprachler bei Fragen zur englischen Sprache beim Verfassen von Veröffentlichungen und meiner Dissertation.
Gabriele Dörsch und **Biggy Perey** möchte ich für ihre Unterstützung bei verwaltungstechnischen Fragen sowie bei Konferenzorganisationen herzlich danken.

Unzählige Stunden wissenschaftlicher Diskussionen halfen diverse Probleme zu verstehen und Fragestellungen aus verschiedene Sichtwinkeln zu beleuchten. Meine Bürokollegen der letzten drei Jahre, **Dr. Felician Mink** und **Dr. Javier Pinzon**, sind hierbei ganz besonders zu nennen. Sie halfen mir nicht nur Computer- und Programmierprobleme zu bewältigen, sondern auch sämtliche anderen Hürden zu überwinden, mit welchen man sich im Laufe der Doktorarbeit konfrontiert sieht. Ich werde unsere gemeinsame Bürozeit definitiv vermissen.
Ferner gilt mein Dank auch meinen weiteren Kollegen **Dr. Michael Faitsch** und **Stephan Glöggler**, welche wie ich aus Ulm den Weg zur Fusionsforschung gefunden haben. Zusammen etablierten wir Spieleabende, bei denen wir uns mit meinen Bürokollegen sowie **Dr. Dominik Brida** und **Georg Harrer** über Berufliches und Privates austauschen konnten, wie auch beim Mittagessen mit **Klara Höfler**.

Konferenzen eignen sich ebenso bestens dafür, Berufliches und Privates zu verknüpfen. Dies war im Anschluss an diese im Rahmen gemeinsamer Aktivitäten und Reisen zusammen mit **Dr. Alexander Mlynek** nach der HTPD 2016, mit **Dr. Michael Faitsch** nach der EPS 2017 sowie mit **Ana Kostic** und **Mariia Usoltceva** nach der HTPD 2018 möglich. All diese Reisen waren eine großartige Erfahrung, welche die tolle Zeit während der Doktorarbeit nochmals aufwerteten. Bei letzteren beiden Reisen begleitete mich auch meine Freundin **Dr. Angela Braig**,

die mich nicht nur während meiner Doktorarbeit, sondern auch schon während meines gesamten Studium stets unterstützte. In exzellenter Weise konnte sie mich nicht nur motivieren, sondern mich auch durch intensive Diskussionen in zahlreichen wissenschaftlichen Fragen weiterbringen. Zuletzt möchte ich meinen Eltern **Ludwig** und **Maria Griener** danken, welche mich in meinem gesamten Leben uneingeschränkt unterstützten und stets an mich glauben.